

# **Influence of Linked Hydrologic and Geomorphic Processes on the Terrestrial Carbon Cycle**

A Dissertation  
Presented to  
The Academic Faculty

by

Ioannis Minas (Yannis) Dialynas

In Partial Fulfillment  
of the Requirements for the Degree  
of Doctor of Philosophy in the  
School of Civil and Environmental Engineering

Georgia Institute of Technology  
May, 2017

**Copyright © 2017 by Yannis Dialynas**

# **Influence of Linked Hydrologic and Geomorphic Processes on the Terrestrial Carbon Cycle**

Approved by:

Dr. Rafael L. Bras, Advisor  
School of Civil and Environmental Engineering and  
School of Earth and Atmospheric Sciences  
*Georgia Institute of Technology*

Dr. Aris P. Georgakakos  
School of Civil and Environmental Engineering  
*Georgia Institute of Technology*

Dr. Jingfeng Wang  
School of Civil and Environmental Engineering  
*Georgia Institute of Technology*

Dr. Daniel deb. Richter  
Nicholas School of the Environment and Earth Sciences  
*Duke University*

Dr. Athanasios Nenes  
School of Earth and Atmospheric Sciences and  
School of Chemical & Biomolecular Engineering  
*Georgia Institute of Technology*

Date Approved: January 06, 2017

To my parents, Giorgos and Manolia, and to my siblings, Katerina and Manolis.

## ACKNOWLEDGEMENTS

This research has been supported by the National Science Foundation under the Luquillo Critical Zone Observatory effort (Awards EAR-0722476 and EAR-1331841), and the Calhoun Critical Zone Observatory effort (Award EAR-1331846), and by the NASA Headquarters under the NASA Earth and Space Science Fellowship Program (Grant 16-EARTH16F-33).

Studying concepts of stochastic hydrology at the age of 22 from the book “Random Functions and Hydrology” [*Bras and Rodriguez-Iturbe*, 1985] during my undergraduate studies at the National Technical University of Athens, little did I know that I would soon be pursuing a Ph.D. degree under the advising of Prof. Rafael L. Bras at Georgia Tech. An inspiring figure and a great mentor, Dr. Bras taught me to not take anything for granted, and always ask “why”. Following his scientific vision and research methodology I learned how to identify scientifically and socially important problems, and address research questions following different approaches. Dr. Bras’ persistence and dedication to advising significantly contributed to both my academic and professional development. This work would not have been possible without his close guidance, intuitive remarks, and didactic comments.

Words cannot express how grateful I am for the continuous support of Prof. Aris P. Georgakakos throughout the entire course of my graduate studies. I consider myself very lucky to have served as a member of his research team in the Georgia Water Resources Institute at Georgia Tech. Dr. Georgakakos has been a very charismatic advisor and mentor, and a dear friend. He taught me to never give up, and that humility and confidence

are the two most important character traits to be successful. His mentoring and advising have played a crucial role on my academic progress, and have greatly influenced this doctorate research.

I am very grateful to the rest of my Ph.D. Committee members: Prof. Daniel deb. Richter, Prof. Jingfeng Wang, and Prof. Athanasios Nenes. Their insightful and constructive comments led to substantial improvements of this thesis, and their guidance helped me view research problems from different perspectives. I am especially grateful for the substantial contribution of Prof. Richter to this work. Dan is an extremely enthusiastic individual, characterized by a unique ability to impart his excitement for soil science to his students and mentees.

I would also like to thank my undergraduate thesis advisor, Prof. Demetris Koutsoyiannis, for being a wonderful teacher and a friend, and for guiding me through my first steps in the world of research. Demetris is responsible for me beginning to realize at a relatively early stage that natural phenomena are not necessarily described by deterministic rules. His vision and enthusiasm for basic research and advanced concepts of hydroclimatic stochastics inspired me to pursue a career in the area of hydrology and water resources.

I would like to thank Profs. Valerio Noto, Sharon Billings, Daniel Markewitz, Whendee Silver, Erika Marin-Spiotta, Thanos Papanicolaou, and Praveen Kumar for our collaboration and discussions on the topic of hydrologically-induced soil and organic carbon erosion, which influenced the research directions and methodologies followed in this work. I would like to especially thank Sharon Billings, with whom I had several

meetings discussing fundamentals of soil biogeochemistry, and modelling of soil organic carbon fluxes.

I can't thank enough my colleagues within the Bras group, Elisa Arnone, Prof. Ardeshir Ebtehaj, Prof. Jingfeng Wang, Satish Bastola, Liao-Fan Lin, Shawna McKnight, Sanaz Moghim, Hao-Lin Hu, and Jiaying Zhang, who provided extremely useful feedback over the years. I will most certainly miss working with such a wonderful group of individuals.

From chasing landslides in Puerto Rico's Luquillo Mountains to building models of natural systems, collaborating with Elisa Arnone has been an exciting experience. Elisa's exceptional contribution in chapter 5 is acknowledged and greatly appreciated. Satish Bastola has been an amazing colleague, and has significantly helped me in this effort. Also, working side by side with my good friend and mentor, Ardeshir Ebtehaj, has been a great pleasure.

In these last words of appreciation, I would like to thank my parents, Giorgos and Manolia, and my siblings, Katerina and Manolis, to whom this thesis is dedicated, for their endless love and support. My father taught me that the road to success is long, and that success is about reaching where others simply cannot. This paradigm may have motivated me to focus on working at the best of my ability in this beautiful journey.

# TABLE OF CONTENTS

ACKNOWLEDGEMENTS .....	iv
LIST OF TABLES .....	xiii
LIST OF FIGURES .....	xvi
SUMMARY.....	xxiii
CHAPTER 1. Introduction: Significance of coupled and spatially-explicit representations of hydro-geomorphic and biogeochemical processes across scales.....	1
CHAPTER 2. Topographic variability and the influence of soil erosion on the carbon cycle in a degraded agricultural landscape .....	7
2.1 Introduction .....	7
2.2 Materials and methods.....	8
2.2.1 Spatially- and depth-explicit model of carbon dynamics .....	8
2.2.2 Physically-based hydro-geomorphic model .....	12
2.2.3 SOrCERO model .....	15
2.3 Study area .....	15
2.4 Model inputs .....	17
2.4.1 Biogeochemical parameters.....	17
2.4.2 Carbon Oxidation and Production Parameters: Sensitivity Analysis on Effects of Management Practices .....	21
2.4.3 Land Surface Data .....	24
2.4.4 Hydrometeorological forcing and validation of the hydrologic model .....	24

2.4.5	Biogeomorphic properties .....	28
2.5	Results.....	31
2.5.1	Influence of episodic erosion on the carbon exchange with the atmosphere.....	31
2.5.2	Watershed-integrated analysis.....	38
2.6	Discussion.....	42
2.6.1	Erosion-induced soil-atmosphere carbon exchange .....	42
2.6.2	Episodic erosion of soil organic carbon .....	44
2.6.3	Spatial variation of carbon replacement .....	46
2.7	Summary.....	48
CHAPTER 3. Uncertainty associated with the impact of erosion and deposition on soil-atmosphere carbon exchange.....		
3.1	Introduction .....	50
3.2	Stochastic representation of the influence of land management practices on eroding soils.....	51
3.3	Model inputs and parameters.....	54
3.3.1	Evolution of vegetation cover during reforestation.....	54
3.3.2	Topography, soil types, and soil biogeochemical properties .....	57
3.3.3	Uncertainty in carbon storage prediction associated with the influence of land management practices .....	58
3.3.4	Calibration of the hydro-geomorphic model .....	63
3.4	Results.....	64
3.4.1	Accelerated soil erosion and deposition .....	64



3.4.2	Erosion-induced carbon exchange with the atmosphere at the watershed scale .....	65
3.4.3	Soil organic carbon erosion and burial at alluvial sediments .....	66
3.5	Discussion.....	68
3.5.1	Sediment and organic carbon transport and burial across the landscape .....	68
3.5.2	Decline of upland sediment and organic carbon erosion with reforestation.....	73
3.5.3	Uncertainty associated with management practices in estimates of watershed-integrated net soil-atmosphere carbon exchange .....	75
3.6	Summary.....	78
CHAPTER 4. Impact of hydrologically driven hillslope erosion and landslide occurrence on soil organic carbon dynamics at tropical watersheds.....		
4.1	Introduction .....	80
4.2	Physical representation of hillslope erosion and landslide occurrence .....	82
4.3	Study Area .....	84
4.4	Input data and parameters.....	88
4.4.1	Biogeochemical parameters.....	88
4.4.2	Effects of land uses on soil organic carbon fluxes .....	92
4.4.3	Topography and soil textural classes.....	95
4.4.4	Hydrometeorological forcing .....	95
4.4.5	Hydrologic model calibration.....	96
4.4.6	Geomorphologic model calibration .....	99

4.5	Results.....	101
4.5.1	Hillslope erosion and deposition .....	101
4.5.2	Watershed-integrated carbon exchange with the atmosphere .....	104
4.5.3	Erosion-induced carbon fluxes in different forest types.....	107
4.5.4	Soil organic carbon burial in alluvial sediments .....	110
4.6	Discussion.....	111
4.6.1	Hillslope erosion and landscape equilibrium .....	111
4.6.2	Soil organic carbon redistribution across the landscape.....	113
4.6.3	Assessing the likelihood of modelled scenarios .....	115
4.6.4	Influence of forest types on the erosion-induced carbon fluxes.....	116
4.6.5	Net atmospheric carbon sink or source .....	117
4.6.6	Soil organic carbon replacement at landslide scars .....	118
4.6.7	Potential limitations of the approach .....	120
4.7	Summary.....	120
CHAPTER 5. Uncertainty in rainfall-triggered landslide modelling associated with the spatial variation of soil hydrological and geotechnical properties .		122
5.1	Introduction .....	122
5.2	Methods .....	125
5.2.1	Coupled Hydrological-Stability Model .....	125
5.2.2	Probabilistic Framework .....	127
5.3	Case study.....	130
5.3.1	Input data and model parameters.....	131

5.3.2	Selection of Digital Elevation Model .....	134
5.4	Factor of safety probability distribution .....	142
5.5	Rainfall analysis .....	145
5.6	Results .....	149
5.6.1	Time series model output .....	150
5.6.2	Effect of rainfall temporal distribution .....	154
5.6.3	Discussion.....	160
5.7	Summary.....	164
CHAPTER 6.	Lithological control on the hydro-geomorphic response of tropical watersheds to changing climate.....	166
6.1	Introduction .....	166
6.2	Materials and methods.....	169
6.2.1	Study area .....	169
6.2.2	Climatic scenarios and projected change .....	171
6.3	Results .....	173
6.3.1	Projected rates of hillslope erosion and deposition .....	173
6.3.2	Simulated slope instability .....	176
6.4	Discussion.....	178
6.4.1	Propensity for landslide occurrence .....	178
6.4.2	Landscape equilibrium in changing climate.....	184
6.5	Summary.....	188
CHAPTER 7.	Thesis summary and future research .....	190

7.1	Hydrologically-induced erosion of soil organic carbon in diverse tropical montane and temperate forest ecosystems .....	190
7.2	Conclusions .....	197
7.2.1	Understanding a severely degraded agricultural landscape: Soil erosion and burial of soil organic carbon .....	197
7.2.2	Hillslope erosion, landslide occurrence and carbon dynamics at tropical watersheds .....	200
7.3	Future Research Directions .....	204
APPENDIX A. Estimation of SOC content at each time step .....		207
APPENDIX B. Estimation of initial depth-dependent SOC production rates .....		208
APPENDIX C. Estimation of the variability of carbon storage .....		209
REFERENCES.....		211

## LIST OF TABLES

Table 2.1. Initial values of tRIBS-ECO and SOrCERO biogeochemical model parameters. Three values for $C_b$ and for $I_b$ are given, corresponding to ridges, upper slopes, and lower slopes, respectively. Observations of C content and bulk density (site B in Figure 2-2a) were obtained from previous studies at the site [Billings <i>et al.</i> , 2010; Markewitz and Richter, 1998; Richter <i>et al.</i> , 1999]. Three values for $a_k$ and $a_l$ (tRIBS-ECO) and for $n_{ox}$ and $n_{prod}$ (SOrCERO) are given, corresponding to the maximum sink, the intermediate, and the maximum source scenarios, respectively (see section 2.4.2). SOrCERO was initialized by the observed C concentration and bulk density illustrated in Figures 3a and 3b, respectively, and by the depth-dependent SOC oxidation rate estimated by Billings <i>et al.</i> [2010] (Figure 2-3c). .....	23
Table 2.2. Hydrologic and geomorphic soil parameters for each soil type. ....	31
Table 2.3. Ecological parameters of the hydro-geomorphic model. ....	31
Table 2.4. Soil organic carbon (SOC) content at soil profiles in relatively undisturbed hardwood stands and in eroded old-field pine stands, at the Calhoun Critical Zone Observatory [Billings <i>et al.</i> , 2010; Markewitz and Richter, 1998; Richter and Markewitz, 2001; Richter <i>et al.</i> , 1999]. Data from four soil profiles of each forest type were available. The coefficients of variation are given in parentheses. The estimated mean difference in SOC content ( $\Delta$ SOC approximately equal to $1.7 \text{ kg m}^{-2}$ ) represents the cumulative SOC loss to erosion during the agricultural history of the area [Trimble, 1974]. ....	37
Table 2.5. Comparison of watershed-integrated estimates of the net soil-atmosphere C exchange with published estimates. Positive and negative values correspond to net erosion-induced C sources and sinks, respectively (values in $\text{g C m}^{-2} \text{ yr}^{-1}$ ). ....	39
Table 2.6. Statistics of the total eroded and replaced soil organic carbon (SOC) at eroding sites, and of the net total SOC difference ( $\Delta$ SOC) at the watershed scale for the 100-year intermediate scenario (values in $\text{kg m}^{-2}$ ). ....	41
Table 3.1. Marginal and joint statistical properties and ranges of $a_l$ and $a_k$ . $E[\cdot]$ denotes the mean value. Equal coefficients of variation (CV) and autocorrelation coefficients for $a_l$ and $a_k$ , were assumed ( $\rho_{a_k}$ and $\rho_{a_l}$ ), respectively. ....	62
Table 3.2. Ecological parameters of the geomorphic model. The first two rows (gray) correspond to the agro-ecosystem period; the remaining rows correspond to the secondary forest ecosystem period. ....	63
Table 4.1. Aboveground NPP (ANPP) and belowground NPP (BNPP) values for different forest types across the Luquillo CZO. The ANPP values were derived from observations [Weaver and Murphy, 1990]. The BNPP values were reported by Wang	

<i>et al.</i> [2003], based on belowground and aboveground biomass estimates for the entire Luquillo CZO.....	91
Table 4.2. Values of $a_k$ and $a_i$ for the Mameyes and the Icacos watersheds. I, II, and III correspond to the maximum source, the intermediate, and the maximum sink scenarios, respectively. ....	94
Table 4.3. Soil hydrological and mechanical parameters. Two sets of values of shear stress based soil erodibility ( $K_b$ ) are given, corresponding to the Mameyes and to the Icacos (in parenthesis) watersheds, respectively. ....	98
Table 4.4. Metrics of hydrologic and geomorphic validation performances.....	99
Table 4.5. Total difference in soil organic carbon storage ( $\Delta SOC$ ) in eroding soil profiles at different forest cover in the Mameyes (M) and Icacos (I) watersheds. ....	109
Table 4.6. Soil organic carbon (SOC) deposition at the floodplains of Rio Mameyes and Rio Icacos. I, II, and III correspond to the maximum source, the intermediate, and the maximum sink scenarios, respectively.....	110
Table 5.1. Hydrological and mechanical soil properties and their statistics for the four soil types present in the Mameyes basin.....	132
Table 5.2. Number of DEM cells, TIN nodes, and Voronoi cells for each Grid-DEM resolution.....	136
Table 6.1. Comparison of simulated rates of hillslope erosion with reported erosion rates in the Mameyes and Icacos watersheds. Simulations correspond B1 and A2 scenarios of climatic projections (section 6.2.2).....	175
Table 6.2. Observed and simulated (B1 and A2 scenarios) landslide area at the two watersheds. Observations [ <i>Larsen</i> , 1997; <i>Larsen</i> , 2012] correspond to relatively recent scars, and to total observed scars which include landslides dated up to 1,000 years. ....	176
Table 6.3. Comparison of projected hillslope erosion rates (B1 and A2 climatic scenarios) with recently reported bedrock weathering rates (values are given in mm kyr <sup>-1</sup> )......	187
Table 7.1. Mean annual precipitation (MAP) and mean annual temperature at the Holcombe's Branch (Calhoun CZO) and at the Mameyes and Icacos watersheds (Luquillo CZO). ....	191
Table 7.2. Simulated soil erosion rates at the Holcombe's Branch (Calhoun CZO) and at the Mameyes and Icacos watersheds (Luquillo CZO). ....	193
Table 7.3. Simulated erosion-induced soil-atmosphere C exchange in the Calhoun CZO and the Luquillo CZO for the maximum source, the intermediate, and the	

maximum sink scenarios (sections 3.3.3 and 4.4.2) of C fluxes (values in $\text{g C m}^{-2} \text{yr}^{-1}$ ). .....	194
---	-----

Table 7.4. Proportions of C erosion occurring in dry vs. wet years, and in relatively dry vs. relatively wet days, in the Calhoun CZO and in the Luquillo CZO. ....	197
--	-----

## LIST OF FIGURES

Figure 2-1. Illustration of the effect of management practices on altered depth-dependent SOC oxidation $k_i(z)$ . Assume that by time $t_2$ soil erosion leads to the removal of a soil layer with the new surface having an oxidation rate $k_{i_2}(z=0)$ , altered from $k_{i_1}(z=0)$ . It is proposed that land management practices can have an effect on altered oxidation at a rate $a_k$ . The framework is also applied to SOC production [Billings <i>et al.</i> , 2010]. .....	11
Figure 2-2. Digital Elevation Model of the Holcombe's Branch watershed (a), topographic classification of the watershed; initial total SOC storage (calculated in the upper 5 m of soil) at ridges, upper, and lower slopes is equal to $10.3 \text{ kg m}^{-2}$ , $12.7 \text{ kg m}^{-2}$ , and $16.7 \text{ kg m}^{-2}$ , respectively (b), spatial distribution of soil textural classes (c), and of vegetation types (d).....	16
Figure 2-3. Exponential functions fitted to observations, to parsimoniously represent the depth variation of soil biogeochemical properties at multiple horizons: organic carbon concentration (a), bulk density (b), and oxidation rate of organic carbon (c). The observations were obtained from site B (Figure 2-2a). The variation of initial organic carbon concentration at different hillslope positions illustrated in (a) corresponds to the topographic classification of Figure 2-2b. The initial depth-dependent SOC concentration at ridges was obtained by fitting equation (2) to the observations [Billings <i>et al.</i> , 2010]. The depth-dependence of initial organic carbon concentration at upper and lower slopes was estimated based on the analysis conducted by Rosenbloom <i>et al.</i> [2006] (see section 2.4.1). The associated parameters are given in Table 2.1. ....	19
Figure 2-4. Sensitivity analysis on the effect of management practices to the total difference in soil organic carbon storage ( $\Delta\text{SOC}$ ). The net result of soil organic carbon (SOC) production, oxidation, and SOC loss to erosion is illustrated, as the effects of management practices on altered oxidation and production ( $a_k$ and $a_l$ , respectively) vary. Positive values of $\Delta\text{SOC}$ indicate net increase of SOC at the eroding site, while negative values represent net SOC loss to the atmosphere and to erosion. ....	22
Figure 2-5. Hydrologic model validation in terms of soil moisture content. Soil moisture observations from four gypsum blocks at a depth of 15 cm versus simulated series, and corresponding rainfall intensity; $S$ denotes effective saturation [Rawls <i>et al.</i> , 1982]: $S = \frac{\theta - \theta_r}{\theta_s - \theta_r}$ , where $\theta$ is the volumetric soil moisture content, $\theta_r$ is the residual volumetric water content, and $\theta_s$ is the saturated volumetric water content. ....	28
Figure 2-6. Spatially-explicit representation of soil erosion and of soil organic carbon redistribution. Higher sediment deposition rates are illustrated in blue (e.g., across the stream network), while eroding sites (yellow to red) dominate hillslopes (a). Total difference in soil organic carbon storage ( $\Delta\text{SOC}$ ) across the landscape corresponding	



to the maximum source scenario ( $14.5 \text{ g C m}^{-2} \text{ yr}^{-1}$ ) (b), the intermediate scenario ( $0.08 \text{ g C m}^{-2} \text{ yr}^{-1}$ ) (c), and the maximum sink scenario ( $-18.2 \text{ g C m}^{-2}$ ) (d)..... 30

Figure 2-7. Temporal evolution of soil erosion at site A. The episodic character of soil erosion is evident (in blue), compared to the case of constant erosion (around  $3 \text{ mm yr}^{-1}$ , in black). Negative values of elevation change ( $\Delta z$ ) denote erosion-induced net depression of soil surface, as a result from the 100-year hydro-meteorological forcing. .... 32

Figure 2-8. Temporal evolution of the difference in total profile soil organic carbon storage ( $\Delta \text{SOC}$ ) resulting from SOC fluxes at eroding site A for tRIBS-ECO (in blue) and for SOrCERO (in black), and  $\Delta \text{SOC}$  based on the observations of Table 2.4 (red points; the associated range corresponds to one standard deviation). Maximum sink and maximum source scenarios for both models are illustrated in (a) and (b), respectively. The positive vertical axis in (a) is at a different scale. Positive and negative values of  $\Delta \text{SOC}$  represent a net sink and source of atmospheric  $\text{CO}_2$ , respectively. In (a) and (b) for each model two extreme cases on the fate of eroded SOC are illustrated: The series with relatively higher value of total  $\Delta \text{SOC}$  correspond to the case where eroded SOC leaving the soil profile is completely oxidized during transport and burial; the series with relatively lower value of total  $\Delta \text{SOC}$  correspond to the case where the eroded SOC is fully protected from oxidation. Depending on the fate of eroded SOC, estimates by the two scenarios are in the vicinity of the net C exchange with the atmosphere of the site. Simulated net SOC losses to erosion corresponding to intermediate scenarios for the two models are compared against the observed  $\Delta \text{SOC}$  in (c). The quantitative equivalency of the illustrated intermediate scenarios is discussed in section 2.5.1. The episodic erosion in tRIBS-ECO leads to a closer representation of the history of SOC erosion of the site. .... 35

Figure 2-9. Topographic variation of simulated soil organic carbon storage across the watershed. Total soil organic carbon (SOC) storage at the upper 5 m of soil is illustrated for the maximum source (a), intermediate (b), and maximum sink (c) scenarios, respectively. .... 40

Figure 2-10. Net carbon flux into eroding soils due to replacement by vegetation inputs versus erosion-induced lateral carbon flux. This figure illustrates the wide topographic variation of carbon (C) fluxes across the landscape for the intermediate scenario. 34% of the eroding C is being replaced by sequestered C from the atmosphere. A significant coefficient of variation (defined as the ratio of standard deviation over the mean) of around 8 characterizes the large natural spatial variability of the C replacement ratio (i.e., the ratio of C uptake over C loss to erosion). .... 42

Figure 3-1. The Holcombe's Branch; site A corresponds to an undisturbed soil profile; sites B to F correspond to sampling locations of legacy sediments (a), spatial distribution of vegetation cover in 1933 (agro-ecosystem period (Figure 3-2)) (b), and in 2014 (secondary forest ecosystem period [NCALM, 2014]) (c), and spatial distribution of soil textural classes (d). .... 55

Figure 3-2. Aerial photo of the Holcombe's Branch watershed during the agro-ecosystem period (1933) [Brecheisen and Cook, 2015]. The black line illustrates the watershed divide. ....	57
Figure 3-3. Observations and model inputs of depth-dependent soil organic carbon (SOC) fraction (a), and estimated SOC decomposition rate at multiple soil horizons (b) [Billings et al., 2010; Markewitz and Richter, 1998; Richter and Markewitz, 2001; Richter et al., 1999]. The depth-variation of observations is represented by exponential functions.....	58
Figure 3-4. Temporal evolution of soil loss at eroding sites.....	64
Figure 3-5. Simulated soil erosion and deposition and net soil organic carbon content difference ( $\Delta$ SOC) across the Holcombe's Branch. Relatively high erosion rates characterize hillslopes (yellow and orange colors); depositional sites (in blue) are mainly located across the stream network (a). Redistribution of organic material for the maximum source ( $10.3 \text{ g m}^{-2} \text{ yr}^{-1} \text{ C}$ source strength) (b), the intermediate ( $-1.5 \text{ g m}^{-2} \text{ yr}^{-1} \text{ C}$ sink strength) (c), and the maximum sink scenarios ( $-8.4 \text{ g m}^{-2} \text{ yr}^{-1} \text{ C}$ sink strength) (d), respectively. ....	65
Figure 3-6. Simulated temporal evolution of net soil organic carbon loss ( $\Delta$ SOC) at upland eroding sites and $\Delta$ SOC inferred from observations (section 2.5). Error bars correspond to one standard deviation. The total $\Delta$ SOC for the intermediate scenario is in close agreement with the observations. ....	67
Figure 3-7. Observed and simulated soil organic carbon (SOC) content in alluvial deposits; observations at depositional sites are based on measurements from sites B, C, D, E, and F at the upper 1.8 m of soil (error bars correspond to one standard deviation); point comparisons between observed and simulated SOC storage at sites B, C, and D, respectively. ....	68
Figure 3-8. Approximately 117 cm of legacy sediment (light brown color) deposited above redox-active Holocene sediments (gray-brown color) at the Holcombe's Branch (site S7) [Richter, 2016].....	70
Figure 3-9. Simulated and observed legacy sediment deposition across the stream network. Sites S1 to S8 are located at approximately 100 - 200 m intervals along the main stream in the Holcombe's Branch watershed, in clayey soils and sandy loams. ....	72
Figure 3-10. Means and standard deviations of soil organic carbon (SOC) storage observations at different depths from alluvial sediments at depositional sites B to F. SOC storage across soil horizons of these alluvial sites is higher than the storage in eroded and relatively undisturbed soil profiles. ....	73
Figure 3-11. Simulated soil organic carbon (SOC) ranges (i.e., difference of maximum source from maximum sink scenario estimates) at each site across the watershed versus slope and curvature (a), and versus contributing area and topographic index ( $\ln(A/\tan\beta)$ , where $A$ is the upslope contributing area and $\beta$ is the local slope) (b) .....	77

Figure 4-1. Digital Elevation Model of the Mameyes watershed; site B corresponds to the location of the Bisley tower (a), spatial distribution of soil textural classes (b), spatial distribution of vegetation types (c).....	86
Figure 4-2. Digital Elevation Model of the Icacos watershed (a), spatial distribution of soil types (b), spatial distribution of vegetation species (c).....	87
Figure 4-3. Observed organic carbon content [Johnson <i>et al.</i> , 2015] and model inputs at different topographic locations corresponding to colorado (a), palm (b), and tabonuco (c) soils at the Mameyes watershed, and colorado (d) and palm (e) soils at the Icacos watershed, respectively .....	89
Figure 4-4. Sensitivity analysis on the influence of land uses to the total soil organic carbon storage difference ( $\Delta$ SOC) for the Icacos (a) and the Mameyes (b) watersheds. $\Delta$ SOC results from the net effect of soil organic carbon (SOC) production, oxidation, and SOC loss to erosion, as the effects of land uses to SOC oxidation and production ( $a_k$ and $a_l$ , respectively) vary. Positive values of $\Delta$ SOC indicate net increase of SOC storage, while negative values represent net SOC loss at the eroding site (color variation corresponds to vertical axis ( $\Delta$ SOC)). .....	94
Figure 4-5. Hydrologic model calibration in terms of river discharge at the Icacos (a) and the Mameyes (b) watersheds. The observed rainfall intensity during the calibration period (01/01/2001 - 06/24/2001) is also provided.....	97
Figure 4-6. Calibration of the geomorphic model in terms of accumulated sediment yield for the Icacos (a) and the Mameyes (b) watersheds. The calibration period starts in January, 1995 and ends in November, 1999.....	101
Figure 4-7. Heavily eroding hillslopes (yellow to red) and landslide sites (red) at the Icacos (a) and the Mameyes (b) watersheds. Depositional sites across river floodplains and at landslide run out tracks are illustrated in blue.....	102
Figure 4-8. Comparison of the simulated landslide occurrence at the Icacos (a) and Mameyes (b) watersheds with the landslide scars (black) reported in Larsen [1997] and in Larsen [2012], who documented a total of 345 landslides in the two watersheds from aerial photographs (1937, 1951, 1962, 1972, 1974, 1979, 1990, and 1995).....	104
Figure 4-9. Spatially-explicit representation of the redistribution of soil organic carbon at the Mameyes watershed. Total difference in soil organic carbon storage ( $\Delta$ SOC) at the watershed scale for the maximum sink scenario (net sink strength of $21.5 \text{ g C m}^{-2} \text{ yr}^{-1}$ ) (a), the intermediate scenario (net sink strength of $6.0 \text{ g C m}^{-2} \text{ yr}^{-1}$ ) (b), and the maximum source scenario (net source strength of $18.3 \text{ g C m}^{-2} \text{ yr}^{-1}$ ) (c). .....	106
Figure 4-10. Spatially-explicit representation of the redistribution of soil organic carbon at the Icacos watershed. Total difference in soil organic carbon storage ( $\Delta$ SOC) at the watershed scale for the maximum sink scenario (net sink strength of $21.5 \text{ g C m}^{-2} \text{ yr}^{-1}$ ) (a), the intermediate scenario (net sink strength of $3.3 \text{ g C m}^{-2} \text{ yr}^{-1}$ ) (b), and the maximum source scenario (net source strength of $14.9 \text{ g C m}^{-2} \text{ yr}^{-1}$ ) (c). .....	107

Figure 4-11. Total difference in soil organic carbon storage ( $\Delta$ SOC) at eroding sites with different forest cover at the Icacos (a) and Mameyes (b) watersheds. Positive and negative values of $\Delta$ SOC represent a net C sink and source, respectively. Maximum sink and maximum source scenarios are illustrated in positive and negative axes, respectively. The effect of erosion on SOC production and oxidation at tabonuco and palm soils is more significant compared to colorado soils. ....	108
Figure 5-1. Catchment slope cumulative frequency distribution for different DEM resolutions. ....	135
Figure 5-2. Catchment slope cumulative frequency distributions corresponding to the 10 m (grid) DEM, and to Voronoi meshes derived from 10 m, 20 m, 30 m , 50 m, and 70 m DEMs. ....	138
Figure 5-3. Spatial slope (in radians) distribution of voronoi cells corresponding different DEM resolutions: 10 m (a), 20 m (b), 30 m (c), and 50 m (d). ....	139
Figure 5-4. Spatial model outputs: FS distributions for Voronoi meshes corresponding to DEM resolutions of 10, 20, 30 and 50 m. The percentage of failing Voronoi cells for each depth (and up to of 2 m) is shown in the relative frequency histogram reported on top of each map. ....	140
Figure 5-5. Box plots of failure slope values (i.e., slope at which each element has failed) for Voronoi meshes corresponding to DEM resolutions of 10, 20, 30 and 50 m. ....	141
Figure 5-6. Comparison of the empirical FS quantiles vs the theoretical FS quantiles of Normal (purple), Lognormal (blue), and Inverse Gamma (red) distributions, for (a) clay, (b) clay-loam, (c) sandy-loam, and (d) silty-clay. The values of slope, depth of failure surface and volumetric water content correspond to 40°, 1000 mm, and 0.3 mm <sup>3</sup> /mm <sup>3</sup> , respectively, while the associated statistical properties are reported on Table 5.1. ....	143
Figure 5-7. Different types of rainfall temporal distributions of 24 hours duration. ....	147
Figure 5-8. Hyetographs at Bisley tower location (indicated in Figure 4-1a) for each type of rainfall events. Total precipitation volume is about 500 mm. ....	148
Figure 5-9. Spatial distribution of total rainfall estimate of hyetograph Q1. Total rainfall ranges from 485 mm of the zone approaching to the basin outlet, to 615 mm of the highest zones. The spatial coefficient of variation is 0.05. ....	149
Figure 5-10. Time series model output response of a clay loam element (52°): rainfall type Q1 (a); volumetric soil content ( $\theta$ ) profile and time series (b); probability of failure at each layer at selected times, $PrF_i$ (c); profile and time series of probability of plane of failure at given depth, $PrPF_i$ (d); $PrPF_i$ at selected times (e). ....	151

Figure 5-11. Time series model output response of a silty-clay element with gentler slope (21°): rainfall type Q1 (a); volumetric soil moisture content ( $\theta$ ) profile and time series (b); profile and time series of probability of plane of failure at given depth, $PrPF_i$ (c); time series of the probability of failure of the column, $PrFC$ (d) (see section 5.2.2) .....	153
Figure 5-12. Spatial distribution of the maximum values of $PrFC$ recorded at each pixel across the run time for each rainfall type.....	155
Figure 5-13. Relative frequency distribution across the basin of (a) the $PrFC$ occurrence for the 4 rainfall events, (b) the time of occurrence of the maximum value of $PrFC$ and (c) 1m depth average soil moisture at time of maximum $PrFC$ values.....	156
Figure 5-14. Spatial distribution of the difference of maximum $PrFC$ between Q4 and Q3 ( $\Delta Q_4 Q_3$ ) overlapped with the maps of soil type (a) and slope range 0.20 and 0.45 rad (10° and 25°) (b). .....	159
Figure 5-15. Distribution of maximum $PrFC$ with slope for Q1, Q3 and Q4 (Q2 is omitted because it is similar to Q3). (a); distribution of difference of maximum $PrFC$ between Q4 and Q3 ( $\Delta Q_4 Q_3$ ) with slope (b).....	160
Figure 5-16. Comparison between historical landslide scars caused by intense or prolonged storms during the 20 <sup>th</sup> century [Larsen, 2012] and observed through recent satellite images (from Google Earth) with the classified maximum $PrFC$ of Q4. ....	163
Figure 6-1. Spatially explicit representation of hillslope erosion and deposition in the Icacos watershed for climatic scenarios B1 (a) and A2 (b). Eroding slopes (yellow to red), landslide locations (red) and depositional sites (blue) are illustrated across the watershed. ....	174
Figure 6-2. Hillslope erosion and deposition across the Mameyes watershed in response to climatic projections B1 (a) and A2 (b). Eroding sites (yellow to red) and landslide locations (red) are illustrated, in addition to depositional sites (blue) in valleys and lower slopes. ....	175
Figure 6-3. Landslide area distributions for Icacos (a) and Mameyes (b) watersheds. Fitted power-type distributions corresponding to exponents $b$ (equation (6.1)) equal to 1.3 for Icacos and 2.2 for Mameyes watersheds, respectively.....	178
Figure 6-4. Comparison of observed landslide scars with predicted landslides (red) at the Icacos watershed for climatic scenarios B1 (a) and A2 (b). ....	180
Figure 6-5. Comparison of landslide scars with predicted landslides (red) at the Mameyes watershed corresponding to climatic scenarios B1 (a) and A2 (b).....	182
Figure 7-1. Conceptual diagram of feedbacks among coupled hydrological, geomorphic, and biogeochemical processes modelled using tRIBS-ECO at diverse ecosystems. Geophysical and biogeochemical properties (section 2.4) controlling	

different processes are given in parentheses. Geomorphic processes include topsoil erosion, which is the primary erosional mechanism in the Calhoun CZO and shallow landslides, which are the main erosional drivers at the Luquillo CZO larsen [Larsen, 2012]. Arrows denote dynamic feedbacks among linked processes. For example, increase in moisture conditions at soils characterized by low values of cohesion and friction angle (e.g., sandy loam) may lead to slope instability at relatively steep slopes. Dynamic replacement of eroded soil organic C (SOC) in landslide sites by C sequestration [Harden *et al.*, 1999] and subsequent SOC burial can drive a net atmospheric C sink (chapter 4). Depending on the rates of SOC oxidation and production, and on the influence of land management practices on C fluxes, soil C sequestration and SOC erosion may induce a net atmospheric C sink or a net C source (see sections 3.4.2 and 4.6.5). ..... 192

## SUMMARY

Soil erosion driven by hydro-climatic factors and anthropogenic activity is closely linked to the global carbon (C) cycle. Elucidating complex interrelations between climate, vegetation, soils, and human impacts is critical for advancing our understanding on how diverse ecosystems respond to global environmental change. This work introduces a spatially-explicit process-based model of soil organic C dynamics (Triangulated Irregular Network-based Real-time Integrated Basin Simulator-Erosion and Carbon Oxidation), developed within with an existing coupled physically-based hydro-geomorphic model, to quantify the influence of linked hydrologic and geomorphic processes on the C cycle in a range of ecosystems. Two sites are studied: the Calhoun Critical Zone Observatory (CZO) in South Carolina, USA, which has experienced some of the most serious agricultural soil erosion in North America, and the Luquillo CZO (Puerto Rico), a tropical site of particular hydro-geomorphological interest. This study uses multiple observations of hydrologic and geomorphic processes and soil biogeochemical properties.

The substantial topographic variability in the redistribution of soil organic C in agricultural landscapes as soil erosion and deposition proceed is highlighted. The uncertainty characterizing estimates of the hydrologically driven CO<sub>2</sub> exchange with the atmosphere in intensively managed landscapes is significant. In the Luquillo CZO, the capacity of contrasting tropical landscapes to act as a net atmospheric C source or a C sink in response to hydro-climatic perturbations is demonstrated. This work highlights that the natural spatial variation of soil hydrological and geotechnical properties greatly influences slope instability in tropical watersheds. Also, as shown, hillslope erosion and landslide occurrence in the Luquillo CZO are expected to remain significant in the 21<sup>st</sup> century,

despite a projected precipitation decline in south Caribbean. It is recommended that future studies assessing the contribution of erosion on atmospheric CO<sub>2</sub>, and the response of diverse landscapes to natural and anthropogenic perturbations systematically account for the fine spatio-temporal variability of linked hydro-climatic, geomorphological, and biogeochemical processes at a range of settings.



# **CHAPTER 1. Introduction: Significance of coupled and spatially-explicit representations of hydro-geomorphic and biogeochemical processes across scales**

Soils affected by human interventions are complex systems [Doetterl *et al.*, 2012; Richter and Markewitz, 2001]. They are affected by many processes, the interrelations of which are poorly understood [Van Oost *et al.*, 2007]. Topsoil erodes from upland soil profiles in response to anthropogenic and natural perturbations, and is accumulated in floodplains, wetlands, and valleys, altering the hydrologic, biologic, riparian, and chemical functions of the disturbed environments [James, 2013]. Land use and land use change have accelerated soil erosion rates, effectively degrading soil structure and depleting soil fertility [Harden *et al.*, 1999; Lal, 2003]. Sediment transport in mountainous landscapes is controlled by different interacting hydro-geomorphic processes (e.g., topsoil erosion and landslide occurrence), which are driven by climatic and non-climatic factors over a range of scales [Dykes and Warburton, 2007; Gabet *et al.*, 2015; Kim *et al.*, 2016; Larsen and Montgomery, 2012; Larsen, 2012; Larsen *et al.*, 1999; Stark and Passalacqua, 2014]. Hillslope erosion rates depend on a multitude of factors including topography, lithological characteristics, land management, and soil and forest properties [De Rose, 2013; Formetta *et al.*, 2016; Hales *et al.*, 2009; Moos *et al.*, 2016; Roering *et al.*, 1999; Simoni *et al.*, 2008], and on the frequency of extreme hydro-meteorological events [Casadei *et al.*, 2003; Chen *et al.*, 2013; von Ruetten *et al.*, 2014]. Understanding the associated interrelations within the

complex structures of the Earth's critical zones<sup>1</sup> [Anderson *et al.*, 2007; Brantley *et al.*, 2007] remains a challenge.

Soil erosion redistributes soil organic carbon (SOC) across the landscape. The extent to which eroded SOC is protected from decomposition in moist environments at depositional sites has significant impacts on the global C cycle [Billings *et al.*, 2010; Harden *et al.*, 1999; Stallard, 2012; Van Oost *et al.*, 2007]. Understanding the influence of land management practices on C erosion and burial is hence crucial for developing strategies for climate change mitigation [Battin *et al.*, 2009]. Atmospheric CO<sub>2</sub> sequestration at eroding soils and C burial at depositional sites have the potential to offset CO<sub>2</sub> emissions due to fossil fuels and help mitigate the threat of future global warming [Lal, 2004]. Stallard [1998] and Harden *et al.* [1999] suggested that SOC burial and replacement by sequestered atmospheric CO<sub>2</sub> may explain a significant portion of the so called “missing sink” in atmospheric CO<sub>2</sub> [Lal, 2003; Liu *et al.*, 2003]. Global estimates of this effect range from a C sink exceeding 1 Pg yr<sup>-1</sup> [Harden *et al.*, 1999; Stallard, 1998] to a C source of around 1 Pg yr<sup>-1</sup> [Jacinthe and Lal, 2001; Lal, 2004].

The wide range of erosion-induced C flux estimates can be attributed to diametrically different assumptions about the processes that drive soil erosion and C burial [Billings *et al.*, 2010; Harden *et al.*, 1999; Jacinthe and Lal, 2001; Lal, 2003; 2004; Regnier *et al.*, 2013; Smith *et al.*, 2001; Stallard, 1998; Van Oost *et al.*, 2012; Van Oost *et al.*, 2007]. The variation of published estimates of the net soil-atmosphere C exchange depends on

---

<sup>1</sup>The Earth's critical zone is defined (NRC (2001), *Basic Research Opportunities in Earth Science*, National Academy Press.) as: “the heterogeneous, near-surface environment in which complex interactions involving rock, soil, water, air, and living organisms regulate the natural habitat and determine the availability of life-sustaining resources”.

assumptions about the rate of C replacement at upland eroding sites, which is an important determinant of the contribution of erosion to atmospheric CO<sub>2</sub>. For example, according to *Van Oost et al.* [2007] 11% to 55% of eroded C can be replaced by plant inputs, while other studies [*Smith et al.*, 2001; *Smith et al.*, 2005] assume that the amount of mobilized C is replaced to its entirety. Moreover, different assumptions have also been invoked to explain the fate of eroded C. Changes in the reactivity of mobilized C may exert a strong control on the erosion-induced soil-atmosphere C exchange [*Harden et al.*, 1999]. Previous studies have assumed that eroded C is decomposed upon transport [*Lal*, 1995; *Schlesinger*, 1995] while others assume that it is protected from decomposition by burial [*Smith et al.*, 2001].

Models that quantify different drivers of SOC storage dynamics (e.g., [*Billings et al.*, 2010; *Chappell et al.*, 2016; *Coleman et al.*, 1997; *Doetterl et al.*, 2016; *Fiener et al.*, 2015; *Harden et al.*, 1999; *Liu et al.*, 2003; *Rosenbloom et al.*, 2006; *Stallard*, 1998; *Van Oost et al.*, 2005; *Van Oost et al.*, 2012; *Wang et al.*, 2015; *Yoo et al.*, 2005]) often neglect fundamental linkages among coupled operating processes, and simulate linked natural mechanisms in isolation [*Van Oost et al.*, 2007]. Systematically representing feedbacks that link geophysical and biogeochemical processes at a range of spatial scales is critical for understanding the influence of erosion on the soil-atmosphere CO<sub>2</sub> exchange [*Berhe and Kleber*, 2013; *Liu et al.*, 2003]. Also important is the representation of land management practices, [*Abaci and Papanicolaou*, 2009; *Dlugoff et al.*, 2012; *Hu and Kuhn*, 2014; *Richter et al.*, 2007], such as enhancement or degradation of system productivity. Management practices may regulate the extent to which SOC oxidation and production, important components of the soil-atmosphere CO<sub>2</sub> exchange, are altered by erosion [*Billings et al.*, 2010; *Harden et al.*, 1999]. The effect of management practices on SOC

redistribution via erosion and deposition in complex topographies remains poorly investigated. The net effect of erosion and deposition on the C exchange between terrestrial ecosystems and the atmosphere continues to be studied, and the potential of physically-based modelling to clarify the influence of erosional processes on the C cycle has been widely recognized [Billings *et al.*, 2010; Hu and Kuhn, 2014; Liu *et al.*, 2003; Papanicolaou *et al.*, 2015; Rosenbloom *et al.*, 2006].

The aim of this thesis is: 1) to develop a novel physically-based, spatially-explicit framework to assess the impact of episodic erosion on atmospheric CO<sub>2</sub> by systematically accounting for dynamic feedbacks among coupled hydrological, geomorphological, and biogeochemical processes, 2) to assess the influence of erosion on the C cycle in a degraded landscape undergoing recovery from past agricultural use, much as many other regions of the world, and 3) to characterize different factors controlling hillslope erosion, landslide occurrence, and erosion-induced C fluxes in two diverse tropical watersheds underlain by contrasting lithology.

This thesis presents the process-based spatially-explicit model of SOC dynamics tRIBS-ECO (*Triangulated Irregular Network-based Real-time Integrated Basin Simulator-Erosion and Carbon Oxidation*), which is based on an existing coupled hydro-geomorphic model [Francipane *et al.*, 2012; Ivanov *et al.*, 2004a; b]. The thesis is organized in seven chapters that discuss in detail the development of coupled physically-based models and model applications that use multiple observations, to elucidate linkages between climate, vegetation, soils, and human impacts in diverse ecosystems.

*Chapter 2* of this thesis studies the influence of episodic erosion on the C cycle in a degraded agricultural landscape located at the Calhoun Critical Zone Observatory (CZO) in South Carolina, USA, a site that has experienced some of the most serious agricultural soil erosion in North America [Trimble, 1974]. This work introduces the coupled model of SOC dynamics tRIBS-ECO, and uses observations of hydro-geomorphic processes and of soil biogeochemical properties from multiple soil profiles. This study demonstrates the substantial topographic variability in the redistribution of SOC at agricultural landscapes as soil erosion and deposition proceed.

*Chapter 3* presents the implementation of a stochastic formulation in the tRIBS-ECO model to quantify the uncertainty introduced by land management practices on estimates of the net erosion driven soil-atmosphere C exchange at the landscape scale. The significant uncertainty characterizing published estimates of the hydrologically-induced CO<sub>2</sub> exchange with the atmosphere in intensively managed landscapes is highlighted.

*Chapter 4* focuses on the Luquillo CZO in northeastern Puerto Rico, a tropical site of particular hydrological and geomorphological interest. This work couples existing landslide and topsoil erosion models [Arnone *et al.*, 2011; Francipane *et al.*, 2012] with a spatially explicit model of C dynamics, to assess the capacity of diverse tropical settings to act as a net atmospheric C source or a C sink in response to hydro-geomorphic perturbations.

*Chapter 5* introduces a probabilistic approach that quantifies the significant uncertainty in the prediction of rainfall-triggered landslide occurrence, associated with the natural spatial variation of soil hydrological and geotechnical properties. The methodology

is used to evaluate how the spatial and temporal patterns of precipitation influence slope instability at the watershed scale

*Chapter 6* assesses the influence of climate change on the rates of hillslope erosion at two adjacent tropical watersheds in the Luquillo CZO, underlain by contrasting lithology (volcaniclastic rock and quartz diorite [Buss and White, 2012]). This work studies the landslide area frequency distributions projected in the two watersheds, and assesses the extent to which the two diverse landscapes reach a state of equilibrium.

*Chapter 7* compares and contrasts hydrologically-induced erosion rates of soil and SOC in the tropical montane ecosystem of the Luquillo CZO and in the temperate forest ecosystem of the Calhoun CZO, and summarizes the thesis. This chapter addresses implications of linked hydrologic and geomorphic processes on the global carbon cycle, and highlights future research needs.

## **CHAPTER 2.      Topographic variability and the influence of soil erosion on the carbon cycle in a degraded agricultural landscape**

### **2.1 Introduction**

Soil erosion, particularly that caused by agriculture, is closely linked to the global C cycle. Assessing the role of erosion and deposition on the C cycle is critical not only for understanding future challenges posed by climate change, but also for providing strategies for climate change mitigation [Battin *et al.*, 2009; Lal, 2004].

As discussed in chapter 1, global assessments of the net effect of soil erosion on the C cycle are currently based on a variety of different assumptions about the associated operating processes [Harden *et al.*, 1999; Jacinthe and Lal, 2001; Lal, 2003; 2004; Regnier *et al.*, 2013; Smith *et al.*, 2001; Stallard, 1998; Van Oost *et al.*, 2012; Van Oost *et al.*, 2007]. This has led to a wide range of contrasting global estimates of how erosion alters soil-atmosphere C exchange [Harden *et al.*, 1999; Jacinthe and Lal, 2001; Lal, 2004; Stallard, 1998], which can be partly attributed to limited understanding of how geomorphology, topography, and management practices affect erosion and oxidation of SOC [Van Oost *et al.*, 2007].

This study proposes a novel approach to assess the impact of episodic erosion on atmospheric CO<sub>2</sub> by systematically accounting for dynamic feedbacks among coupled hydrological, geomorphological, and biogeochemical processes in a physically-based, spatially-explicit framework, and by utilizing measurements of depth-dependent biogeochemical properties [Billings *et al.*, 2010; Richter *et al.*, 1999]. This work assesses

the influence of soil erosion on the net soil-atmosphere C exchange at the Calhoun Critical Zone Observatory, one of the most severely eroded regions in the U.S. [Trimble, 1974], and emphasizes the dynamic interaction between eroding and depositional sites on the redistribution of SOC. The fate of eroded SOC is estimated across a topographically heterogeneous landscape, and the role of management practices on the C exchange with the atmosphere is explored. The work carried out in this chapter has formed the basis of different publications [Dialynas *et al.*, 2017; Dialynas *et al.*, 2014; Dialynas *et al.*, 2016a].

## **2.2 Materials and methods**

### **2.2.1 Spatially- and depth-explicit model of carbon dynamics**

To quantify the influence of soil erosion and deposition on atmospheric CO<sub>2</sub> the tRIBS-ECO (Triangulated Irregular Network-based Real-time Integrated Basin Simulator-Erosion and Carbon Oxidation) model is introduced, a spatially-explicit model of SOC dynamics developed within the existing coupled physically-based hydro-geomorphic model [Francipane *et al.*, 2012] discussed in section 2.2.2. The model incorporates a SOC mass balance equation for each computational cell. Continuous functions of depth-dependent quantities representing SOC storage and C fluxes with the atmosphere, including SOC production and oxidation losses are used, in addition to lateral SOC fluxes due to soil erosion and deposition. Depth-dependent variables are integrated over soil thickness, which constitutes a temporally variant boundary condition, as it is locally controlled by episodic erosion and deposition. For each cell and at each time step the SOC mass balance equation (for a unit area) is:



$$\frac{\Delta SOC}{\Delta t} = \int_0^{H_t} I_t(z) dz - \int_0^{H_t} k_t(z) \rho(z) C_t(z) dz - \frac{1}{\Delta t} \int_0^{h_t} \rho(z) C_t(z) dz \Big|_{out} + \frac{1}{\Delta t} \sum_{i=1}^n \int_0^{h_{t,i}} \rho_i(z) C_{t,i}(z) dz \Big|_{in} \quad (2.1)$$

where  $t$  is time;  $z$  denotes depth;  $H_t$  denotes temporally-variant thickness of the soil profile;  $SOC$  denotes SOC content;  $\Delta t$  is the discrete time interval;  $k_t(z)$  and  $I_t(z)$  are the oxidation and production rates of soil organic carbon, respectively;  $\rho(z)$  is the bulk density;  $C_t(z)$  is the C mass fraction; and  $h_t$  denotes the thickness of the eroded layer. At each time step,  $h_t$  is estimated by the hydro-geomorphic model (section 2.2.2). At each Voronoi cell, the first two terms in equation (2.1) give the  $CO_2$  exchange with the atmosphere, resulting from C sequestration and from SOC decomposition and  $CO_2$  release. The third term (“out”) represents efflux of organic material by means of eroded sediment. The amount of eroded organic material in the third term is estimated by integrating the SOC content of the eroding cell ( $\rho(z)C_t(z)$ ) over the eroded layer thickness,  $h_t$ . The fourth term (“in”) represents organic C influx from upstream Voronoi cells (the associated SOC amount is estimated similar to the third transport term). SOC erosion from surficial soil horizons is mainly associated with the active SOC pool with turnover times from years to decades [Harden *et al.*, 1999; Van Oost *et al.*, 2007].  $I_t(z)$  represents the ecosystem’s capacity to produce SOC. C inputs to soils associated with this term include canopy litterfall, rhizo-deposition (fine-root sloughing and turnover), and hydrological leaching of dissolved organic C (DOC) [Richter *et al.*, 1999].

In tRIBS-ECO the watershed's hydro-geomorphic response to hydrometeorological forcings leads to spatially heterogeneous, episodic erosion. Equation (2.1) is applied at eroding and depositional sites with a daily time resolution to systematically account for the fate of eroded SOC across the landscape. Eroded SOC can be oxidized upon transport or it

can be stored at deeper horizons at depositional sites, where oxidation is mitigated. This framework quantifies the watershed-integrated net contribution to atmospheric CO<sub>2</sub> derived from erosional processes.

The model systematically accounts for the influence of management practices on the rates of C decomposition and C production.  $k_t(z)$  and  $I_t(z)$  may significantly decline at relatively deep soil horizons because of reduced, for example, aeration, changes in temperature and moisture conditions, and recalcitrance of organic matter [Berhe *et al.*, 2007]) (section 2.4). Severe erosion events can significantly alter the depth-dependent SOC oxidation and production at disturbed sites by the lateral removal of topsoil. However, this can be moderated by management practices, which alter SOC oxidation and production over surficial and deeper horizons [Billings *et al.*, 2010]. This study introduces coefficients  $a_k$  and  $a_I$ , corresponding to the influence of management practices on altered SOC oxidation and production rates, respectively. To clarify this framework an example is given in Figure 2-1. Assume that by time  $t_2$  removal of an eroding soil layer leads to the new surface having an oxidation rate  $k_{t_2}(z=0)$ , which can be significantly different from the original rate,  $k_{t_1}(z=0)$  [Billings *et al.*, 2010]. Management practices restore the initial  $k_{t_1}(z)$  at a rate specified by the coefficient  $a_k$ . This framework is also applied to the depth-dependent SOC production. Moreover,  $a_I$  and  $a_k$  are applied with no reference to ongoing erosion rate. Thus, the effect of management practices on disturbed soil profiles is represented even for periods characterized by low erosion rates. Also, while the influence of management practices on  $k_t(z)$  and  $I_t(z)$  is modelled at upland eroding sites, it is assumed that the depth-dependence of  $k_t(z)$  and  $I_t(z)$  at lower slopes and valleys does not change with sediment deposition.

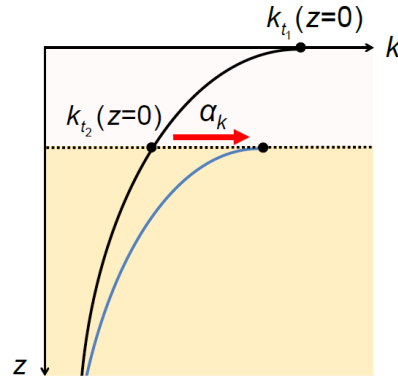


Figure 2-1. Illustration of the effect of management practices on altered depth-dependent SOC oxidation  $k_i(z)$ . Assume that by time  $t_2$  soil erosion leads to the removal of a soil layer with the new surface having an oxidation rate  $k_{t_2}(z=0)$ , altered from  $k_{t_1}(z=0)$ . It is proposed that land management practices can have an effect on altered oxidation at a rate  $\alpha_k$ . The framework is also applied to SOC production [Billings *et al.*, 2010].

This spatially- and depth-explicit approach has important advantages and novel features over existing efforts (e.g., [Billings *et al.*, 2010; Liu *et al.*, 2003; Rosenbloom *et al.*, 2006; Yoo *et al.*, 2005]) that attempt to describe erosion effects on soil-atmosphere C exchange. Advances of this physically-based framework include the coupling of hydrologic, geomorphic, and biogeochemical processes at the watershed scale, leading to an episodic representation of SOC erosion; tracking the potential of eroded SOC to undergo mineralization or be stabilized based on local topographic variation; and dynamically representing the effect of land management practices on altered SOC oxidation and production at eroding sites.

### 2.2.2 Physically-based hydro-geomorphic model

Hydrologic and geomorphic processes are represented in this study with an existing spatially-explicit coupled hydro-geomorphic model. The Triangulated Irregular Network (TIN) - based Real-time Integrated Basin Simulator (tRIBS) simulates various hydrologic processes typical of a basin [*Ivanov et al.*, 2004a; b]. tRIBS explicitly accounts for the spatial variability of precipitation fields and land-surface descriptors. It represents soil moisture dynamics and stresses the role of topography in lateral soil moisture redistribution by accounting for the effects of heterogeneous and anisotropic soil. The computational elements of the model are Voronoi polygons defined by the TIN network. The geometry and properties of the Voronoi polygons are described in *Vivoni et al.* [2004]. The basin's hydrologic response can be simulated at very fine temporal (hourly) and spatial (10 to 100 m) scales. Modelled hydrological processes include runoff routing, rainfall canopy interception, evapotranspiration and surface energy balance, infiltration, and lateral redistribution of soil moisture in the unsaturated and saturated zones. The underlying hydrological processes are described by a set of physically-based formulations. The model accounts for different soil types and vegetation species in representing hydrological processes in a spatially-explicit, physically-based manner.

Infiltration is modelled by assuming gravity-dominated flow in heterogeneous, anisotropic soil [*Garrote and Bras*, 1995]. In each computational element, the evolution of a wetting front and a top front may lead to unsaturated, perched-, surface-, or completely saturated states. The unsaturated and saturated zones are coupled to account for the interaction of the dynamic groundwater table with the moving wetting front. Lateral moisture transfer in the unsaturated zone is controlled by topography, while continuous

soil moisture allows for redistribution during both storm and interstorm periods, which allows long-term simulations over a range of hydrometeorological forcings. Groundwater flow is represented by means of a quasi three-dimensional “cascade” model. The groundwater model allows for lateral redistribution in the saturated zone, in addition to dynamic interaction with the unsaturated zone. Surface runoff is generated by different mechanisms, as a result of the dynamic interaction of lateral soil moisture redistribution, infiltration fronts, and water table depth. Saturation excess, infiltration excess, perched subsurface stormflow, and groundwater exfiltration are the four runoff-generating mechanisms in the model.

tRIBS was coupled with a geomorphic model (tRIBS-Erosion [*Francipane et al.*, 2015; *Francipane et al.*, 2012]), which is based on CHILD, the Channel-Hillslope Integrated Landscape Development model [*Tucker et al.*, 2001a; *Tucker et al.*, 2001b]. The hydro-geomorphic model represents main erosive processes on hillslopes and in channels, including rainsplash erosion, and sheet erosion entrainment. The main modelled erosional processes are described below, taken directly from *Francipane et al.* [2012] and *Francipane et al.* [2015]:

a) Rainsplash erosion is an important erosion-inducing mechanism on interfluvies and hillslopes. Raindrop impact breaks soil aggregates, driving the initiation of motion of sediment. The geomorphic model simulates both the effects of direct rainsplash detachment and leaf drip. Rainsplash erosion in the modelling framework is controlled by different factors, including rainfall characteristics, soil type, ground and canopy cover, and depth of overland flow. Features such as vegetation, and bare soil, as well as the variability of

processes like throughfall are characterized by subgrid variation within the computational element through areal fractions of Voronoi cells.

b) Erosion and deposition by overland flow at hillslopes and channels is also simulated by physically-based formulations. The framework is based on shear stress-based expressions for sediment initiation of motion, entrainment, and transport capacity by sheet flow. The estimation of effective boundary stress assumes uniform water flow, and uses Manning's equation for the flow velocity. The associated formulations are applied both in overland and channel flows.

At each Voronoi polygon and at each time step the coupled model quantifies the rate of elevation change, which is either limited by the magnitude of detachment/entrainment erosional processes, or by the divergence of local sediment flux. Mobilized sediment is routed following the direction of steepest descent. The model computes sediment discharge and local changes in elevation at eroding and depositional sites, and modifies the associated terrain characteristics, accordingly. More specifically, the model applies elevation changes at each time step, and re-estimates the local slope, aspect, flow direction, and drainage area at each computational cell. The alteration of the watershed's morphological characteristics results in changes of the drainage network configuration, and of the available energy for driving hydrological and sediment fluxes. The modelled erosional processes and calculation steps are discussed in *Francipane et al.* [2012] and in *Francipane et al.* [2015].

### 2.2.3 SOrCERO model

The SOrCERO (Soil Organic Carbon, Erosion, Replacement, and Oxidation) model was introduced by *Billings et al.* [2010]. The depth-explicit model quantifies the effect of constant erosion and altered SOC production and oxidation on CO<sub>2</sub> release to the atmosphere at a single eroding soil profile. Model inputs include an assumed constant erosion rate, depth-dependent SOC content, oxidation and production rates. The moderating effect of management practices on erosion driven C fluxes is explicitly considered. More precisely, the mixing coefficients  $n_{ox}$  and  $n_{prod}$  express the extent to which erosion alters SOC oxidation and production rates at the eroding site. Outputs include SOC storage and eroded SOC, and maximum C sink or source strengths depending on the amount of eroded SOC assumed to be oxidized.

## 2.3 Study area

The watershed-integrated hydro-geomorphic response of the 4.3 km<sup>2</sup> Holcombe's Branch watershed (34.6177° N, 81.6914° W, Figure 2-2a) is studied in terms of SOC redistribution and atmospheric CO<sub>2</sub> flux. The Holcombe's Branch is a tributary of the Tyger River, which drains into the Broad, Congaree, and Santee Rivers before entering the Atlantic Ocean. The watershed is part of the Calhoun Critical Zone Observatory and USFS Calhoun Experimental Forest in the southern Piedmont of South Carolina, USA. The region has experienced some of the most serious agricultural land degradation in North America [Trimble, 1974]. The mean annual precipitation is around 1,260 mm, and the mean annual temperature is about 17 °C. Elevation ranges from 113 m to 196 m above sea level.

The watershed is covered for the most part by highly weathered acidic Ultisol and Inceptisol soils [Richter and Markewitz, 2001; Richter et al., 2014]. The soil and vegetation types characterizing the study area are discussed in section 2.4. Cultivation of cotton, corn, wheat, and other crops led to significant soil erosion starting about 1800 and continuing to the early 20<sup>th</sup> century [Richter and Markewitz, 2001]. The Calhoun Experimental Forest includes one of the longest running experiments on soil properties and processes worldwide [Richter et al., 1999], providing insights that support this study [Richter and Markewitz, 2001; Richter et al., 2006].

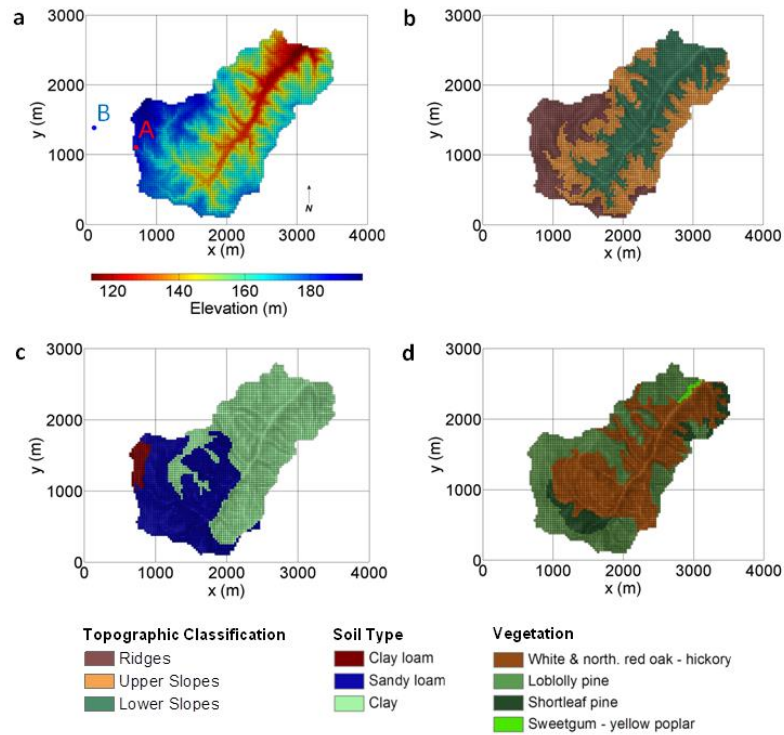


Figure 2-2. Digital Elevation Model of the Holcombe's Branch watershed (a), topographic classification of the watershed; initial total SOC storage (calculated in the upper 5 m of soil) at ridges, upper, and lower slopes is equal to 10.3 kg m<sup>-2</sup>, 12.7 kg m<sup>-2</sup>,



and 16.7 kg m<sup>-2</sup>, respectively (b), spatial distribution of soil textural classes (c), and of vegetation types (d)

## 2.4 Model inputs

### 2.4.1 Biogeochemical parameters

Biogeochemical input variables to tRIBS-ECO were obtained from a relatively undisturbed soil profile in a hardwood stand nearby (site B in Figure 2-2a) which is considered to have never been cultivated [Billings *et al.*, 2010; Richter and Markewitz, 2001]. Distributions with depth of SOC content and bulk density were obtained from previous studies at the site [Billings *et al.*, 2010; Markewitz and Richter, 1998; Richter *et al.*, 1999]. First-order mean oxidation rate constants ( $k$ , yr<sup>-1</sup>) for the undisturbed soil profile were estimated in Billings *et al.* [2010] from mean residence times calculated using bulk radiocarbon signatures of organic C from several soil horizons sampled in 1962 [Richter *et al.*, 1999], likely before the presence of thermonuclear bomb-produced <sup>14</sup>C [Billings *et al.*, 2010; Richter *et al.*, 1999]. The corresponding input parameters to tRIBS-ECO were estimated by fitting the following exponential functions with depth to the associated data, by means of constrained non-linear optimization (see Figure 2-3):

$$C_t(z) = C_{a,t} e^{C_b z} + C_c \quad (2.2)$$

$$k_t(z) = k_{a,t} e^{k_b z} + k_c \quad (2.3)$$

$$\rho(z) = \rho_a e^{\rho_b z} + \rho_c e^{\rho_d z} + \rho_e e^{\rho_f z} \quad (2.4)$$

for SOC content, oxidation rate, and soil bulk density, respectively (see section 2.2.1 for notation), where  $C_{a,t}$ ,  $C_b$ ,  $C_c$ ,  $k_{a,t}$ ,  $k_b$ ,  $k_c$ ,  $\rho_a$ ,  $\rho_b$ ,  $\rho_c$ ,  $\rho_d$ ,  $\rho_e$ , and  $\rho_f$  are parameters. Equations (2) and (3) correspond to dynamic exponential profiles of SOC content and of SOC decomposition rate (see section 2.4.2). Mechanisms that induce advection-diffusion phenomena (e.g., bioturbation, tillage, soil creep) may lead to the mixing of SOC content estimated by equation (2.1) across different horizons within the soil column [Chaopricha and Marín-Spiotta, 2014]. At each time step, the SOC depth-variation is estimated by applying equation (A.3), assuming mixing of the estimated SOC content (equation (2.1)) across soil horizons. Further details on the estimation of SOC content at each time step are given in Appendix A.

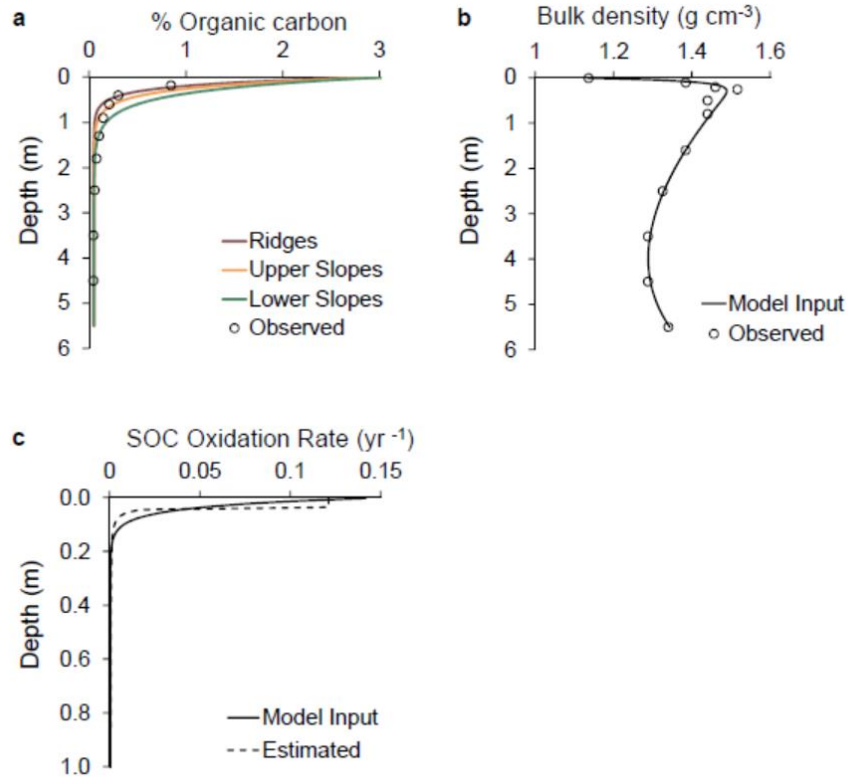


Figure 2-3. Exponential functions fitted to observations, to parsimoniously represent the depth variation of soil biogeochemical properties at multiple horizons: organic carbon concentration (a), bulk density (b), and oxidation rate of organic carbon (c). The observations were obtained from site B (Figure 2-2a). The variation of initial organic carbon concentration at different hillslope positions illustrated in (a) corresponds to the topographic classification of Figure 2-2b. The initial depth-dependent SOC concentration at ridges was obtained by fitting equation (2) to the observations [Billings *et al.*, 2010]. The depth-dependence of initial organic carbon concentration at upper and lower slopes was estimated based on the analysis conducted by *Rosenbloom et al.* [2006] (see section 2.4.1). The associated parameters are given in Table 2.1.

To quantify erosion-induced C fluxes, steady state conditions were assumed at the beginning of simulation, with zero net soil-atmosphere C exchange [Billings *et al.*, 2010; Jenny, 1941; Van Oost *et al.*, 2007]. This assumption represents the state of the ecosystem before the extensive forest cutover that started in the area in the late 18<sup>th</sup> century, which,

combined with inadequate soil management practices most likely led to the beginning of severe erosion of millions of hectares of land in the broader region [Trimble, 1974]. The model is initialized with estimates of depth-dependent soil bulk density, SOC oxidation rate and SOC concentration. The SOC production term is assumed to exponentially decay with depth [Yoo *et al.*, 2005; 2006]:

$$I_t(z) = I_{a,t} e^{I_b z} \quad (2.5)$$

where  $I_{a,t}$ , and  $I_b$  are parameters. The estimation of the initial depth-dependent SOC production rate is discussed in Appendix B.

In addition to the dependence of SOC on depth, the spatially-explicit model considers the variation with topography. Deep C accumulation varies topographically depending on slope morphology. This work systematically accounts for topographic controls on the initial SOC content (Figure 2-2b) based on the analysis given by *Rosenbloom et al.* [2006], who fitted exponential depth-profiles of C concentration to observations across different landscape positions. They reported that C concentration attenuates rapidly with depth in ridges in comparison to middle slopes, while lower slopes exhibit slower depth attenuation. They represent the C attenuation at each location with different coefficients of exponential decay with depth (equivalent to  $C_b$  in equation (2.2)). In this thesis the depth-dependent C content at the Holcombe's Branch's ridges is initialized based on observations [*Billings et al.*, 2010] illustrated in Figure 2-3a. The depth-attenuation of initial C concentration at upper and lower slopes is captured by using different values for  $C_b$  (exponential decay of C concentration with depth). More specifically, the ratio of  $C_b$  corresponding to upper slopes over the  $C_b$  that corresponds to ridges was assumed equal to the one *Rosenbloom et*

*al.* [2006] derived from observations. This method was also applied for the estimation of the depth attenuation of initial C concentration at lower slopes. The initial spatial distribution of C content, and the depth-dependence of C concentration at different topographic locations are illustrated in Figures 2-2b and 2-3a, respectively. The associated parameters are given in Table 2.1.

#### 2.4.2 Carbon Oxidation and Production Parameters: Sensitivity Analysis on Effects of Management Practices

The effect of land management practices on the interaction of erosion and soil-atmosphere C exchange is represented by the coefficients  $a_k$ , and  $a_l$  for oxidation and production, respectively (see section 2.2.1). In order to clarify the role of  $a_k$ , and  $a_l$  on the net C flux and to select a set of parameters to use in the watershed simulations, a preliminary sensitivity analysis was conducted on an eroding site, assuming a  $1 \text{ mm yr}^{-1}$  constant erosion rate in 100-year simulations. The total SOC difference ( $\Delta\text{SOC}$ ) for 100 years is illustrated in Figure 2-4, which reflects the net result of SOC production, oxidation, and loss to erosion, based on the modelling framework. Depending on the values of  $a_k$  and  $a_l$  different scenarios range from a net increase to a net loss of SOC at the eroding soil profile. High values of  $a_k$  ( $a_l$ ) represent a rapid restoration of the altered  $k_t$  ( $l_t$ ), while low values have little effect on eroded profiles. A high value of  $a_k$  combined with low  $a_l$  lead to a net C source (i.e., net flux of  $\text{CO}_2$  from soil to atmosphere); low values of  $a_k$  combined with relatively high  $a_l$  may lead to a net C sink.

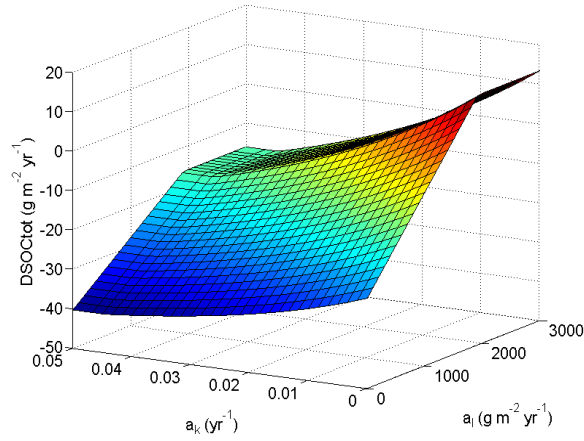


Figure 2-4. Sensitivity analysis on the effect of management practices to the total difference in soil organic carbon storage ( $\Delta\text{SOC}$ ). The net result of soil organic carbon (SOC) production, oxidation, and SOC loss to erosion is illustrated, as the effects of management practices on altered oxidation and production ( $a_k$  and  $a_l$ , respectively) vary. Positive values of  $\Delta\text{SOC}$  indicate net increase of SOC at the eroding site, while negative values represent net SOC loss to the atmosphere and to erosion.

To assess the watershed's integrated response in terms of atmospheric  $\text{CO}_2$  fluxes three scenarios were considered: a) a maximum C sink scenario, b) a maximum C source scenario, and c) an intermediate scenario. For the maximum sink scenario, based on Figure 2-4  $a_l=3 \text{ g m}^{-3} \text{ yr}^{-1}$  (i.e., the value for  $a_l$  above which the SOC difference in Figure 2-4 does not significantly change) is used and  $a_k$  is minimized ( $a_k=0 \text{ yr}^{-1}$ ). Similarly, for the maximum source scenario  $a_l=0 \text{ g m}^{-3} \text{ yr}^{-1}$  and  $a_k=0.05 \text{ yr}^{-1}$  are used. For the intermediate scenario  $a_l=1.5 \text{ g m}^{-3} \text{ yr}^{-1}$  and  $a_k=0.025 \text{ yr}^{-1}$  were selected. The simulated response surface of Figure 2-4 depends on the cumulative erosion for the time period of the simulation (100 years). This range of  $a_k$  and  $a_l$  values (see Table 2.1) reflects plausible states of the ecosystem during its long agricultural history.

Table 2.1. Initial values of tRIBS-ECO and SOrCERO biogeochemical model parameters. Three values for  $C_b$  and for  $I_b$  are given, corresponding to ridges, upper slopes, and lower slopes, respectively. Observations of C content and bulk density (site B in Figure 2-2a) were obtained from previous studies at the site [Billings *et al.*, 2010; Markewitz and Richter, 1998; Richter *et al.*, 1999]. Three values for  $a_k$  and  $a_l$  (tRIBS-ECO) and for  $n_{ox}$  and  $n_{prod}$  (SOrCERO) are given, corresponding to the maximum sink, the intermediate, and the maximum source scenarios, respectively (see section 2.4.2). SOrCERO was initialized by the observed C concentration and bulk density illustrated in Figures 3a and 3b, respectively, and by the depth-dependent SOC oxidation rate estimated by Billings *et al.* [2010] (Figure 2-3c).

Parameter	Units	Values	Description	Source
$C_a$	[g g <sup>-1</sup> ]	0.03	Parameters of initial depth-dependent C concentration (equation (2.2))	Fitting to Observations (Figure 2-3a)
$C_b$	[m <sup>-1</sup> ]	-6.00/-4.50/-3.18		Fitting to Observations (Figure 2-3a) and Rosenbloom <i>et al.</i> [2006]
$C_c$	[g g <sup>-1</sup> ]	0.0005		Fitting to Observations (Figure 2-3a)
$\rho_a$	[g m <sup>-3</sup> ]	-0.42	Parameters of bulk density profile (equation (2.4))	Fitting to Observations (Figure 2-3b)
$\rho_b$	[m <sup>-1</sup> ]	-14		
$\rho_c$	[g m <sup>-3</sup> ]	1.475		
$\rho_d$	[m <sup>-1</sup> ]	-0.0836		
$\rho_e$	[g m <sup>-3</sup> ]	0.05084		
$\rho_f$	[m <sup>-1</sup> ]	0.381		
$k_a$	[yr <sup>-1</sup> ]	0.15	Parameters of initial depth-dependent SOC oxidation rate (equation (2.3))	Fitting to the SOC oxidation rate estimates reported by Billings <i>et al.</i> [2010] (Figure 2-3c)
$k_b$	[m <sup>-1</sup> ]	-30		
$k_c$	[yr <sup>-1</sup> ]	0.000417		
$I_a$	[g m <sup>-2</sup> yr <sup>-1</sup> ]	5.059	Parameters of initial depth-dependent SOC production rate	Estimated according to Appendix B
$I_b$	[m <sup>-1</sup> ]	-32.5/-31.1/-29.8		
$a_k$	[yr <sup>-1</sup> ]	0/0.025/0.05	$a_k$ and $a_l$ in tRIBS-ECO represent the effect of management practices on SOC oxidation and production, respectively (section 2.2.1)	Sensitivity analysis (Figure 2-4)
$a_l$	[g m <sup>-2</sup> yr <sup>-1</sup> ]	3/1.5/0		
$n_{ox}$	[-]	0/0.5/1	$n_{ox}$ and $n_{prod}$ in SOrCERO represent the effect of management practices on SOC oxidation and production, respectively	Billings <i>et al.</i> [2010] (see section 2.5.1)
$n_{prod}$	[-]	1/0.5/0		

#### 2.4.3 Land Surface Data

This work uses a fine (5 m) Digital Elevation Model (DEM) and information on the spatial distribution of vegetation from the South Carolina Department of Natural Resources [2009]. A 30 m mesh of computational elements was obtained based on the 5 m DEM (Figure 2-2a). The soil classification map (Figure 2-2c) of the area was obtained from local soil surveys (<http://websoilsurvey.nrcs.usda.gov/>) conducted by the U.S. Department of Agriculture (USDA). Soil textural classes characterizing the area were grouped into three soil types according to the corresponding *USDA* [1951] classification.

The vegetation map of the area is shown in Figure 2-2d. The watershed is covered by several kinds of forest stands: those dominated by loblolly pine (*Pinus taeda*) and shortleaf pine (*Pinus echinata*), mixed stands of hardwoods such as white oak (*Quercus alba*), northern red oak (*Quercus rubra*) and hickory (*Carya sp.*), and hardwoods such as sweetgum (*Liquidambar styraciflua*), and yellow poplar (*Liriodendron tulipifera*). The pine stands are modelled [Hansen *et al.*, 2000] as evergreen needleleaf forest with a vegetation height of 30 m, while hardwood forests are modelled as deciduous broadleaf forest with a vegetation height of 25 m. In this first order modelling approach, the observed vegetation patterns are assumed time invariant. Selection of soil and ecological parameters is discussed in section 2.4.5.

#### 2.4.4 Hydrometeorological forcing and validation of the hydrologic model

A 100-year simulation was conducted to study the hydro-geomorphic response of the watershed and the influence on soil-atmosphere C exchange. Daily rainfall depth (1949-



2005) and air temperature data (1965-1999) were used from Union Station (Cooperative Observer Program (COOP) ID: 388786, lat. 34.6052 N, long. 81.6627 W, east of the watershed), in addition to hourly records of other meteorological data (vapor pressure, atmospheric pressure, wind speed, and cloud cover (1987-1999)) from the Greenville-Spartanburg airport, which are representative of the area. The data were used for the hydrologic model validation, and as inputs to a weather generator to reproduce a 100-year hydroclimatic scenario for the simulation's hydrometeorological forcing.

Weather generators (e.g., AWE-GEN [Fatichi *et al.*, 2011; Ivanov *et al.*, 2007], Castalia [Efstratiadis *et al.*, 2014], EARWIG [Kilsby *et al.*, 2007]) produce random hydroclimatic scenarios by preserving essential statistical properties of historical records. The Advanced Weather Generator (AWE-GEN [Fatichi *et al.*, 2011]) was used, which produces stationary climatic scenarios based on in situ observations of hydro-climatic variables. AWE-GEN produces hourly series of multiple hydro-meteorological variables (e.g., rainfall, air temperature, cloud cover, wind speed, vapor pressure, relative humidity, atmospheric pressure, and solar radiation) by reproducing marginal and joint statistics of the historical series at different timescales. A detailed description of AWE-GEN is given in Fatichi *et al.* [2011].

Initial hydrologic conditions are specified in the hydrologic model in terms of the mean groundwater table depth and initial moisture profile, which can be considered as initial wetness conditions of the basin. An initialization (spin-up) run of the hydrologic model is required to define the initial conditions [Ivanov *et al.*, 2004a; Noto *et al.*, 2008]. The initialization procedure defines the mean groundwater depth corresponding to an equilibrium state of the basin, at which the basin discharges at a specified mean annual

rate. The equilibrium basin discharge at the outlet is taken as the mean annual discharge (e.g.,  $0.1 \text{ m}^3 \text{ s}^{-1}$ ), which resulted in a mean initial groundwater depth of 3.5 m.

Soil moisture data obtained with gypsum blocks (soil moisture meter model 5910A) were used to validate the hydrological model's performance. Four gypsum blocks buried at 15-cm depth were monitored biweekly (site B in Figure 2-2a) at the Calhoun's Long-Term Soil Experiment site. The utilized soil moisture data are plotted in Figure 2-5 along with the model's rainfall forcing (rainfall records from Union Weather Station). Despite the convenient character of gypsum blocks in terms of sampling volumetric soil moisture, the inability to capture soil moisture dynamics at very fine (e.g., hourly) scales requires comparison with simulated data at coarser (e.g., weekly) scales.

Ecological properties controlling important hydrologic processes (e.g., evapotranspiration, rainfall interception and canopy storage [Ivanov *et al.*, 2004a]) were parameterized from literature [Bras, 1990; Ivanov *et al.*, 2004a; b; Rutter *et al.*, 1975; Rutter *et al.*, 1971]. The most essential parameters were calibrated which characterize the effect of different soil textural classes on the modelled hydrologic processes: the saturated conductivity ( $K_s$ ), the saturated volumetric water content ( $\theta_s$ ), the residual volumetric water content ( $\theta_r$ ), the air entry bubbling pressure ( $\psi_b$ ), the pore distribution index ( $m$ ), the conductivity depth decay parameter ( $f$ ), the saturated anisotropy ( $A_s$ ), and the unsaturated anisotropy ( $A_u$ ) [Ivanov *et al.*, 2004a].  $K_s$  represents the rate of water movement through saturated porous media,  $\theta_s$  is the total soil porosity,  $\theta_r$  expresses the minimum amount of soil moisture in a particular soil type,  $\psi_b$  represents the minimum capillary pressure in the porous medium,  $m$  is the exponent of the soil retention model suggested by Brooks and Corey [1964],  $f$  is the rate at which saturated hydraulic conductivity exponentially decays

with depth, and  $A_s$  and  $A_u$  are defined as the ratios of the saturated conductivities in the parallel over the normal to the soil surface directions, for the saturated and unsaturated zones, respectively. These properties vary across different soil types [Rawls *et al.*, 1982], and control the dynamics and the lateral redistribution of soil moisture at the element scale. A detailed description of the associated physically-based formulations of the hydrologic model is given by Ivanov *et al.* [2004b].

Calibration of the aforementioned soil properties started from literature values [Arnold *et al.*, 2011; Ivanov *et al.*, 2004a; b; Noto *et al.*, 2008; Rawls *et al.*, 1982]. To validate the hydrologic model's performance, simulated results at site A (Figure 2-2a), which is characterized by similar surface properties as site G, were compared to the soil moisture measurements. The final values of hydrologic soil parameters resulting from the calibration procedure are presented in Table 2.2. Comparison between simulated soil moisture against measurements is illustrated in Figure 2-5. In periods when discrepancies exceed the magnitude of measurement errors, the model's response to the rainfall forcing is rather evident compared to the response of the gypsum blocks. This can be attributed to the spatial gradient of rainfall between the location of the Union station and site A.

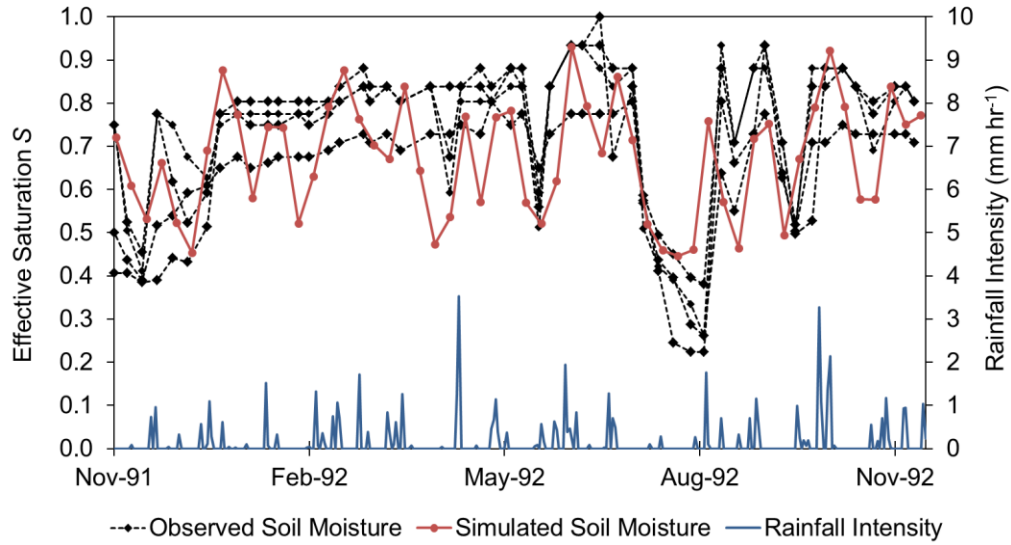


Figure 2-5. Hydrologic model validation in terms of soil moisture content. Soil moisture observations from four gypsum blocks at a depth of 15 cm versus simulated series, and corresponding rainfall intensity;  $S$  denotes effective saturation [Rawls *et al.*, 1982]:  $S = \frac{\theta - \theta_r}{\theta_s - \theta_r}$ , where  $\theta$  is the volumetric soil moisture content,  $\theta_r$  is the residual volumetric water content, and  $\theta_s$  is the saturated volumetric water content.

#### 2.4.5 Biogeomorphic properties

Geomorphic variables controlling raindrop impact detachment erosion and overland flow erosion were selected from the literature [Finney, 1984; Francipane *et al.*, 2012; Meyer and Harmon, 1984; Yalin, 1977]. The most important soil properties affecting soil erosion are the shear stress based soil erodibility ( $K_b$ ), the raindrop detachment soil erodibility ( $K_r$ ), and the critical shear stress ( $\tau_c$ ).  $K_b$  expresses the soil tendency to be eroded by overland flow.  $K_r$  characterizes how susceptible the soil is on rainsplash erosion, and depends on soil textural classes.  $\tau_c$  is the threshold stress value associated with particle entrainment. Ecological parameters controlling rainsplash erosion include the fraction of

vegetation ( $v$ ) of each computational element, the percentage of non-vegetated area (e.g., rock cover) protected against drop erosion ( $C_r$ ), and the drip coefficient ( $F_l$ ), which expresses the percentage of intercepted rainfall reaching the soil in the form of leaf drip. A detailed description on the structure of the geomorphic model is given by *Francipane* [2010] and by *Francipane et al.* [2012].

Starting from literature values, the soil and ecological parameters were tuned to mimic the history of severe erosion characterizing the area [Trimble, 1974] which led to the loss of the A horizon of many soil profiles [Richter and Markewitz, 2001]. This implies erosion rates of at least  $1 \text{ mm yr}^{-1}$  at eroding hillslopes across the Holcombe's Branch [Billings et al., 2010]. The selected values of characteristic soil properties and ecological parameters are given in Tables 2.2 and 2.3, respectively. Results of a 100-year scenario of accelerated soil erosion and redistribution are illustrated in Figure 2-6a. Erosion rates in the vicinity of  $1 \text{ mm yr}^{-1}$  or higher dominate the watershed hillslopes (illustrated in yellow color in Figure 2-6a). Depositional sites are mainly located in the proximity to the stream network. The geomorphic model parameterization is directly linked to and depends on the calibration of the hydrologic model.

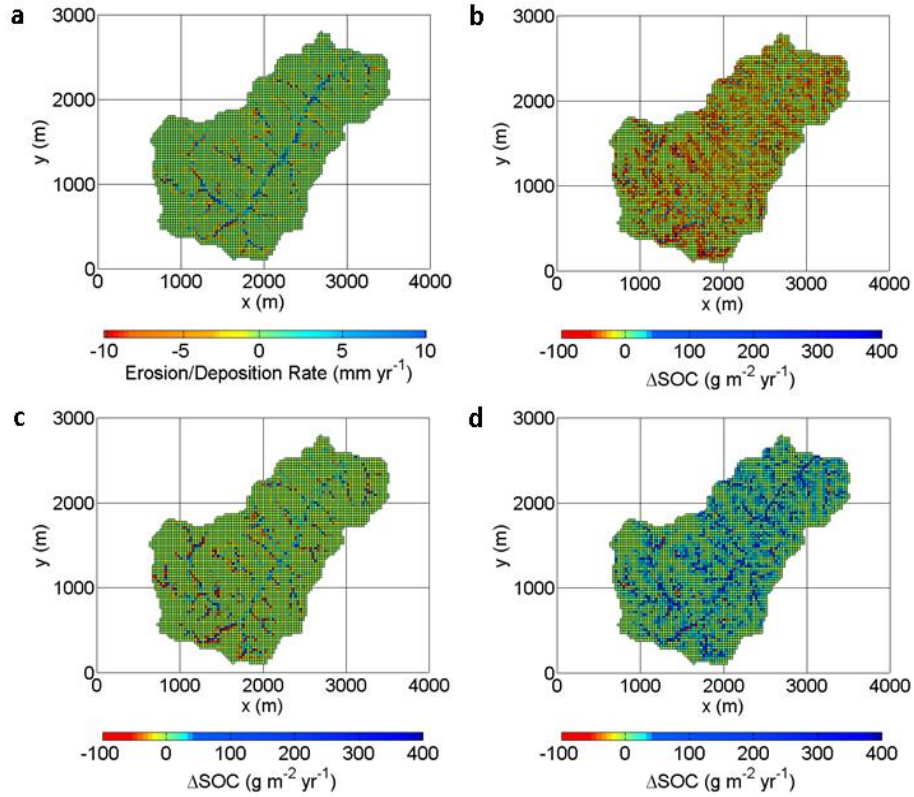


Figure 2-6. Spatially-explicit representation of soil erosion and of soil organic carbon redistribution. Higher sediment deposition rates are illustrated in blue (e.g., across the stream network), while eroding sites (yellow to red) dominate hillslopes (a). Total difference in soil organic carbon storage ( $\Delta\text{SOC}$ ) across the landscape corresponding to the maximum source scenario ( $14.5 \text{ g C m}^{-2} \text{ yr}^{-1}$ ) (b), the intermediate scenario ( $0.08 \text{ g C m}^{-2} \text{ yr}^{-1}$ ) (c), and the maximum sink scenario ( $-18.2 \text{ g C m}^{-2}$ ) (d).

Table 2.2. Hydrologic and geomorphic soil parameters for each soil type.

Parameter	Units	Clay	Sandy Loam	Clay Loam
$K_s$	[mm hr <sup>-1</sup> ]	1	8	6
$\theta_s$	[mm <sup>3</sup> mm <sup>-3</sup> ]	0.43	0.35	0.54
$\theta_r$	[mm <sup>3</sup> mm <sup>-3</sup> ]	0.15	0.13	0.04
$m$	[-]	0.17	0.1	0.4
$\psi_b$	[mm]	-860	-750	-360
$f$	[mm <sup>-1</sup> ]	0.006	0.005	0.1
$A_s$	[-]	150	250	200
$A_u$	[-]	150	250	200
$\theta_c$	[Pa]	0.1	0.1	0.1
$K_b$	[(m s <sup>-1</sup> kg <sup>-1</sup> s <sup>-2</sup> ) <sup>1.5</sup> ]	10 <sup>-9</sup>	10 <sup>-9</sup>	10 <sup>-9</sup>
$K_r$	[J <sup>-1</sup> ]	20	32	20

Table 2.3. Ecological parameters of the hydro-geomorphic model.

Parameter	Evergreen Needleleaf Forest	Deciduous Broadleaf Forest
$F_l$	0.6	0.5
$\nu$	0.7	0.6
$C_r$	0.1	0.1

## 2.5 Results

### 2.5.1 Influence of episodic erosion on the carbon exchange with the atmosphere

To assess the influence of episodic erosion on the redistribution of SOC the results of tRIBS-ECO were compared to those of SOrCERO, which uses an assumed constant erosion rate. Because SOrCERO operates at a point in the landscape, a heavily eroding site (site A in Figure 2-2a) was selected. The C exchange with the atmosphere estimated by the two models was compared for a 100-year scenario of severe erosion (section 2.4.4). Site A is characterized by a mean erosion rate of around  $3 \text{ mm yr}^{-1}$ . SOrCERO was initialized with depth-dependent SOC content, oxidation and production rates corresponding to the undisturbed site discussed in section 2.4.1. A constant erosion rate of  $3 \text{ mm yr}^{-1}$  was assumed for SOrCERO. The erosion time series simulated by tRIBS-ECO at site A is illustrated in Figure 2-7. The episodic character of the hydro-meteorological forcing and the dynamic response of the watershed lead to time-varying soil erosion.

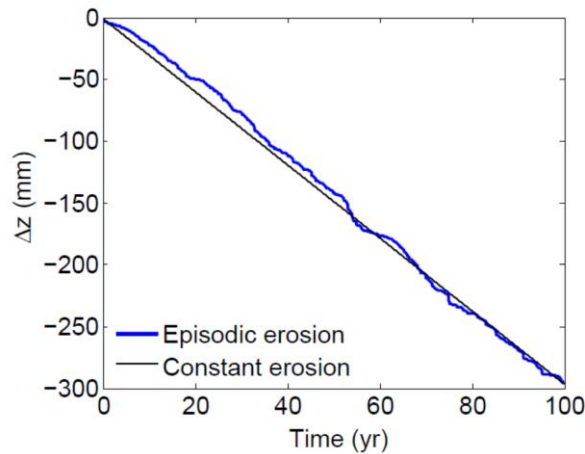


Figure 2-7. Temporal evolution of soil erosion at site A. The episodic character of soil erosion is evident (in blue), compared to the case of constant erosion (around  $3 \text{ mm yr}^{-1}$ , in black). Negative values of elevation change ( $\Delta z$ ) denote erosion-induced net depression of soil surface, as a result from the 100-year hydro-meteorological forcing.



To represent different states of the ecosystem during its agricultural history, a maximum C source and a maximum C sink scenario were studied based on the effect of management practices on CO<sub>2</sub> release. In tRIBS-ECO the two scenarios are defined by the  $a_k$  and  $a_l$  values specified in section 2.4.2. In SOrCERO the corresponding scenarios are represented by the mixing coefficients  $n_{ox}$ , and  $n_{prod}$  (described in section 2.2.3). Extreme values of the mixing coefficients (i.e.,  $n_{ox}=0$  and  $n_{prod}=1$  for the maximum sink scenario, and  $n_{ox}=1$  and  $n_{prod}=0$  for the maximum source scenario) were selected, as discussed by *Billings et al.* [2010].

The fate of eroded SOC is a crucial factor to quantifying the impact of erosion on the atmospheric CO<sub>2</sub> pool [*Harden et al.*, 1999]. The influence of the decomposition of eroded SOC on soil-atmosphere C exchange has been studied by *Billings et al.* [2010], at a single eroding profile under different assumptions about management practices. However, SOrCERO does not explicitly track the dynamics of eroded SOC. Thus, assumptions are required about the fate of eroded SOC. These assumptions facilitate the point comparison between tRIBS-ECO and SOrCERO. Note that tRIBS-ECO operates at the watershed, not point, scale and does not require assumptions on the amount of eroded SOC that is protected from oxidation because its spatially (and thus topographically) explicit structure dictates that fate. Two extreme cases were considered for the two models: (1) all eroded SOC leaving the soil profile is completely oxidized during transport and burial [*Lal*, 1995], and (2) eroded SOC is stored in deeper horizons at depositional sites, inhibiting oxidation [*Smith et al.*, 2001]. The two cases define the envelope of possible atmospheric CO<sub>2</sub> fluxes illustrated in Figure 2-8. tRIBS-ECO results corresponding to the two cases are also plotted in Figure 2-8. The illustrated series of C fluxes span the full range of scenarios regarding

the fate of the eroded SOC. Thus, both for the maximum sink (Figure 2-8a) and maximum source (Figure 2-8b) scenarios (section 2.4.2), C fluxes obtained from the change in SOC between the uneroded profile (i.e., model start) and the model result after 100 years of erosion history for each model and assumption about the fate of eroded C illustrated in Figure 2-8. The tRIBS-ECO model thus yields a max source of  $70.7 \text{ g C m}^{-2} \text{ yr}^{-1}$  and a maximum sink of  $-65.5 \text{ g C m}^{-2} \text{ yr}^{-1}$ , while the maximum source and sink values using SOrCERO were  $46.3 \text{ g C m}^{-2} \text{ yr}^{-1}$  and  $-199.2 \text{ g C m}^{-2} \text{ yr}^{-1}$ , respectively. The range estimated by SOrCERO is markedly larger than the one estimated by tRIBS-ECO (section 2.6).

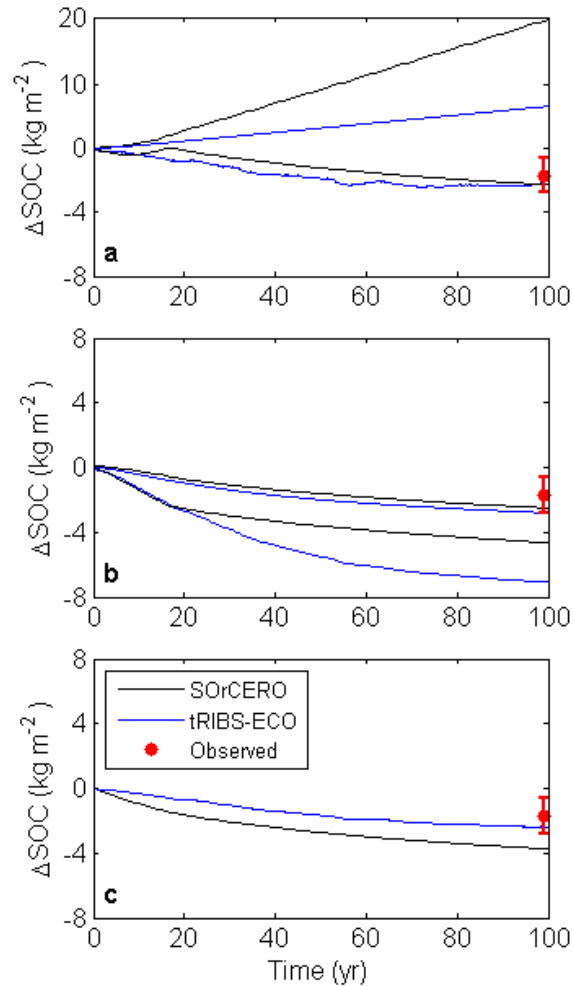


Figure 2-8. Temporal evolution of the difference in total profile soil organic carbon storage ( $\Delta\text{SOC}$ ) resulting from SOC fluxes at eroding site A for tRIBS-ECO (in blue) and for SOrCERO (in black), and  $\Delta\text{SOC}$  based on the observations of Table 2.4 (red points; the associated range corresponds to one standard deviation). Maximum sink and maximum source scenarios for both models are illustrated in (a) and (b), respectively.

The positive vertical axis in (a) is at a different scale. Positive and negative values of  $\Delta\text{SOC}$  represent a net sink and source of atmospheric  $\text{CO}_2$ , respectively. In (a) and (b) for each model two extreme cases on the fate of eroded SOC are illustrated: The series with relatively higher value of total  $\Delta\text{SOC}$  correspond to the case where eroded SOC leaving the soil profile is completely oxidized during transport and burial; the series with relatively lower value of total  $\Delta\text{SOC}$  correspond to the case where the eroded SOC is fully protected from oxidation. Depending on the fate of eroded SOC, estimates by the two scenarios are in the vicinity of the net C exchange with the atmosphere of the site. Simulated net SOC losses to erosion corresponding to intermediate scenarios for the two models are compared against the observed  $\Delta\text{SOC}$  in (c). The quantitative equivalency of

the illustrated intermediate scenarios is discussed in section 2.5.1. The episodic erosion in tRIBS-ECO leads to a closer representation of the history of SOC erosion of the site.

SOC content observations from four soil profiles in undisturbed hardwood stands were also compared with four profiles in eroded pine stands at the Calhoun CZO [Billings *et al.*, 2010; Markewitz and Richter, 1998; Richter and Markewitz, 2001; Richter *et al.*, 1999] (Table 2.4). It is estimated that the mean SOC loss to erosion is equal to  $1.7 \text{ kg m}^{-2}$  (32% loss of the original SOC storage), and the coefficient of variation (defined as the ratio of the standard deviation over the mean) is equal to 0.65. This estimate represents the cumulative SOC loss to erosion during the agricultural history of the area [Trimble, 1974], and is equivalent to  $17 \text{ g C m}^{-2} \text{ yr}^{-1}$  over 100 years of agriculture. Figures 2-8a and 2-8b illustrate the observation-based  $\Delta\text{SOC}$  (red points) and the associated spatial variation (one standard deviation), in comparison to the maximum sink and maximum source scenarios, respectively. For the maximum sink scenario (Figure 2-8a), simulations corresponding to different assumptions about the fate of eroded SOC encompass the average  $\Delta\text{SOC}$  inferred from observations. For the maximum source scenario (Figure 2-8b), the simulations that assume protection of eroded SOC from oxidation ( $2.8 \text{ kg m}^{-2} \text{ C}$  loss for tRIBS-ECO and  $2.5 \text{ kg m}^{-2}$  for SOrCERO, respectively) are not statistically different from observations.

Table 2.4. Soil organic carbon (SOC) content at soil profiles in relatively undisturbed hardwood stands and in eroded old-field pine stands, at the Calhoun Critical Zone Observatory [Billings *et al.*, 2010; Markewitz and Richter, 1998; Richter and Markewitz, 2001; Richter *et al.*, 1999]. Data from four soil profiles of each forest type were available. The coefficients of variation are given in parentheses. The estimated mean difference in SOC content ( $\Delta$ SOC approximately equal to  $1.7 \text{ kg m}^{-2}$ ) represents the cumulative SOC loss to erosion during the agricultural history of the area [Trimble, 1974].

Depth (m)	SOC ( $\text{kg m}^{-2}$ )	SOC ( $\text{kg m}^{-2}$ )	$\Delta$ SOC ( $\text{kg m}^{-2}$ )
	Undisturbed sites	Eroded sites	
0-0.30	3.252 (0.24)	1.907 (0.13)	1.345 (0.62)
0.30-0.55	0.959 (0.18)	0.760 (0.32)	0.199 (1.49)
0.55-0.875	0.749 (0.33)	0.711 (0.54)	0.037 (12.2)
0.875-1.1	0.347 (0.47)	0.232 (0.28)	0.114 (1.54)
0-1.1	5.307 (0.18)	3.611 (0.16)	1.696 (0.65)

The performance of the two models at site A for an intermediate scenario of SOC fluxes was contrasted. For tRIBS-ECO the intermediate scenario discussed in section 2.4.2 was used. For SOrCERO  $n_{ox}$  and  $n_{prod}$  values equal to 0.5 [Billings *et al.*, 2010] were used. The quantitative equivalency of the two model runs is clear by comparing the result of Figure 2-4 (for  $a_l=1.5 \text{ g m}^{-3} \text{ yr}^{-1}$  and  $a_k=0.025 \text{ yr}^{-1}$ ) with the sensitivity analysis of  $n_{ox}$  and  $n_{prod}$  conducted by Billings *et al.* [2010]. The simulated time series of SOC loss to erosion is shown in Figure 2-8c. While SOrCERO significantly overestimated the net erosion-induced SOC loss ( $3.7 \text{ kg m}^{-2}$ ), the mean SOC flux predicted by tRIBS-ECO ( $2.4 \text{ kg m}^{-2}$ ) is within one standard deviation of the observation-based  $\Delta$ SOC ( $1.7 \text{ kg m}^{-2}$ ). In this point comparison the two models were initialized in the same manner (i.e., with data from the undisturbed site discussed in section 2.4.1), and the time average of the erosion rate is the

same (around 3 mm yr<sup>-1</sup>) in the two simulations. The most important structural difference between the two models is the assumed constant erosion in SOrCERO versus the time varying erosion in tRIBS-ECO. The more satisfactory performance of tRIBS-ECO is attributed to its ability to depict episodic SOC erosion at fine time scales. The episodic erosion significantly affects the lateral C flux and the dynamics of oxidation and production of SOC, compared to the assumption of constant erosion [Billings *et al.*, 2010].

### 2.5.2 Watershed-integrated analysis

The watershed-integrated hydro-geomorphic response of Holcombe's Branch and the erosion-induced soil-atmosphere CO<sub>2</sub> flux were modelled using tRIBS-ECO. The model was forced with the 100-year hydroclimatic scenario discussed in section 2.4.4. The effect of management practices on the interaction of erosion and soil-atmosphere C flux was illustrated using the maximum source, intermediate, and maximum sink scenarios discussed in section 2.4.2. Spatially-explicit results for the three scenarios are presented in Figure 2-6, illustrating the difference between the initial and final SOC storage at each computational element. The total SOC storage predicted in 5 m of soil for the three scenarios is illustrated in Figure 2-9. Watershed-integrated results yielded a 14.5 g m<sup>-2</sup> yr<sup>-1</sup> C source for the maximum source scenario, a -18.2 g m<sup>-2</sup> yr<sup>-1</sup> C sink for the maximum sink scenario, and a relatively small (0.08 g m<sup>-2</sup> yr<sup>-1</sup> C source) net C exchange with the atmosphere for the intermediate scenario. Results correspond to 100-year mean C fluxes averaged over the watershed area. The simulated range of erosion-induced soil-atmosphere C exchange (-18.2 to 14.5 g C m<sup>-2</sup> yr<sup>-1</sup>) encompasses net C sink estimates by Yoo *et al.*

[2005] (-1.7 to -2.8 g C m<sup>-2</sup> yr<sup>-1</sup>) and by *Van Oost et al.* [2005] (-3 to -10 g C m<sup>-2</sup> yr<sup>-1</sup>), and is in agreement with the net C sink estimates reported in *Harden et al.* [1999] (-10 to -20 g C m<sup>-2</sup> yr<sup>-1</sup>). *Jacinthe and Lal* [2001] predicted a greater erosion-induced C source strength (6 to 52 g C m<sup>-2</sup> yr<sup>-1</sup>) (Table 2.5).

Significant SOC loss is evident across hillslopes for the maximum source scenario (Figures 2-6b and 2-9a). For the intermediate scenario (Figures 2-6c and 2-9b) there are losses of SOC at eroding hillslopes and increases in the amount of SOC at depositional sites, across the stream network (statistics of  $\Delta$ SOC are given in Table 2.6). For the maximum sink scenario relatively higher SOC content at the surficial horizons of eroding sites leads to larger amounts of SOC in the mobilized sediment (Figures 2-6d and 2-9c). The SOC loss to erosion estimated from observations (17 g m<sup>-2</sup> yr<sup>-1</sup>) is in the vicinity of the simulated range of C fluxes, even though the exact fraction of the eroded SOC that contributed to atmospheric CO<sub>2</sub> cannot be determined.

Table 2.5. Comparison of watershed-integrated estimates of the net soil-atmosphere C exchange with published estimates. Positive and negative values correspond to net erosion-induced C sources and sinks, respectively (values in g C m<sup>-2</sup> yr<sup>-1</sup>).

Source	Range
tRIBS-ECO	-18.2 to 14.5
<i>Harden et al.</i> [1999]	-10 to -20
<i>Yoo et al.</i> [2005]	-1.7 to -2.8
<i>Van Oost et al.</i> [2005]	-3 to -10
<i>Jacinthe and Lal</i> [2001]	6 to 52

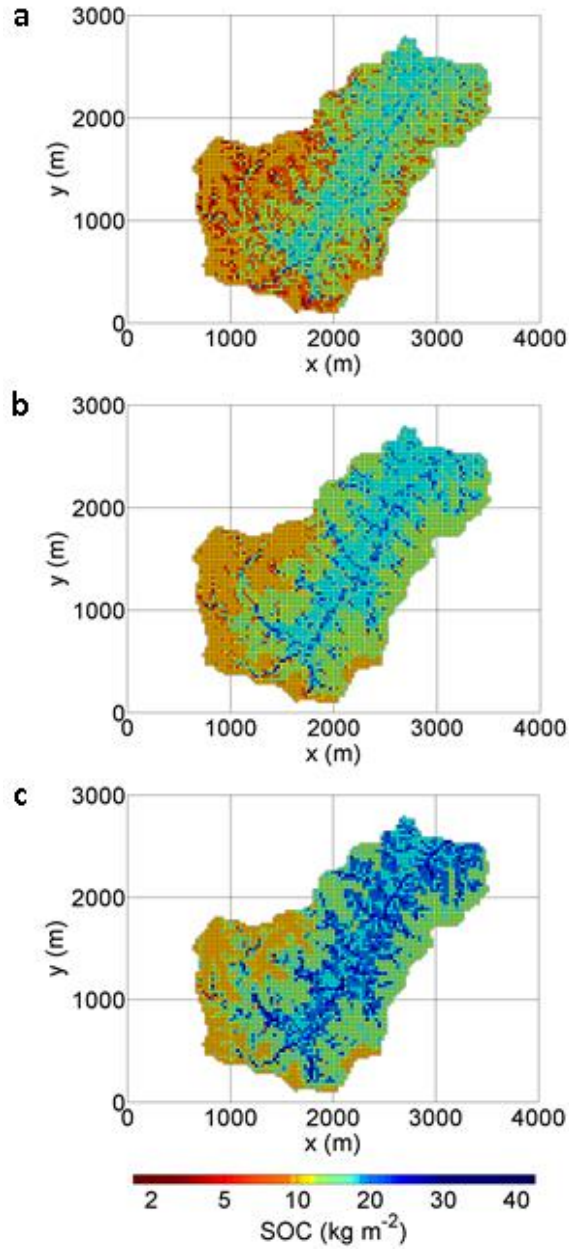


Figure 2-9. Topographic variation of simulated soil organic carbon storage across the watershed. Total soil organic carbon (SOC) storage at the upper 5 m of soil is illustrated for the maximum source (a), intermediate (b), and maximum sink (c) scenarios, respectively.



The proportion of eroding C replaced by newly sequestered C [*Harden et al.*, 1999; *Stallard*, 1998] was estimated across the watershed. The ratio of net vertical (i.e., exchange between the soil profile and the atmosphere) to lateral C fluxes at eroding sites across the watershed was studied for the 100-year intermediate scenario (Figure 2-10), which is more representative of the C exchange with the atmosphere at eroding sites (demonstrated in section 2.5.1). Table 2.6 gives the statistical properties of the total eroded and replaced SOC at eroding sites, respectively. On average, 34% of eroded C has been replaced by C sequestration. The results highlight the wide topographic variability of C replacement across sites with varying hillslope morphology (Figure 2-10).

Table 2.6. Statistics of the total eroded and replaced soil organic carbon (SOC) at eroding sites, and of the net total SOC difference ( $\Delta$ SOC) at the watershed scale for the 100-year intermediate scenario (values in kg m<sup>-2</sup>).

	Eroding sites		Watershed scale
	Eroded SOC	Replaced SOC	$\Delta$ SOC
Mean	0.97	0.38	0.01
Standard deviation	1.52	0.56	1.59
Minimum	0	0	-8.14
Maximum	8.66	2.18	17.26

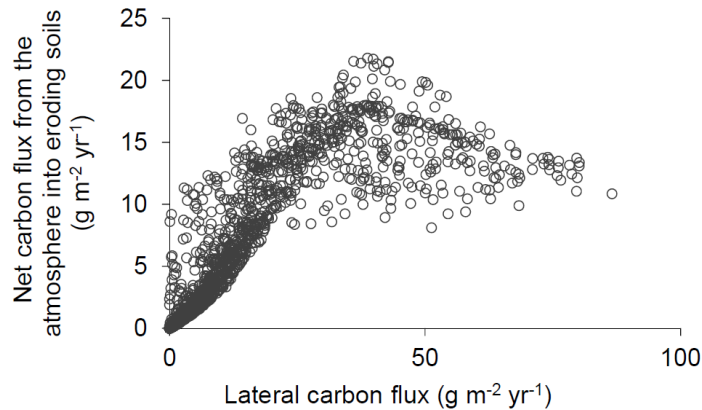


Figure 2-10. Net carbon flux into eroding soils due to replacement by vegetation inputs versus erosion-induced lateral carbon flux. This figure illustrates the wide topographic variation of carbon (C) fluxes across the landscape for the intermediate scenario. 34% of the eroding C is being replaced by sequestered C from the atmosphere. A significant coefficient of variation (defined as the ratio of standard deviation over the mean) of around 8 characterizes the large natural spatial variability of the C replacement ratio (i.e., the ratio of C uptake over C loss to erosion).

## 2.6 Discussion

### 2.6.1 Erosion-induced soil-atmosphere carbon exchange

This work models movement of SOC across the landscape as induced by accelerated erosion, and how erosion and lateral SOC redistribution (Figures 2-6 and 2-9) exhibit significant spatial heterogeneity controlled by hillslope characteristics, variation of soil physical and biochemical properties, and management practices. Severe erosion can transfer subsoil from eroding to depositional sites, and the reallocated sediment can bury formerly surficial horizons at depositional areas [Quinton *et al.*, 2010; Stallard, 1998; Van Oost *et al.*, 2005]. This process combined with advection/diffusion phenomena among different horizons results in continuously evolving vertical profiles of SOC. Consequently,

in agreement with *Van Oost et al.* [2007], sampling of deeper C storage is required to strengthen previous conclusions that rely on measurements at surficial horizons.

Based on the significant topographic variability of C fluxes presented in the results (section 2.5.2), this study highlights the strong control that slope morphology exerts on the redistribution of SOC as a function of erosion and deposition. Systematically tracking the dynamics of eroded SOC across the landscape (section 2.5.1) is critical for estimating the strength of erosion-induced atmospheric CO<sub>2</sub> flux [*Harden et al.*, 1999; *Van Oost et al.*, 2007]. In the modelling framework, eroded SOC is redistributed across the landscape, and can experience oxidation upon transport or storage at depositional sites. This analysis demonstrates that SOC burial at depositional sites is either short-term [*Van Oost et al.*, 2012] or long-term, depending on geomorphological characteristics, the rate of sediment transport, and oxidation rates at depositional sites. This representation of spatial heterogeneity of erosion and of the dynamics of mobilized SOC is an important improvement to studies based on conceptual scenarios regarding the fate of eroded SOC [*Billings et al.*, 2010; *Lal*, 1995; *Smith et al.*, 2001].

To quantify the influence of the spatially-explicit, physically-based representation of C erosion and deposition on the net atmospheric CO<sub>2</sub> flux, a comparison with the SOrCERO model (section 2.5.1) was carried out at the watershed scale for the 100-year scenario of severe erosion discussed in section 2.4.4. The SOrCERO annual erosion rate was fixed at 1 mm yr<sup>-1</sup> characterizing eroding sites at the Holcombe's Branch [*Billings et al.*, 2010], and the input data given in Figure 2-3 were used. Maximum sink and maximum source scenarios were considered for SOrCERO which provided a maximum net C source and sink of 27.5 g m<sup>-2</sup> yr<sup>-1</sup> and -53.7 g m<sup>-2</sup> yr<sup>-1</sup>, respectively. This range encompasses the

SOC loss of  $17 \text{ g m}^{-2} \text{ yr}^{-1} \text{ C}$  deduced from observations (section 2.5.1), yet is markedly larger than the range estimated by tRIBS-ECO (i.e., maximum net C source and sink strength of 14.5 and  $-18.2 \text{ g m}^{-2} \text{ yr}^{-1}$ , respectively). The approach implemented in tRIBS-ECO is more faithful to the actual erosion-inducing mechanisms and involves a significantly more detailed description of the study area (see section 2.4). The large discrepancies are attributed to the inability of SOrCERO to constrain the range of possible C fluxes by accounting for the fate of eroded SOC, including the role of depositional sites in storing eroded SOC, and by representing time varying erosion (section 2.5.1).

#### 2.6.2 Episodic erosion of soil organic carbon

The watershed's response to hydro-meteorological events leads to episodic events on soil erosion. The magnitude and frequency of erosion events control lateral C losses [Dlugob *et al.*, 2012]. This study accounts for the episodic character of erosion rates resulting from the watershed's hydro-geomorphic response to hydro-meteorological forcings at the hourly time scale. This work demonstrates the potential of a time varying representation of erosion and management practices on assessing the SOC redistribution across a watershed, and quantifying the net atmospheric CO<sub>2</sub> flux. For this purpose, a point comparison was used at an eroding profile of the results of tRIBS-ECO and SOrCERO, the latter assuming a constant erosion rate. The simulated scenarios were evaluated based on SOC erosion inferred from observations at the site (section 2.5.1). In this point comparison, different assumptions about management practices and the fate of eroded SOC (Figure 2-8) lead to a relatively wide range of erosion-induced C fluxes. Accounting for effects of

episodic erosion in estimates of net soil-atmosphere C exchange may lead to a significantly more constrained range of possible C fluxes compared to the case when a constant erosion rate is assumed. More precisely, while the maximum source strength estimated by SOrCERO is 35% lower than the one obtained by the proposed approach, the maximum sink strength is more than 3 times greater than the one estimated by tRIBS-ECO. As a result, the total range of possible C fluxes estimated by SOrCERO is 80% larger than the one estimated by tRIBS-ECO (Figure 2-8). Depending on the fate of eroded SOC, the extreme scenarios may approximate the net C exchange with the atmosphere that characterized the site during its agricultural history [Trimble, 1974]. The extent to which eroded SOC is oxidized upon transport and burial has an important role in the erosion-induced C sink or source strength [Billings *et al.*, 2010]. There is a clear need to systematically track the dynamics of eroded SOC to accurately estimate the net soil-atmosphere C exchange. Moreover, it is reasonable that changes in management practices and land uses [Trimble, 1974] may lead to a transition between an erosion-induced net C source and a net C sink over time [Harden *et al.*, 1999; Van Oost *et al.*, 2012].

Accounting for time varying erosion may lead to a more accurate representation of the total SOC losses to erosion at the site. The performance of the two models to mimic the SOC erosional history of site A was evaluated for an intermediate scenario of C fluxes (section 2.5.1). While SOrCERO overestimated the SOC loss to erosion by more than twice, the C loss estimate of tRIBS-ECO is significantly closer to the observed one. This point comparison demonstrates that the episodic representation of erosion and management practices can have a meaningful impact on soil-atmosphere CO<sub>2</sub> exchange, and hence should be taken into account in studies assessing the influence of erosion on the C cycle.

Neglecting the fine temporal dynamics associated with the episodic character of natural erosion-inducing mechanisms [Billings *et al.*, 2010; Liu *et al.*, 2003; Rosenbloom *et al.*, 2006; Van Oost *et al.*, 2005; Yoo *et al.*, 2005] may significantly affect estimates of the net C exchange with the atmosphere.

### 2.6.3 Spatial variation of carbon replacement

Assumptions about the proportion of eroding C replaced by newly sequestered C (“dynamic replacement” [Harden *et al.*, 1999; Stallard, 1998]) vary in the literature [Harden *et al.*, 1999; Smith *et al.*, 2001; Van Oost *et al.*, 2007] leading to markedly different conclusions on the net C exchange with the atmosphere. Results for the intermediate indicate that 34% of the eroding C across the watershed has been replaced by sequestered C from the atmosphere, which is consistent with the range of 11% to 55% reported in the global study of Van Oost *et al.* [2007]. The associated replacement mainly occurs at the active SOC pool with turnover times up to decades [Harden *et al.*, 1999; Van Oost *et al.*, 2007]. Though accounting for preferential erosion of varying sized soil aggregates is out of the scope of this study, preferential erosion of soil particles (e.g., nutrient rich clays with relatively high moisture retention capacity) can lead to changes in soil characteristics at the eroding site, altering the ability to produce and store SOC [Billings *et al.*, 2010; Hu and Kuhn, 2014]. Erosion of surficial horizons may reduce the potential of the remaining soil system to promote SOC production [Billings *et al.*, 2010]. As a result, in unfertilized systems C inputs at eroding sites may decline relative to their pre-erosion rate [Harden *et al.*, 1999]. In contrast, in managed systems fertilization may enhance system productivity

at eroding sites [*Harden et al.*, 1999; *Stallard*, 1998]. The moderating effect of management practices on altered SOC production at eroding sites [*Billings et al.*, 2010] is explicitly accounted for by the proposed framework in the simulated scenarios.

This study stresses the role of small scale dynamics of soil erosion driven by topography on the variability of C fluxes. SOC replacement varies across the landscape depending on a multitude of factors including SOC content, oxidation rate, and bulk density, and it can be influenced by management practices (chapter 7), as episodic erosion proceeds. The distinctive (hook-shaped) pattern formed by the relationship between net lateral C loss at eroding sites and net C influx from the atmosphere to the soil (Figure 2-10) suggests high erosion rates such as those occurring on steep hillslopes can promote C losses to a greater extent than SOC can be regenerated. These sites correspond to points in Figure 2-6c with relative higher net lateral C loss. The wide topographic variation (Table 2.6) depicts the strong control hillslope morphology exerts on the soil's ability to store sequestered atmospheric C. This highlights the significant spatial variability of the associated C fluxes, which cannot be reflected in studies focusing at a single eroding site [*Billings et al.*, 2010].

The natural variability on the C replacement ratio across the watershed can be quantified by a coefficient of variation of approximately equal to 8. The strong variation of C replacement (Figure 2-10) at small spatial scales (tens of meters) is comparable to that reported by *Van Oost et al.* [2007] who conducted an analysis of 1,400 profile measurements. The results of this study were obtained for various settings of hillslope characteristics, based on a detailed representation of episodic and spatially heterogeneous soil erosion. The large spatial variability of soil-atmosphere C flux is attributed to the

complexity of erosion-inducing processes at small scales, which exerts a strong control on depth-dependent biogeochemical properties of soils, including SOC oxidation and production.

## **2.7 Summary**

This work presents a physically-based approach to assess the influence of soil erosion on atmospheric CO<sub>2</sub>, that stresses the heterogeneity at fine spatial scales of SOC erosion, SOC burial, and associated soil-atmosphere C fluxes. The Holcombe's Branch watershed, part of the Calhoun Critical Zone Observatory in South Carolina, USA is the case study used. The site has experienced some of the most serious agricultural soil erosion in North America. This study uses SOC content measurements from contrasting soil profiles, and estimates of SOC oxidation rates at multiple soil depths. The methodology was implemented in the tRIBS-ECO (Triangulated Irregular Network-based Real-time Integrated Basin Simulator-Erosion and Carbon Oxidation), a spatially- and depth-explicit model of SOC dynamics built within an existing coupled physically-based hydro-geomorphic model. According to observations from multiple soil profiles, about 32% of the original SOC content has been eroded in the study area. The results indicate that C erosion and its replacement exhibit significant topographic variation at relatively small scales (tens of meters). The episodic representation of SOC erosion reproduces the history of SOC erosion better than models that use an assumption of constant erosion in space and time. The net atmospheric C exchange at the study site is estimated to range from a maximum source of 14.5 g m<sup>-2</sup> yr<sup>-1</sup> to a maximum sink of -18.2 g m<sup>-2</sup> yr<sup>-1</sup>. The small-scale



complexity of C erosion and burial driven by topography exerts a strong control on the landscape's capacity to serve as a C source or a sink.

## **CHAPTER 3.      Uncertainty associated with the impact of erosion and deposition on soil-atmosphere carbon exchange**

### **3.1 Introduction**

Soils disturbed by anthropogenic activity constitute dynamic and rapidly changing systems [Doetterl *et al.*, 2012; Richter and Markewitz, 2001]. The extent to which land use and management practices (e.g., forest logging, cultivation, grazing, or fertilization) enhance SOC decomposition or significantly increase SOC production is important in quantifying the erosion-induced soil-atmosphere C exchange [Abaci and Papanicolaou, 2009; Billings *et al.*, 2010; Dlugoß *et al.*, 2012; Hu and Kuhn, 2014]. The influence of management practices on SOC storage at eroding soils contributes to the variability of C erosion and replacement in diverse soil profiles [Kuhn *et al.*, 2009; Van Oost *et al.*, 2012] and to uncertainties in regional and global C budgets [Berhe *et al.*, 2007; Billings *et al.*, 2010].

This work proposes a method to quantify the uncertainty introduced by land management practices on estimates of the net erosion-driven soil-atmosphere C exchange at the landscape scale. A stochastic formulation is used to quantify this uncertainty at eroding soil profiles. In particular, the variability and temporal dependence of the influence of management practices on SOC decomposition and production rates are represented by means of a bivariate stochastic process (section 3.2). The methodology is implemented in

the coupled and spatially-explicit biogeochemical model (tRIBS-ECO) introduced in section CHAPTER 2, which tracks the dynamics of mobilized organic material and quantifies the net effect of erosion on C fluxes using depth-dependent soil biogeochemical properties from multiple soil profiles at different catena positions. This study focuses on the Holcombe's Branch watershed (Figure 3-1a) in the Calhoun Critical Zone Observatory, the environmental history of which is characterized by intensive land uses, and by land use change (see section 2.3). This work quantifies the potential decline in upland soil and SOC erosion rates driven by the rapid reforestation that characterized the study area. More specifically, this study extends previous modelling efforts that studied this site [*Billings et al.*, 2010], as it explicitly accounts for changes in land use and land cover and associated controls on sediment transport and C burial, using recently obtained elevation data and forest cover information from two characteristic periods (agro-ecosystem and secondary forest ecosystem periods, respectively (section 3.3)). Unpublished data based on observations of alluvial sediment thickness and SOC storage in depositional sites (section 3.5) were used to quantify rates of soil erosion and burial of organic material across the landscape. This work highlights the spatio-temporal variability that characterizes upland SOC erosion and burial, depending on land uses, land use change, and hydro-climatic perturbations. This chapter is a verbatim recompilation of *Dialynas et al.* [2017] and *Bras et al.* [2015].

### **3.2 Stochastic representation of the influence of land management practices on eroding soils**

The spatially-explicit and physically-based model of C dynamics tRIBS-ECO (section 2.2) is used in this study. This work proposes a method to assess and quantify uncertainties associated with management practices on estimates of SOC erosion and SOC storage predictions by accounting for the variability of  $a_k$  and  $a_l$  in the tRIBS-ECO model and their dependence on time. In agricultural areas where management practices (e.g., fertilization, cultivation, grazing [Richter *et al.*, 1999]) exhibit little variation in subsequent years [Harden *et al.*, 1999; Trimble, 1974], the influence of land management on eroding soils can be characterized by significant temporal autocorrelation at relatively short time lags. Also,  $a_k$  and  $a_l$  may co-vary for different management regimes [Mobley *et al.*, 2015; Richter *et al.*, 2007] (section 3.3.3).

In this study  $a_k$  and  $a_l$  are treated as correlated stochastic processes. The temporal dependence is represented by the autoregressive model of order 1 (AR(1)) [Box *et al.*, 2011]. The AR(1) is a simple parsimonious stationary stochastic model, widely used in hydrology [Bras and Rodriguez-Iturbe, 1985], and is characterized by an exponential decay of autocorrelation with time. The bivariate AR(1) model is given by

$$\underline{z}_t = \mathbf{A}\underline{z}_{t-1} + \mathbf{B}\underline{\varepsilon}_t \quad (3.1)$$

where  $\underline{z}_t$  corresponds to the  $2 \times 1$  vector of states at time  $t$  ( $T$  denotes transpose):

$$\underline{z}_t = \begin{bmatrix} a_{k,t} & a_{l,t} \end{bmatrix}^T \quad (3.2)$$

$\underline{\varepsilon}_t$  is the  $2 \times 1$  vector of innovations at time  $t$ , independent in time and space,  $\mathbf{A}$  is a  $2 \times 2$  matrix given by

$$\mathbf{A} = \mathbf{M}_1 \mathbf{M}_0^{-1} \quad (3.3)$$

where  $\mathbf{M}_0$  and  $\mathbf{M}_1$  are lag-zero and lag-one covariance matrices, respectively:

$$\mathbf{M}_0 = \begin{bmatrix} \text{Var}[a_k] & \text{Cov}[a_I, a_k] \\ \text{Cov}[a_k, a_I] & \text{Var}[a_I] \end{bmatrix} \quad (3.4)$$

$$\mathbf{M}_1 = \begin{bmatrix} \rho_{a_k} \text{Var}[a_k] & 0 \\ 0 & \rho_{a_I} \text{Var}[a_I] \end{bmatrix}$$

$\rho_{a_k}$  and  $\rho_{a_I}$  are the lag-one autocorrelation coefficients of  $a_k$  and  $a_I$ , respectively.  $\mathbf{B}$  is a  $2 \times 2$  matrix of parameters obtained by decomposing the variance-covariance matrix [Bras and Rodriguez-Iturbe, 1985; Koutsoyiannis, 1999]:

$$\mathbf{B}\mathbf{B}^T = \mathbf{M}_0 - \mathbf{M}_1 \mathbf{M}_0^{-1} \mathbf{M}_1^T \quad (3.5)$$

The marginal distributions of  $a_k$  and  $a_I$  are Normal and, by definition, time invariant.

At time step  $t$ , the variance of  $a_{I,t}$  conditioned to the previous state  $a_{I,t-1}$  is estimated as a function of the statistical properties of the stationary process  $a_I$  [Bras and Rodriguez-Iturbe, 1985]:

$$\text{Var}[a_{I,t} | a_{I,t-1}] = \text{Var}[a_I] (1 - \rho_{a_I}^2) \quad (3.6)$$

The conditional variance of  $a_{k,t}$  at each time step is estimated in the same manner.

### **3.3 Model inputs and parameters**

#### **3.3.1 Evolution of vegetation cover during reforestation**

The recent history of southern Piedmont is characterized by impressive reforestation of the seriously eroded agricultural soils [Mobley *et al.*, 2015; Trimble, 1974]. This study assesses the extent to which reforestation leads to gradual decline of erosion of upland soil and SOC, and quantifies the hydro-geomorphic behavior of the watershed and the associated SOC redistribution in a 100-year simulation. The temporal evolution of forest cover is represented using surface information of two characteristic periods: a) the agro-ecosystem period, and b) the secondary forest ecosystem period [Richter *et al.*, 2000]. The agro-ecosystem and the secondary forest ecosystem periods are represented in two consecutive 50 years of simulation.

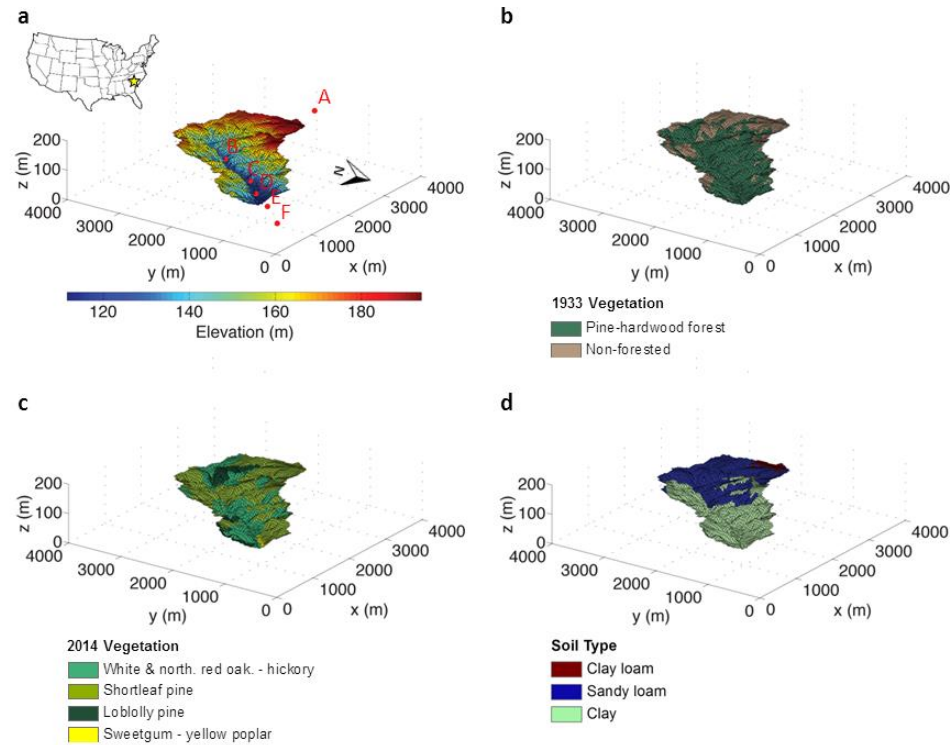


Figure 3-1. The Holcombe's Branch; site A corresponds to an undisturbed soil profile; sites B to F correspond to sampling locations of legacy sediments (a), spatial distribution of vegetation cover in 1933 (agro-ecosystem period (Figure 3-2)) (b), and in 2014 (secondary forest ecosystem period [NCALM, 2014]) (c), and spatial distribution of soil textural classes (d).

The spatial distribution of forest cover at the late agro-ecosystem period is specified by analyzing a U.S. Forest Service aerial photograph obtained in 1933 [Brecheisen and Cook, 2015] (Figure 3-2). During the agro-ecosystem period the watershed was largely covered by low density mixed pine-hardwood forest, pastures, and cultivated fields [Richter and Markewitz, 2001]. Several parts of the watershed were characterized by little or no forest cover, including north-eastern slopes, areas in the vicinity of the watershed boundary, and the western part of the watershed. Agricultural practices are evident at the western ridge in Figure 3-2. Land management practices during the agro-ecosystem period

included the extensive use of fertilizers [Richter *et al.*, 2000]. Based on Figure 3-2 forested versus non-forested areas are classified across the watershed (see Figure 3-1b). It is estimated that around 36% of the total watershed area was not forested during the agro-ecosystem period.

The forest cover at the secondary forest ecosystem period was characterized using a vegetation cover map obtained from recent LiDAR surface data [NCALM, 2014] (Figure 3-1c). Naturally regenerating pine forests significantly expanded in the area during the mid-20<sup>th</sup> century [Richter *et al.*, 2000]. The Holcombe's Branch is covered by various forest types: pine stands (loblolly pine (*Pinus taeda*), shortleaf pine (*Pinus echinata*)), mixed hardwood stands consisting of northern red oak (*Quercus rubra*), white oak (*Quercus alba*), and hickory (*Carya sp.*), and hardwood stands dominated by yellow poplar (*Liriodendron tulipifera*) and sweetgum (*Liquidambar styraciflua*). The pine forest types were represented as evergreen needleleaf forest [Hansen *et al.*, 2000], and the remaining classes were modelled as deciduous broadleaf forest.



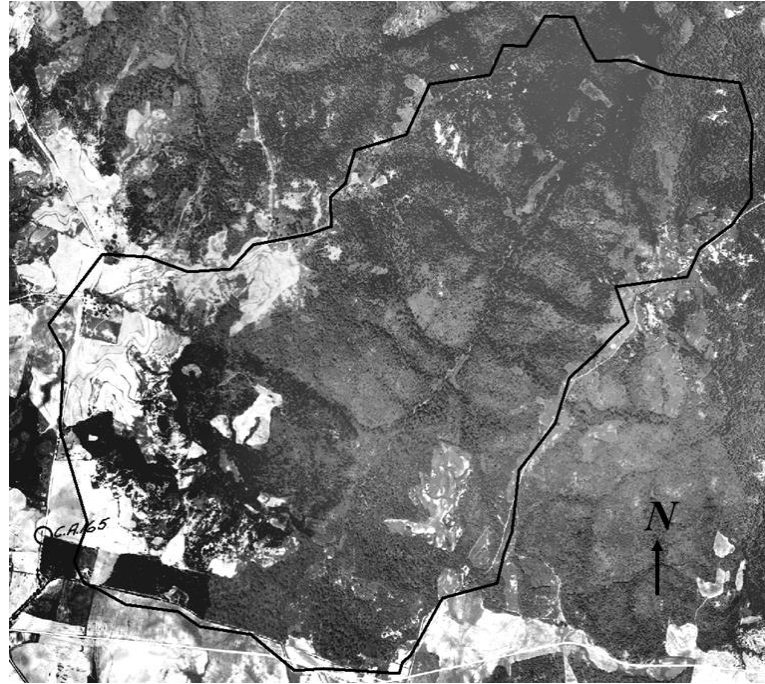


Figure 3-2. Aerial photo of the Holcombe's Branch watershed during the agro-ecosystem period (1933) [Brecheisen and Cook, 2015]. The black line illustrates the watershed divide.

### 3.3.2 Topography, soil types, and soil biogeochemical properties

A DEM was used [NCALM, 2014], which is significantly finer (less than 1 m) than the ones used in previous studies at the site [James *et al.*, 2007]. This DEM depicts important morphologic features such as contributing area, slope, and curvature in detail. A 30 m mesh of Voronoi polygons was derived based on the elevation data set (Figure 3-1a), to reduce computational cost [Ivanov *et al.*, 2004a; b]. The classification of soil properties across the watershed (Figure 3-1b) is discussed in section 2.4.3. The selection of hydrologic and geomorphic soil properties for each soil type is given in section 3.3.4.

The tRIBS-ECO model was initialized by fitting equations (2.2) to (2.4) to the observations of biogeochemical properties ( $C_t(z)$ ,  $k_t(z)$ , and  $\rho(z)$ ) discussed in section 2.4.1. The observations correspond to a relatively undisturbed soil profile located in site A (Figure 3-1a). The initial depth-dependent  $C_t(z)$ ,  $k_t(z)$  are given in Figure 3-3. The depth-variation of modelled bulk density is given in Figure 2-3b. Also, the estimation of the initial depth-dependent rate of SOC production assumes steady state conditions for time  $t=0$ , and is given in Appendix B.

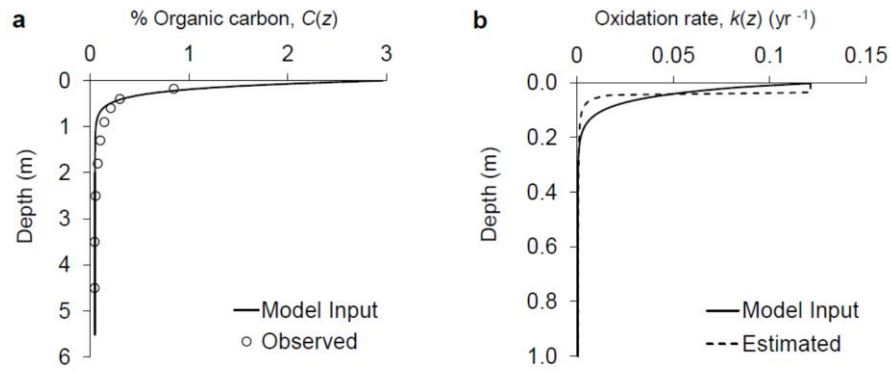


Figure 3-3. Observations and model inputs of depth-dependent soil organic carbon (SOC) fraction (a), and estimated SOC decomposition rate at multiple soil horizons (b) [Billings *et al.*, 2010; Markewitz and Richter, 1998; Richter and Markewitz, 2001; Richter *et al.*, 1999]. The depth-variation of observations is represented by exponential functions.

### 3.3.3 Uncertainty in carbon storage prediction associated with the influence of land management practices

SOC can be rapidly destabilized by accelerated decomposition associated with land management practices (e.g., forest cutover, and cultivation) [Richter *et al.*, 1999]. Systematic use of fertilizers enhanced productivity during the agricultural history of the site [Richter *et al.*, 2000]. This study quantifies the variability of SOC storage at the Holcombe's Branch driven by the uncertainty of the influence of management practices on  $k_t(z)$  and  $I_t(z)$  (section 3.2). From equation (2.1) for a discrete time step:

$$SOC_t = SOC_{t-1} + \int_0^{H_t} I_t(z) dz - \int_0^{H_t} k_t(z) \rho(z) C_t(z) dz + L_t \quad (3.7)$$

where  $L_t$  denotes the net lateral SOC flux at each Voronoi cell:

$$L_t = \sum_i \int_0^{h_{t,i}} \rho_i(z) C_{t,i}(z) dz \Big|_{in} - \int_0^{h_t} \rho(z) C_t(z) dz \Big|_{out} \quad (3.8)$$

By using equations (2.3) and (2.5) in equation (3.7) we obtain:

$$SOC_t = SOC_{t-1} + \int_0^{H_t} I_{a,t} e^{I_{b,z}} dz - \int_0^{H_t} (k_{a,t} e^{k_{b,z}} + k_c) \rho(z) C_t(z) dz + L_t \quad (9)$$

It can be shown (see Appendix C) that at each time step the variance of SOC storage, conditioned on the previous state, is given by:

$$Var[SOC_t | SOC_{t-1}] = \underline{P}_t^T \mathbf{B} \mathbf{B}^T \underline{P}_t \quad (3.10)$$

where  $SOC_{t-1}$  is the value of SOC storage estimated at time step  $t-1$  ( $\mathbf{B} \mathbf{B}^T$  is the covariance matrix given in equation (3.5)), and  $\underline{P}_t$  is a  $2 \times 1$  time variant vector of coefficients:

$$\underline{\mathbf{P}}_t = [c_{1,t} \ c_{2,t}]^T \quad (3.11)$$

where  $c_{1,t}$  and  $c_{2,t}$  are given by

$$\begin{aligned} c_{1,t} &= \int_0^{H_t} e^{I_b z} dz \\ c_{2,t} &= - \int_0^{H_t} e^{k_b z} \rho(z) C(z) dz \end{aligned} \quad (3.12)$$

The conditional distribution of SOC storage is normal at each time step. Three scenarios of C fluxes are studied: a) a maximum sink, b) an intermediate, and c) a maximum source scenario. SOC storage at the maximum source, the intermediate, and the maximum sink scenario is approximated by the 1% quantile, the median, and the 99% quantile of the conditional normal distribution, respectively, as:

$$Q_{SOC_t} = SOC_t + \sqrt{2(\underline{\mathbf{P}}_t^T \mathbf{B} \mathbf{B}^T \underline{\mathbf{P}}_t)} \text{erf}^{-1}(2p-1) \quad (3.13)$$

where  $SOC_t$  is the C storage calculated at time step  $t$  by equation (3.7),  $\text{erf}^{-1}$  is the inverse error function, and  $p$  is the probability associated with the normal distribution quantile, equal to 0.01, 0.50, and 0.99 for the maximum source, the intermediate, and the maximum sink scenario, respectively. The difference of maximum source from maximum sink scenario estimates reflects the uncertainty associated with the influence of land management on the rates of C decomposition and production at eroding sites (section 3.5.3).

With farmers constantly fertilizing their soils in the southern Piedmont during the agro-ecosystem period [Metz, 1958; Richter and Markewitz, 2001], the influence of

management practices on the rates of SOC production and decomposition likely did not exhibit substantial year to year variation [Revels, 2005; Richter *et al.*, 2000]. Systematic fertilization and liming of agricultural soils in the study area may lead to increase in soil nutrient availability and enhancement of system productivity with high biomass inputs from crops, promoting SOC production in eroding soil profiles (higher  $a_I$ ) [Stallard, 1998]. Soil microbes prefer nutrient rich labile SOC, which is produced at high rates in fertilized soils, characterized by accelerated SOC decomposition rates [Billings *et al.*, 2010]. Tillage induces mixing in the soil profile [Yoo *et al.*, 2011] exposing substrate organic matter, and promoting higher microbial turnover and decomposition rates, with increased aeration and increased soil moisture dynamics in eroding soils (high values of  $a_k$ ). On the contrary, rapidly eroding and poorly managed soils in the recent history of the study area [Metz, 1958] can be characterized by lower production rates of labile SOC associated with crop inputs, and by increased proportions of recalcitrant organic matter, which is not decomposed by soil microbes [Billings *et al.*, 2010]. The influence of poor management practices on eroding soils can be represented by relatively low values of  $a_k$  and  $a_I$ . Thus, for different management regimes  $a_I$  and  $a_k$  may co-vary in the soil profiles under study. However, the assumed influence of land management on C fluxes cannot be generalized to diverse ecosystems. The extent to which  $a_I$  and  $a_k$  are positively or negatively correlated may depend on the stoichiometry of surficial and deeper soil horizons, edaphic characteristics, climatic factors, and landscape position [Billings *et al.*, 2010; Richter *et al.*, 2007].

The marginal statistical properties of  $a_k$  and  $a_I$  were selected based on the ranges of possible  $a_k$  and  $a_I$  values derived in section 2.4.2. The ranges of  $a_k$  and  $a_I$  values are given

in Table 3.1. Relatively higher values of  $a_k$  and  $a_I$  represent significant influence of management practices on  $k_I(z)$  and  $I_I(z)$ , respectively (section 2.2). Mean values of  $a_k$  and  $a_I$  were selected corresponding to the middle points of the ranges of Table 3.1. The standard deviations of  $a_k$  and  $a_I$  were selected such that the associated ranges include 95% of the probability mass of the normally distributed  $a_k$  and  $a_I$ , respectively (i.e., four standard deviations). Moreover, a significant lag-zero cross-correlation coefficient ( $\rho_{a_I, a_k}$ ) and relatively high values of  $\rho_{a_k}$  and of  $\rho_{a_I}$  were assumed (see section 3.2). The marginal and joint statistical properties of  $a_k$  and  $a_I$  are summarized in Table 3.1.

Table 3.1. Marginal and joint statistical properties and ranges of  $a_I$  and  $a_k$ .  $E[\cdot]$  denotes the mean value. Equal coefficients of variation (CV) and autocorrelation coefficients for  $a_I$  and  $a_k$ , were assumed ( $\rho_{a_k}$  and  $\rho_{a_I}$ ), respectively.

Parameter	Units	Value
Min / Max $a_I$	[yr <sup>-1</sup> ]	0 / 3.0
Min / Max $a_k$	[g m <sup>-2</sup> yr <sup>-1</sup> ]	0 / 0.050
$E[a_I]$	[yr <sup>-1</sup> ]	1.5
$E[a_k]$	[g m <sup>-2</sup> yr <sup>-1</sup> ]	0.025
CV	[-]	0.5
$\rho_{a_k}$ or $\rho_{a_I}$	[-]	0.7
$\rho_{a_I, a_k}$	[-]	0.5

### 3.3.4 Calibration of the hydro-geomorphic model

The hydrometeorological forcing used in this simulation and the calibration of the soil hydrologic properties are discussed in section 2.4.4. The standing-wood volume significantly increased (probably more than doubled) in the study site between the agro-ecosystem and the secondary forest ecosystem periods [Richter *et al.*, 2000]. The rapid increase in forest density and the associated feedbacks to soil erosion are represented by different values of the ecological parameters  $\nu$ ,  $P$ , and  $F_l$  (section 2.4.5) between the two periods. The selected ecological parameters associated with erosional processes are given in Table 3.2. The simulated temporal evolution of soil loss at eroding sites is presented in Figure 3-4. The cumulative soil loss to erosion over the 100-year simulation (i.e., the total topsoil removal averaged over upland eroding sites) is in agreement with reported erosion rates for the Calhoun CZO, i.e., at least 12 cm per 100 years [Billings *et al.*, 2010; Trimble, 1974]. Model validation based on alluvial deposits is discussed in section 3.5.1.

Table 3.2. Ecological parameters of the geomorphic model. The first two rows (gray) correspond to the agro-ecosystem period; the remaining rows correspond to the secondary forest ecosystem period.

Forest cover	$\nu$	$P$	$C_r$	$F_l$
Non-forested	0	N/A	0.10	N/A
Pine-Hardwood Forest	0.30	0.70	0.10	0.70
Evergreen Needleleaf Forest	0.70	0.25	0.10	0.50
Deciduous Broadleaf Forest	0.60	0.45	0.10	0.40

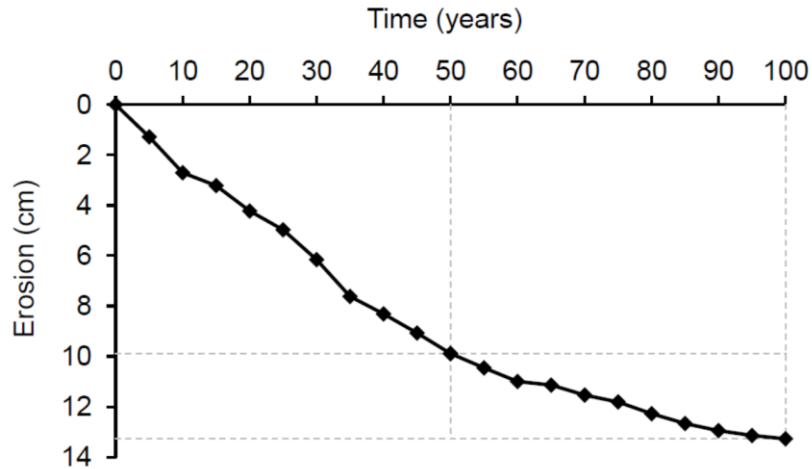


Figure 3-4. Temporal evolution of soil loss at eroding sites.

### 3.4 Results

#### 3.4.1 Accelerated soil erosion and deposition

The 100-year erosion and deposition of upland soil and saprolite at the study site is given in Figure 3-5a. The watershed's relatively steep slopes erode at rates of around  $1 \text{ mm yr}^{-1}$  or greater (illustrated in yellow and orange colors in Figure 3-5a). There is substantial sediment deposition (in blue) across the stream network. The mean sediment yield over the 100 year simulation is equal to  $14.7 \text{ t km}^{-2} \text{ yr}^{-1}$  (assuming bulk density equal to  $1.4 \text{ g cm}^{-3}$  [Richter and Markewitz, 2001]). The sediment loss at the agro-ecosystem period (9.9 cm) is around 3 times greater than the one (3.4 cm) during the secondary forest ecosystem period (Figure 3-4). The total soil loss to erosion (13.3 cm) is consistent with the topsoil erosion rate of at least 12 cm per 100 years that characterizes the study area [Billings *et al.*, 2010; Trimble, 1974] (section 3.3.4).



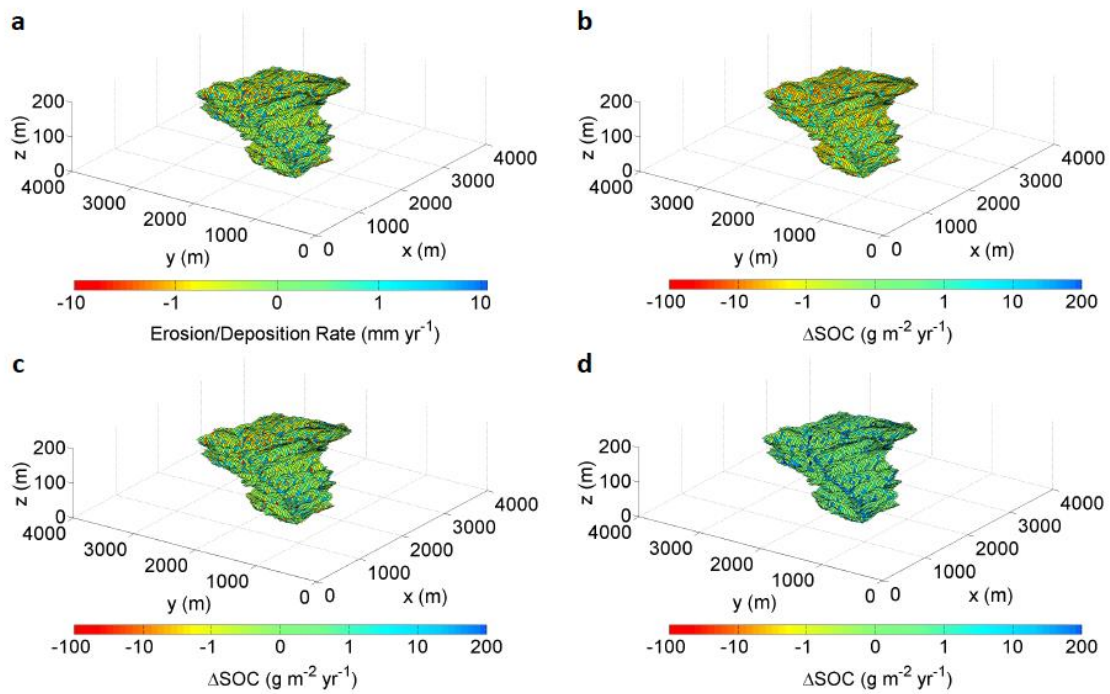


Figure 3-5. Simulated soil erosion and deposition and net soil organic carbon content difference ( $\Delta$ SOC) across the Holcombe's Branch. Relatively high erosion rates characterize hillslopes (yellow and orange colors); depositional sites (in blue) are mainly located across the stream network (a). Redistribution of organic material for the maximum source ( $10.3 \text{ g m}^{-2} \text{ yr}^{-1}$  C source strength) (b), the intermediate ( $-1.5 \text{ g m}^{-2} \text{ yr}^{-1}$  C sink strength) (c), and the maximum sink scenarios ( $-8.4 \text{ g m}^{-2} \text{ yr}^{-1}$  C sink strength) (d), respectively.

### 3.4.2 Erosion-induced carbon exchange with the atmosphere at the watershed scale

This study quantifies the erosion-driven SOC redistribution and  $\text{CO}_2$  exchange with the atmosphere at the watershed scale. The effect of management practices on soil-atmosphere  $\text{CO}_2$  exchange is systematically accounted for in the three scenarios under study (section 3.3.3). Figure 3-4 illustrates the net  $\Delta$ SOC at diverse soil profiles across the

landscape. Estimates of C source or sink strength at the watershed scale ranged from a net C source of  $10.3 \text{ g m}^{-2} \text{ yr}^{-1}$  (maximum source scenario) to a net C sink of  $-8.4 \text{ g m}^{-2} \text{ yr}^{-1}$  (maximum sink scenario). A net C sink of  $-1.5 \text{ g m}^{-2} \text{ yr}^{-1}$  was estimated for the intermediate scenario. The maximum source scenario is characterized by significant erosion of organic material, and by oxidation upon transport and burial (Figure 3-4b). At the intermediate scenario, eroded SOC is partially replaced at eroding hillslopes by newly sequestered atmospheric  $\text{CO}_2$ . Eroded SOC is buried in depositional sites across the stream network (Figure 3-4c). The maximum sink scenario is characterized by rapid replacement of eroded SOC by atmospheric  $\text{CO}_2$  sequestration (Figure 3-4d).

#### 3.4.3 Soil organic carbon erosion and burial at alluvial sediments

The temporal evolution of  $\Delta\text{SOC}$  at upland eroding sites over the 100-year simulations for the three scenarios is given in Figure 3-6. For the maximum sink scenario, replacement of eroded organic material with sequestered atmospheric  $\text{CO}_2$  led to limited decrease in C storage ( $0.08 \text{ kg m}^{-2}$ ). For the intermediate scenario the net SOC loss at eroding soil profiles is  $2.1 \text{ kg m}^{-2}$ . Accelerated SOC decomposition at the maximum source scenario led to a significantly higher net C loss to erosion ( $4.3 \text{ kg m}^{-2}$ ).

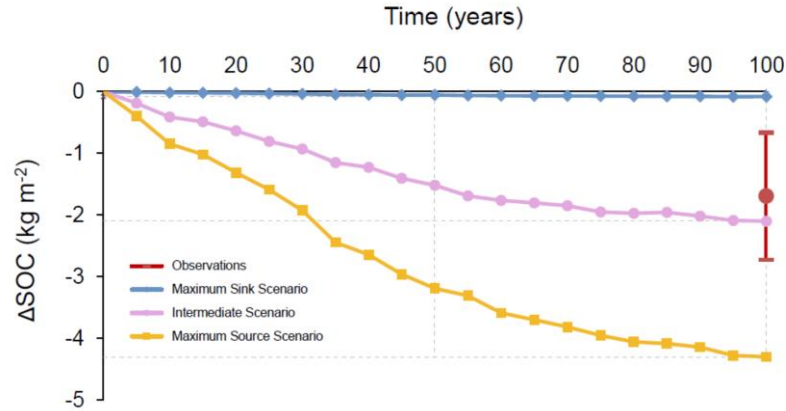


Figure 3-6. Simulated temporal evolution of net soil organic carbon loss ( $\Delta\text{SOC}$ ) at upland eroding sites and  $\Delta\text{SOC}$  inferred from observations (section 2.5). Error bars correspond to one standard deviation. The total  $\Delta\text{SOC}$  for the intermediate scenario is in close agreement with the observations.

The simulated SOC storage in alluvial sediments was estimated for the three scenarios. Evaluation of simulations based on observations of SOC content in alluvial sediments is presented in section 3.5.1. Figure 3-7 illustrates the SOC storage in the upper 1.8 m of soil for each scenario, and the associated spatial variation. The average SOC content is lower for the maximum source scenario, because an important part of eroded SOC has been oxidized upon transport before it reaches burial. At the maximum sink scenario, a significantly higher amount of eroded SOC is buried at depositional sites. There is continuous replacement of upland eroded SOC with atmospheric C sequestration and subsequent erosion and burial of newly sequestered C. Furthermore, the spatial variation of SOC storage increases when substantial depletion of SOC stocks is predicted (maximum source scenario). The coefficients of variation (defined as the ratio of the standard deviation over the mean) of SOC storage over the watershed's depositional sites for the maximum

sink, the intermediate, and the maximum source scenarios are approximately equal to 14%, 24%, and 43%, respectively (Figure 3-7).

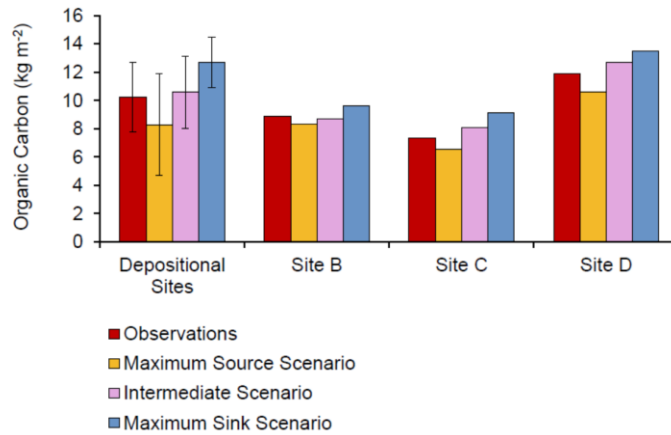


Figure 3-7. Observed and simulated soil organic carbon (SOC) content in alluvial deposits; observations at depositional sites are based on measurements from sites B, C, D, E, and F at the upper 1.8 m of soil (error bars correspond to one standard deviation); point comparisons between observed and simulated SOC storage at sites B, C, and D, respectively.

### 3.5 Discussion

#### 3.5.1 Sediment and organic carbon transport and burial across the landscape

The hydro-geomorphic model's performance was evaluated by comparing simulated soil thickness corresponding to legacy sediments, with observations. Legacy sediments are defined as episodically eroded soil from upland sites following land uses that has accumulated in colluvial deposits at lower hillslopes and in alluvium along stream corridors, altering pre-existing slope morphologies and stream networks [James, 2013].

Human disturbances leading to the formation of legacy sediments include plowing, deforestation, mining, and other land uses. Legacy sediments have led to alteration of the hydrological, biogeochemical, biological, and riparian functions of disturbed environments [James, 2013].

This study uses observations of legacy sediment thickness from eight depositional sites in the Holcombe's Branch watershed (sites S1 to S8), conducted in 2015 and 2016 (unpublished data of Dan Richter, 2016). The sampling sites are located at approximately 100 - 200 m intervals along the main stream, in clayey soils and sandy loams. The observed legacy sediment thickness was inferred from field studies informed by soil texture, carbon, and nitrogen data at different soil profiles [Richter, 2016]. Figure 3-8 shows 117 cm of legacy sediment (site S7) deposited above redox-active Holocene sediments at the study site: the light brown legacy sediment is distinguished from the gray-brown pre-legacy sediment. A comparison between simulated legacy sediment depths against observations is given in Figure 3-9. Simulated soil thickness of legacy sediments was estimated based on the sediment accumulation at depositional sites computed by the hydro-geomorphic model. While this comparison does not support a robust model calibration, it shows that the model has the potential to reasonably simulate the accelerated legacy sediment deposition at the study site.

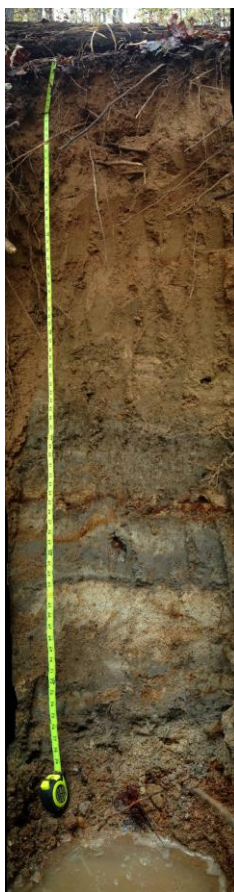


Figure 3-8. Approximately 117 cm of legacy sediment (light brown color) deposited above redox-active Holocene sediments (gray-brown color) at the Holcombe's Branch (site S7) [Richter, 2016].

To evaluate the likelihood of each of the simulated scenarios of SOC erosion and burial, observations of SOC content in legacy sediments were used [Richter, 2016]. Measurements of SOC content from five soil profiles (depositional sites B to F in Figure 3-1a) analyzed in 2015 are given in Figure 3-10. The associated analysis included processing of soil samples, soil texture and bulk density analysis, and combustion and analysis of organic matter [Richter, 2016]. The observations correspond to multiple mineral

soil horizons at the upper 1.8 m of depth. At each soil layer the standard deviation reflects the spatial variation among sampling locations. Comparison of the observed and simulated total SOC storage (upper 1.8 m of soil) at locations B, C, and D is given in Figure 3-7. The ranges of predicted SOC storage for different scenarios at sites B, C, and D (i.e., difference of maximum source from maximum sink scenario estimates at each depositional site, illustrated in Figure 3-7) are, respectively, 1.3, 2.6, and 2.9 kg C m<sup>-2</sup>. Observations are consistent with the ranges of simulated SOC content at the three sites. Moreover, the predicted SOC content across depositional sites was compared with measurements at sites B to F (Figure 3-7). For the maximum source scenario the simulated SOC content is 19% lower (within a standard deviation) from the mean measured one (average of all depositional sites). The maximum sink scenario overestimates by 24% the observed SOC storage. The mean SOC storage estimate for the intermediate scenario is in closer agreement with observations (about 4% deviation). This comparison demonstrates the ability of tRIBS-ECO to simulate the fate of eroded SOC at the watershed scale in response to hydro-geomorphic perturbations.

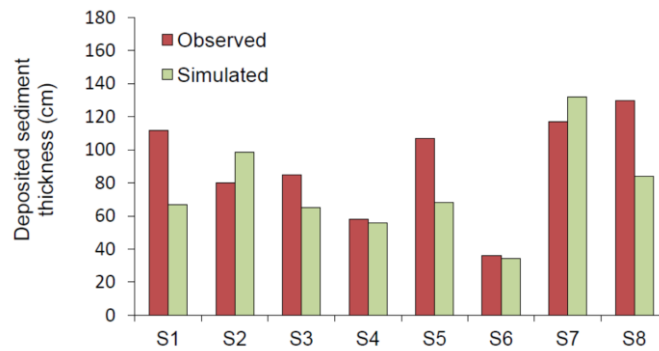


Figure 3-9. Simulated and observed legacy sediment deposition across the stream network. Sites S1 to S8 are located at approximately 100 - 200 m intervals along the main stream in the Holcombe's Branch watershed, in clayey soils and sandy loams.

The observed SOC storage (Figure 3-10) at legacy sediments presented in this study (e.g., 4.1 kg C m<sup>-2</sup> in the top 20 cm of soil) is significantly greater than previous measurements from undisturbed (3.3 kg C m<sup>-2</sup> in the top 30 cm of soil) and eroded soil profiles (1.9 kg C m<sup>-2</sup> in the top 30 cm of soil) at slopes and interfluvies [Richter and Markewitz, 2001]. The observed topographic controls on SOC storage are consistent with Rosenbloom et al. [2006]. More specifically, the mean observed C content is about 8.2, 5.3, and 3.6 kg m<sup>-2</sup> at depositional, undisturbed, and eroded sites, respectively (upper 1.1 m of soil). The relatively high SOC storage at depositional sites indicates that an important fraction of upland mobilized organic material is only partially decomposed upon transport. These findings contrast with those of Schlesinger [1995], who reported that SOC lost to erosion is mainly oxidized, instead of being transferred with eroded sediment. Moreover, observations of storage suggest that eroded SOC is mainly stored in alluvial sediments, rather than being fluvially exported to the ocean. Therefore, the primary C export of the



Calhoun ecosystem is not fluvial. SOC oxidation and CO<sub>2</sub> release to the atmosphere constitute the largest C output at the degraded landscape.

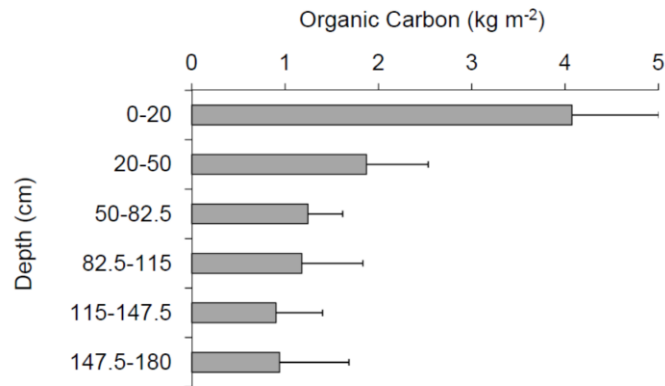


Figure 3-10. Means and standard deviations of soil organic carbon (SOC) storage observations at different depths from alluvial sediments at depositional sites B to F. SOC storage across soil horizons of these alluvial sites is higher than the storage in eroded and relatively undisturbed soil profiles.

### 3.5.2 Decline of upland sediment and organic carbon erosion with reforestation

This work assesses the geomorphic behavior of the landscape under study during the recent agro-ecosystem and the secondary forest ecosystem periods. Rainsplash erosion and overland flow transfer sediment and SOC from upland sites and steep slopes to depositional sites (Figure 3-5a). Reforestation likely led to a substantial decline in soil erosion rates. On the average, erosion at the secondary forest ecosystem period is around 3 times lower compared to the agro-ecosystem period (Figure 3-4). However, the soil erosion estimate at

the reforested period (around  $0.7 \text{ mm yr}^{-1}$ ) indicates that the degraded landscape is characterized by significant erosional potential.

The temporal evolution of upland soil erosion had a meaningful impact on the redistribution of SOC at the Holcombe's Branch. The decrease in sediment transport rates with reforestation led to a decline in the net lateral SOC flux (Figure 3-6). The net loss of upland SOC decreased during the reforestation period by 65%, 62%, and 52% for the maximum source, intermediate, and maximum sink scenarios, respectively. The simulated decline of net SOC losses at upland sites reflects the transition of the Calhoun ecosystem from a legacy of intensive land use practices [Trimble, 1974] to a state of partial recovery and reforestation [Mobley *et al.*, 2015]. The SOC loss during the simulated 100-year period (Figure 3-6) was compared with the observed rate of SOC erosion of  $1.7 \text{ kg m}^{-2}$  (in 100 years of agricultural practices), discussed in section 2.5.1. The SOC losses predicted at the maximum sink and maximum source scenario deviate from the observed SOC losses. At the intermediate scenario, the total SOC loss is consistent with observations. Moreover, the rate of C replacement at eroding sites is accelerated, because exposed soil horizons are characterized by significant C stabilization potential. Simulated C fluxes at the intermediate scenario suggest that a substantial part of eroded SOC has been rapidly replaced by atmospheric  $\text{CO}_2$  sequestration (see section 3.4.2), which generally agrees with SOC gains observed in previous long-term field studies at the site [Mobley *et al.*, 2015; Richter and Markewitz, 2001].

This work emphasizes the influence of topography and slope morphology on SOC erosion and burial among diverse soil profiles (Figure 3-5). In contrast to previous studies that quantify the erosion-induced soil-atmosphere  $\text{CO}_2$  exchange based on *a priori*

specified amounts of eroded SOC assumed to be mineralizable [Billings *et al.*, 2010; Jacinthe and Lal, 2001], the distributed structure of tRIBS-ECO calculates the fate of eroded organic material with no *a priori* assumptions about mineralizable fractions. Episodic erosion redistributes SOC from interfluvies and upper slopes to colluvial deposits, stream corridors, and valley bottoms. Eroded organic material undergoes decomposition in transport, or storage with burial. Accounting for the topographic heterogeneity of the dynamics of eroded SOC affected by anthropogenic perturbations is important on estimates of the strength of atmospheric CO<sub>2</sub> sink or source.

### 3.5.3 Uncertainty associated with management practices in estimates of watershed-integrated net soil-atmosphere carbon exchange

The uncertainty associated with the influence of management practices (chapter 7) on erosion-induced C flux estimates can be significant at fine spatial scales. Anthropogenic disturbance related to past land uses and land use changes has markedly increased the complexity of the associated processes at the Calhoun ecosystem. To assess different topographic controls on this uncertainty, the SOC storage range (i.e., difference of maximum source from maximum sink scenario estimates) at each Voronoi cell was plotted against watershed topographic characteristics (Figure 3-11), including the topographic index [Beven and Kirkby, 1979], which is a surrogate of flow accumulation at any point in the basin based on topographic information [Quinn *et al.*, 1995]. This index is defined as  $\ln(A/\tan\beta)$ , where  $A$  is the upslope contributing area per unit contour length, and  $\beta$  is the local slope. Based on the analysis presented in Figure 3-11a, relatively higher ranges of

SOC storage are simulated at sites with gentler slopes and positive curvature, corresponding to alluvial deposits in the upward concave stream. Uncertainty in SOC prediction is also higher at sites with greater contributing area and topographic index, characteristic of lower elevation depositional sites with increased wetness conditions across the stream network (Figure 3-11b). The predicted accumulation of organic material at the maximum sink scenario is significantly greater compared to the maximum source scenario estimates at these sites. Figure 3-11 qualitatively indicates that simulated SOC ranges in sites across the stream network increase with upslope contributing area (and topographic index), which suggests that uncertainty in SOC storage prediction [Berhe *et al.*, 2007] increases with the spatial scale of analysis.

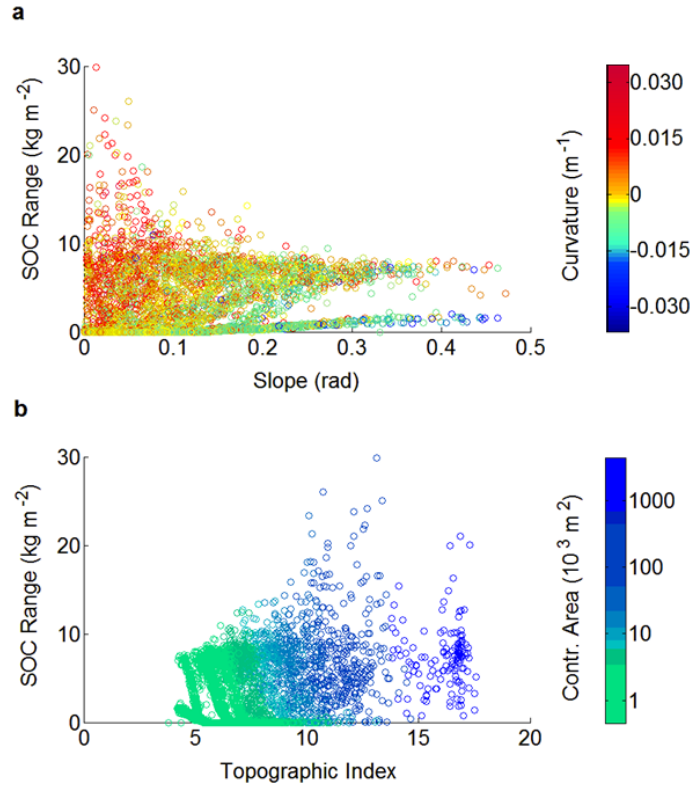


Figure 3-11. Simulated soil organic carbon (SOC) ranges (i.e., difference of maximum source from maximum sink scenario estimates) at each site across the watershed versus slope and curvature (a), and versus contributing area and topographic index ( $\ln(A/\tan\beta)$ , where  $A$  is the upslope contributing area and  $\beta$  is the local slope) (b)

According to results, the erosion driven C exchange with the atmosphere at the watershed scale (Figure 3-5) ranged from a C source of  $10.3 \text{ g m}^{-2} \text{ yr}^{-1}$  to a C sink of  $-8.4 \text{ g m}^{-2} \text{ yr}^{-1}$ , for the maximum source and the maximum sink scenarios, respectively. The simulated spectrum of possible net C source and sink strengths characterizes the agricultural history of the Calhoun CZO. Changes in management practices [Harden *et al.*, 1999; Richter *et al.*, 2000] may have led to transitions between erosion driven C sinks or sources over time [Van Oost *et al.*, 2012]. Comparison of the observations based rate of upland SOC erosion ( $17 \text{ g C m}^{-2} \text{ yr}^{-1}$ ) with the watershed-integrated results also suggests

that a substantial part of mobilized organic material is likely preserved in depositional environments, with marginal net contribution to atmospheric CO<sub>2</sub> [Smith *et al.*, 2001]. The watershed-integrated results correspond to a narrower range of erosion driven C fluxes compared to previous estimates at the study site [Billings *et al.*, 2010]. Results encompass the C sink strengths reported in Van Oost *et al.* [2005] (-3 to -10 g m<sup>-2</sup> yr<sup>-1</sup>) and in Yoo *et al.* [2005] (up to -2.8 g m<sup>-2</sup> yr<sup>-1</sup>). The estimated maximum C sink strength is smaller than that of Harden *et al.* [1999] (up to -20 g m<sup>-2</sup> yr<sup>-1</sup>).

### 3.6 Summary

This study proposes a method to quantify the uncertainty introduced by the influence of land management on soil organic C (SOC) generation and decomposition at eroding soils. The framework is implemented in tRIBS-ECO (Triangulated Irregular Network-based Real-time Integrated Basin Simulator-Erosion and Carbon Oxidation), a spatially- and depth-explicit model of C dynamics coupled with a process-based hydro-geomorphic model. The impact of soil erosion on the net soil-atmosphere CO<sub>2</sub> exchange was assessed at the Calhoun Critical Zone Observatory, one of the most severely agriculturally eroded regions in the U.S. Measurements of SOC storage are used from different catena positions. It is demonstrated that the spatio-temporal variations of land management practices introduce significant uncertainty in estimates of the erosion-induced CO<sub>2</sub> exchange with the atmosphere. According to results, recent reforestation led to a partial decline in soil and SOC erosion rates. Observations and simulations suggest that a substantial portion of eroded organic material is buried in alluvial sediments at the study site, rather than being

fluvially exported to the ocean. CO<sub>2</sub> release to the atmosphere is the primary C output at the Calhoun ecosystem. It is suggested that the representation of the fine spatio-temporal variability of the dynamics of eroded C is important in the computation of C budgets in regional and global scales.

## **CHAPTER 4.     Impact of hydrologically driven hillslope erosion and landslide occurrence on soil organic carbon dynamics at tropical watersheds**

### **4.1 Introduction**

Tropical forests play an important role in the global C cycle through high rates of net primary production and long-term storage in biomass and soils [Ciais *et al.*, 2013]. The humid tropics presently occupy about 25 % of the Earth's land surface [Stallard, 2012]. 45 % to 52 % of the global terrestrial biomass C, and eleven to fourteen percent of the global soil C is located in tropical forests [Prentice *et al.*, 2001]. Intense hydro-meteorological phenomena in the humid tropics have the potential to trigger events of rapid sediment and C transport [Heartsill Scalley *et al.*, 2012; Hilton *et al.*, 2008; Larsen and Torres-Sánchez, 1992; Ramos Scharrón *et al.*, 2012; West *et al.*, 2011; Wohl and Ogden, 2013]. The propensity for shallow landslide occurrence in montane tropical ecosystems can be significantly influenced by land uses and human disturbance [Gellis *et al.*, 2006; Guns and Vanacker, 2014; Larsen, 2012]. Moreover, tropical vegetation, and warm and humid conditions favor high rates of net primary productivity (NPP) and decomposition, leading to highly dynamic SOC in time and space [Stallard, 2012]. Tropical forests are generally a net atmospheric C sink, through plant uptake and C burial [Ciais *et al.*, 2013]. At the same time, land use and land cover change in the tropics have contributed large CO<sub>2</sub> emissions to the atmosphere [Houghton, 2012]. For these reasons, tropical ecosystems are important settings for studying hillslope erosion and the associated effects on C exchange with the atmosphere.



The Luquillo Critical Zone Observatory (CZO) is a tropical site of particular hydrological and geomorphological interest characterized by diverse topography and different underlying lithologies [Murphy *et al.*, 2012]. Past land use has influenced the soils and the density of forest cover at the Luquillo CZO [Foster *et al.*, 1999]. The hydro-geomorphic behavior of different watersheds under relatively similar climatic conditions is strongly dependent on local topographic and lithological characteristics and on the exact geographic location relative to the Luquillo Mountains [Murphy and Stallard, 2012]. This is the case for the morphologically diverse adjacent watersheds of Rio Mameyes and Rio Icacos in the Luquillo CZO (section 4.3), which are characterized by comparable mean annual precipitation (MAP) and by contrasting lithology [Buss and White, 2012]. The Icacos watershed is underlain by the Rio Blanco quartz diorite, while the Mameyes is for the most part underlain by volcanoclastic rock [Dosseto *et al.*, 2014]. This setting provides the unique opportunity to test for the effects of underlying parent material and different forest types on SOC erosion under comparable climatic conditions.

In this study, a novel spatially-explicit framework was developed and used to quantify the impact of erosion and landslide occurrence on the redistribution of SOC and on the associated C exchange with the atmosphere in the Mameyes and Icacos watersheds. The model of C dynamics is based on tRIBS-ECO, introduced in section 2.2.1, which accounts for dynamic feedbacks among hydrological, geomorphological, and biogeochemical processes in a physically-based manner at the watershed scale. This work uses measurements of SOC content across a range of depths and catena locations [Johnson *et al.*, 2015], and stresses the role of different forest types on the erosion-induced C

exchange with the atmosphere. This chapter is a verbatim recompilation of *Dialynas et al.* [2016b] and *Dialynas et al.* [2015].

## 4.2 Physical representation of hillslope erosion and landslide occurrence

To simulate feedbacks of topsoil erosion and landslide occurrence on the dynamics of SOC at the Luquillo CZO, a slope stability module was included in the tRIBS-ECO framework. The underlying physically-based model of hydrologically-driven topsoil erosion is discussed in section 2.2. Previous landslide modelling efforts at the Mameyes basin [Arnone *et al.*, 2011; Lepore *et al.*, 2013] focused on landslide occurrence in response to tropical storms at fine (e.g., hourly) time scales, and also used versions of the tRIBS framework [Ivanov *et al.*, 2008a; b; Ivanov *et al.*, 2004a]. The slope stability component is based on the infinite slope model [Arnone *et al.*, 2011], which assumes that the plane of failure is parallel to the soil surface. The level of stability is typically assessed by evaluating the factor of safety ( $FS$ ), which expresses the extent to which destabilizing forces exceed in magnitude forces that favor slope stability. At each time step and at each computational element the  $FS$  is estimated by [Arnone *et al.*, 2011]:

$$FS_t = \frac{c}{h_s \rho_s \sin a_t} + \left( 1 - \left( \frac{\theta_t - \theta_r}{\theta_s - \theta_r} \right) \frac{\rho_w}{\rho_s} \right) \frac{\tan \varphi}{\tan \alpha_t} \quad (4.1)$$

where  $c$  is the combined effect of root cohesion and effective soil cohesion,  $\varphi$  is the friction angle,  $h_s$  is the thickness of the landslide soil mass,  $\rho_s$  and  $\rho_w$  are the soil and water densities, respectively,  $a_t$  is the time variant local slope angle,  $\theta_t$  is the average soil moisture content in the landslide control volume at each time step,  $\theta_s$  is the saturated volumetric water

content, and  $\theta_r$  the residual volumetric water content. A detailed description of the limit equilibrium method of the stability module is given by [Arnone *et al.*, 2011]. The landslide module explicitly accounts for the spatial heterogeneity of factors that control slope stability, such as the mechanical and hydrological characteristics of different soil types, local terrain characteristics, and the time varying soil moisture content at each Voronoi polygon.

The model estimates the possible landslide deposition path based on the concept of run-out distance [Bathurst *et al.*, 1997], and alters the topographic characteristics of the landscape to account for elevation changes caused by erosion or deposition. The length of the maximum run-out distance can be estimated as a proportion (e.g., 40 % [Arnone *et al.*, 2011]) of the elevation difference between the landslide head and the deposition starting point [Vandre, 1985]. Furthermore, soil deposition depends on slope morphology [Burton and Bathurst, 1998]. For steep slopes (typically greater than 10°-15°) landslides move downhill unconditionally, and for gentle slopes (usually less than 4°-5°) the detached material halts unconditionally. For intermediate slopes, the movement of the landslide material is either limited by the maximum run-out distance, or by reaching gentler slopes along the landslide path, as discussed above [Arnone *et al.*, 2011]. Moreover, in the implemented framework the deposited landslide mass at each cell of the post-failure movement is inversely proportional to the local slope. Smaller sediment volumes are being deposited at relatively steeper slopes, and larger ones are being deposited at downhill gentler slopes, respectively.

Landslides and severe rainsplash and sheet erosion are processes that both depend on, and alter the landscape morphology. Therefore, the geomorphic processes are

interconnected by dynamic feedbacks. More precisely, at each time step landslides and soil erosion and deposition alter the slope morphology at the watershed scale. The updated slopes are estimated across the watershed, which in turn control the soil erosional potential of the landscape.

### 4.3 Study Area

The hydro-geomorphic response of the Mameyes and Icacos watersheds in the Luquillo CZO (northeastern Puerto Rico) was simulated in terms of erosion of upland SOC and soil-atmosphere C exchange. The Rio Mameyes drains into the Atlantic Ocean on the north side of Puerto Rico. The Rio Icacos is a tributary of the Rio Blanco, which discharges into the Caribbean Sea on the southeast side of the island [Dosseto *et al.*, 2014]. The elevation at the Mameyes watershed (Figure 4-1a) ranges from 104 to 1,046 m. The elevation at the Icacos watershed (Figure 4-2a) ranges from 615 to 845 m [Larsen, 2012]. The two watersheds have been focal points of several hillslope erosion and bedrock weathering studies [Buss and White, 2012; Chabaux *et al.*, 2013; Dosseto *et al.*, 2012; Dosseto *et al.*, 2014; Larsen, 2012; Lepore *et al.*, 2013; Stallard, 2012] because of their particular geomorphological interest. On average, the Mameyes watershed is characterized by steeper slopes compared to the Icacos watershed (mean slope of 21° for Mameyes, and 13° for Icacos, respectively) [Larsen, 1997]. The two watersheds are characterized by frequent rainfall-triggered landslides [Larsen, 2012]. The spatial distribution of different soil textures is described in Figures 4-1b, 4-2b and section 4.4.3. The unweathered volcanoclastic bedrock is located at the depth of 16 m [Dosseto *et al.*, 2012]. Soil erosion and the rate of regolith production control the soil thickness. The contrasting lithology in

the study area contributes to different morphology and sediment yield at the two watersheds, with direct implications on the hydrological behavior of the Mameyes and Icacos watersheds. *Murphy and Stallard* [2012] discussed the climatological and hydrological characteristics of the two watersheds. The mean annual temperature at the Mameyes and Icacos watersheds are 22.8 °C and 21.4 °C, respectively. The MAP at the Icacos watershed, which is characterized by a mean elevation of 686 m [*Murphy et al.*, 2012], is 4,150 mm yr<sup>-1</sup>. The MAP at the Mameyes watershed, with a mean elevation of 508 m, is 3,760 mm yr<sup>-1</sup>. Rio Icacos has a mean annual discharge of 3,760 mm yr<sup>-1</sup> with a drainage area of 3.26 km<sup>2</sup>. The mean annual runoff of Rio Mameyes is 2,750 mm yr<sup>-1</sup>, and the drainage area is equal to 17.8 km<sup>2</sup>.

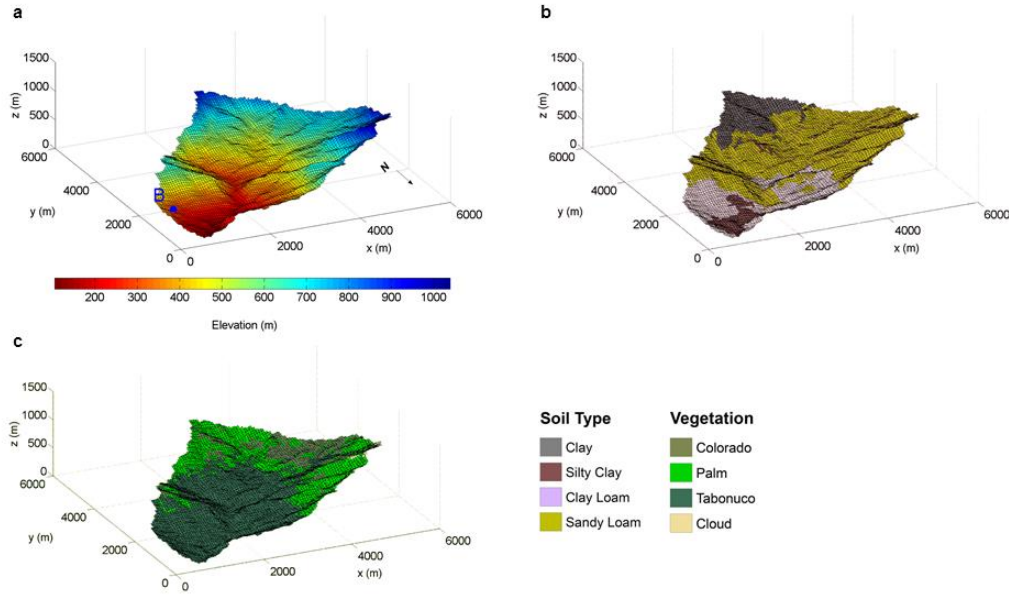


Figure 4-1. Digital Elevation Model of the Mameyes watershed; site B corresponds to the location of the Bisley tower (a), spatial distribution of soil textural classes (b), spatial distribution of vegetation types (c).

The Luquillo CZO is characterized by four forest life zones [Ewel and Whitmore, 1973; Holdridge, 1967]: subtropical wet forest, subtropical rain forest (below 600 m of elevation), lower montane wet forest, and lower montane rain forest (above 600 m). Based on species composition, the vegetation can be classified into: tabonuco forest (dominated by *Dacryodes excelsa*), colorado forest (dominated by *Cyrilla racemiflora*), palm forest (dominated by *Prestoea montana*), and dwarf (cloud) forest (with *Tabebuia rigida* as a common species) [Ewel and Whitmore, 1973; Waide et al., 1998; Weaver and Murphy, 1990]. The tabonuco forest dominates lower slopes up to elevations of around 650 m, while the colorado forest typically occupies higher elevations at the lower montane life zones, up to 900 m [Lepore et al., 2013]. Palm stands are common in most life zones throughout the Luquillo CZO, and they may occupy steep and poorly drained locations, while dwarf forest

is located at higher ridges, at poorly drained soils, and corresponds to less than 10 % of the vegetation of Luquillo CZO [Johnson *et al.*, 2015; Waide *et al.*, 1998]. The spatial distribution of forest cover for the Mameyes and Icacos watersheds is illustrated in Figures 4-1c and 4-2c, respectively [Helmer *et al.*, 2002; PRGAP, 2006]. The Mameyes watershed is dominated by tabonuco forest. Higher elevation sites at the watershed are dominated by colorado and palm forest. The Icacos watershed is primarily covered by colorado forest with sites of palm forest at the western slopes.

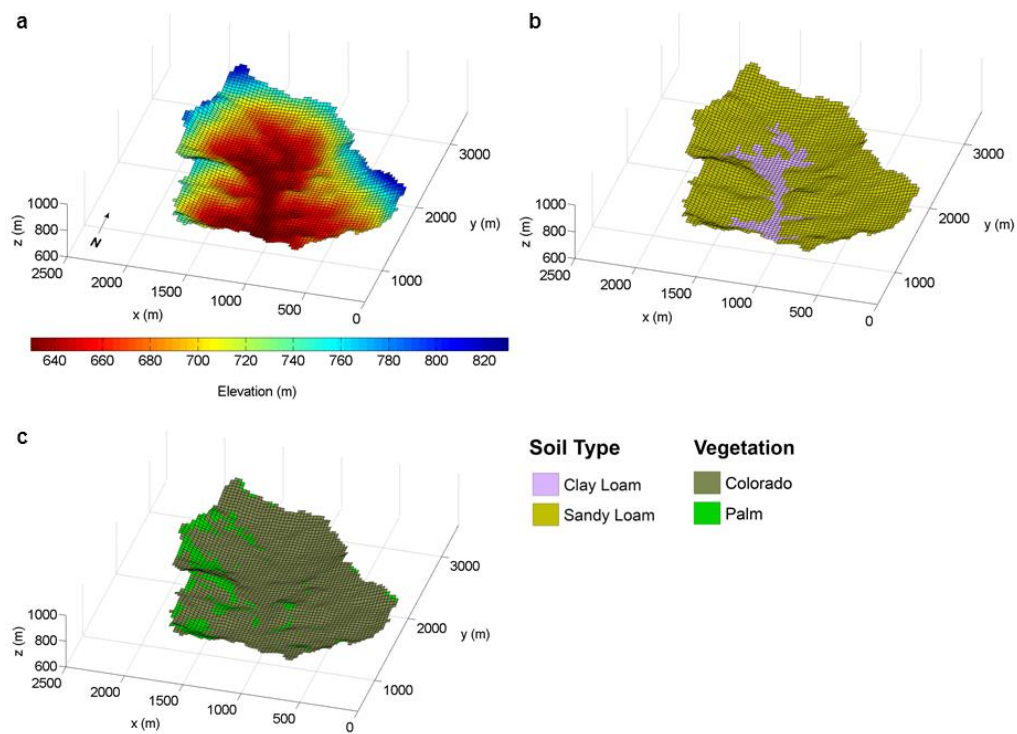


Figure 4-2. Digital Elevation Model of the Icacos watershed (a), spatial distribution of soil types (b), spatial distribution of vegetation species (c).

The patterns and density of vegetation at the Luquillo CZO have been altered by human land use change during the recent history of the island. Forest cutting in Puerto Rico started in the 16<sup>th</sup> century for pasture, cropland, timber, and fuelwood [Wadsworth, 1950], and peaked around 1900 [Foster *et al.*, 1999], with almost complete deforestation of the island in the early 1900s [Larsen, 2012; Murphy *et al.*, 2012]. Sites at lower elevations of the Luquillo mountains have been subject to land use, primarily for pasture and farming. Isolated selective timber harvesting and cutting of tabonuco and colorado forests for fuelwood and charcoal took place through 1940 [Foster *et al.*, 1999]. Human land use influenced the forest density at various locations within the area [Thomlinson *et al.*, 1996], which was followed by reforestation after the 1930s [Foster *et al.*, 1999].

## **4.4 Input data and parameters**

### **4.4.1 Biogeochemical parameters**

Soil biogeochemical properties were obtained from previous studies at the site [Johnson *et al.*, 2015; Wang *et al.*, 2003; Weaver and Murphy, 1990]. Johnson *et al.* [2015] measured SOC content in the Luquillo CZO at various catena positions and from different soil horizons reaching deep soils (140 cm). The analysis included SOC measurements at different depths in colorado and palm forests at the Icacos watershed, and in tabonuco, colorado, and palm forest at the Mameyes watershed (three replicates were obtained per topographic position at each site). SOC depth profiles exhibited significant variation among forest types (Figure 4-3). Average SOC stocks at colorado, palm, and tabonuco soils were 21, 18, and 14 kg m<sup>-2</sup> respectively. Moreover, on average Johnson *et al.* [2015]



reported a 37.5 % increase of total SOC content at the root zone (top 80 cm) in valleys compared to ridges.

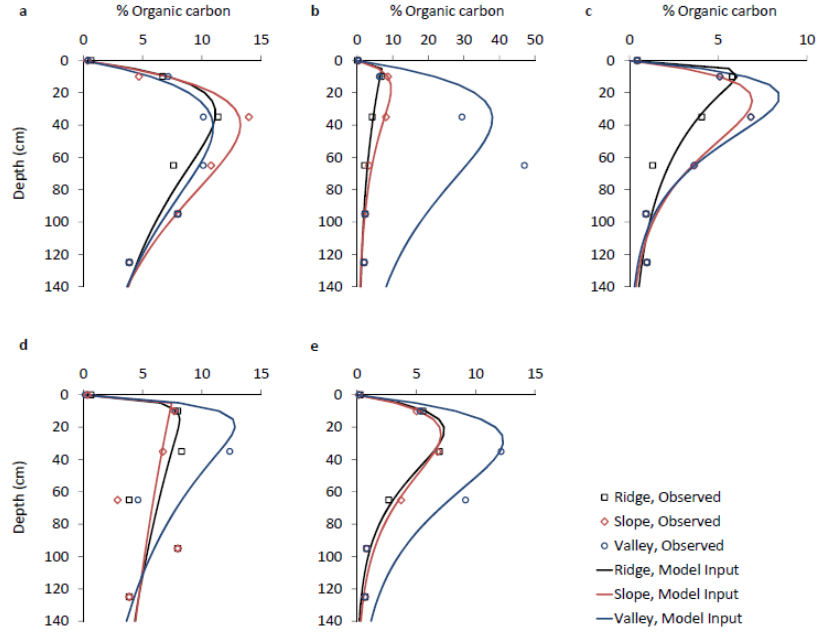


Figure 4-3. Observed organic carbon content [Johnson *et al.*, 2015] and model inputs at different topographic locations corresponding to colorado (a), palm (b), and tabonuco (c) soils at the Mameyes watershed, and colorado (d) and palm (e) soils at the Icacos watershed, respectively

In this model the depth-dependence of SOC content is represented by the following exponential expression:

$$C_i(z) = C_{a,t} \left( e^{C_b z} + e^{C_c z} \right) \quad (4.2)$$

where  $C_{a,t}$ ,  $C_b$ , and  $C_c$  are parameters (see also section 2.2.1 for notation). Equation (4.2) corresponds to dynamic depth-profiles of SOC content. At time  $t = 0$  the initial SOC content at different catena locations within the two watersheds was represented by fitting equation (4.2) to the SOC profiles reported by *Johnson et al.* [2015] (Figure 4-3). Equation (4.2) roughly approximated the available SOC measurements at multiple soil profiles. At each time step, the depth-variation of SOC in the parsimonious model is estimated by calculating  $C_{a,t}$  based on equations (2.1) and (4.2).

Hillslope erosion leads to the redistribution of the initial SOC content across the landscape. Mechanisms that drive advection-diffusion phenomena (e.g., bioturbation, tillage, soil creep) can lead to the mixing of the SOC content estimated by equation (2.1) across different horizons within the soil column [*Chaopricha and Marín-Spiotta*, 2014]. Mixing of the calculated SOC content (equation (2.1)) in the soil profile is assumed on an annual basis. The associated SOC depth-dependence is estimated based on equation (4.2). This simplifying assumption can reasonably represent the significant mixing [*Koven et al.*, 2013] that may characterize the SOC-rich surficial horizons.

The depth-dependence of SOC oxidation rate is described by an exponential function [*Wang et al.*, 2015; *Yoo et al.*, 2006] (see section 2.2.1 for notation):

$$k_t(z) = k_{a,t} e^{k_b z} \quad (4.3)$$

where  $k_{a,t}$ ,  $k_b$  are parameters (subscripts  $a$  and  $b$  correspond to soil parameters expressing topsoil values, and depth-variation, respectively). The depth-dependence of the rate of SOC production rates is given by equation (2.5) (section 2.4.1). The topsoil values of SOC oxidation and production rates ( $k_{a,t}$  and  $I_{a,t}$ , respectively) are time variant in eroding soils

(section 2.2.1). The parameters  $k_b$  and  $I_b$  express the depth-dependence of SOC oxidation and production, respectively.  $I_{a,t}$  was initialized based on measured values of aboveground NPP [Wang *et al.*, 2003; Weaver and Murphy, 1990] for different forest types in the Luquillo CZO (Table 4.1). For each soil profile,  $I_b$  was constrained such that at time  $t = 0$  the total SOC production over depth (equation (2.5)) is equal to the belowground NPP in each forest type (Table 4.1).

Table 4.1. Aboveground NPP (ANPP) and belowground NPP (BNPP) values for different forest types across the Luquillo CZO. The ANPP values were derived from observations [Weaver and Murphy, 1990]. The BNPP values were reported by Wang *et al.* [2003], based on belowground and aboveground biomass estimates for the entire Luquillo CZO.

	Tabonuco	Palm	Colorado	Cloud
ANPP ( $\text{g m}^{-2} \text{ yr}^{-1}$ )	1,404	1,268	527	540
BNPP ( $\text{g m}^{-2} \text{ yr}^{-1}$ )	324	293	122	170

The topsoil SOC oxidation rates ( $k_{a,t=0}$ ) for each vegetation type were initialized based on the SOC turnover characteristics reported in Cusack *et al.* [2010], who performed radiocarbon measurements at shallow soils at the Luquillo CZO. They analyzed soils covered by colorado forest at the Icacos watershed (640 m of elevation) and soils from tabonuco-type forest located at the Bisley Experimental watersheds (260 m), which are part of the Rio Mameyes drainage system [Scatena, 1989]. The oxidation rates were applied to the corresponding forest types in the Icacos and Mameyes watersheds. Results from the upper-elevation site ( $k_{a,t=0}$  of  $0.095 \text{ yr}^{-1}$ ) were applied to sites with higher altitude colorado

and cloud forests, which are also characterized by similar NPP (Table 4.1). Estimates from the lower elevation site ( $k_{a,t=0}$  of  $0.085 \text{ yr}^{-1}$ ) were applied to tabonuco and palm forest soils (the NPP of which is also comparable). At time  $t = 0$  the depth-dependence of SOC oxidation rate (parameter  $k_b$ ) was constrained by assuming steady state conditions at time  $t = 0$  with zero net soil-atmosphere C exchange [Jenny, 1941; Van Oost *et al.*, 2007].

#### 4.4.2 Effects of land uses on soil organic carbon fluxes

Land use plays a key role in the interaction between terrestrial sediment transport and soil-atmosphere C exchange [Billings *et al.*, 2010]. In tropical forests, land use and land use change may have an important effect on C sequestration and on CO<sub>2</sub> emissions to the atmosphere [Ciais *et al.*, 2013]. This work explores a variety of parameterized land use scenarios and their effect on anthropogenic erosion at the Luquillo CZO. To define potential land use scenarios, a sensitivity analysis on  $a_k$  and  $a_l$  was conducted at single eroding sites at the Icacos and the Mameyes watersheds by using equation (2.1) in 100-year simulations of eroding soil profiles, at an erosion rate of  $1 \text{ mm yr}^{-1}$  [Larsen, 2012]. The assumed erosion rate is consistent with estimates of average hillslope sediment flux at the two watersheds (see section 4.6.1). A soil profile in colorado forest and in tabonuco forest were considered for the case of Icacos and Mameyes watersheds, respectively.

The results of the sensitivity analysis for the two watersheds are illustrated Figure 4-4. The total net difference in SOC content ( $\Delta\text{SOC}$ ) at the soil profile for each set of  $a_k$  and  $a_l$  values expresses the erosion-induced net C exchange with the atmosphere. Relatively high values of  $a_k$  represent a significant effect of land use on altered oxidation,

while low values reflect little effect on eroding soil profiles. Similar is the effect of  $a_I$  to SOC production, respectively. According to Figure 4-4, a net erosion-induced C sink can result from relatively low values of  $a_k$  and high values of  $a_I$ . A net decrease in SOC storage can result from higher values of  $a_k$  and lower  $a_I$  as soil erosion proceeds (section 2.4.2). To assess the range of  $\Delta$ SOC resulting from different values of  $a_k$  and  $a_I$  three scenarios of C fluxes were considered: I) a maximum source scenario; II) an intermediate scenario; and III) a maximum sink scenario (Table 4.2). At the maximum sink scenario  $a_k$  is minimized, and  $a_I$  values were selected above which the  $\Delta$ SOC in Figure 4-4 does not significantly change. Similarly, at the maximum source scenario  $a_I$  was minimized and  $a_k$  was maximized, accordingly. At the intermediate scenario moderate values of  $a_k$  and  $a_I$  were selected, based on Figure 4-4. The three scenarios of C fluxes were defined based on the aforementioned simplifying assumptions (e.g., constant erosion rates) by applying equation (2.1) to eroding soil profiles, and they can roughly represent erosion-induced C fluxes at eroding soil profiles in the two watersheds. The ranges of  $a_k$  and  $a_I$  reflect plausible states of the Luquillo CZO ecosystem under different land uses (section 4.6.5). The likelihood of the assumed scenarios is studied in section 4.6.3.

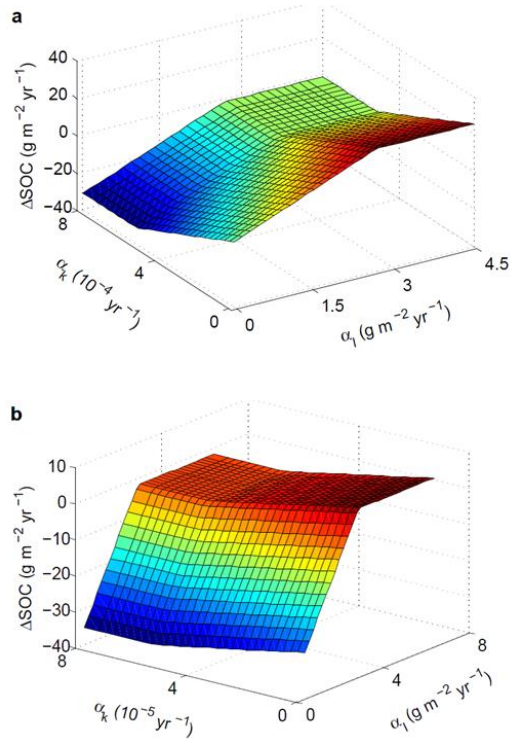


Figure 4-4. Sensitivity analysis on the influence of land uses to the total soil organic carbon storage difference ( $\Delta\text{SOC}$ ) for the Icacos (a) and the Mameyes (b) watersheds.  $\Delta\text{SOC}$  results from the net effect of soil organic carbon (SOC) production, oxidation, and SOC loss to erosion, as the effects of land uses to SOC oxidation and production ( $a_k$  and  $a_l$ , respectively) vary. Positive values of  $\Delta\text{SOC}$  indicate net increase of SOC storage, while negative values represent net SOC loss at the eroding site (color variation corresponds to vertical axis ( $\Delta\text{SOC}$ )).

Table 4.2. Values of  $a_k$  and  $a_l$  for the Mameyes and the Icacos watersheds. I, II, and III correspond to the maximum source, the intermediate, and the maximum sink scenarios, respectively.

	Mameyes			Icacos		
	I	II	III	I	II	III
$a_k (\text{yr}^{-1})$	0.00008	0.00004	0	0.0008	0.0004	0
$a_l (\text{g m}^{-2} \text{yr}^{-1})$	0	4	8	0	2.25	4.5

#### 4.4.3 Topography and soil textural classes

This study uses a recent fine resolution (10 m) Digital Elevation Model (DEM) obtained from the US Geological Survey's National Elevation Dataset [U.S.G.S., 2009]. To reduce the computational cost of the simulations, a 30 m mesh (Figure 4-2) of computational elements was obtained for the Icacos watershed (3.26 km<sup>2</sup>), and a 50 m mesh (Figure 4-1) for the significantly larger Mameyes watershed (17.8 km<sup>2</sup>) [Ivanov *et al.*, 2004a; Lepore *et al.*, 2013; Vivoni *et al.*, 2004]. Soil classification maps of the two watersheds were obtained from local soil surveys (<http://websoilsurvey.nrcs.usda.gov/>) conducted by the U.S. Department of Agriculture (USDA). According to the U.S.D.A. [1951] classification system, the soil textural classes of the Mameyes and Icacos watersheds were grouped into four soil types, i.e., clay-loam, sandy-loam, silty-clay, and clay (Figures 4-1b and 4-2b).

#### 4.4.4 Hydrometeorological forcing

The redistribution of sediment and SOC was studied at the two diverse watersheds using a spatially-explicit simulation of hydro-geomorphic and biogeochemical processes in tRIBS-ECO driven by a 100-year hydro-meteorological forcing, which was obtained from a stochastic weather generator (AWE-GEN [Fatichi *et al.*, 2011] (section 2.4.4)). Daily rainfall series (1973-2006) were used from the Pico Del Este station (NOAA, station ID: 666992, lat. 18.27, long. 65.76) as inputs to AWE-GEN, in addition to daily meteorological data (air temperature, wind speed, relative humidity (1993-2010)) from the Bisley tower (USGS, station ID: 50065549, lat. 18.31, long. 65.74), and to hourly time

series of atmospheric pressure and cloud cover (1993-2010) from the San Juan airport weather station (NOAA, station ID: 668812, lat. 18.44 long. 66.0), to parameterize the weather generator.

#### 4.4.5 Hydrologic model calibration

Calibration of the hydrologic model of the Mameyes and Icacos watersheds was conducted by comparing the simulated watershed response to observed river discharge. Daily rainfall from the Bisley tower and the meteorological data discussed in section 4.4.4 were used as model inputs. The corresponding rainfall time series is illustrated in Figure 4-5. Daily river discharge records provided by the USGS at the outlets of the two watersheds (station ID 50065500 for Rio Mameyes, and 50075000 for Rio Icacos, respectively) during 2001 were used (Figure 4-5). The calibration period (01/01/2001 - 06/24/2001) was selected based on the availability of fine hydro-climatic data and river discharge observations for the two watersheds.



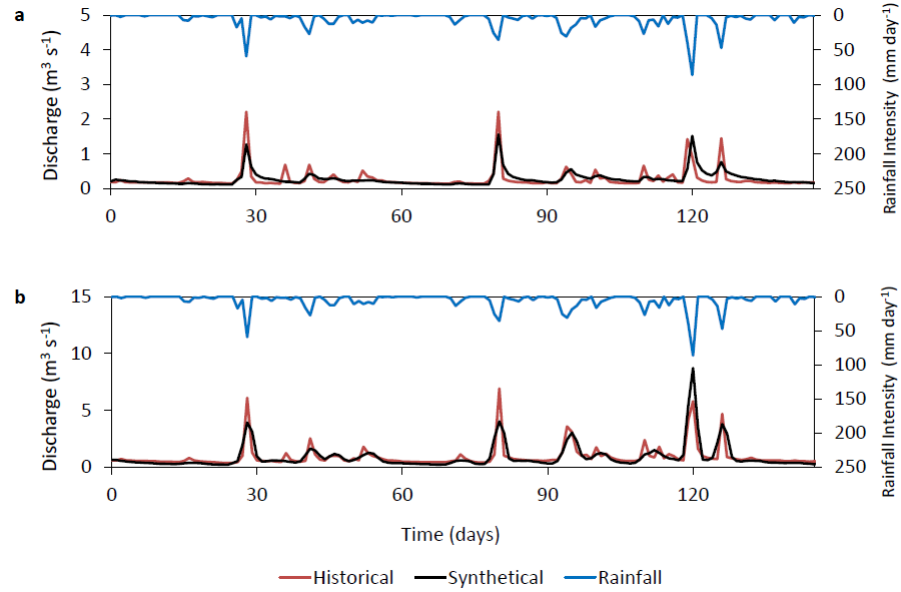


Figure 4-5. Hydrologic model calibration in terms of river discharge at the Icacos (a) and the Mameyes (b) watersheds. The observed rainfall intensity during the calibration period (01/01/2001 - 06/24/2001) is also provided.

In a modelling effort based on tRIBS, *Lepore et al.* [2013] tuned the hydrological parameters of the model for the Mameyes watershed using series of observed soil moisture content. As stated previously the response of Mameyes and Icacos watersheds was tuned with recorded river discharge. The values of  $K_s$ ,  $\theta_s$ ,  $\theta_r$ ,  $\psi_b$ , and  $m$  reported in *Lepore et al.* [2013] (Table 4.3) for each soil type were used (see section 2.4.4 for notation).  $A_s$ ,  $A_u$ , and  $f$  were calibrated, which are key parameters affecting the hydrological dynamics at the watershed scale (Table 4.3). Values from the literature [*Bras*, 1990; *Ivanov et al.*, 2004a; b; *Lepore et al.*, 2013; *Rutter et al.*, 1975; *Schellekens*, 2000; *Weaver and Murphy*, 1990] were used for plant properties [*Ivanov et al.*, 2004a] controlling hydrologic processes such as evapotranspiration, rainfall interception and canopy storage.

Table 4.3. Soil hydrological and mechanical parameters. Two sets of values of shear stress based soil erodibility ( $K_b$ ) are given, corresponding to the Mameyes and to the Icacos (in parenthesis) watersheds, respectively.

	Clay Loam	Sandy Loam	Silty Clay	Clay
$K_s$ [mm hr <sup>-1</sup> ]	50	50	50	10
$\theta_s$ [mm <sup>3</sup> mm <sup>-3</sup> ]	0.56	0.55	0.55	0.53
$\theta_r$ [mm <sup>3</sup> mm <sup>-3</sup> ]	0.075	0.041	0.051	0.090
$m$	0.200	0.322	0.127	0.130
$\psi_b$ [mm]	-250	-150	-340	-370
$f$ [mm <sup>-1</sup> ]	0.002 (0.001)	0.002 (0.001)	0.002 (0.001)	0.002 (0.001)
$A_s$ [-]	200 (100)	200 (100)	200 (100)	200 (100)
$A_u$ [-]	200 (100)	200 (100)	200 (100)	200 (100)
$c$ [kPa]	8	6	6	10
$\phi$ [deg.]	31	28	31	25
$\tau_c$ [Pa]	0.5	0.5	0.5	0.5
$K_b$ [(m s <sup>-1</sup> kg <sup>-1</sup> s <sup>-2</sup> ) <sup>1.5</sup> ]	$5 \times 10^{-10}$ ( $10^{-11}$ )	$5 \times 10^{-10}$ ( $10^{-11}$ )	$5 \times 10^{-10}$ ( $10^{-11}$ )	$5 \times 10^{-10}$ ( $10^{-11}$ )
$K_r$ [J <sup>-1</sup> ]	20	32	20	20

The model reasonably reproduced the hydrologic response of the two watersheds (Figure 4-5). The model simulation satisfactorily reproduced both baseflow and hydrograph recession limbs, two factors that characterize the watershed's hydrological behavior. Discrepancies in the Icacos watershed were attributed to the spatial gradient of rainfall between the watershed and the location of Bisley tower (Figure 4-1a). The Pearson's squared correlation ( $r^2$ ) among the observed and simulated discharge for the period of calibration, and the total water mass balance error (i.e., percentile difference of the simulated from the observed total water mass) are given in Table 4.4. Because  $r^2$  can

be sensitive to extreme events, the Nash-Sutcliffe efficiency (NSE) was estimated, which quantifies the variance of residuals normalized by the variance of observations [A.S.C.E., 1993]. Acceptable NSE values range between 0 and 1, and  $r^2$  values greater than 0.5 are considered as generally accepted levels of performance [Bennett *et al.*, 2013]. The associated values for Mameyes and Icacos watersheds are included in the acceptable ranges, and the percentile differences of total water volume suggest that the performance of the calibration procedure is satisfactory.

Table 4.4. Metrics of hydrologic and geomorphic validation performances.

	River Discharge		Sediment Yield	
	Mameyes	Icacos	Mameyes	Icacos
Mass Balance Error	-4.7%	5.4	-1.0%	2.2%
$r^2$	0.68	0.62	0.87	0.56
NSE	0.62	0.61	0.85	0.28

#### 4.4.6 Geomorphologic model calibration

The hydro-geomorphic model was calibrated by reproducing events and accumulation of sediment at the outlets of the two watersheds. Daily rainfall records from Pico Del Este station (section 4.4.4) were used, which cover the length of the calibration period (01/1995 - 11/1999). Daily series of observed sediment yield were used from the

USGS stations discussed in section 4.4.5. Mechanical properties of each soil type controlling landslide occurrence are the cohesion ( $c$ ) and friction angle ( $\varphi$ ). Soil properties affecting erosion are discussed in section 2.4.5.

The geomorphic model was calibrated in terms of the observed sediment yield (Figure 4-6).  $c$  was calibrated for each soil texture, and  $K_b$ ,  $\theta_c$ , and  $K_r$  were tuned starting from literature values [Francipane *et al.*, 2012; Meyer and Harmon, 1984; Yalin, 1977]. Friction angle values for each soil type were selected from the literature [Bjerrum and Simons, 1960; Lumb, 1966; 1970]. The soil mechanical parameters for each soil type are given in Table 4.3. The values of vegetation parameters used in this study are:  $v$  equal to 0.7 and  $F_l$  equal to 0.6. The simulated accumulated volumes of sediment yield for the two watersheds are illustrated in Figure 4-6. Furthermore, the calibration of the geomorphic model was assessed using the metrics described in section 4.4.5 (Table 4.4). For both watersheds, the estimates were included in the ranges of acceptable performance (i.e., from 0 to 1 for NSE, and from 0.5 to 1 for  $r^2$ ), and the total sediment mass balance error was acceptable [Moriassi *et al.*, 2007]. This suggests that the model efficiently reproduced the observed accumulated sediment yield for the period of calibration at the Mameyes and Icacos watersheds. The simulation of geomorphic processes in this framework depends on the parameterization of the hydrologic model for the two watersheds.

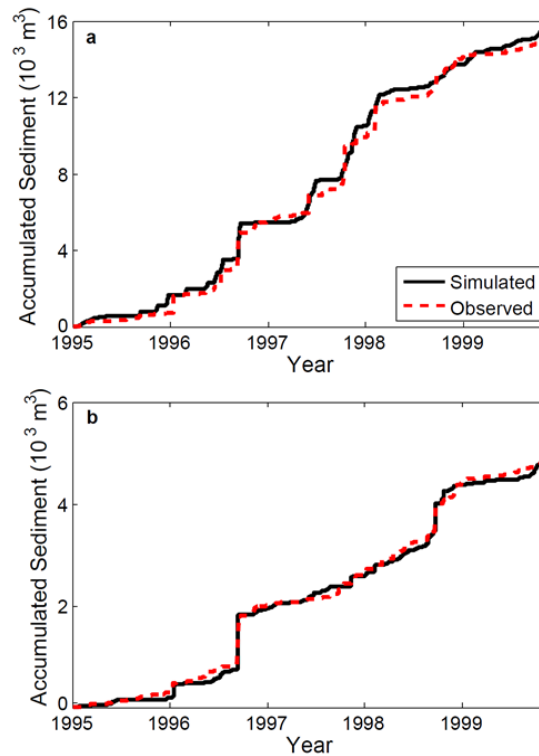


Figure 4-6. Calibration of the geomorphic model in terms of accumulated sediment yield for the Icacos (a) and the Mameyes (b) watersheds. The calibration period starts in January, 1995 and ends in November, 1999.

## 4.5 Results

### 4.5.1 Hillslope erosion and deposition

The 100-year simulated landscape evolution at the Mameyes and Icacos watersheds is presented in Figure 4-7. Landslides, rainsplash erosion, and overland flow erosion drive the redistribution of sediment. Significant loss of topsoil is evident at the eroding hillslopes of the two watersheds. A substantial part of the eroded material was deposited across the stream network. Rates of total hillslope erosion at the Mameyes and Icacos watersheds

were equal to  $937 \text{ t km}^{-2} \text{ yr}^{-1}$ , and  $1,123 \text{ t km}^{-2} \text{ yr}^{-1}$ , respectively. These estimates correspond to the total simulated hillslope erosion (i.e., topsoil erosion and landslide occurrence) at the two watersheds over the 100-year period.

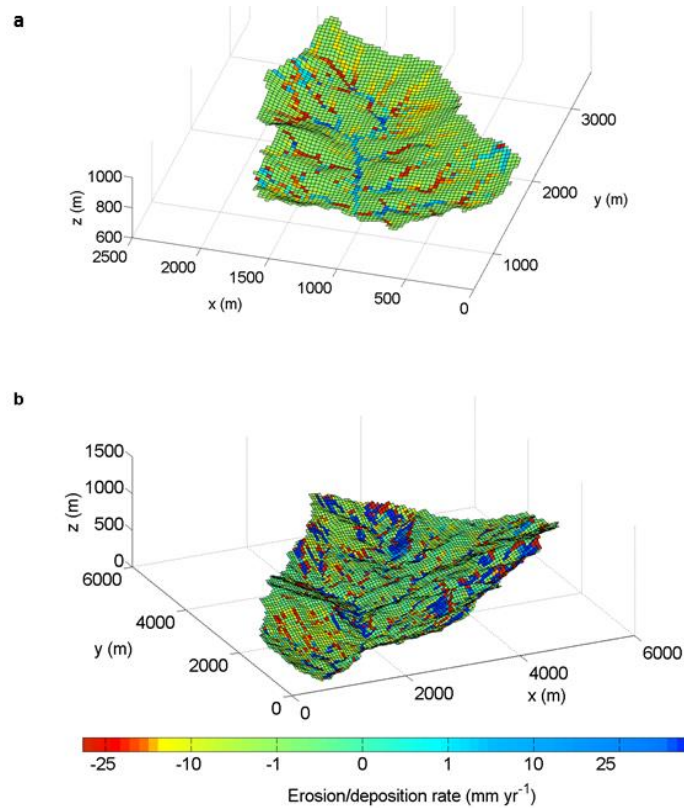


Figure 4-7. Heavily eroding hillslopes (yellow to red) and landslide sites (red) at the Icacos (a) and the Mameyes (b) watersheds. Depositional sites across river floodplains and at landslide run out tracks are illustrated in blue.

The propensity for landslide occurrence was higher on relatively steeper slopes at the two watersheds. In the Icacos watershed, slope instability occurred mainly at the north-western and south-western parts of the watershed, but there is also landslide occurrence in

southern and south-eastern areas. In the Mameyes watershed there was significant landslide occurrence in the north-western part of the watershed, and at the south-east side of the relatively steep south-western ridge. Also, landslides were triggered at the steep slopes in the proximity of Rio Mameyes in the northern part of the watershed. Landslide sediment was deposited along the run-out path.

A comparison of simulated landslide occurrence with observed landslide scars [Larsen, 1997; Larsen, 2012] at the study site is given in Figure 4-8. The two watersheds are characterized by significant slope instability potential. Soil accumulation in relatively older landslide scars has led to the formation of landslide-prone slopes. Simulated landslide heads and potential deposition paths are consistent with landslide locations at the Mameyes watershed. More specifically, simulated run-out distances match observed landslide paths in different parts of the watershed (i.e., in southern, northern, and northwestern areas). Locations of relatively large simulated landslides are collocated with observed scars at the south-eastern Icacos watershed. Landslides are triggered at the relatively steeper slopes of the western part, which is consistent with observations. The simulated landslide locations and potential deposition paths at the two watersheds are in agreement with the observed landslide scars.

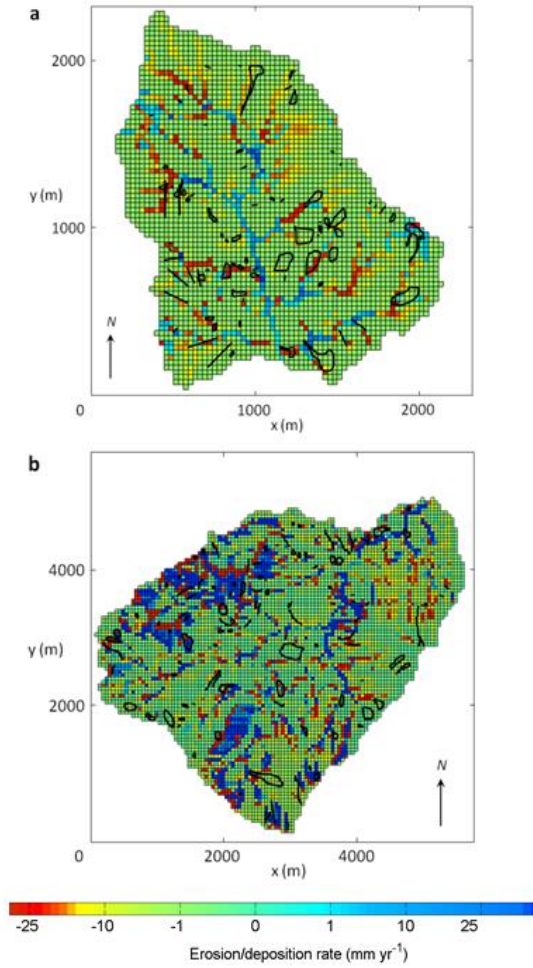


Figure 4-8. Comparison of the simulated landslide occurrence at the Icacos (a) and Mameyes (b) watersheds with the landslide scars (black) reported in *Larsen* [1997] and in *Larsen* [2012], who documented a total of 345 landslides in the two watersheds from aerial photographs (1937, 1951, 1962, 1972, 1974, 1979, 1990, and 1995).

#### 4.5.2 Watershed-integrated carbon exchange with the atmosphere

The hydro-geomorphic response of the two watersheds to the imposed 100-year hydrometeorological forcings was estimated in terms of SOC redistribution and C exchange with the atmosphere. Watershed-integrated results for the maximum source, maximum sink, and intermediate scenarios are illustrated in Figures 4-9 and 4-10 for



Mameyes and Icacos watersheds, respectively. The simulated watershed-integrated C exchange with the atmosphere for the Mameyes yielded a source of  $18.3 \text{ g m}^{-2} \text{ yr}^{-1} \text{ C}$  for the maximum source scenario, a sink of  $21.5 \text{ g m}^{-2} \text{ yr}^{-1} \text{ C}$  for the maximum sink scenario, and a sink of  $6.0 \text{ g m}^{-2} \text{ yr}^{-1} \text{ C}$  for the intermediate scenario. The corresponding results for the Icacos watershed yielded a source of  $14.9 \text{ g m}^{-2} \text{ yr}^{-1} \text{ C}$  for the maximum source scenario, a sink of  $17.1 \text{ g m}^{-2} \text{ yr}^{-1} \text{ C}$  for the maximum sink scenario, and a sink of  $3.3 \text{ g m}^{-2} \text{ yr}^{-1} \text{ C}$  for the intermediate scenario.

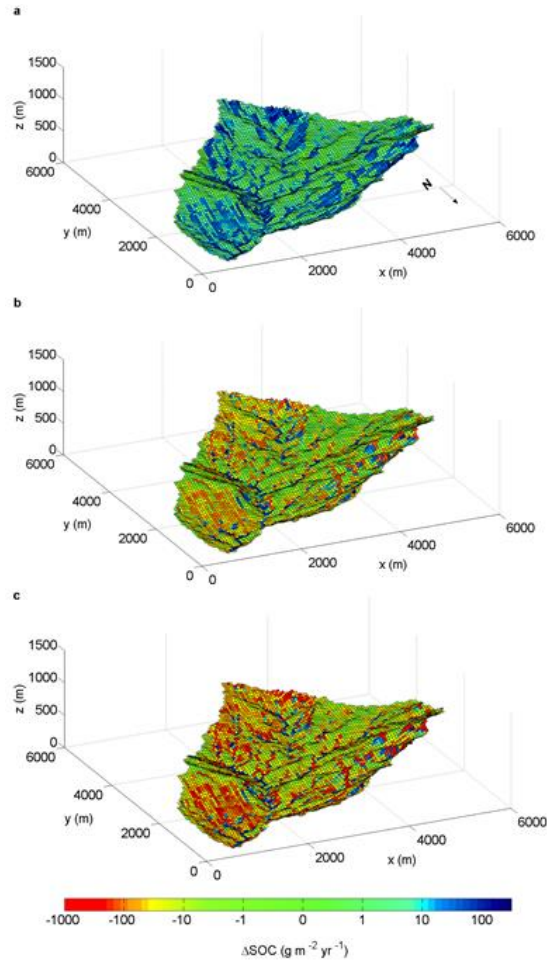


Figure 4-9. Spatially-explicit representation of the redistribution of soil organic carbon at the Mameyes watershed. Total difference in soil organic carbon storage ( $\Delta\text{SOC}$ ) at the watershed scale for the maximum sink scenario (net sink strength of  $21.5 \text{ g C m}^{-2} \text{ yr}^{-1}$ ) (a), the intermediate scenario (net sink strength of  $6.0 \text{ g C m}^{-2} \text{ yr}^{-1}$ ) (b), and the maximum source scenario (net source strength of  $18.3 \text{ g C m}^{-2} \text{ yr}^{-1}$ ) (c).

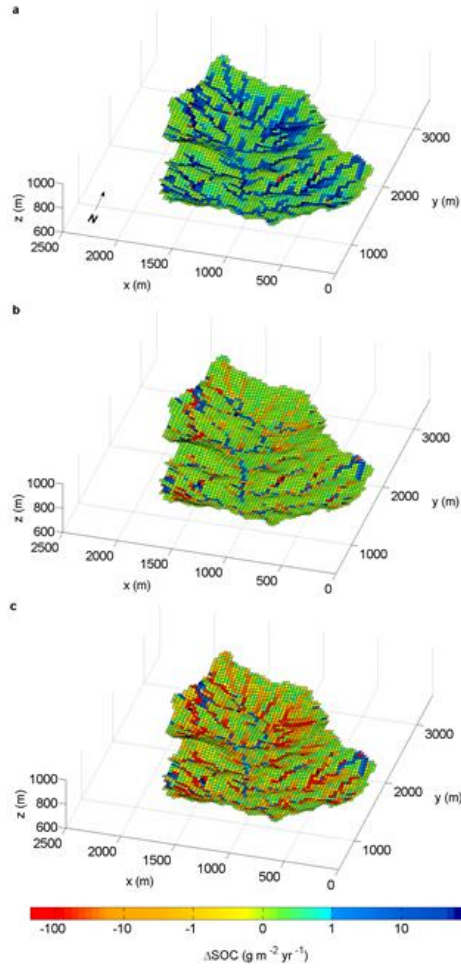


Figure 4-10. Spatially-explicit representation of the redistribution of soil organic carbon at the Icacos watershed. Total difference in soil organic carbon storage ( $\Delta\text{SOC}$ ) at the watershed scale for the maximum sink scenario (net sink strength of  $21.5 \text{ g C m}^{-2} \text{ yr}^{-1}$ ) (a), the intermediate scenario (net sink strength of  $3.3 \text{ g C m}^{-2} \text{ yr}^{-1}$ ) (b), and the maximum source scenario (net source strength of  $14.9 \text{ g C m}^{-2} \text{ yr}^{-1}$ ) (c).

#### 4.5.3 Erosion-induced carbon fluxes in different forest types

This work simulated SOC losses with mobilized sediment, and the influence of erosion on the soil's capacity to produce SOC at tropical sites characterized by different forest cover. The temporal variation of SOC storage at eroding soil profiles covered by tabonuco, colorado, and palm vegetation at the Mameyes watershed, and by colorado and

palm vegetation at the Icacos watershed, respectively, for the maximum source and maximum sink scenarios, are illustrated in Figure 4-11. The simulated erosion rates corresponding to the five soil profiles were comparable, ranging from 4.0 to 6.0 mm yr<sup>-1</sup> (Table 4.5). The series corresponding to the two extreme scenarios in Figure 4-11 form the envelope of possible erosion-induced C fluxes for the soil profiles under study.

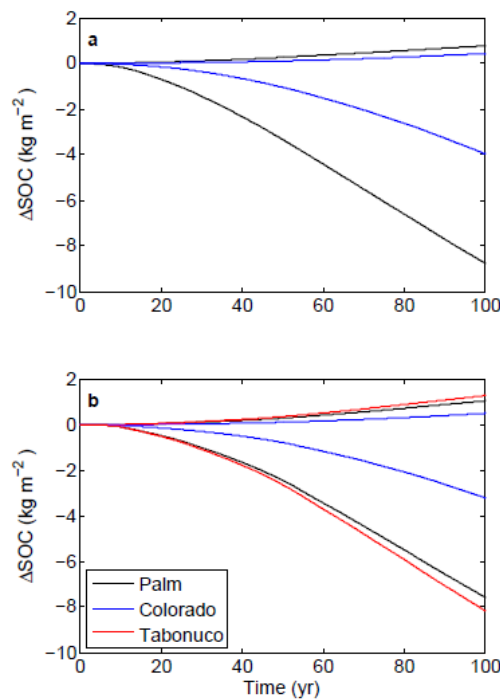


Figure 4-11. Total difference in soil organic carbon storage ( $\Delta\text{SOC}$ ) at eroding sites with different forest cover at the Icacos (a) and Mameyes (b) watersheds. Positive and negative values of  $\Delta\text{SOC}$  represent a net C sink and source, respectively. Maximum sink and maximum source scenarios are illustrated in positive and negative axes, respectively. The effect of erosion on SOC production and oxidation at tabonuco and palm soils is more significant compared to colorado soils.

In the Icacos watershed, the palm forest soil profile exhibited an 85 % increase in SOC storage for the maximum sink scenario relative to the soil profile covered by colorado

forest. For the maximum source scenario the palm soil profile experienced significant erosion-induced SOC loss, approximately 120 % greater than the colorado forest soil profile. In the Mameyes watershed, significantly greater SOC loss was simulated under tabonuco and palm than in the colorado forest for the maximum source scenario (i.e., higher loss by 155 % and 137 %, respectively). The SOC production was also greater (by 151 % and 106 %, respectively) for tabonuco and palm soils for the maximum sink scenario, compared to the soil profile covered by colorado forest. The percent of total SOC losses due to erosion was somewhat larger for tabonuco (47 %) and palm (44 %) soils at the Mameyes watersheds, and for the palm (51 %) soil profile at the Icacos watershed. These percentile losses are lower compared to estimates of potential SOC loss to erosion reported in the literature [*Harden et al.*, 1999]. The colorado soil profiles experienced relatively lower SOC loss (Table 4.5).

Table 4.5. Total difference in soil organic carbon storage ( $\Delta$ SOC) in eroding soil profiles at different forest cover in the Mameyes (M) and Icacos (I) watersheds.

Forest type	Erosion rate (mm yr <sup>-1</sup> )	$\Delta$ SOC (kg m <sup>-2</sup> )		% $\Delta$ SOC	
		Max. sink	Max. source	Max. sink	Max. source
Colorado (M)	5.0	0.51	-3.19	1.4	-8.5
Palm (M)	5.2	1.05	-7.56	6.1	-43.6
Tabonuco (M)	4.0	1.28	-8.15	7.3	-46.7
Colorado (I)	5.1	0.41	-3.97	1.3	-12.4
Palm (I)	6.2	0.76	-8.74	4.5	-51.3

#### 4.5.4 Soil organic carbon burial in alluvial sediments

The total simulated amount of lateral SOC influx to alluvial sediments was calculated, to quantify the rate of SOC burial in the floodplains of the two rivers. The associated SOC flux estimates for different scenarios, and the corresponding SOC concentrations in deposited sediment are presented in Table 4.6.

*Stallard* [2012] reported total organic C (TOC) yields approximately equal to 13 t km<sup>-2</sup> yr<sup>-1</sup> for Rio Mameyes, and 32 t km<sup>-2</sup> yr<sup>-1</sup> for Rio Icacos, respectively. The model used in this study estimated that the approximate portion of the total SOC influx to depositional sites that undergoes long-term burial for the intermediate scenario was 49 % and 20 % of SOC for Rio Mameyes and Rio Icacos, respectively (see Table 4.6). The associated rates of C burial in alluvial sediments at the two rivers were significant at the maximum sink scenario. At the maximum source scenario, most of the deposited SOC was eventually exported fluvially in the form of particulate or dissolved organic C.

Table 4.6. Soil organic carbon (SOC) deposition at the floodplains of Rio Mameyes and Rio Icacos. I, II, and III correspond to the maximum source, the intermediate, and the maximum sink scenarios, respectively

	Lateral SOC influx to river floodplains (t km <sup>-2</sup> yr <sup>-1</sup> )			SOC concentration in sediment influx to river floodplains (%)			Rates of long-term SOC burial at river floodplains (t km <sup>-2</sup> yr <sup>-1</sup> )			Observed total organic C yield (t km <sup>-2</sup> yr <sup>-1</sup> )
	I	II	III	I	II	III	I	II	III	
Mameyes	14.9	25.3	39.2	1.6	2.7	4.1	1.9	12.3	26.2	13
Icacos	32.4	40.1	52.1	2.9	3.6	4.6	0.4	8.1	20.1	32

## 4.6 Discussion

In this study, a coupled and physically-based representation of watershed hydrology, and erosion and landslide processes was used to simulate the hydro-geomorphic behavior of two morphologically diverse watersheds in Puerto Rico. This framework reproduced the natural spatial variability of sediment transport at the watershed scale and the dynamics of mobilized SOC, which is an important advance to conceptual approaches that are based on simpler assumptions on the fate of eroded SOC [Billings *et al.*, 2010; Schlesinger, 1995; Smith *et al.*, 2001].

### 4.6.1 Hillslope erosion and landscape equilibrium

This study modelled dynamic feedbacks of landslide occurrence and topsoil erosion to hydrologic and geomorphic processes at the watershed scale. Both landslides and topsoil erosion alter local geomorphological characteristics of hillslopes, such as the slope and curvature, which control the rate of soil erosion, landslide activity, and the deposition of detached soil. Exposed landslide scars and depositional sites characterized by heterogeneous unconsolidated soil can be susceptible to runoff-driven erosion [Stark and Passalacqua, 2014] at higher rates compared to undisturbed soils. Severe soil erosion and deposition at steep hillslopes may alter the limit equilibrium that controls shallow landslide occurrence, and may therefore feed back to slope stability. The complexity that characterizes this dynamic interrelation can be significant, given the large small-scale

variability of the natural processes that drive erosion and shallow landslides at the watershed scale [Bras, 2015; Kim *et al.*, 2016].

The calculated hillslope erosion rates of Mameyes and Icacos watersheds ( $937 \text{ t km}^{-2} \text{ yr}^{-1}$  and  $1,123 \text{ t km}^{-2} \text{ yr}^{-1}$ , respectively) derive from a physically-based representation of the hydro-geomorphic behavior of the two watersheds. *Larsen* [2012] reported a range of total hillslope erosion for the Mameyes watershed equal to 523 to  $2,143 \text{ t km}^{-2} \text{ yr}^{-1}$ , and a hillslope erosion estimate for the Icacos watershed equal to  $750 \text{ t km}^{-2} \text{ yr}^{-1}$ . These rates are in acceptable agreement with the results of this study, yet they include relatively large inherent uncertainties in the measuring and in the estimation procedures (e.g., uncertainty on landslide scars dating).

The soil thickness in the two tropical watersheds can be determined by the relative balance between erosion and bedrock conversion to soil. This modelling study assessed whether the landscape at the two watersheds, which are characterized by contrasting lithology (quartz diorite in Icacos, and volcanoclastic rock in Mameyes watersheds, respectively) had reached a state of equilibrium. The estimated magnitudes of total hillslope erosion at the two watersheds were compared with the results of recent studies, which used Uranium-series isotopes to quantify weathering rates leading to regolith production. *Chabaux et al.* [2013] reported that the quartz diorite at the Icacos watershed is characterized by a weathering rate of around  $45 \text{ mm kyr}^{-1}$ . *Dosseto et al.* [2012] reported a markedly larger weathering rate for the volcanoclastic rock of the Mameyes watershed, equal to  $335 \text{ mm kyr}^{-1}$ . The rates of total hillslope erosion simulated in this study are equivalent to  $1,123 \text{ mm kyr}^{-1}$  for Icacos, and  $937 \text{ mm kyr}^{-1}$  for Mameyes watersheds, respectively (assuming an average soil density of  $1 \text{ t m}^{-3}$ , as suggested by *Larsen* [2012]).



The erosion rate in Icacos exceeds regolith production by a factor of 25. High estimates of sediment export for Rio Icacos were also reported by *McDowell and Asbury* [1994], *Shanley et al.* [2011], and *Stallard and Murphy* [2012]. The comparison of simulated results with observations suggests that there is a significant rate of landscape denudation at the landscape underlain by quartz diorite. For the Mameyes watershed, soil erosion is in the same order of magnitude with the rate of bedrock weathering. The landscape underlain by volcaniclastic rock may therefore be closer to a state of equilibrium. This is in agreement with the findings of *Stallard* [2012]. Results for the Icacos watershed contrast the findings of *Brown et al.* [1995] and *Brocard et al.* [2015] who used cosmogenic  $^{10}\text{Be}$  to estimate landscape denudation rates of  $43 \text{ mm kyr}^{-1}$  and up to  $100 \text{ mm kyr}^{-1}$ , respectively (see chapter 6). The simulated erosion estimate of  $1,123 \text{ mm kyr}^{-1}$  suggests that cosmogenic rates underestimate the erosional potential of the current state of the system. This may be attributed to the relatively larger time scales (tens of thousands of years)  $^{10}\text{Be}$  derived denudation rates are averaged over, which may not reflect short-term fluctuations of soil denudation rates driven by climatic oscillations, vegetation dynamics, and land use [*Brocard et al.*, 2015].

#### 4.6.2 Soil organic carbon redistribution across the landscape

The importance of the episodic nature of erosion on the estimation of the associated C exchange with the atmosphere was demonstrated in chapter 2. According to the results of this study, the amount of mobilized organic material by landslides and by episodic erosion exhibits significant topographic variation (Figures 3-9 and 3-10). This variation is

controlled by slope morphology, forest cover, and by the depth-dependence of soil biogeochemical properties.

This work quantitatively estimated the amount of SOC that is transported with sediment from eroding hillslopes and landslide sites across the watershed. For the time scales under study, the length of possible SOC transport paths depended on local geomorphological characteristics and surface descriptors (e.g., forest cover). The SOC transport path can be relatively short in the case of slope failure, where SOC is rapidly transferred from unstable slopes to depositional sites, located directly downhill. Longer paths are associated with soil aggregates travelling from upland eroding sites to river floodplains. During transport, SOC may experience oxidation which depends on the length of the transport path and on the stability of soil aggregates [Lal, 1995].

According to the simulations conducted in this study, relatively flat ridge tops did not have significant landslide occurrences (Figure 4-7). Geomorphically-stable ridges favor SOC accumulation, and the average biomass turnover time associated with geomorphic perturbations was significantly higher compared to lower catena positions [Scatena and Lugo, 1995]. Moreover, the residence time of buried SOC at depositional sites depended on local rates of sediment transport, and on the extent to which SOC burial effectively mitigates oxidation [Chaopricha and Marín-Spiotta, 2014; Van Oost et al., 2012]. Therefore, this study emphasizes that systematically tracking the dynamics of mobilized SOC at the watershed scale is crucial for estimating the combined effects of hillslope erosion [Harden et al., 1999], and landslide activity [Stallard, 2012] on soil-atmosphere C exchange.

#### 4.6.3 Assessing the likelihood of modelled scenarios

To evaluate the extent to which modelled scenarios represent the erosion-induced SOC redistribution across the two watersheds, the deposition rate of upland eroded SOC was quantitatively estimated at the floodplains of Rio Mameyes and Rio Icacos (section 4.5.4). The relatively large simulated estimates of total SOC deposition in alluvial sediments (Table 4.6) suggest that the two watersheds are characterized by significant rates of upland SOC erosion. Soils that have been forming uplands for hundreds to thousands of years may erode at rates greater than their rate of development [Stallard, 2012]. Hillslope erosion at relatively steep slopes and interfluvies may lead to depletion of upland SOC stocks. The results of this study suggest that the dynamics of soil thickness (section 4.6.1) exert a strong control on the soil's capacity to produce and store SOC.

The SOC concentration in the surficial mineral soils of the Luquillo CZO roughly ranges from around 1 % to 3 % [Beinroth *et al.*, 1992; Johnson *et al.*, 2015]. The preferential mobilization of soil aggregates that contain SOC can lead to the enrichment of the eroded sediment in SOC [Berhe *et al.*, 2012; Wilson *et al.*, 2009]. The enrichment factor that expresses the associated increase in SOC concentration has been estimated to be equal to 1.7 or lower [Kuhn *et al.*, 2009; Polyakov and Lal, 2004; Rumpel *et al.*, 2006]. Thus, it is reasonable that SOC concentrations in mobilized sediments at the Luquillo CZO are greater than 1 % and up to around 5 %. This range encompasses the simulated SOC concentration in eroded soils for the scenarios explored here (Table 4.6), and indicates that the three scenarios may reasonably quantify the SOC concentration in eroded sediment that is transferred to alluvial sites.

#### 4.6.4 Influence of forest types on the erosion-induced carbon fluxes

The most important C export from the tropical ecosystems at the Luquillo CZO is SOC oxidation to atmospheric CO<sub>2</sub> [Stallard, 2012]. This study demonstrates the importance of forest type on the net erosion-induced C exchange with the atmosphere at the study site (section 4.5.3). Severely eroding soil profiles under different forest types at the Mameyes and Icacos watersheds were compared, for the simulated maximum sink and maximum source scenarios (Figure 4-11). In the maximum source scenario, erosion of surficial soil horizons reduced the potential of the remaining soil system to produce SOC. In the maximum sink scenario soil erosion may significantly alter the depth-dependent rate of SOC oxidation in the soil profile.

Tabonuco and palm forests are characterized by markedly greater (more than double) NPP values compared to colorado forests (Table 4.1). Despite differences in NPP, the depth-dependence of SOC production rate can be similar for soil profiles across different forest types in the Luquillo CZO [Wang *et al.*, 2003]. Lateral removal of topsoil may alter the rate of SOC production in tabonuco and palm soils more significantly, compared to colorado soils. This was reflected in the considerably higher C loss to erosion at tabonuco and palm soils, simulated in the maximum source scenario (Figure 4-11 and Table 4.5). In the maximum sink scenario the erosion-induced alteration of the SOC oxidation rate was more significant in tabonuco and palm soils, while SOC production was maintained at high levels. This led to a greater net increase of SOC storage at tabonuco and palm soil profiles. Thus, the range of possible erosion-induced C fluxes illustrated in Figure 4-11 for the

maximum sink and maximum source scenarios was greater for palm and tabonuco soils. As a result, in the extreme scenarios modelled here, sediment transport had a stronger effect on the C exchange with the atmosphere at palm and tabonuco soils, compared to colorado soils. The results of this study highlight that the spatial distribution of forest types is a key factor that controls the simulated erosion-induced soil-atmosphere C exchange at the watershed scale.

#### 4.6.5 Net atmospheric carbon sink or source

The hydro-geomorphic response of the sites under study was quantitatively estimated in terms of SOC erosion and C exchange with the atmosphere at the watershed scale. SOC loss to erosion at the maximum source scenario was significant across the two watersheds. The maximum sink scenario is characterized by rapid replacement of eroded C by atmospheric C sequestration. The results of this study ranged from a maximum source strength of  $18.3 \text{ g C m}^{-2} \text{ yr}^{-1}$ , to a maximum sink strength of  $21.5 \text{ g C m}^{-2} \text{ yr}^{-1}$  for Mameyes, and from a maximum source strength of  $14.9 \text{ g C m}^{-2} \text{ yr}^{-1}$ , to a maximum sink strength of  $17.1 \text{ g C m}^{-2} \text{ yr}^{-1}$  for Icacos watersheds. The inferred range encompasses the previous estimates of erosion-induced C sink strengths by *Harden et al.* [1999] (10 to  $20 \text{ g C m}^{-2} \text{ yr}^{-1}$ ), *Van Oost et al.* [2005] (3 to  $10 \text{ g C m}^{-2} \text{ yr}^{-1}$ ), and *Yoo et al.* [2005] (up to  $2.8 \text{ g C m}^{-2} \text{ yr}^{-1}$ ). The simulated soil-atmosphere C exchange for the intermediate scenario ( $6.0 \text{ g m}^{-2} \text{ yr}^{-1}$  C sink for Mameyes, and  $3.3 \text{ g m}^{-2} \text{ yr}^{-1}$  C sink for Icacos, respectively) is in agreement with the C sink strength estimates reported by *Van Oost et al.* [2005], and *Yoo et al.* [2005]. The different scenarios may reflect changes in the effect of hillslope erosion on the soil-

atmosphere C exchange as a result of different perturbations at the Luquillo CZO [Stallard, 2012]. Changes in land use and extreme hydro-climatic phenomena [Larsen and Torres-Sánchez, 1992; Scatena and Larsen, 1991] may lead to a transition between a net C source and a net C sink over time at the watershed scale in tropical ecosystems [Ciais *et al.*, 2013; Harden *et al.*, 1999; Van Oost *et al.*, 2007].

This work studied how the spatial distribution of forest cover is inferred to control the ranges of potential erosion-induced C exchange with the atmosphere at the watershed scale. Colorado forest primarily (around 86 % of the area) covers the Icacos watershed (Figure 4-2c), while the Mameyes watershed is for the most part (around 87 % of the area) covered by tabonuco and palm trees (Figure 4-1c). As discussed in section 4.6.4, sediment transport can have a stronger impact on soil-atmosphere C exchange in tabonuco and palm soils, which are characterized by greater maximum C sink and C source strengths, compared to soils covered with colorado forest. Therefore, the watershed-integrated response to geomorphic perturbations at the Icacos watershed resulted in a narrower range of potential C fluxes with the atmosphere, compared to the Mameyes watershed.

#### 4.6.6 Soil organic carbon replacement at landslide scars

According to the findings of this study, landslides removed surficial and deeper soil layers and associated SOC. This work assumed rapid revegetation at landslide sites. Part of the eroded C at fresh scars may be rapidly replaced by atmospheric C sequestration during succession [Stallard, 1998; 2012; Zarin, 1993; Zarin and Johnson, 1995]. For the maximum sink scenario, C sequestration led to rapid SOC production at fresh landslide

scars. At the intermediate scenario, a substantial part of the eroded SOC was rapidly replaced at landslide sites. The rate of SOC replacement at landslide sites decreases with time [Stallard, 2012; Zarin and Johnson, 1995]. At the maximum source scenario, C replacement was limited, and the net erosion-induced SOC loss was higher at landslide sites (Figures 4-9 and 4-10).

Simulations suggest that on the average, 62 % of eroded SOC at landslide scars has been replaced by atmospheric CO<sub>2</sub> sequestration in 100 years at the Mameyes watershed. The corresponding SOC replacement in the Icacos watershed was estimated equal to 67 %. The rapid rates of dynamic C replacement at landslide scars highlight the crucial role of landslide occurrence on C erosion and accumulation in tropical watersheds. The estimated rates of C replacement are in agreement with the ones reported by Stallard [2012], who used measurements from Zarin [1993] in a simple single-site mass balance model, to quantify the rate of C replacement at landslide scars in the Luquillo CZO. The data set characterized the regeneration of soils in chronosequences of landslide scars in the Mameyes and Icacos watersheds, in addition to other sites [Zarin and Johnson, 1995]. Stallard [2012] estimated that about half the eroded SOC can be replaced in approximately 80 years, and that replacement of the entire SOC loss occurs over 200 years. The congruence of the results of this study with Stallard's [2012] analysis is notable, as the two estimates derive from different approaches.

#### 4.6.7 Potential limitations of the approach

Different simplifying assumptions were invoked in the coupled spatially-explicit framework. While this study uses SOC observations for the two watersheds under study, SOC content was represented for entire soil profiles by the means of continuous functions with depth (equation (4.2)), which roughly approximated the initial SOC content from diverse soil profiles (Figure 4-3). The soil properties discussed in sections 4.4.5 and 4.4.6 were assumed time invariant and constant with depth for each soil textural class (except the depth-dependent hydraulic conductivity [*Ivanov et al.*, 2004a]), and the spatial variation of forest types and parameters  $F_l$  and  $v$  are constant in time [*Francipane et al.*, 2012; *Lepore et al.*, 2013]. The initial rates of SOC production in surficial soil horizons were assumed spatially uniform (section 4.4.1) within each forest type. This approach does not account for potential feedbacks of SOC content on soil erodibility, which was calibrated (section 4.4.6) and assumed time invariant over the simulation period. Also, the tRIBS-ECO models hydrologically-induced fluvial transport of organic material at the two watersheds, yet it does not explicitly represent sources and sinks of particulate organic C (POC) and dissolved organic C (DOC) in the stream network [*Shanley et al.*, 2011; *Stallard*, 2012; *Stallard and Murphy*, 2012].

### 4.7 **Summary**

The dynamics of soil organic carbon (SOC) in tropical forests play an important role in the global carbon (C) cycle. Past attempts to quantify the net C exchange with the atmosphere in regional and global budgets do not systematically account for dynamic



feedbacks among linked hydrological, geomorphological, and biogeochemical processes, which control the fate of SOC. This work quantifies effects of geomorphic perturbations on SOC oxidation and accumulation in two adjacent wet tropical forest watersheds underlain by contrasting lithology (volcaniclastic rock and quartz diorite) in the Luquillo Critical Zone Observatory. This study uses the spatially-explicit and physically-based model of SOC dynamics tRIBS-ECO (Triangulated Irregular Network-based Real-time Integrated Basin Simulator-Erosion and Carbon Oxidation) and measurements of SOC profiles and oxidation rates. The results suggest that hillslope erosion at the two watersheds may drive C sequestration or CO<sub>2</sub> release to the atmosphere, depending on the forest type and land use. The net erosion-induced C exchange with the atmosphere was controlled by the spatial distribution of forest types. The two watersheds were characterized by significant erosion and dynamic replacement of upland SOC stocks. Results indicate that the landscape underlain by volcaniclastic rock has reached a state close to geomorphic equilibrium, and the landscape underlain by quartz diorite is characterized by greater rates of denudation. These findings highlight the importance of the spatially-explicit and physical representation of C erosion driven by local variation in lithological and geomorphological characteristics and in forest cover.

## **CHAPTER 5.      Uncertainty in rainfall-triggered landslide modelling associated with the spatial variation of soil hydrological and geotechnical properties**

### **5.1 Introduction**

Rainfall-triggered landslides are among the most common types of landslides, which every year cause fatalities and economic losses globally [Keefer and Larsen, 2007]. Coupled spatially-explicit hydrological-stability models can be used to evaluate the risk of shallow rainfall-triggered landslide hazards at catchment scale (section 4.2). The practice is, typically, to utilize the basin hydrological response, evaluated in terms of soil moisture and groundwater fields, to assess a spatially distributed Factor of Safety (*FS*) by using the infinite slope model [Arnone *et al.*, 2011; Capparelli and Versace, 2010; Montgomery and Dietrich, 1994; Rosso *et al.*, 2006; Simoni *et al.*, 2008]. Mechanical and hydrological soil properties play a crucial role in such an evaluation, and the importance of appropriately modelling soil water dynamics has been clearly demonstrated in some studies [Lanni *et al.*, 2009; Lepore *et al.*, 2013].

A limitation in using physically-based and spatial distributed models is the relatively large numbers of model parameters whose reliable estimation is not always possible in a natural catchment. The inability to fully characterize hydrological and geotechnical behavior of soil may have a significant impact on model results. To account for this uncertainty, *FS* can be computed within a probabilistic framework, by considering soil

parameters as random variables. This practice has received considerable attention in the geotechnical engineering literature, which proposes different methodologies for modelling and analyzing the uncertainty related to the shear strength parameters (i.e., soil cohesion and friction angle) at the hillslope scale [Abbaszadeh *et al.*, 2011; Malkawi *et al.*, 2000; Ray and Baidya, 2011]. Based on similar approaches, some studies have been conducted for basin scale applications within coupled hydrological-stability models [Frattini *et al.*, 2009; Melchiorre and Frattini, 2012; Pack *et al.*, 1998; Simoni *et al.*, 2008]; in such applications, the probability of failure, conditioned to soil moisture, is dynamically estimated across the basin, whereas the probability distributions of the shear strength parameters are time independent. However, the uncertainty of soil hydrological properties, which may be predominant in case of unsaturated conditions, is typically neglected in the literature. In particular, soil retention curve parameters are the most significant in determining the contribution of the soil matric suction to slope stability.

The probability distribution of *FS* can be derived numerically, analytically or through analytical approximations. The Monte Carlo simulation method uses independent sets of soil properties, generated through a priori assigned probability distributions at fixed topographic (i.e., slope) and hydrological (i.e., soil moisture) conditions to obtain a solution. However, such an approach may have significant computational cost for basin scale applications, since the aforementioned conditions change in time and space. The *FS* probability distribution can be analytically derived in the case where solely geotechnical parameters (i.e., cohesion and friction angle) are considered as random variables (e.g., for saturated conditions) and the infinite slope model is used for the slope stability analysis [Abbaszadeh *et al.*, 2011; Malkawi *et al.*, 2000]. If the soil retention curve parameters are

also assumed to be random (e.g., for unsaturated conditions), the derivation of *FS* distribution is not analytically tractable. In this case, the First Order Second Moment (FOSM) method [Benjamin and Cornell, 1970] can be used to approximate the spatio-temporal statistics of *FS* (i.e. mean and variance), to ultimately fit a theoretical probability distribution for *FS* and estimate the spatio-temporal dynamics of probability of failure (section 5.2.2).

In order to systematically account for the parameter uncertainty, this study proposes a probabilistic approach for coupled distributed hydrological-stability models based on the FOSM method, which was implemented in the tRIBS-VEGGIE (Triangulated Irregular Network (TIN)-based Real-time Integrated Basin Simulator - VEGetation Generator for Interactive Evolution) - Landslide module [Lepore *et al.*, 2013]. The proposed methodology was applied to the Rio Mameyes Basin in the Luquillo CZO (section 4.3), a site particularly susceptible to rainfall-triggered landslides [Larsen, 2012]. The spatial and temporal patterns of precipitation may have different impacts on the hydrologic response [Ogden and Julien, 1993; Singh, 1997; Wilson *et al.*, 1979] and also influence slope stability [D'Odorico *et al.*, 2005]. In addition to the description and implementation of the probabilistic framework in the coupled physically-based model, this study also aims to assess the effects of different rainfall hyetographs on landslide initiation across the basin. This chapter is a verbatim recompilation of Arnone *et al.* [2016], Arnone *et al.* [2014], and includes material directly from Dialynas *et al.* [2013], and Arnone *et al.* [2013]. The significant contribution of Elisa Arnone to this chapter is acknowledged.

## 5.2 Methods

### 5.2.1 Coupled Hydrological-Stability Model

The methodology is built around the tRIBS-VEGGIE-Landslide model [Lepore *et al.*, 2013] which was developed by embedding a limit equilibrium analysis into the eco-hydrological model tRIBS-VEGGIE [Ivanov *et al.*, 2008a]. The model inherits from tRIBS (see section 2.2.2) the capability to simulate most of the hydrological processes (e.g. infiltration, evapotranspiration, interception, lateral redistribution, soil moisture dynamics), by explicitly considering the spatial variability of land-surface properties as well as in precipitation fields. An irregular triangulated spatial mesh [Vivoni *et al.*, 2004] is used to describe topography (section 5.3.2). The vegetation module (VEGGIE) simulates the plant physiology, and in particular the biophysical energy processes (e.g. transpiration), biophysical hydrologic processes (e.g. unsaturated zone flow) and biochemical processes (e.g. photosynthesis, plant respiration). A detailed description of model is given in Ivanov *et al.* [2008a]. Some key characteristics of the model are discussed below:

- The infiltration module is based on a numerical approximation of the one dimensional Richards' equation [Hillel, 1980], which provides the moisture transfer in the subsurface within an element. Subsurface and surface moisture is then laterally redistributed among the elements along the direction of steepest descent in a rate depending on the unsaturated hydraulic conductivity of the receiving cell.
- As a consequence of the Richard's equation resolution scheme, soil moisture is estimated in a multi-layer scheme parallel to the slope surface, with a number of layers equal to 25.

- The *Brooks and Corey* [1964] (BC) parameterization scheme is used to model the soil retention curve and the unsaturated hydraulic conductivity, as a function of saturated hydraulic conductivity in the normal to the soil surface direction, air entry bubbling pressure, and pore-size distribution index.

The coupled model is capable to dynamically compute the factor of safety,  $FS(t)$ , across a basin as a response of the soil moisture dynamics, by applying the infinite slope analysis. The implemented equation is the following [Lepore *et al.*, 2013]:

$$FS(t) = \frac{c'}{\gamma_s z_n \sin \alpha} + \frac{\tan \phi}{\tan \alpha} + \frac{\gamma_w \psi_b}{\gamma_s z_n} \cdot \left( \frac{\theta(t) - \theta_r}{\theta_s - \theta_r} \right)^{1-\frac{1}{\lambda}} \cdot \frac{\tan \phi}{\sin \alpha} \quad (5.1)$$

where  $FS(t)$  is the time dependent factor of safety (hereinafter simply  $FS$ ),  $c'$  is the effective soil cohesion,  $\gamma_s$  is the total unit weight of soil (varying with soil moisture),  $\gamma_w$  is the water unit weight,  $z_n$  is the soil depth measured along the normal direction to the slope;  $\alpha$  is the slope angle,  $\phi$  is the soil friction angle,  $\psi_b$  is the air entry bubbling pressure,  $\lambda$  is the pore-size distribution index,  $\theta(t)$  is the time depended volumetric water content (hereinafter simply  $\theta$ ), and  $\theta_r$  and  $\theta_s$  are the residual and saturated soil moisture contents, respectively.  $\psi_b$ ,  $\lambda$ ,  $\theta_r$  and  $\theta_s$  are the Brooks-Corey equation parameters used to represent the soil retention curve. As a result of the multi-layer representation of soil moisture, the final products of the module are dynamic maps of instability areas as well as dynamic  $FS$  profiles at selected areas.

### 5.2.2 Probabilistic Framework

A probabilistic framework was developed to take into account the soil parameters uncertainty that characterizes slope stability analyses. The methodology consists of *i*) treating the soil hydrological and geotechnical parameters of the *FS* equation (equation (5.1)) as random variables, *ii*) approximating *FS* moments using the FOSM method, and *iii*) fitting a theoretical *FS* distribution to estimate the probability of failure across the basin.

The FOSM method is the most widely used approximate method in engineering design for the analytical estimation of the mean and variance of a random function and it is based on a Taylor series expansion. Consider a function of variables,  $X_1, \dots, X_n$ :  $Y=y(X_1, \dots, X_n)$ . The approximation used here expands up to second order terms in the Taylor series (e.g., as opposed to *Formetta et al.* [2016], who considered first order terms), resulting in:

$$E[Y] = y(\mu_{X_1}, \dots, \mu_{X_n}) + \frac{1}{2} \sum_{i=1}^n Var[X_i] \frac{d^2 y}{dX_i^2} + \sum_{i=1}^{n-1} \sum_{j=i+1}^n Cov[X_i, X_j] \frac{d^2 y}{dX_i dX_j} \quad (5.2)$$

where  $E[\cdot]$  denotes the expectation,  $Var[\cdot]$  denotes the variance,  $Cov[X_i, X_j]$  denotes the covariance between  $X_i$  and  $X_j$  and  $n$  is the number of random variables. The variance of the random function  $Y$  is approximated by the FOSM method as follows:

$$Var[Y] = E \left[ \left( \sum_{i=1}^n (X_i - \mu_{X_i}) \frac{\partial y}{\partial X_i} \right)^2 \right] = \sum_{i=1}^n \left( \frac{\partial y}{\partial X_i} \right)^2 Var[X_i] + 2 \sum_{i=1}^{n-1} \sum_{j=i+1}^n \left( \frac{\partial y}{\partial X_i} \right) \left( \frac{\partial y}{\partial X_j} \right) Cov[X_i, X_j] \quad (5.3)$$

Derivatives of  $y$  in equations (5.2) and (5.3) are estimated around the mean values  $\mu_{X_i}$ .

Given the marginal (means and variances) and joint statistics (covariances) of the assumed random variables ( $c$ ,  $\phi$ ,  $\theta_r$ ,  $\theta_s$ ,  $\psi_b$ , and  $\lambda$ ), equations (5.2) and (5.3) approximate the mean, and variance of  $FS$ ,  $E[FS]$  and  $Var[FS]$  respectively. Equation (5.1) is continuously differentiable with respect to each assumed random variable, a condition required for the analytical implementation of the FOSM method. First, second and mixed derivatives of equation (5.1) with respect to each of the six parameters were derived. Each term is thus a function of the topographic characteristics and the soil moisture spatial and temporal dynamics ( $\theta$ ), leading the statistics  $E[FS]$  and  $Var[FS]$  that are dependent on both space and time, via changes in the moisture and topography.

By fitting a two-parameter probability distribution to the  $FS$  moment approximations, the soil moisture dependent probability of failure can be estimated, i.e., the probability that  $FS$  is less than a given critical value,  $FS_{crit}$ ,  $Pr[FS < FS_{crit}]$ . This critical value is the one that delimits stable and unstable conditions, and based on the definition of  $FS$  (equation (5.1)), is typically assumed equal to 1. The best-fit theoretical  $FS$  distribution can be identified by Monte-Carlo experiments with fixed hydrologic and topographic conditions (see section 5.4). The Normal distribution has been used in the literature to describe the random character of  $FS$  [Abbaszadeh *et al.*, 2011; Malkawi *et al.*, 2000; Simoni *et al.*, 2008]. However, in those studies only the geotechnical parameters were considered as random variables. Nevertheless, Frattini *et al.* [2009] found that the  $FS$  may exhibit significant positive skewness, with the tail of the distribution located on the right, with considerable probability mass concentrated on the left side of the distribution. In order to capture the asymmetry of the  $FS$  distribution, they used the lognormal distribution, that was verified for different soil formations.



Under saturated conditions, matric suction vanishes and  $FS$  is independent of the BC parameters, becoming a linear function of the normally distributed soil cohesion and friction angle [Lepore *et al.*, 2013]. In this case, the  $FS$  distribution is analytically derived and the use of an approximate method is not required. More precisely, by applying the convolution integral [Feller, 1971] it can be shown that the  $FS$  becomes also a normally distributed random variable, and the  $FS$  statistics (i.e.,  $E[FS]$  and  $Var[FS]$ ) are given by:

$$E[FS] = \frac{\mu_c}{\gamma_s h_s \sin \alpha} + \left(1 - \frac{\gamma_w h_w}{\gamma_s h_s}\right) \frac{\mu_{\tan \phi}}{\tan \alpha} \quad (5.4)$$

$$Var[FS] = \frac{\sigma_c^2}{(\gamma_s h_s \sin \alpha)^2} + \left(1 - \frac{\gamma_w h_w}{\gamma_s h_s}\right)^2 \frac{\sigma_{\tan \phi}^2}{(\tan \alpha)^2} \quad (5.5)$$

where  $\mu_c$ ,  $\sigma_c^2$ , and  $\mu_{\tan \phi}$ ,  $\sigma_{\tan \phi}^2$  are the statistics of cohesion and friction angle respectively,  $h_s$  the soil thickness and  $h_w$  the water level. Given the  $FS$  distribution, the probability of failure for saturated conditions is then computed as the cumulative probability that  $FS$  is less than 1:

$$\Pr(FS < 1) = \frac{1}{2} \left[ 1 + \operatorname{erf} \left( \frac{1 - \mu_{FS}}{\sqrt{2} \sigma_{FS}} \right) \right] \quad (5.6)$$

where  $\operatorname{erf}$  is the error function.

The framework described above was implemented in the tRIBS-VEGGIE-Landslide model to dynamically evaluate the landslide hazard at basin scale. In particular, probabilities of failure are computed for each time step, Voronoi element and soil vertical layer ( $i$ ). The probability of  $FS$  being equal or lower than a critical value at the  $i^{\text{th}}$  layer

(here referred to as event  $E_i$ , corresponding to the Probability of Failure at the  $i^{\text{th}}$  layer,  $PrF_i$ ) is computed. At each timestep, the model estimates the spatial map of the probability of landslide occurrence at each soil column, here referred as *Probability of Failure of the soil Column* ( $PrFC$ ). The  $PrFC$  is equal to the probability of occurrence of the union of events  $E_i$  for the entire soil column. Furthermore, at each soil column the probability of the landslide depth is estimated. The probability that the plane of failure is located at the  $i^{\text{th}}$  layer (here referred as *Probability of Plane of Failure at  $i^{\text{th}}$  layer*,  $PrPF_i$ ) is given by the joint probability of  $FS$  being equal or lower than  $FS_{\text{crit}}$  at layer  $i$ , while there is no failure above that layer. The simplifying assumption of independent and mutually exclusive events among different soil layers allows the estimation of  $PrPF_i$  at each time step. The landslide depth corresponding to the maximum value of  $PrPF_i$  represents the most probable depth of failure. Thus, the model is able to evaluate when and where failure is most probable to be initiated within each soil column and across the basin.

### 5.3 Case study

The Rio Mameyes basin (Figure 4-1a), described in section 4.3 is used as a case study. The Mameyes basin is characterized by a rapid change in elevation from 104.2 m to 1046 m across a horizontal distance of 3 km. An analysis of the slope distribution derived from a 30 m DEM (Figure 4-1a) showed that 10% of the basin area is characterized by slopes greater than  $30^\circ$ , and 30% of the basin area by slopes greater than  $25^\circ$ . The Mameyes basin has been previously modeled in terms of spatio-temporal dynamics of hillslope stability by [Lepore *et al.*, 2013] using the tRIBS-VEGGIE-Landside model. Most of the

required input data, data description and model setup are described in detail in *Lepore et al.* [2013]. The main model data and parameters are described in the following sections.

### 5.3.1 Input data and model parameters

The meteorological data used were obtained from the Bisley Tower (section 4.4.4). The selection of the DEM used to construct the model's Triangulated Irregular Network (TIN) is discussed in section 5.3.2. The modelled soil types are discussed in section 4.4.3 (Figure 4-1b). The main hydrological soil properties (e.g., saturated hydraulic conductivity, anisotropy ratio) were obtained through a validation/confirmation procedure conducted by *Lepore et al.* [2013], based on soil moisture data. In particular, nine soil moisture hourly series measured at a 30 cm depth were used for the model confirmation. The measurements were taken at three locations close to the Bisley Tower (Figure 4-1) and each using three time-domain reflectometry (TDRs) Campbell Scientific Model CS616 instruments. Also, tRIBS-VEGGIE defines the anisotropy ratio as the ratio of the saturated hydraulic conductivities in the directions parallel to the slope and normal to the slope. In this work, an anisotropy ratio of 100 was assumed [*Lepore et al.*, 2013].

The BC soil retention parameters, i.e.  $\theta_r$ ,  $\theta_s$ ,  $\psi_b$ , and  $\lambda$ , and their statistics were estimated from a generalized soil properties database available in the literature (Table 5.1). In particular, *Brakensiek et al.* [1981] suggested transformations of the BC parameters to normality and reported their statistical properties for different soil types. *McCuen et al.* [1981] reported BC parameters statistics and demonstrated the variation that the BC parameters exhibit across different soil textural classes. *Rawls et al.* [1982] provided BC

marginal statistical properties. *Meyer et al.* [1997] and *Flores et al.* [2010] reported marginal distributions of BC parameters by applying parameter equivalency relationships between BC and *van Genuchten* [1980] soil retention parameters. This study uses the statistical properties (i.e., means, variances and cross-correlation coefficients) reported in *Brakensiek et al.* [1981] and *McCuen et al.* [1981] and the corresponding transformations of BC parameters to normal random variables (Table 5.1), which allowed the use of the joint Normal distribution for the BC soil retention parameters (section 5.4).

Table 5.1. Hydrological and mechanical soil properties and their statistics for the four soil types present in the Mameyes basin.

Parameter	Description	Units	Clay – Loam	Sandy – Loam	Silty - Clay	Clay
$K_s$	Saturated hydraulic conductivity	[mm/hr]	50.0	50.0	50.0	10.0
$\mu_{\theta S}$	Mean of saturated soil moisture, $\theta_S$	[mm <sup>3</sup> /mm <sup>3</sup> ]	0.56	0.55	0.55	0.53
$\mu_{\theta R}$	Mean of residual soil moisture, $\theta_R$	[mm <sup>3</sup> /mm <sup>3</sup> ]	0.075	0.041	0.051	0.09
$\mu_{\lambda}$	Mean of pore-size distribution index, $\lambda$	[-]	0.200	0.322	0.127	0.130
$\mu_{\psi b}$	Mean of air entry bubbling pressure, $\psi_b$	[mm]	-250	-150	-340	-370
$\mu_{c'}$	Mean of soil effective cohesion, $c'$	[N/m <sup>2</sup> ]	3000	3000	3000	3000
$\mu_{\phi}$	Mean of soil friction angle, $\phi$	[°]	25	25	25	25
$\sigma_{c'}$	Standard deviation of $c'$	[N/m <sup>2</sup> ]	1200	1200	1200	1200
$\sigma_{\phi}$	Standard deviation of $\phi$	[°]	2.5	2.5	2.5	2.5
$\sigma_{\psi b}$	Standard deviation of $\psi_b$	[mm]	290	210	390	600
$\sigma_{\theta S}$	Standard deviation of $\theta_S$	[mm <sup>3</sup> /mm <sup>3</sup> ]	0.054	0.076	0.064	0.040
$\sigma_{\theta R}$	Standard deviation of $\theta_R$	[mm <sup>3</sup> /mm <sup>3</sup> ]	0.007	0.004	0.022	0.011
$\sigma_{\lambda}$	Standard deviation of $\lambda$	[-]	0.113	0.145	0.094	0.098
$\rho_{\psi b-\theta S}$	Coefficient of correlation $\psi_b-\theta_S$	[-]	0	0	0	-0.216
$\rho_{\psi b-\theta R}$	Coefficient of correlation $\psi_b-\theta_R$	[-]	0.203	0	0	0.154
$\rho_{\psi b-\lambda}$	Coefficient of correlation $\psi_b-\lambda$	[-]	0.151	0.274	0	0.128
$\rho_{\theta S-\theta R}$	Coefficient of correlation $\theta_S-\theta_R$	[-]	0.307	0	0	0
$\rho_{\theta S-\lambda}$	Coefficient of correlation $\theta_S-\lambda$	[-]	0.168	0	0	0
$\rho_{\theta R-\lambda}$	Coefficient of correlation $\theta_R-\lambda$	[-]	0.429	0.518	0.476	0.442

With regard to the geotechnical parameters, *Simon et al.* [1990] and *Lohnes and Demirel* [1973] reported values for cohesive strength and friction angle for some of the geological units of the study area, and illustrated the expected high variability of these two quantities. As in *Lepore et al.* [2013], this study assumed spatially homogenous properties over the entire basin following the predominant geological unit [*Simon et al.*, 1990]. The uncertainty characterizing estimates of soil cohesion and friction angle has been thoroughly studied in the literature. *Lumb* [1966] suggests that  $c'$  and  $\phi$  can be described by the Normal distribution. This assumption has been widely used in the literature [*Abbaszadeh et al.*, 2011; *Frattini et al.*, 2009; *Langejan*, 1965; *Malkawi et al.*, 2000; *Melchiorre and Frattini*, 2012; *Rackwitz*, 2000; *Simoni et al.*, 2008; *Tobutt*, 1982; *Wu and Kraft*, 1967]. *Fredlund and Dahlman* [1972], *Lumb* [1974] and *Schultze* [1975] provided statistical properties of geotechnical parameters. *Matsuo and Kuroda* [1974] and *Lumb* [1974] suggested that correlation between cohesion and friction angle is negligible, and independence between the two random variables has been assumed in past studies [*Abbaszadeh et al.*, 2011; *Christian et al.*, 1994; *Dettinger and Wilson*, 1961; *Malkawi et al.*, 2000; *Yucemen MS et al.*, 1975]. Therefore, this work assumes that  $c'$  and  $\phi$  are independent Normal random variables. The associated statistics of the geotechnical parameters are reported in Table 5.1. Incorporating marginal distributions consistent with the literature is an advantage of the implemented framework over simpler approaches (e.g., *Pack et al.* [1998] who assume input parameters which follow a uniform distribution).

As for the vegetation characteristics, only the Tabonuco forest is considered in this study, because it is the predominant vegetation type of the basin, and it is present where both the meteorological and the soil moisture measurements were taken [*Lepore et al.*,

2013]. The forest is modeled as broadleaf evergreen tropical (BET) class, with vegetation height of 20 m and a LAI of  $6 \text{ m}^2 \text{ m}^{-2}$  [Wang *et al.*, 2003; Weaver and Murphy, 1990]. The root component was modeled with a rectangular density function through a depth of 40 cm (typical of the Tabonuco forest). Other parameters used in the vegetation modelling were obtained from the literature [Ivanov *et al.*, 2008a; b; Wang *et al.*, 2003; Weaver and Murphy, 1990].

### 5.3.2 Selection of Digital Elevation Model

The extraction of topographical information from DEMs (e.g., slope, aspect, flow path, and upstream contributing area) is of great interest in landscape modelling. Particularly, the catchment slope distribution directly affects the location of landslide prone areas, because slope impacts the equilibrium of the involved stabilizing and destabilizing forces [Keijsers *et al.*, 2011; Tarolli and Tarboton, 2006]. Errors in the extraction of slope from DEMs (and other topographical properties, in general) may derive not only from the corresponding applied algorithms, but also from the quality and resolution of the geospatial information depicted in DEMs. In fact, slope frequency distributions vary with different DEM resolutions [Claessens *et al.*, 2005].

The impact of DEM resolution to the simulation of landside occurrence was studied using different DEM resolutions (i.e., 20, 30, 50, and 70 m), resampled from a 10 m DEM, available from the USGS National Elevation Dataset (<http://nationalmap.gov/elevation.html>). The nearest neighbor resampling technique was used, which is a typical interpolation method that does not alter the value of the input cells.

More precisely, the output cell center is located on the input grid dataset. Then, the location of the closest cell center on the input grid is determined, and the value of that cell is assigned to the corresponding output cell. Figure 5-1 illustrates the catchment slope cumulative frequency distribution for different DEM resolutions. DEM resolutions coarser than 10 m underestimate the frequency of steep slopes.

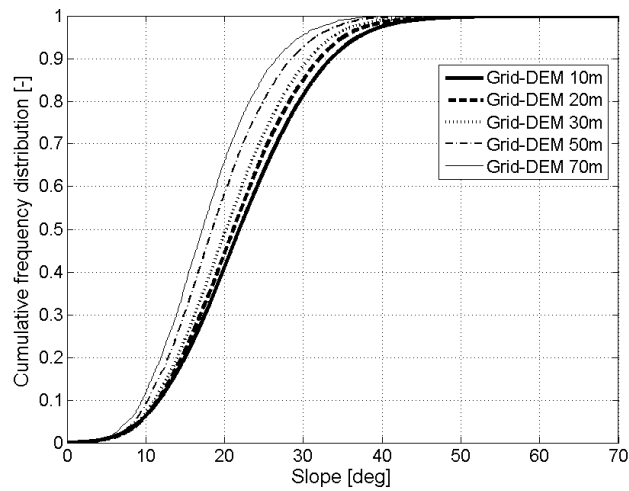


Figure 5-1. Catchment slope cumulative frequency distribution for different DEM resolutions.

A TIN was constructed for each DEM resolution. The hydrographic TIN method was used to derive the hydrologically-significant TIN from the gridded DEM [Vivoni *et al.*, 2004]. The TIN representation of surface aims at reducing the number of elevation nodes, while preserving the distribution of topographic attributes such as slope and curvature, as well as hydrographic features. Moreover, the topographic approach used for the

construction of TINs was the Latticetin sampling method [Lee, 1991]. This traditional approach preserves the catchment slope distribution in a robust and accurate manner (e.g., *Vivoni et al.* [2004]). This method successively removes DEM points, and retains significant points that result in a TIN surface following a specified elevation tolerance. The number of the preserved DEM elevation points was selected according to a reasonable balance between feasible computational cost and efficient preservation of topographic characteristics (e.g., catchment slope distribution). The number of points for each DEM and TIN, and the percentage of retained points are given in Table 5.2: the coarser the resolution, the higher the percentage of points required to preserve the slope frequency distribution.

Table 5.2. Number of DEM cells, TIN nodes, and Voronoi cells for each Grid-DEM resolution.

Grid-DEM Resolution (m)	DEM Cells	TIN Nodes	TIN to DEM Ratio	Voronoi Cells
10	169,615	6,974	4%	6,276
20	42,400	3,605	9%	3,131
30	18,837	2,603	14%	2,190
50	6,782	2,274	34%	1,908
70	3,462	2,416	70%	2,177

Furthermore, for each DEM resolution, the model's mesh of computational elements (Voronoi cells) was constructed [*Ivanov et al.*, 2004a; *Vivoni et al.*, 2004]. The geometry of the Voronoi cells closely follows the TIN network [*Ivanov et al.*, 2004a]: each TIN node



corresponds to a Voronoi cell, the boundaries of which consist of the perpendicular bisectors of the associated TIN edges (similar to Thiessen polygons). Because some nodes are used as catchment boundaries (*closed mesh boundary node*), the final number of Voronoi cells is lower than the TIN nodes (Table 5.2). Although the TIN construction preserves topographic features such as the catchment slope frequency distribution, the Voronoi construction method may alter the DEM slope frequency distribution (Figure 5-2). Analysis at different resolutions showed that Voronoi meshes tend to exhibit higher frequency of occurrence of steeper slopes, compared to the original DEM slope distributions (Figure 5-2). Voronoi meshes also exhibited a smoothing effect within gentler slope classes ( $< 20^\circ$ ). Spatial slope distributions of Voronoi cells corresponding different DEM resolutions are given in Figure 5-3.

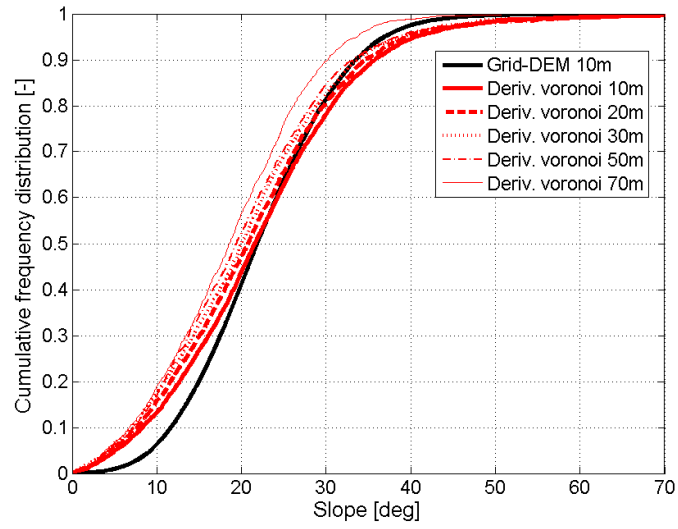


Figure 5-2. Catchment slope cumulative frequency distributions corresponding to the 10 m (grid) DEM, and to Voronoi meshes derived from 10 m, 20 m, 30 m, 50 m, and 70 m DEMs.

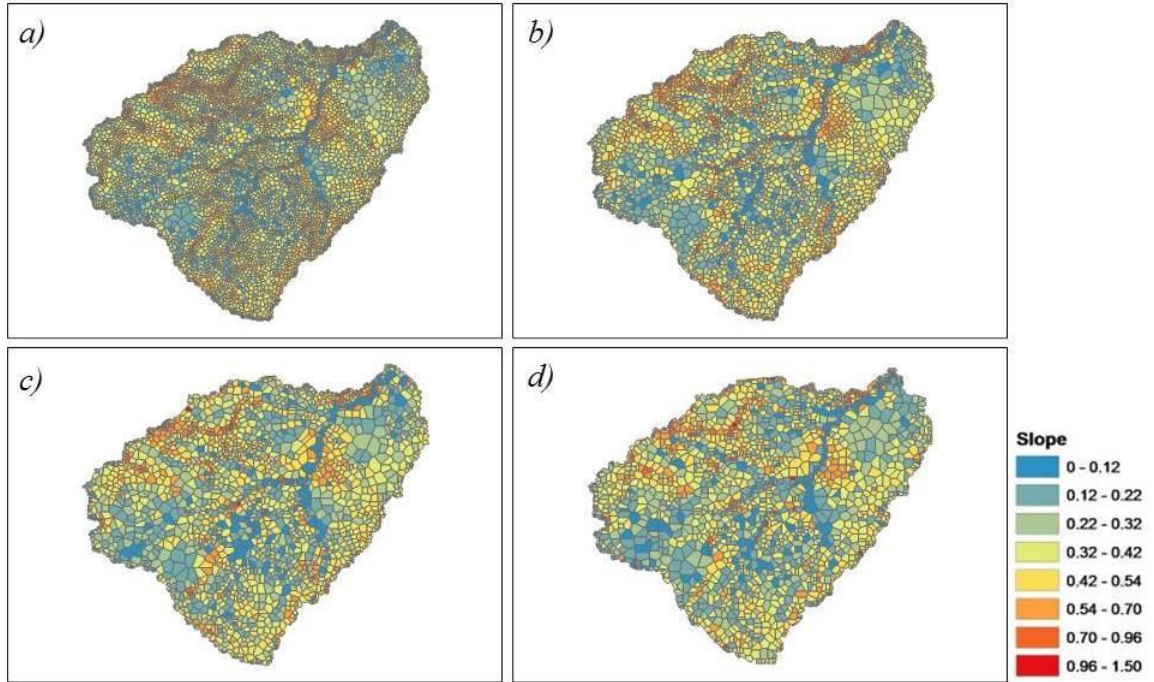


Figure 5-3. Spatial slope (in radians) distribution of voronoi cells corresponding different DEM resolutions: 10 m (a), 20 m (b), 30 m (c), and 50 m (d).

The Voronoi meshes for each DEM resolution were used as inputs to the tRIBS-VEGGIE landslide model (section 5.2.1) in order to compare the results in term of slope stability. The model inputs used for the analysis (meteorological forcing, soil properties, model parameters) are the same described in section 5.3.1 and in *Lepore et al.* [2013]. Particularly, the case of anisotropy ratio (ratio of the saturated hydraulic conductivities in the directions parallel to the slope and normal to the slope) equal to 1 was considered. Results of this sensitivity analysis are presented in Figures 5-4 and 5-5. Figure 5-4 shows the FS spatial distributions at a selected hour (i.e., rainfall of around 100 mm) for Voronoi meshes derived from DEM resolutions of 10, 20, 30 and 50 m (from left to right): black elements denotes areas where  $FS \leq 1$ .

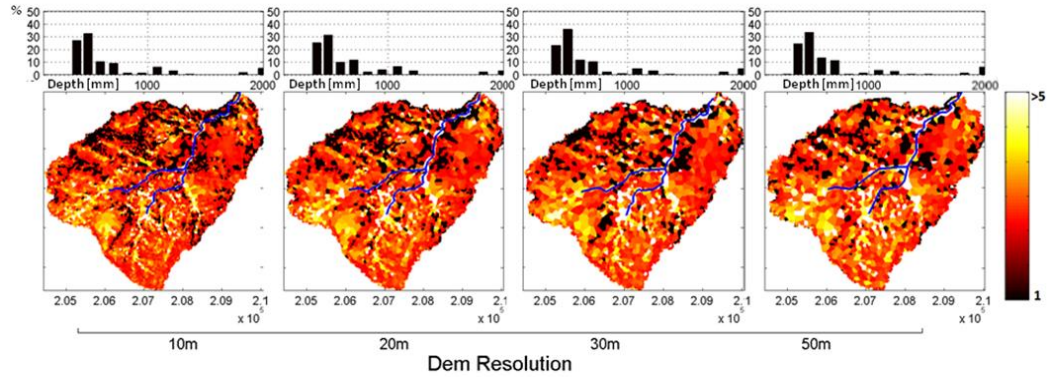


Figure 5-4. Spatial model outputs: FS distributions for Voronoi meshes corresponding to DEM resolutions of 10, 20, 30 and 50 m. The percentage of failing Voronoi cells for each depth (and up to of 2 m) is shown in the relative frequency histogram reported on top of each map.

According to Figure 5-4, the finer the resolution, the slightly larger the area affected by landslide occurrence, particularly in the north-western part of the basin which is characterized by the steepest hillslopes [Lepore *et al.*, 2013]. For all mesh resolutions, failure mainly occurs with similar frequency at depths of about 400 and 500 mm. Figure 5-5 illustrates box plots of failure slope values (i.e., slope at which each element has failed) for each case, confirming the consistent behavior depicted in Figure 5-4 throughout the four DEM resolutions. The average failure slope is equal to about 0.58 rad for each DEM resolution, with minimum and maximum values of about 0.3 and 0.9 rad. The 50 m case exhibits a slightly different range.

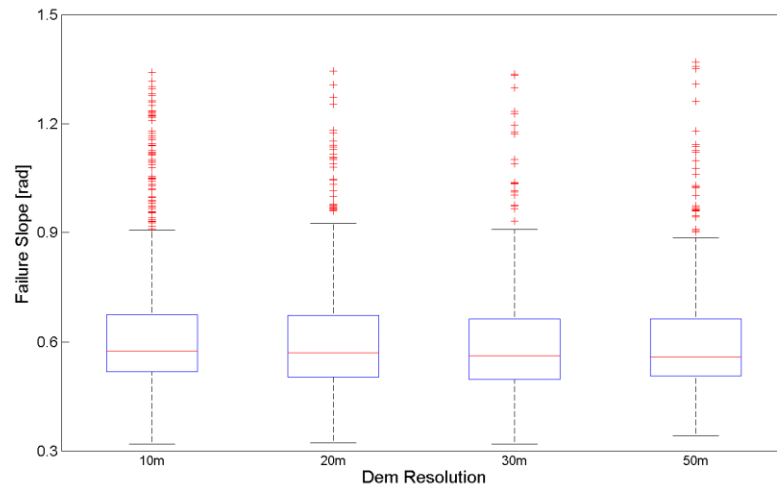


Figure 5-5. Box plots of failure slope values (i.e., slope at which each element has failed) for Voronoi meshes corresponding to DEM resolutions of 10, 20, 30 and 50 m.

This preliminary analysis showed that the use of different DEM resolutions did not lead to significant difference in the watershed-scale landslide model outputs. This can be justified by the tendency of the Voronoi-constructing algorithm to generate steeper slopes compared to the original DEM slope distributions, as previously discussed. Therefore, in this study a 30 m DEM of the Mameyes watershed was selected for the construction of the Voronoi mesh (Figure 5-3c), which significantly reduces computational cost (i.e., compared to the use of a 10 m DEM (Table 5.2)). Also, in cases where model inputs are available in finer spatial scales, high-resolution inputs of hydro-meteorological forcings, soil properties, and forest cover may also become important factors in creating accurate representations of landslide phenomena, and in selecting the optimal scale of Voronoi elements.

## 5.4 Factor of safety probability distribution

As previously discussed, the selection of the probability distribution was based on Monte Carlo experiments for various hydrological and topographical conditions (i.e., soil moisture and slope values and soil depth). First, values of BC parameters, soil cohesion, and friction angle are sampled from the corresponding assumed theoretical distributions (as explained section 5.2.2), given the moments reported in Table 5.1. Then, the  $FS$  is estimated (equation (5.1)) for each set of sampled values, and for the given hydrological and topographical conditions. The results are then used to obtain the empirical distribution of  $FS$ . The procedure was repeated for different sets of slope, soil depth and soil moisture, and for all different soil types characterizing the area, i.e., clay, clay-loam, silty-clay, and sandy-loam. The empirical  $FS$  distributions were compared to different analytical probability distributions, based both on Kolmogorov-Smirnov goodness of fit statistics and visually. The graphical method of Quantile-Quantile (QQ) plots [Wilk and Gnanadesikan, 1968] was used for visual comparison. This study focuses on reproducing the values of  $FS$  probability around 1, which is the  $FS_{crit}$  for failure. Thus, it is important that the theoretical quantiles be as close as possible to the empirical ones around values of  $FS=1$ .

Several two-parameter theoretical distributions were compared against the empirical  $FS$  distribution as well as different combinations of fixed values of slope, depth of failure, and volumetric water content. For the sake of brevity, the comparison of only three probability distributions is shown against the empirical  $FS$  distribution (Figure 5-6), i.e., the normal, lognormal, and inverse gamma distributions, for the case of slope, depth of failure, and volumetric water content equal to  $40^\circ$ , 1000 mm, and  $0.3 \text{ mm}^3/\text{mm}^3$ , respectively, and for hydrological and soil properties given in Table 5.1. The inverse

gamma distribution, which constitutes a special case of Pearson V distribution [Pearson, 1895], is a non-negative skewed distribution, characterized by a heavy tail on the right.

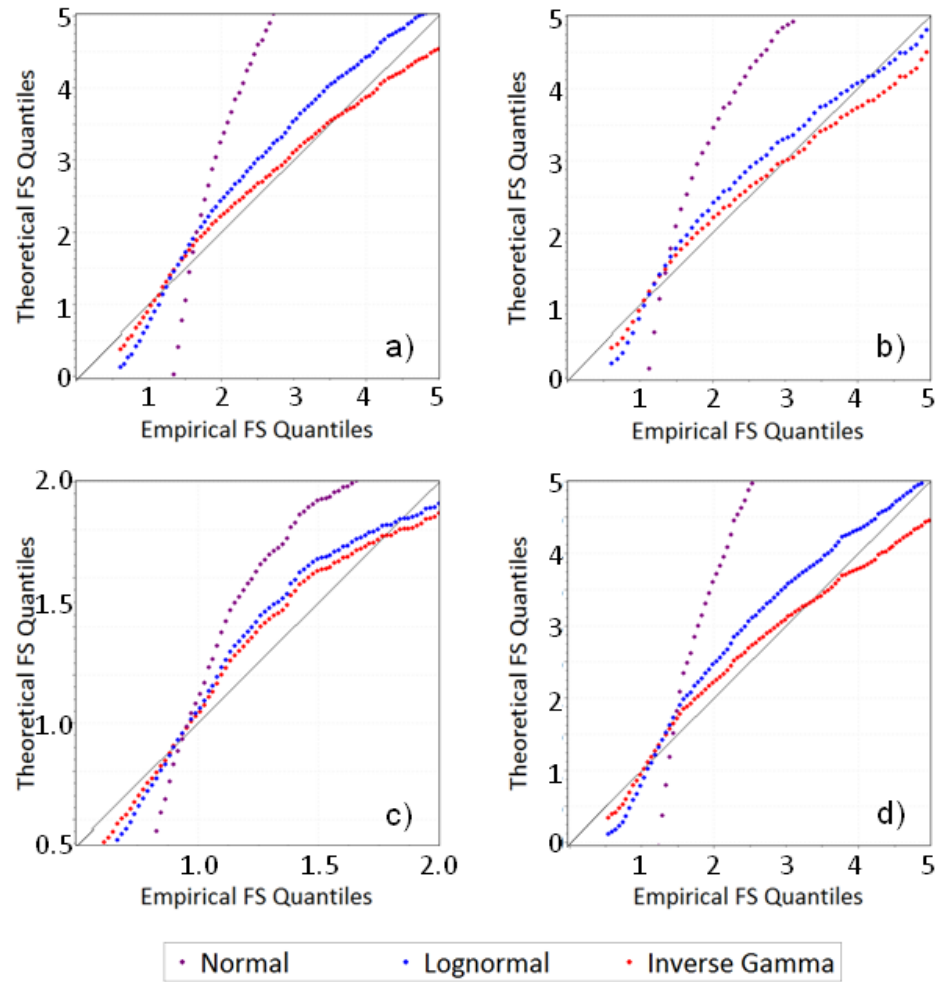


Figure 5-6. Comparison of the empirical *FS* quantiles vs the theoretical *FS* quantiles of Normal (purple), Lognormal (blue), and Inverse Gamma (red) distributions, for (a) clay, (b) clay-loam, (c) sandy-loam, and (d) silty-clay. The values of slope, depth of failure surface and volumetric water content correspond to 40°, 1000 mm, and 0.3 mm<sup>3</sup>/mm<sup>3</sup>, respectively, while the associated statistical properties are reported on Table 5.1.

The ideal agreement between theoretical and empirical quantiles is depicted by the diagonal gray line in the QQ plots of Figure 5-6. This figure demonstrates that the normal distribution (purple dots) is the worst in terms of reconstruction of the empirical quantiles whereas the best results correspond to the inverse (red dots) and the lognormal (blue dots) distributions. Given that the goal is to identify the distribution that provides the most accurate estimation of FS quantiles close to the critical value (1 in this case), the inverse gamma distribution can be considered as the most appropriate distribution for the estimation of the probability of failure. Similar results were obtained for other combinations of slope, depth of failure, and volumetric water content.

The inverse gamma distribution was then used in tRIBS-VEGGIE-Landslide for the dynamic computation of the FS distribution at each cell. The probability of failure for unsaturated conditions is then computed as the cumulative probability that FS is less than 1:

$$\Pr(FS < 1) = \frac{\Gamma\left(\alpha, \frac{\beta}{FS}\right)}{\Gamma(\alpha)} \quad (5.7)$$

where  $\alpha$  and  $\beta$  are the parameters of the distribution, defined as a function of the mean and variance of FS:

$$\beta = E[FS] \cdot (\alpha - 1) \quad (5.8)$$

$$\alpha = \frac{E[FS]^2}{Var[FS]} + 2, \quad \text{for } \alpha > 2 \quad (5.9)$$



Note that the results are strictly dependent on the assumed moments of the random variables (i.e., values given in Table 5.1).

## 5.5 Rainfall analysis

In order to evaluate the effect of the temporal rainfall distribution and provide generalized landslide probability maps for the study area, different synthetic hyetographs representative of extreme rainfall observations were used to force the model. The hyetographs were derived from the precipitation frequency estimates provided by the NOAA Atlas 14 Volume 3 [Bonnin *et al.*, 2006] for Puerto Rico and the U.S. Virgin Islands (available at <http://hdsc.nws.noaa.gov/hdsc/pfds>). Estimates are provided for several durations and return periods and are based on statistical analysis of annual precipitation maxima. These estimates were derived based on a regional frequency analysis that uses the L-moments method [Hosking and Wallis, 1997] for selecting and parameterizing probability distributions. The quantiles are provided at a spatial resolution of 3 arc-seconds ( $80 \times 80$  m) obtained by spatially interpolating the mean annual maximum of the series at each station and duration. In particular, data were spatially interpolated by using the PRISM (Parameter-elevation Regressions on Independent Slopes Model) model [Daly and Neilson, 1992; Daly *et al.*, 2003; Daly *et al.*, 2002], a hybrid statistical-geographic tool for mapping climate data that generates spatial distribution of estimated climatic parameters based on the correlation between point data and other geographic and climatic information. This procedure takes into account the topographic effect on climate and in particular precipitation patterns, which are known to be significant in Puerto Rico [Daly *et al.*, 2003;

*Garcia-Martino et al.*, 1996]. Further details on this analysis are given in *Bonnin et al.* [2006]. This analysis provided spatial distribution of the total precipitation depth at given duration and return period that characterize the study site, as specified above.

NOAA also provides the associated normalized temporal distributions of precipitation corresponding to durations of 1, 6, 12, 24, 96 hours. The temporal distributions are expressed in probabilistic terms as cumulative percentages of precipitation and duration at various percentiles. The data were also subdivided into four categories (identified as “quartiles” in *Bonnin et al.* [2006]) based on where the most precipitation occurred in the distribution. For example, first-quartile group consist of hyetographs where the greatest percentage of the total rainfall precipitates during the first quarter of the time period. This procedure led to four different hyetographs which characterize the area [*Bonnin et al.*, 2006]. A return period of 100 years and duration of 24 hours was selected, which represents a typical event duration that may cause initiation of landslide events according to [*Larsen and Simon*, 1993]. Figure 5-7 shows the corresponding time distributions for each category, which are representative of four different types of precipitation events [*Rosso*, 2002]: in Q1 most of the rainfall precipitates at the beginning of the event (typical of heavy storms), whereas in Q2 and Q3, the peak of precipitation is expected around the middle part of the event (frontal precipitations); finally, in Q4 most of the rainfall volume falls towards the end of the event (typical of tropical cyclones).

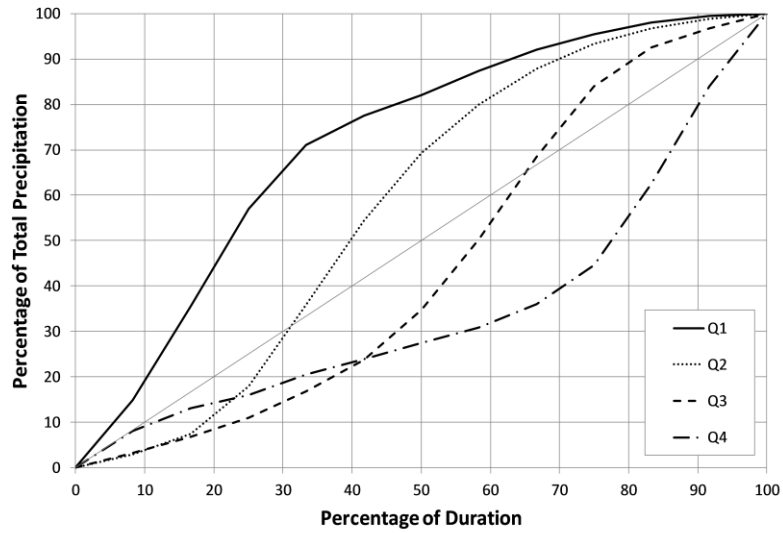


Figure 5-7. Different types of rainfall temporal distributions of 24 hours duration.

For the selected duration, 32% of precipitation types follow the Q1 pattern; 27% follow Q2; 22% follow the Q3 type; and 19% follow Q4 (for more details see NOAA report, A. 1-3 [Bonnin *et al.*, 2006]). Given the temporal distribution and the spatial distribution of total precipitation at selected duration and return period it is then possible to derive, cell by cell, the corresponding hyetographs by simply distributing the total volume through the duration according to the curves showed in Figure 5-7. As an example, Figure 5-8 shows the obtained hyetographs at a selected location (in particular, at the location of the Bisley tower (Figure 4-1a)) for the four types of hyetographs.

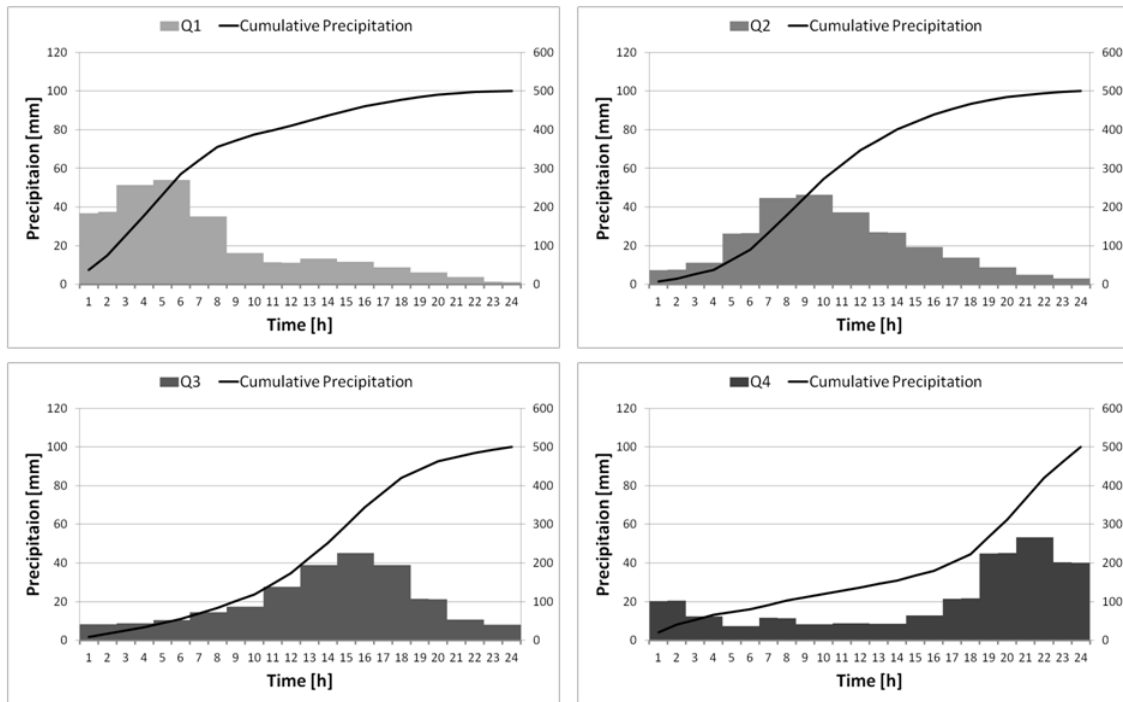


Figure 5-8. Hyetographs at Bisley tower location (indicated in Figure 4-1a) for each type of rainfall events. Total precipitation volume is about 500 mm.

The spatially-averaged precipitation volume for this 24 hr, 100-yr event is around 500 mm; in particular, Figure 5-9 shows the map of the total rainfall estimate of hyetograph Q1. Precipitation is heavier at higher elevations (west and south corners of the basin), with values up to 615 mm, and lower in the extreme north-east area (close to the outlet zone), with values up to 485 mm. The resulting spatial coefficient variation is 0.05. It is worth highlighting that the four types of rain storms have a stationary spatial pattern responding only to elevation (i.e., no dynamic propagation of precipitation has been considered).

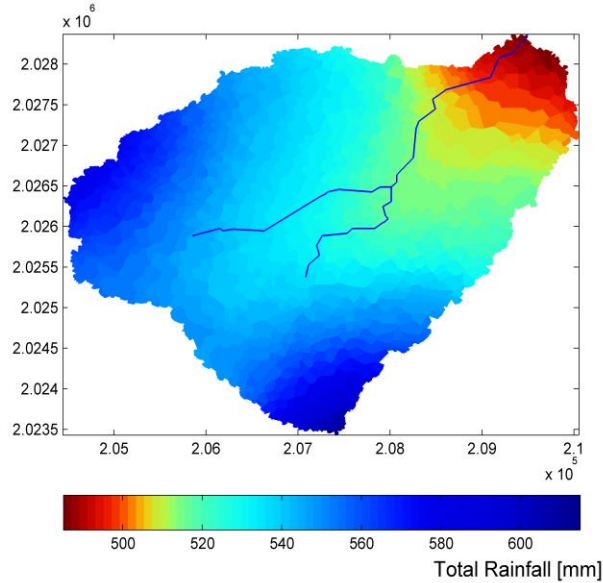


Figure 5-9. Spatial distribution of total rainfall estimate of hyetograph Q1. Total rainfall ranges from 485 mm of the zone approaching to the basin outlet, to 615 mm of the highest zones. The spatial coefficient of variation is 0.05.

## 5.6 Results

As discussed above, four 24 hour, 100-year return period events with different temporal distributions were used to force the model. The initial conditions of the basin were identified using a spin-up procedure, which consists of running the model continuously for a long period (in this case one year) such that the model reaches equilibrium [Lepore *et al.*, 2013]. Equal initial conditions were thus imposed to the 4 storms; the effect of different initial conditions is not analyzed in this work. Results will be analyzed in a time window of 48 hours, which includes 24 hours of no rainfall after the end of the event, to account for soil moisture redistribution effects.

The model output includes: the time series and depth profiles of volumetric soil moisture ( $\theta$ ), probability that  $FS \leq 1$  ( $PrFi$ ) and probability that the plane of failure is located at a given depth ( $PrPF_i$ ), for a given computational element. Spatially, the model provides the distribution of the probability that failure occurs at any depth within the element-soil column ( $PrFC$ ) and the distribution of the most probable depth of failure. In order to provide a comprehensive description of the model variables, section 5.6.1 discusses results of a single model application, i.e., results of the model forced with a single rainfall series, whereas the analysis of the effect of different rainfall temporal distributions is discussed in section 5.6.2.

#### 5.6.1 Time series model output

A time series output is given in Figure 5-10, which shows the response to the rainfall type Q1 (Figure 5-10a) at the element scale (the time window includes a period before the event, useful to assess the initial conditions in terms of soil moisture profiles, which are different across the basin). The selected element falls within the clay-loam soil type and has a slope value of  $52^\circ$ , and thus can be considered as relatively steep. The element is located upstream and has a small contributing area of about 1.3 ha. The soil moisture distribution (Figure 5-10b) shows moderately fast dynamics within the shallow layers of the column, down to 600 mm of depth where the soil reaches full saturation at the time of rainfall peak. Although this part of the basin is characterized by high value of hydraulic conductivity (see Table 5.1), saturation is not reached throughout the entire column

because a significant portion of water is laterally redistributed, at a rate which depends on the local steepness and which is governed by the anisotropy ratio coefficient.

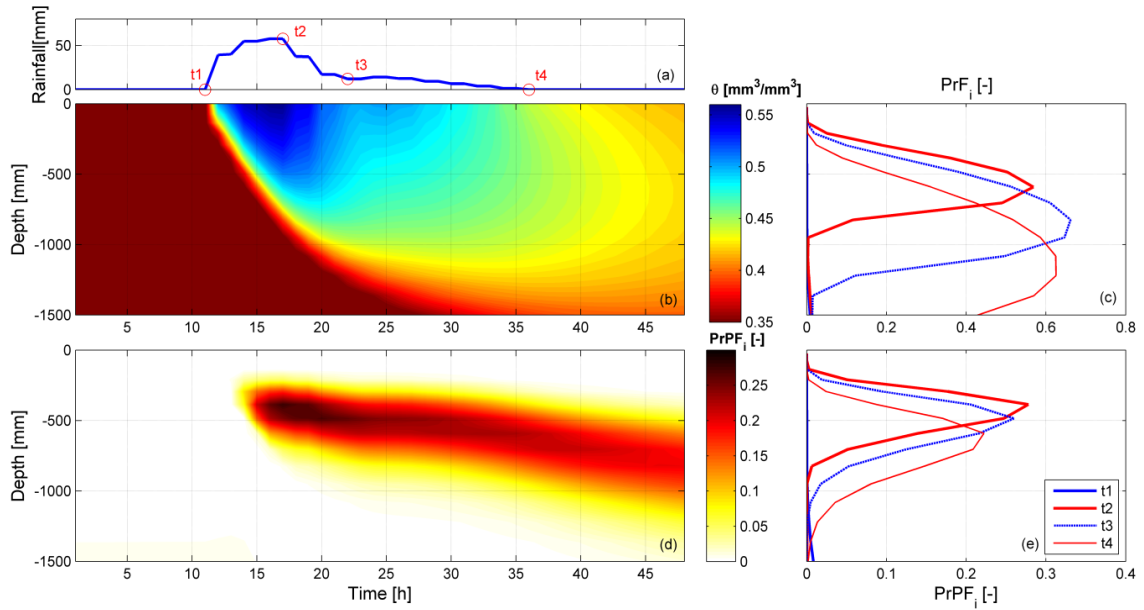


Figure 5-10. Time series model output response of a clay loam element (52°): rainfall type Q1 (a); volumetric soil content ( $\theta$ ) profile and time series (b); probability of failure at each layer at selected times,  $PrF_i$  (c); profile and time series of probability of plane of failure at given depth,  $PrPF_i$  (d);  $PrPF_i$  at selected times (e).

Figure 5-10c shows the probability of failure ( $PrF_i$ ) for a selected time at each soil depth. This type of probability is representative of the likelihood of failure occurrence at each depth conditioned on the local soil moisture content (time variant) and soil weight (time invariant). At  $t1$  the probability of failure is zero along the entire column and  $\theta$  corresponds to the initial conditions, with the soil water content uniform with depth. At  $t2$  the soil moisture rapidly increases to a depth of 600 mm where the  $PrF_i$  reaches its peak

(0.58). Apart from the soil moisture conditions, the cohesion and the soil weight are also important factors controlling the model estimates. Thus, the probability of failure is generally very low at shallow depths, due to relatively low soil weight. At  $t_3$  the  $PrF_i$  reaches its maximum value (0.65) at a depth of 800 mm where both the contribution of moisture and soil weight are significant. Panels  $d$  and  $e$  show the probability that the failure occurs at a given depth. At each layer, the  $PrPF_i$  depends on the probability that the failure does not occur in the above layers (see definition in section 5.2.2). Consequently, the most probable planes of failure (i.e., where  $PrPF_i$  is high) are located at the medium depth layers where the effects of soil moisture and soil weight are significant, which, in this case, is around 300-500 mm at the time of rainfall peak (dark red area in Figure 5-10d). Deeper layers have lower probability of becoming failure planes, as shown in Figure 5-10d for timesteps  $t_3$  and  $t_4$ . Finally, Figure 5-10d also shows how the high risk of failure occurrence is prolonged in time and the probability gradually decreases at shallower layers and increases at deeper layers, as long as the soil moisture conditions are close to saturation.

Figure 5-11 shows the response to the same rainfall type Q1 of a silty-clay element with a slope value of  $21^\circ$ , gentle relative to the previous case. Note that the hyetograph over this element (Figure 5-11a) is slightly different than that over the previously discussed element, as a result of the spatially distributed precipitation across the basin. The element is located in the downstream flatter part of the basin, with a contributing area of about 2.5 ha. In this case, the initial soil moisture profile (Figure 5-11b) is wetter than the previous case (due to slightly higher convergence of fluxes and lower redistribution to adjacent to the cells) and is not homogeneous with depth, with dryer conditions at shallower layers, due to the evapotranspiration processes. At the rainfall peak the column almost reaches full



saturation. In fact, the combination of gentler topography and medium-high hydraulic conductivity results in faster soil moisture dynamics within the column but slower among the adjacent cells, since the lateral redistribution is slower for gentler slopes.

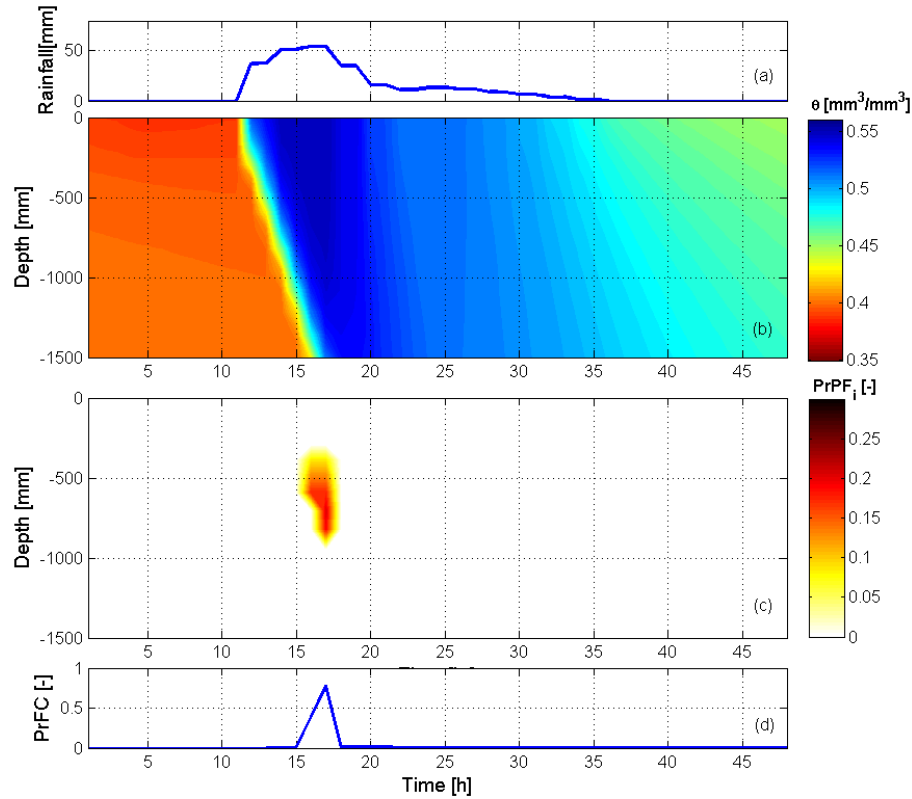


Figure 5-11. Time series model output response of a silty-clay element with gentler slope (21°): rainfall type Q1 (a); volumetric soil moisture content ( $\theta$ ) profile and time series (b); profile and time series of probability of plane of failure at given depth,  $PrPF_i$  (c); time series of the probability of failure of the column,  $PrFC$  (d) (see section 5.2.2)

In terms of probability of failure, the  $PrPF_i$  distribution (Figure 5-11c) depicts a restricted risk of failure limited to depths between 600 and 800 mm and to the peak of the storm. Figure 5-11d shows the probability of failure associated with the entire column

(*PrFC*). This variable takes into account the model assumption that failure may occur anywhere within the soil column, rather than occurring exclusively at an a priori defined depth. Here the maximum value is reached at the peak of the storm and is strictly dependent on the fully saturated conditions.

#### 5.6.2 Effect of rainfall temporal distribution

The basin response to the four different hyetographs described in section 5.5 was analyzed in terms of the probability of landslide occurrence. Variables are dynamically evaluated by the model, which produces a spatial distribution of the most probable areas of failure at each computational time step. The most severe scenario associated with each event is evaluated as the maximum value of the probability of failure anywhere in the column, *PrFC*, recorded at each voronoi cell over the entire run time (e.g., the peak shown in Figure 5-11d). Maps illustrating *PrFC* for each rainfall forcing are shown in Figure 5-12. Across the four maps, the likelihood of failure occurrence is particularly high in the steepest part of the basin (yellow regions). The dark green regions depict the areas where the probability of failure is zero or close to zero, which correspond mostly to the flat areas. In the remaining part of the basin, the probability of failure is the result of the interaction of rainfall type with basin soils and morphology.

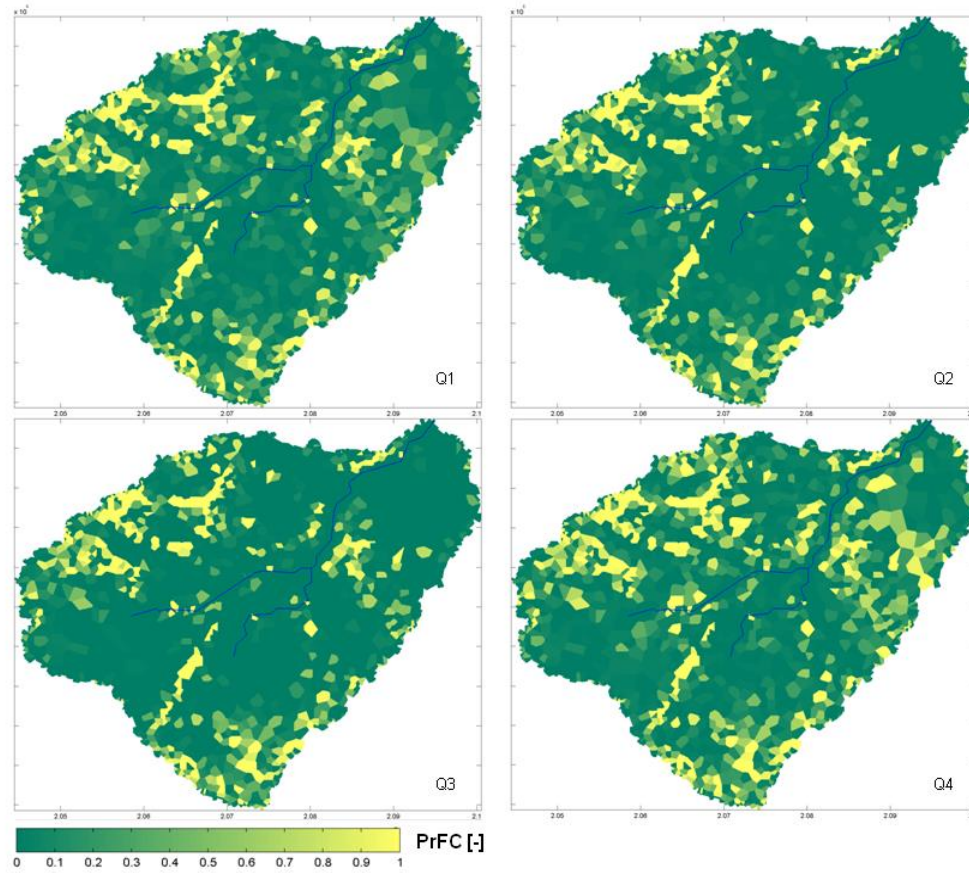


Figure 5-12. Spatial distribution of the maximum values of  $PrFC$  recorded at each pixel across the run time for each rainfall type.

In order to compare the results better, five classes of landslide hazards are defined (in terms of probability of landslide failure) at equal intervals: very low ( $VL$ ), 0-0.2; low ( $L$ ), 0.2-0.4; medium ( $M$ ), 0.4-0.6; high ( $H$ ), 0.6-0.8; very high ( $VH$ ), 0.8-1.0. Differences are then quantified in terms of relative frequency distribution over the basin. Results across the four rainfall events (Figure 5-13a) indicate that events Q2 and Q3 resulted in the safest scenarios, with highest landslide frequency in the  $VL$  class, and lowest in the remaining classes, respectively. Q4 is the rainfall event that provides the most severe landslide hazard, with the highest relative frequency within the  $VH$  landslide probability class and the lowest

within the *VL* class. The response to the Q1 event exhibits an intermediate behavior between Q4 and Q2-Q3, with a frequency distribution similar to Q2 and Q3 within the most hazardous class, and similar to Q4 for *H*, *M*, and *L* landslide probability classes. The *VL* class is slightly less frequent during events Q2 and Q3, yet more frequent for the Q4 event.

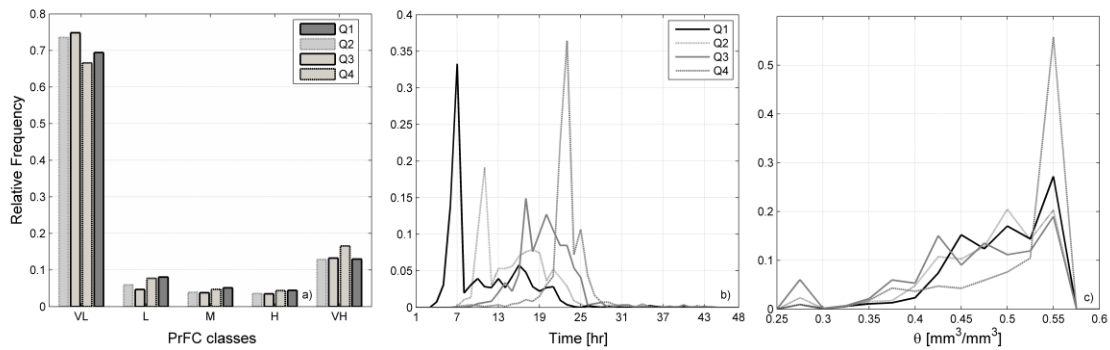


Figure 5-13. Relative frequency distribution across the basin of (a) the *PrFC* occurrence for the 4 rainfall events, (b) the time of occurrence of the maximum value of *PrFC* and (c) 1m depth average soil moisture at time of maximum *PrFC* values.

The analysis discussed above highlights the clear and strong effect of the hyetograph type on the probability of landslide occurrence. This effect depends on the complex interactions between rainfall forcing, topography and soil characteristics, which induce different soil moisture redistribution and, in particular, it depends on the extent to which complete saturation is achieved. In fact, saturation leads to the loss of suction with a significant increase of probability of failure. The Q1 and Q4 events induce saturation in a larger portion of the basin, leading to higher failure probability, although the timing of the

maximum landslide probability is different over the run time. This is depicted in Figure 5-13b which shows the frequency distribution of the time of occurrence of the maximum value of *PrFC*. The peak of the distributions follows the peak of the rainfall intensity for each hyetograph, with 1 hr time lag (i.e., at times corresponding to 7, 11, 17 and 23 hour respectively). Q1 and Q4 exhibit the highest peaks of frequency. Moreover, for the Q1 event, the effects of the rainfall are more prolonged. *PrFC* remains at relatively high levels after 13 hours from the rainfall peak. Q3 is the event that provides the highest probability of failure almost throughout the entire duration of the precipitation event. These results can be particularly interesting in terms of basin risk assessment, since the high probability of failure is significantly different for the four cases, despite the same total precipitation volume over the 24 hr period. The fact that the maximum *PrFC* for Q4 is higher than the one corresponding to the Q1 event, highlights the importance of the moisture conditions prior to the rainfall peak. Although Q1 and Q4 have comparable storm peaks, the response with respect to landslide occurrence does differ because soil moisture conditions at time of the rainfall peak are not the same for the two scenarios.

In order to understand how the rainfall forcing interacts differently with the soil types of the basin, the responses in terms of soil moisture were analyzed in conjunction with the main basin characteristics (i.e. topography and soil types). Figure 5-13c shows the relative frequency distribution of the average (in depth) soil moisture in the root zone (equal to 1 m) reached at time of the maximum value of *PrFC* across the basin. Clearly, the response to the Q4 event exhibited the highest occurrence of failing elements at saturation (here equal to  $0.55 \text{ mm}^3/\text{mm}^3$ ). In order to identify the portion of the basin that experiences the highest differences in terms of probability of failure, the spatial distribution of the

difference in maximum *PrFC* was analyzed between the events Q4 and Q3 (which are the two configurations that differ the most), denoted as  $\Delta Q_4 Q_3$  and evaluated for each single element. The corresponding map is depicted in Figure 5-14 and it reports the differences that exceed a threshold, fixed at 0.05; in several cases, this difference is greater than 0.5 (blue). Because soil moisture redistribution processes are driven by topography (i.e., slope) and hydrological soil properties (i.e., hydraulic conductivity and anisotropy), it may be reasonable to expect that this difference follows somewhat similar patterns to either soil types (Figure 5-14a) or slope distributions (Figure 5-14b). However, the map in Figure 5-14a highlights that  $\Delta Q_4 Q_3$  values greater than the threshold are distributed all over the basin, falling within all soil types, with absence of a clear spatial pattern related to soil characteristics. Instead, Figure 5-14b clearly shows that the spatial distribution of  $\Delta Q_4 Q_3$  values fall within the part of basin characterized by a particular slope range i.e., between 0.20 and 0.45 rad (10° and 25°), which is the only interval shown in the map.

The reason for this behavior is the relative contribution of soil moisture and soil weight to landslide occurrence. Flat areas (saturated or not) are very likely to be stable (or ‘unconditionally stable’, as defined by *Montgomery and Dietrich* [1994]); steep areas, although they may not reach complete saturation, can be characterized by relatively high probability of failure, given the significant component of destabilizing forces due to local steepness (‘unconditionally unstable’ as defined by *Montgomery and Dietrich* [1994]). Therefore, as previously discussed, different rainfall forcings influence mostly areas where both factors, soil moisture and soil weight, primarily control landslide initiation. In this case, those are areas of medium slope (from 10° and 25°).

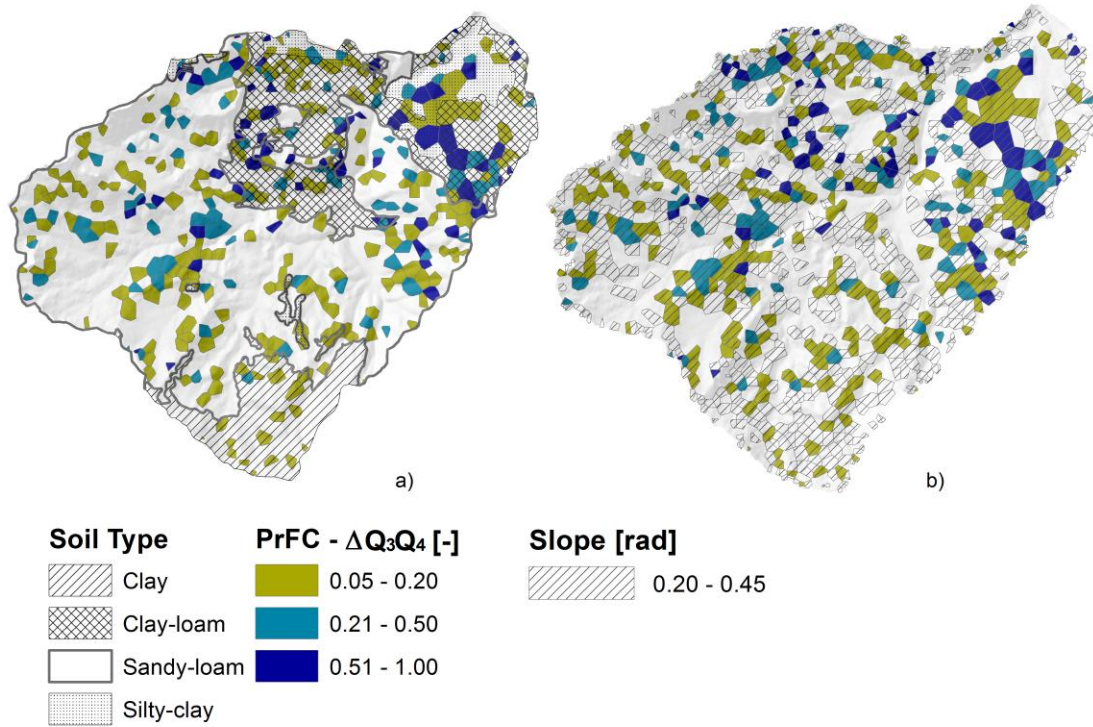


Figure 5-14. Spatial distribution of the difference of maximum *PrFC* between Q4 and Q3 ( $\Delta Q_4 Q_3$ ) overlapped with the maps of soil type (a) and slope range 0.20 and 0.45 rad (10° and 25°) (b).

Figure 5-15 provides a confirmation of these results. Figure 5-15a shows the relationship, for each element, between slope and the max value of *PrFC* for Q1, Q3 and Q4 (Q2 is not discussed, because of its similarity to Q3). Clearly, the *PrFC* increases with slope following a well-defined trend (at given soil moisture and for fixed hydrological parameters, probability of failure only changes with slope, according to equation (5.1)). At a given slope (i.e., within a given Voronoi cell) Q4 results are shifted up with respect to Q1 (blue) and Q3 (red), i.e., corresponding to higher values of maximum *PrFC*. Figure

5-15b shows the distribution of  $\Delta Q_4 Q_3$  values with the slope, separately for each soil type. The variable jumps to high values within the slope range 0.2 – 0.45, except for the clayey soil where differences are not significant, due to the substantially slower soil moisture dynamics (i.e., lower hydraulic conductivity).

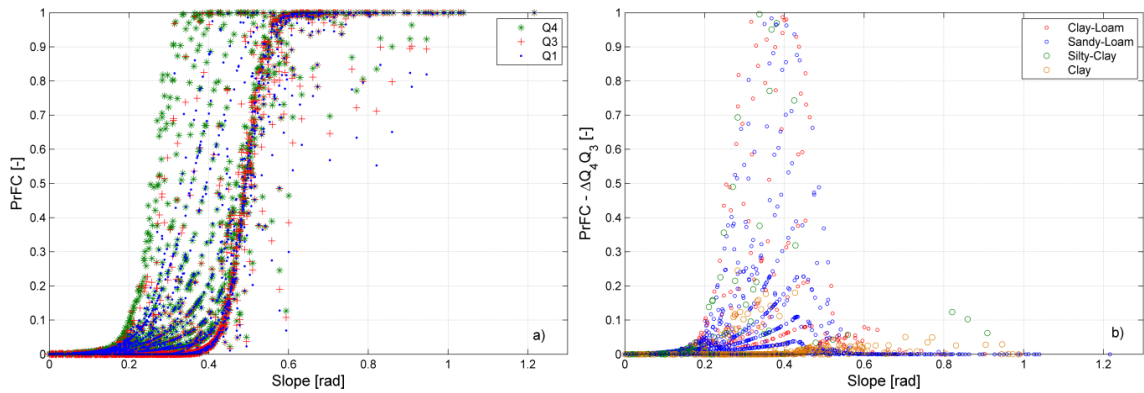


Figure 5-15. Distribution of maximum  $PrFC$  with slope for  $Q_1$ ,  $Q_3$  and  $Q_4$  ( $Q_2$  is omitted because it is similar to  $Q_3$ ). (a); distribution of difference of maximum  $PrFC$  between  $Q_4$  and  $Q_3$  ( $\Delta Q_4 Q_3$ ) with slope (b).

### 5.6.3 Discussion

The results of this study show the capability of the proposed methodology in accounting for uncertainty of soil parameters, and in evaluating how the temporal variability of storms may influence the initiation of shallow landslides in terms of probability of failure. The model considers different definitions of probability of failure, and estimates the likelihood of landslide initiation at multiple soil depths. The most probable depth of failure and the probability of failure of the soil column (generated



anywhere within the column) are the two main representative model outputs. The results demonstrate that, in agreement with typical depths of shallow landslide occurrence, the most probable failure surfaces occurred at depths between 300 and 1000 mm.

The precipitation fields in the case study area are strongly variable both in space and in time. The analysis of the influence of different hyetograph shapes indicates that heavy rainfall concentrated during the latter part of event (as the case of Q4) leads to higher probability of failure across the basin, making Q4 the most critical type of event. This agrees with *Odorico et al.* [2005] who demonstrated that hyetographs with the peak near the end of the storm produce peak pressure heads higher compared to uniform hyetographs, decreasing the return period of rainfall events that trigger landslides. Although events Q1 and Q4 correspond to equal maximum rainfall intensity (55 mm/hr at the selected location reported in Figure 5-7), the Q1 event has the maximum rainfall intensity closer to the beginning of the storm, resulting in a less hazardous scenario. These outcomes depend on how the rainfall distribution affects the hydrological basin response, which is mainly driven by the hydraulic-hydrological soil properties and topography. The spatial analysis of the differences in the maximum *PrFC* between Q3 and Q4 ( $\Delta Q_4 Q_3$ ), clearly demonstrates that the shape of the hyetograph, and in particular the timing of the peak, controls the resulting stability mainly at moderate slopes (from 10° and 25°). As previously discussed, at these slopes, both the soil moisture and soil weight contribute to instability. Events Q2 and Q3, which are characterized by a lower peak rainfall intensity (45 mm hr<sup>-1</sup> for the location shown in Figure 5-7) and a less skewed hyetographs, resulted in larger portions of the basin with lower probability of failure.

In order to evaluate the consistency of the model results, the classified map of probability of failure obtained for Q4 is compared with the map of historical landslide scars (Figure 5-16). The study area is historically characterized by a high frequency of landslide occurrence, with a multitude of landslide events mapped over the years. Landslide scars reported in Figure 5-16 are obtained from *Larsen* [2012], who mapped historical landslide scars at the study site (section 4.5.1). According to *Larsen and Simon* [1993], 61% of the rainfall triggered landslides were likely triggered by the tropical disturbances that struck the central mountain of Puerto Rico between 1960 and 1990. Also, the reported map includes different type of movements, i.e., shallow soil slip, debris avalanche, debris flow, slump). Soil slips are the second most common type of scar after debris flow [*Larsen*, 2012], and both these landslide types are characteristic of high-intensity, short-duration storms. Figure 5-16 reports also some landslide scars identified from more recent satellite images (2006-2014) obtained from Google Earth.

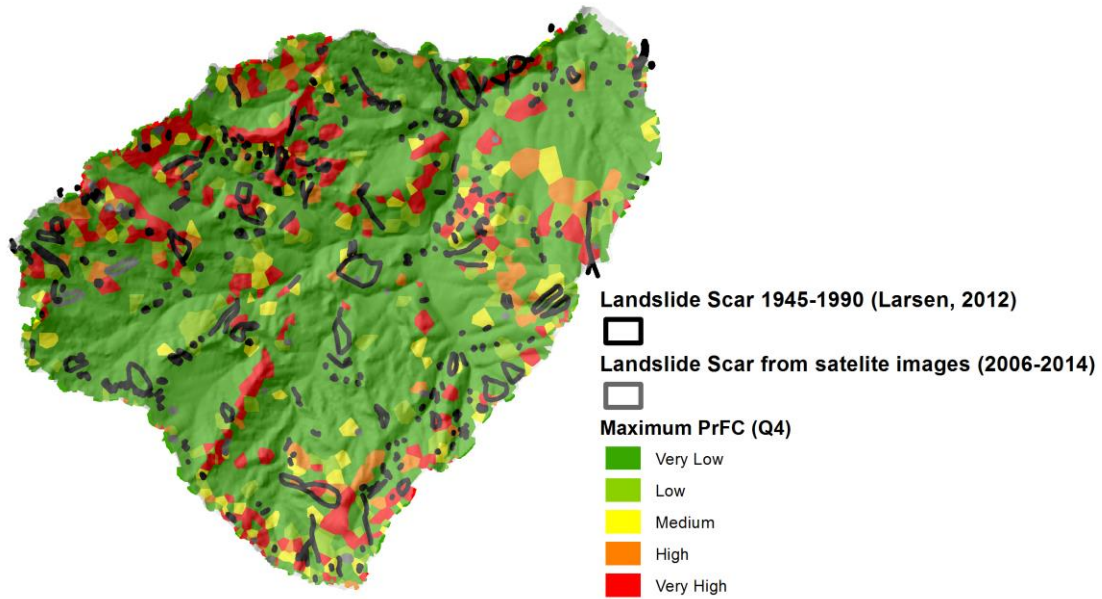


Figure 5-16. Comparison between historical landslide scars caused by intense or prolonged storms during the 20<sup>th</sup> century [Larsen, 2012] and observed through recent satellite images (from Google Earth) with the classified maximum *PrFC* of Q4.

Visual comparison indicates that the areas of high and very high probability of landslide occurrence are consistent with areas of past landslide zones. For instance, the northwest, south, and southeast parts of the basin correspond to areas dense in landslide scars which are adequately reproduced by the model. Other areas classified as probable to fail are not included in the historical record of landslide scars (central north-eastern part of the basin). Part of the southwest strip of the watershed perimeter is mostly classified as stable by the model, while in the past it did experience various failure events.

This comparison cannot be interpreted as model validation, because a rigorous validation of dynamic modelling approaches requires a functional database which records

the locations of failure associated with the exact timing of the failure, the corresponding meteorological data, and the topographical data prior to the failure events, information that is not available at the study site. Moreover, the map reported by *Larsen* [2012] includes various type of landslides (mainly debris flow) that are not of the nature represented in this work. About 43% of historical landslide mapped in the Mameyes basin were associated with road construction and maintenance, anthropogenic disturbance that is not accounted for in this study. Nevertheless, the rough comparison between historical landslides and model results demonstrate the model capability in identifying the most critical landslide areas of the basin.

## **5.7 Summary**

A probabilistic approach for coupled distributed hydrological-hillslope stability models is proposed that accounts for soil parameters uncertainty at basin scale. The geotechnical and soil retention curve parameters are treated as random variables across the basin and theoretical probability distributions of the Factor of Safety (*FS*) are estimated. The derived distributions are used to obtain the spatio-temporal dynamics of probability of failure, in terms of parameters uncertainty, conditioned to soil moisture dynamics. The framework has been implemented in the tRIBS-VEGGIE (Triangulated Irregular Network (TIN)-based Real-time Integrated Basin Simulator-VEGetation Generator for Interactive Evolution)-Landslide model and applied to a basin in the Luquillo Critical Zone Observatory (Puerto Rico) where shallow landslides are common. In particular, the methodology was used to evaluate how the spatial and temporal patterns of precipitation,

whose variability is significant over the basin, affect the distribution of probability of failure, through event scale analyses. Results indicate that hyetographs with heavy precipitation towards the end of the event may lead to the most critical conditions in terms of probability of failure.

## **CHAPTER 6.     Lithological control on the hydro-geomorphic response of tropical watersheds to changing climate**

### **6.1 Introduction**

Climatic extremes and anthropogenic perturbations have influenced soil erosion rates in mountainous landscapes globally. Soil mantled hillslopes are complex systems shaped by bedrock weathering and by different interacting erosional processes (e.g., topsoil erosion and landslide occurrence), which are driven by climatic and non-climatic factors over a range of scales [Bestland *et al.*, 2016; Dykes and Warburton, 2007; Gabet *et al.*, 2015; Kim *et al.*, 2016; Larsen and Montgomery, 2012; Larsen, 2012; Larsen *et al.*, 1999; Stark and Passalacqua, 2014]. Weathering processes lead to depletion of primary minerals increasing the soil's erosional potential, and are influenced by climate through moisture and temperature controls [Dixon and Earls, 2009; White and Brantley, 2003], and by local environmental factors (e.g., by the rate of supply of weatherable minerals) and landscape characteristics [Dietrich *et al.*, 1995; Heimsath *et al.*, 1999; Riebe *et al.*, 2003]. Hillslope erosion is controlled by rainfall-triggered landslides, which constitute an important source of soil and saprolite. The propensity for shallow landslides depends on a multitude of factors including slope morphology and soil and forest properties [De Rose, 2013; Formetta *et al.*, 2016; Hales *et al.*, 2009; Moos *et al.*, 2016; Roering *et al.*, 1999; Simoni *et al.*, 2008], and on the frequency of extreme hydro-meteorological events [Casadei *et al.*, 2003; Chen *et al.*, 2013; von Ruetten *et al.*, 2014]. Clarifying the relative contribution of climatic vs. nonclimatic factors to hillslope erosion and landscape denudation is no trivial task [Cook *et al.*, 2015; Riebe *et al.*, 2003]. Understanding the associated interrelations in

the complex structure of the critical zone at diverse landscapes [Anderson *et al.*, 2007; Brantley *et al.*, 2007] remains a challenge.

The Luquillo Mountains (Luquillo Critical Zone Observatory (CZO)) are of particular hydro-geomorphological interest because they are characterized by different bedrock and diverse landscape morphologies. For this reason, several studies have focused on landscape processes at the Luquillo CZO [Brocard *et al.*, 2015; Brown *et al.*, 1995; Buss and White, 2012; Chabaux *et al.*, 2013; Dosseto *et al.*, 2012; Dosseto *et al.*, 2014; Larsen, 2012; Larsen *et al.*, 1999; Lebedeva and Brantley, 2013; Lepore *et al.*, 2013; Murphy *et al.*, 2012; Pike *et al.*, 2010; Riebe *et al.*, 2003; Stallard, 2012]. An episode of tectonic uplift that occurred a million years ago in Puerto Rico, followed by gradual erosion, have shaped the Luquillo Mountains into morphologically different domains [Brocard *et al.*, 2015]. Knick points in the Luquillo CZO have segmented longitudinal river profiles, which deviate from smooth concave-upward profiles [Pike *et al.*, 2010]. Erosion rates at diverse watersheds in the Luquillo CZO depend on local geomorphological and lithological characteristics [Murphy and Stallard, 2012]. This study focuses on the Mameyes and Icacos watersheds, which are characterized by similar climatic conditions and by contrasting lithology (chapter 4). The Mameyes watershed is underlain by volcanoclastic rock, and the Icacos watershed is underlain by the Rio Blanco quartz diorite [Buss and White, 2012]. Shallow landslide initiation constitutes the main erosion mechanism at the two watersheds [Larsen, 2012]. This site provides the opportunity to assess the role of contrasting bedrock and diverse landscape morphology on hillslope erosion rates under similar climatology [Dosseto *et al.*, 2012].

The Icacos watershed is one of the very first sites where detrital  $^{10}\text{Be}$  methods have been used to estimate erosion rates [Brown *et al.*, 1995; Brown *et al.*, 1998]. These studies relate production rates of cosmogenic nuclides in quartz grains with landscape denudation rates. While the use of cosmogenic nuclides has provided important insights on denudation rates at the Luquillo CZO landscape [Brocard *et al.*, 2015; Riebe *et al.*, 2003], this approach may have potential limitations [Carretier *et al.*, 2015], which depend on the spatial and temporal scales of analysis. Because cosmogenic nuclides are used to estimate total denudation rates, the use of  $^{10}\text{Be}$  may not quantify the relative contributions of saprolite lowering and topsoil erosion on landscape denudation [Riebe *et al.*, 2003]. This method may consider steady-state soil thickness [Brown *et al.*, 1995], an assumption likely not representative of the present state of the Luquillo CZO landscape (section 4.6). Also, providing short-term estimates of erosional potential using  $^{10}\text{Be}$  can be challenging, because cosmogenic rates are typically averaged over tens of thousands of years, and may not capture fluctuations in the magnitude of erosion rates at relatively fine time scales [Brocard *et al.*, 2015; Kirchner *et al.*, 2001].

Landscape denudation modelling [Lebedeva and Brantley, 2013; Lebedeva *et al.*, 2010] can be used to clarify the relative influence of climatic and nonclimatic factors on the current and future states of the Luquillo CZO landscape. Process-based models [Arnone, 2011; Bovy *et al.*, 2016; Burton and Bathurst, 1998; Casadei *et al.*, 2003; Dietrich *et al.*, 1995; Francipane *et al.*, 2012; Kim *et al.*, 2013; Lepore *et al.*, 2013; Simoni *et al.*, 2008; Tucker *et al.*, 2001a] have the potential to quantify physical mechanisms controlling landscape dynamics at different spatio-temporal resolutions. This work uses a high resolution coupled hydro-geomorphic model and observations on hillslope erosion and



bedrock weathering in the Mameyes and Icacos watersheds to characterize the current and future hydro-geomorphic behaviors of diverse landscapes in the Luquillo CZO. Landslide occurrence and topsoil erosion are simulated in morphologically different watersheds in response to changing climate. This study quantifies soil thickness dynamics based on the relative contribution of hillslope erosion (landslides and topsoil erosion) and saprolite deepening. Hydro-meteorological forcings corresponding to a range of climatic projections are used to investigate whether the equilibrium conditions characterizing the Luquillo CZO landscapes are likely to remain relatively invariant with future climatic perturbations. This chapter is a verbatim recompilation of *Dialynas and Bras* [2017], and *Dialynas and Bras* [2016].

## **6.2 Materials and methods**

### **6.2.1 Study area**

This study uses the physically-based hydro-geomorphic model described in sections 2.2.2 and 4.2. The model was applied in the Mameyes and Icacos watersheds, discussed in section 4.3. The 17.8 km<sup>2</sup> Mameyes watershed is underlain by Cretaceous, marine-deposited, quartz-poor volcanoclastic rocks, while the 3.26 km<sup>2</sup> Icacos watershed is underlain by Upper Cretaceous and Tertiary granitic rocks [*Murphy et al.*, 2012]. The Icacos watershed is primarily underlain by Rio Blanco quartz diorite, which intruded the surrounding volcanoclastic rock about 49 to 42 Ma [*Smith et al.*, 1998]. The unweathered parent material is located 16 m deep [*Dosseto et al.*, 2012].

The contrasting lithology in the study site influences the diverse landscape morphologies and sediment properties at the two tropical watersheds [Murphy *et al.*, 2012]. Relatively steeper slopes characterize the Mameyes watershed (mean slope of 21°) compared to the Icacos watershed (mean slope of 13°) [Larsen, 1997]. Rainfall-triggered landslides are the primary hillslope erosion component at the two watersheds, i.e., 93 % and 98 % of the total hillslope erosion at the Mameyes and Icacos watersheds, respectively [Larsen, 2012]. The influence of geology on channel morphology is evident in the bed material and sediment size [Murphy *et al.*, 2012]. Sandy beds and floodplains characterize the stream network in the Icacos watershed. The fine sediment bed (median grain size ( $D_{50}$ ) is 0.6 mm) is mobilized by moderate runoff [Larsen, 1997]. The bed material in the Mameyes watershed is significantly coarser ( $D_{50}$  equal to 70 mm). The channels are characterized by little or no floodplains, and they are lined with boulders and cobbles [Murphy *et al.*, 2012].

As discussed in section 4.4.3, a 30 m mesh was used to represent the topography of the Icacos watershed (Figure 4-2a), and a 50 m mesh was used for the 17.8 km<sup>2</sup> Mameyes watershed (Figure 4-1a). The soils of the two watersheds were classified into four soil types based on the U.S.D.A. [1951] classification system (Figures 4-1b and 4-2b). The vegetation cover of Icacos and Mameyes watersheds is given in Figures 4-1c and 4-2c, respectively [Helmer *et al.*, 2002; PRGAP, 2006]. Calibration of tRIBS for the Icacos and Mameyes watersheds was conducted in section 4.4.5, by comparing simulated river discharge with daily records. The geomorphic model was calibrated by reproducing events and total sediment yield at the Icacos and Mameyes watersheds (see section 4.4.6).

### 6.2.2 Climatic scenarios and projected change

This study uses daily projections (2016-2099) of climatic variables (precipitation, temperature, cloud cover, sea level pressure, wind speed, and vapor pressure) for the study site, based on the B1 and A2 IPCC (Intergovernmental Panel on Climate Change) SRES (Special Report on Emission Scenarios [2000]) climatic scenarios, corresponding to the Canadian General Circulation Model (CGCM3.1(T47); Canadian Centre for Climate Modelling and Analysis). The B1 and A2 scenarios are the two of the three scenarios that have been the focus of model intercomparison studies, and predict the lowest and highest global temperature increases by 2099, respectively [IPCC, 2007]. The selection criteria for the climatic projections were:

- a) the relatively good performance of the CGCM3.1 in reproducing the precipitation seasonality and the sea surface temperature at the Central Caribbean compared to other General Circulation Models (GCM), as demonstrated in *Ryu and Hayhoe* [2013], and
- b) the completeness of selected climatic scenarios: in contrast to other GCM projections, the selected records for the B1 and A2 scenarios are continuous at the daily scale for the entire period under study (2016-2099).

This work uses precipitation and temperature projections (CGCM3.1) which have been downscaled for the Luquillo CZO area [Hayhoe, 2013; Ryu and Hayhoe, 2013] based on the statistical downscaling method recently proposed by *Stoner et al.* [2013]. The method (asynchronous regional regression model (ARRM)) uses piece-wise regression to correct for bias in low resolution hydro-climatic predictions. Downscaled climate projections indicate a significant future increase in temperature coupled with decrease in

precipitation at the study site. More precisely, the precipitation decline at the Luquillo CZO is projected (when compared to the 2090-2099 average) to be 23% and 31%, for B1 and A2 scenarios, respectively. These trends are consistent with the findings of *Campbell et al.* [2011], with *Hayhoe* [2013] who compared several climatic predictions, and with the analysis of *IPCC* [2007] which included results from 21 global models.

Temperature in the entire Caribbean is projected to increase by 2099 at rates that by far exceed natural variability [*Campbell et al.*, 2011]. Puerto Rico may warm more rapidly compared to the global average, with increases in both average and extreme temperatures [*Hayhoe*, 2013]. Different atmospheric and oceanic drivers likely contribute to a future precipitation decline in Puerto Rico [*Hayhoe*, 2013]. Annual rainfall in the Caribbean is projected to increase north of 22 °N, and significantly decrease (around 25-50%) south of 22 °N, with decline in precipitation intensity and more dry days in the southern Caribbean [*Campbell et al.*, 2011]. The projected pattern exacerbates during the dry season (December to April). This gradient is linked to tropical circulations (Hadley circulation of the North tropical Atlantic), and is characteristic of the dry season for warm phases of the El Niño–Southern Oscillation (ENSO) [*Campbell et al.*, 2011; *Stephenson et al.*, 2007]. Climatic projections suggest that observed circulation patterns in the Caribbean are expected to strengthen by 2099 [*IPCC*, 2007]. Also, a substantial drying of the wet season (May to November) is projected for the central Caribbean [*Hayhoe*, 2013]; precipitation is expected to decline, with more frequent dry days.

## 6.3 Results

### 6.3.1 Projected rates of hillslope erosion and deposition

The simulated topsoil erosion and landslide occurrence for the two climatic scenarios (2016-2099) are illustrated in Figures 6-1 and 6-2 for the Icacos and Mameyes watersheds, respectively. The two landscapes are characterized by substantial topsoil erosion rates and slope instability. Hydrologically-induced erosion and landslide occurrence lead to the accumulation of eroded soil and saprolite in colluvial deposits and in alluvial sediments at lower valleys. Soil redistribution alters local topographic gradients and the stream configuration in the two watersheds. The simulated total hillslope erosion rates are given in Table 6.1. Erosion rates at the two watersheds are lower for the A2 scenario, which is characterized by greater reduction in precipitation (section 6.2.2). The simulated erosion rates for the Icacos watershed are consistent with the erosion rates *Larsen* [2012] derived from multiple observations. The projected erosion rate for the Mameyes watershed is at the lower end of the erosion spectrum reported in *Larsen* [2012] (Table 6.1).

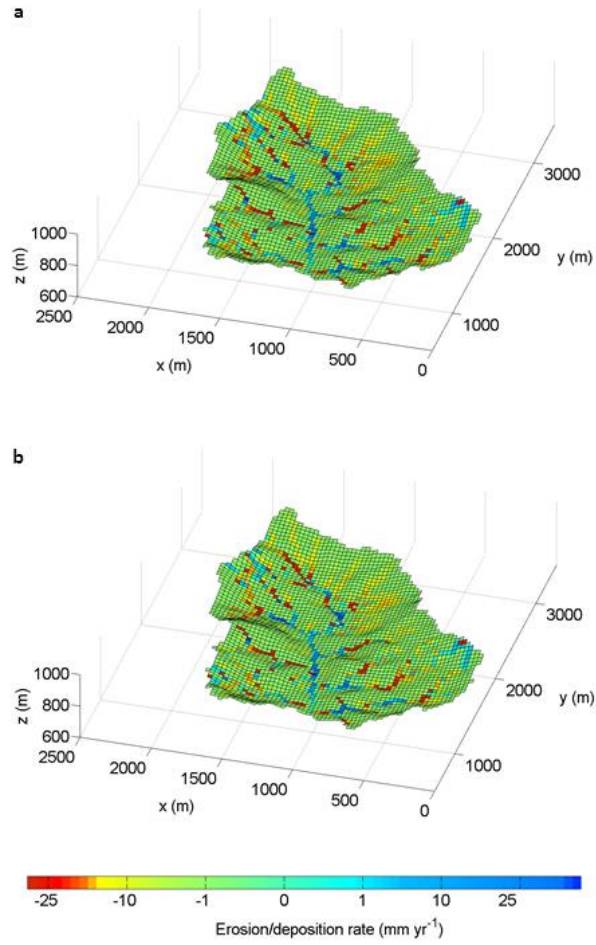


Figure 6-1. Spatially explicit representation of hillslope erosion and deposition in the Icacos watershed for climatic scenarios B1 (a) and A2 (b). Eroding slopes (yellow to red), landslide locations (red) and depositional sites (blue) are illustrated across the watershed.

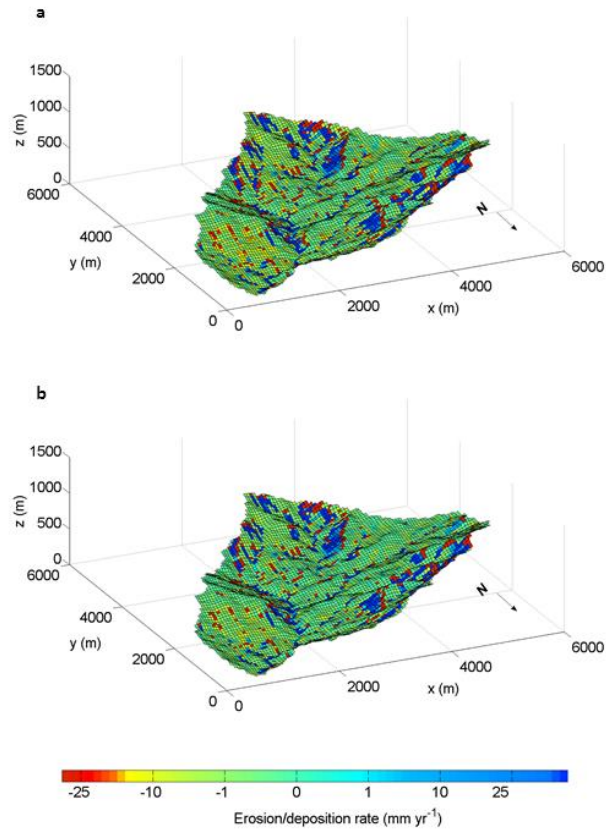


Figure 6-2. Hillslope erosion and deposition across the Mameyes watershed in response to climatic projections B1 (a) and A2 (b). Eroding sites (yellow to red) and landslide locations (red) are illustrated, in addition to depositional sites (blue) in valleys and lower slopes.

Table 6.1. Comparison of simulated rates of hillslope erosion with reported erosion rates in the Mameyes and Icacos watersheds. Simulations correspond B1 and A2 scenarios of climatic projections (section 6.2.2).

Erosion rate (mm kyr <sup>-1</sup> )	Scenario B1	Scenario A2	Chapter 4	<i>Larsen</i> [2012]	<i>Brown et al.</i> [1995], <i>Brocard</i> <i>et al.</i> [2015]
Icacos watershed	887	815	1,123	750	43 - 100
Mameyes watershed	738	703	937	523 - 2,143	

### 6.3.2 Simulated slope instability

According to results, landslides mainly occur at the relative steep slopes of the southern, south-western and north-western Icacos watershed. At the Mameyes watershed, there is significant landslide occurrence at the southern and north-western parts of the watershed, and at the northern slopes in the vicinity of the main stream. The total simulated landslide area is greater for the B1 scenario in both watersheds (Table 6.2). The landslide area is compared with *Larsen* [1997], who documented a total of 345 landslides in the two watersheds from aerial photographs (section 4.5.1). Table 6.2 presents area estimates of landslide scars, as approximately dated by *Larsen* [2012]. This includes area estimates of relatively recent scars, and total landslide area, which includes larger scars that occurred during the last 1,000 years. The landslide area estimates reported in *Larsen* [2012] correspond to different climatic conditions, yet they encompass the simulated landslide area for the two climate scenarios in the Mameyes and Icacos watersheds (see section 6.4.1).

Table 6.2. Observed and simulated (B1 and A2 scenarios) landslide area at the two watersheds. Observations [*Larsen*, 1997; *Larsen*, 2012] correspond to relatively recent scars, and to total observed scars which include landslides dated up to 1,000 years.

Landslide area ( $10^3 \text{ m}^2$ )	Scenario B1	Scenario A2	Recent landslide scars	Total observed landslide scars
Mameyes watershed	680.0	665.0	70.6	1,101.6
Icacos watershed	98.1	93.6	42.0	194.0



This work assesses the extent to which the coupled physically-based model reproduces the natural spatial variation of landslide magnitude. The capability of the hydro-geomorphic model to simulate the propensity for relatively larger and smaller landslides at the Mameyes and Icacos watersheds is examined. More specifically, the frequency distributions of landslide area for B1 scenario were estimated at the two watersheds (Figure 6-3). Different studies focusing on diverse regions [Guzzetti *et al.*, 2002; Pelletier *et al.*, 1997; Stark and Hovius, 2001] have demonstrated that landslides naturally exhibit a fractal (or scale invariant) character. More precisely, the landslide area frequency distribution tends to follow a power law [Hergarten and Neugebauer, 1998]:

$$\log N = a - bA \quad (6.1)$$

where  $N$  is the number of landslides in the set with areas greater than  $A$ , and  $a$  and  $b$  are parameters. Power type distributions are called scale-invariant because they are not restricted by characteristic scales describing different phenomena. More precisely, the number of landslides of area  $A$  or greater differs from the number of events of area  $\lambda A$  or greater by  $\lambda^{-b}$ , where  $\lambda$  is an arbitrary factor [Hergarten, 2002]. Results suggest that the projected landslide occurrence at the Mameyes and Icacos watersheds over the simulation period can be roughly approximated by scale-invariant distributions (Figure 6-3). The associated  $b$  exponents are equal to 1.3 and 2.2 for Icacos and Mameyes watersheds, respectively (see section 6.4.1). The range of  $b$  values reported in Hergarten [2003] (0.7 - 2.3), which is based on several landslide mapping studies, encompasses the  $b$  values estimated here.

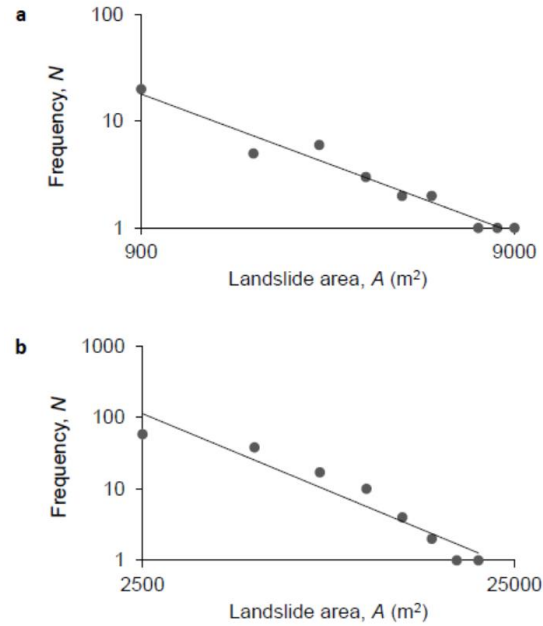


Figure 6-3. Landslide area distributions for Icacos (a) and Mameyes (b) watersheds. Fitted power-type distributions corresponding to exponents  $b$  (equation (6.1)) equal to 1.3 for Icacos and 2.2 for Mameyes watersheds, respectively

## 6.4 Discussion

### 6.4.1 Propensity for landslide occurrence

The simulated landslide locations for B1 and A2 scenarios were compared with observed scars [Larsen, 1997; Larsen, 2012] in the study sites (Figures 6-4 and 6-5 for Icacos and Mameyes watersheds, respectively). While landslides that occurred in the past 1,000 years [Larsen, 2012] have led to partial diffusion of topographic gradients, the two landscapes are characterized by several landslide-prone slopes. The two tropical watersheds are dominated both by shallow soil-slips, slumps, debris-flow, and by relatively larger landslides, and are characterized by slopes that are only conditionally stable (i.e., the

stability of which depends on soil moisture fluctuations) [Arnone *et al.*, 2011]. The simulated unstable slopes and landslide deposition paths are consistent with observations in the Mameyes watershed (Figure 6-5). Projected landslide run-out distances are in agreement with observed landslide paths at the northern, southern, and northwestern parts of the watershed. Large landslides simulated at the south-eastern Icacos watershed (Figure 6-4) are collocated with past landslide scars. Simulated landslides at the relatively steep slopes of the western Icacos watershed are in reasonable agreement with observations.

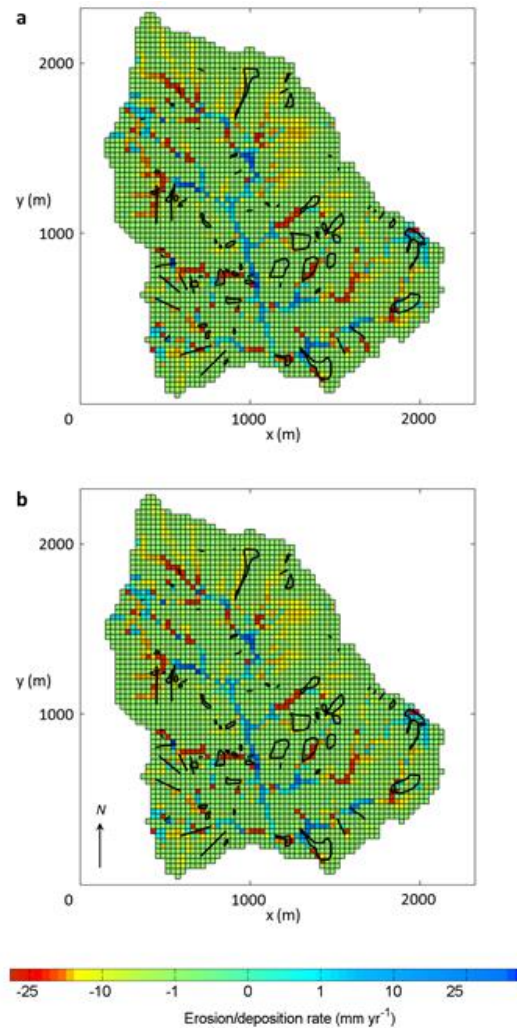


Figure 6-4. Comparison of observed landslide scars with predicted landslides (red) at the Icacos watershed for climatic scenarios B1 (a) and A2 (b).

The predicted climate change at the study site is depicted in a range of hydro-climatic scenarios in the Luquillo CZO (section 6.2.2). Despite the projected decrease in the mean precipitation, the simulated landslide frequency is significant, and is comparable to past landslide activity. This is attributed to the key role of lateral soil moisture redistribution at the steep slopes of the two tropical watersheds [Schellekens *et al.*, 2004], and to the

nonlinear threshold behavior of shallow landslides [Frattini *et al.*, 2009; Huggel *et al.*, 2012]. The initiation of mass movement heavily depends on the rate of water infiltration and on capillary forces in unsaturated soils, processes that are related non-linearly with the rate of moisture influx, and depend on topography and on soil mechanical and hydrological properties [Brooks and Corey, 1964; Iverson, 2000]. The lateral redistribution of soil moisture in the vadose and saturated zones during interstorm periods exerts a strong control on landslide initiation [Formetta *et al.*, 2016; Simoni *et al.*, 2008]. Lateral moisture flux after tropical storms leads to increase in the degree of saturation at conditionally stable slopes, inducing exceedance of the slope stability threshold and subsequent slope failure [Lepore *et al.*, 2013]. Results suggest that the role of this landslide-triggering factor remains important during the relatively drier 21<sup>st</sup> century. The combined effects of water infiltration during tropical storms and moisture increase at interstorm periods lead to significant landslide occurrence in the two watersheds by 2099. Also, the total simulated landslide area for each watershed did not substantially vary for different GCM scenarios (Table 6.2). While the exact timing of landslide initiation at the study site depends on storm hyetograph characteristics and land surface descriptors (chapter 5), the cumulative frequency and magnitude of landslide occurrence in the 21<sup>st</sup> century exhibited small variation over the range of imposed hydro-meteorological forcings. This analysis suggests that the time-integrated slope instability projected by 2099 is also controlled by non-climatic factors, including local soil characteristics, forest cover, and by the steep geomorphic gradients of the Luquillo Mountains.

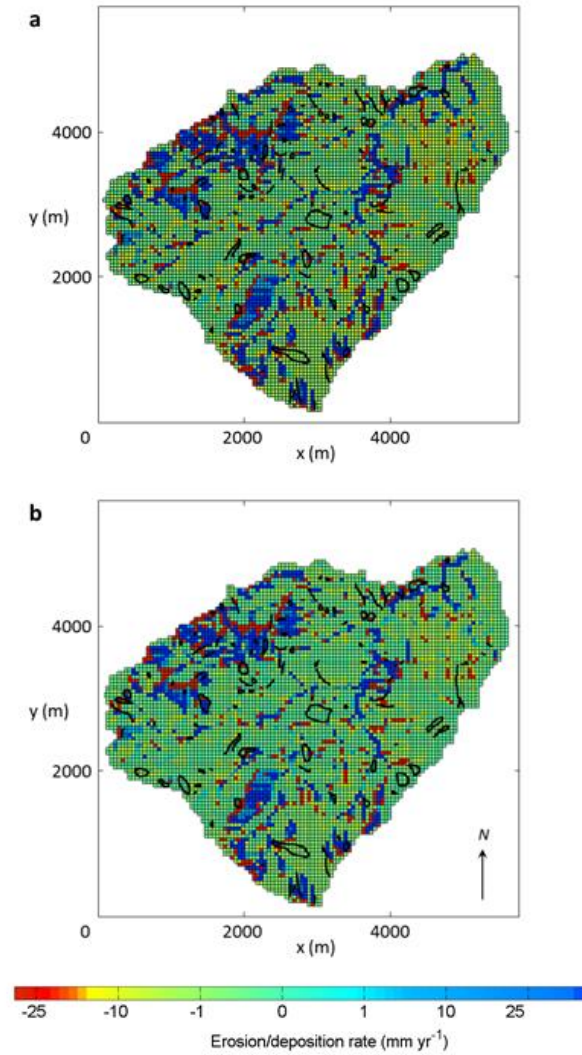


Figure 6-5. Comparison of landslide scars with predicted landslides (red) at the Mameyes watershed corresponding to climatic scenarios B1 (a) and A2 (b).

Despite simplifying assumptions invoked in the landslide failure criterion [Bellugi *et al.*, 2015], the simulated landslide occurrence at the two watersheds can be roughly represented by power type distributions (see section 6.3.2), which are often used to describe critical phenomena [Hergarten, 2003]. The fractal behavior of landslide occurrence is characteristic of the concept of self-organized criticality (SOC) in natural systems,

according to which the system exhibits self organization towards critical states [*Bak et al.*, 1987]. SOC has a meaningful role in the evolution of landslide dominated landscapes [*Hergarten and Neugebauer*, 1998], such as the Luquillo Mountains. It is possible that the combined effects of the island's tectonic uplift and dissipative erosional processes may lead to quasi-stationary states, characteristic of the SOC concept. In this case, the timing and magnitude of hillslope erosional events may occur such that the system moves towards critical states. SOC models [*Hergarten and Neugebauer*, 1998] can be applied to predict locations and timing of slope instability, and potentially improve landslide hazard assessment. However, records of system outputs (e.g., sediment yield) over significantly longer time scales are required to verify that the evolution of the two tropical landscapes in fact follows SOC [*Sapozhnikov and Fouloula-Georgiou*, 1996].

The relative frequency of predicted landslide magnitudes differs significantly between the two watersheds. Larger values of the exponent  $b$  (equation (6.1)) indicate that smaller landslides are more frequent compared to large landslide events. On the contrary, lower values of  $b$  correspond to natural systems characterized by lower relative occurrence of small landslides. According to the simulated frequency of landslide magnitudes,  $b$  is lower for the Icacos ( $b = 1.3$ ) than the Mameyes watershed ( $b = 2.2$ ). Simulations and observations in the Icacos watershed indicate several large landslides. As illustrated in Figure 6-4, large slides occur at the steep slopes of the Icacos watershed, depositing soil and saprolite in the vicinity of the stream network. In the Mameyes watershed, landslides of smaller magnitude are more frequent. The occurrence of multiple intermediate and small landslides across the Mameyes watershed is demonstrated in Figure 6-5. The relative response of the modelled watersheds in terms of landslide occurrence is in agreement with

previous studies [Larsen, 1997; Larsen, 2012] which report a mean area of recent scars equal to 600 m<sup>2</sup> and 400 m<sup>2</sup> for Icacos and Mameyes watersheds, respectively. The magnitude of landslides heavily depends on soils mechanical properties (e.g., cohesion and friction angle) and on local slope morphology. The contrasting lithology at the study area significantly influences the landscape formation and pedogenesis in the two diverse watersheds [Buss and White, 2012; Dosseto *et al.*, 2012]. The weathered soil and saprolite from the quartz diorite underlying the Icacos watershed can be more susceptible to landslide occurrence, compared to the volcanoclastic landscape [Stallard, 2012], leading to frequent occurrence of larger landslides. In contrast, according to the observed scars given in Figure 6-5, the Mameyes watershed is characterized by higher occurrence of small slumps and shallow soil slips. This behavior is consistent with the simulated distributions of landslide magnitudes (Figure 6-3).

#### 6.4.2 Landscape equilibrium in changing climate

The projected decline in precipitation at the Luquillo Mountains could have important impact on hydrologically-induced topsoil erosion and rainfall-triggered landslide occurrence. Rainsplash erosion and topsoil entrainment are likely reduced with the projected decline in surface water flow. The projected rates of total hillslope erosion are lower compared to the ones reported in chapter 4 (Table 6.1). Simulated erosion rates for the two watersheds are lower for the A2 scenario, which is characterized by greater precipitation decline and temperature increase (see section 6.2.2). The simulated erosional potential did not exhibit substantial differences between the climate change scenarios. The



significant topsoil erosion at the steep slopes of the Mameyes and Icacos watersheds is linked with dynamic feedbacks to shallow landslides. Sediment mass movement across the landscape is quantified by the coupled model, effectively altering slope morphology as erosion and deposition proceed. The dynamic response of the landscape feeds back to the erosional potential of diverse hillslopes. The interacting physical mechanisms (e.g., landslides, sheet erosion, and raindrop impact detachment) that drive hillslope erosion and deposition constitute key processes in the evolution of the contrasting landscapes under study. Understanding the relative contribution of different erosional processes and associated feedback loops is crucial in attempts to quantify erosion rates in response to a range of hydro-climatic perturbations.

According to this analysis, topsoil erosion and shallow landslides control the dynamics of soil thickness at different topographic locations. Rainfall-triggered landslides constitute instantaneous events of disproportionally large magnitude compared to rainsplash and overland flow erosion (chapter 4). Substantial part of the soil profile is excavated in landslide sites and is mainly deposited locally, across the landslide deposition path (Figures 6-1 and 6-2). Hillslope erosion in response to different hydro-climatic scenarios drives the redistribution of upland soil and saprolite across the landscape, and exerts a strong control on the spatial variation of soil thickness. The significant rates of simulated divergent soil transport exceed the magnitude of local regolith production at the hillslopes of the two watersheds, leading to gradual exposure of deeper soil horizons and of emerging bedrock. The soil thickness at the Icacos and Mameyes watersheds likely increases at lower slopes and valleys characterized by substantial rates of colluvial and alluvial sediment deposition. The net effect of lower erosion rates and bedrock weathering

at relatively flat ridges may lead to quasi-stationary states of soil thickness equilibrium. Moreover, if the dynamics of soil thickness influence the rate of saprolite deepening [Dietrich *et al.*, 1995; Heimsath *et al.*, 1997], then the spatio-temporal variation of topsoil erosion and landslide occurrence at the two diverse landscapes subsequently affects the rates of regolith production at different catena positions. Results suggest that the assumption of steady-state soil thickness invoked in previous studies [Brown *et al.*, 1995; Riebe *et al.*, 2003; Stallard, 2012] may not be entirely valid across different landscape positions in the Luquillo CZO.

This work assesses the influence of simulated erosion rates on the landscape equilibrium of the two diverse watersheds. Comparison of total hillslope erosion with reported weathering rates at the two contrasting landscapes is given in Table 6.3. A relatively high weathering rate of  $335 \text{ mm kyr}^{-1}$  was estimated in the Uranium-series isotopes based study of Dosseto *et al.* [2012] for the volcanoclastic landscape. This weathering rate is in the same order of magnitude of the erosion rates simulated over a range of climate projections. This suggests that the landscape underlain by volcanoclastic rock may potentially reach a state close to dynamic equilibrium. In contrast, erosion rates in the granitic landscape are significantly higher than the quartz diorite weathering rate ( $45 \text{ mm kyr}^{-1}$ ) reported in Chabaux *et al.* [2013] (Table 6.3). Relatively high rates of erosion in the Icacos watershed over the last decades are also reported in recent studies [McDowell and Asbury, 1994; Shanley *et al.*, 2011; Stallard, 2012; Stallard and Murphy, 2012]. Comparison of hillslope erosion with bedrock weathering rates suggests that the granitic landscape may be characterized by significant denudation rates. Simulations suggest that the present states of landscape equilibrium in the Mameyes and Icacos watersheds (section

4.6), are expected to remain relatively invariant by 2099. These results are in contrast to *Brown et al.* [1995] and *Brocard et al.* [2015], who estimated significantly lower denudation rates at the Icacos watershed (Table 6.1). These studies apply methods that use cosmogenic  $^{10}\text{Be}$  for the estimation of total erosion rates. However, cosmogenic estimates of watershed-averaged denudation rates in sites that include deep landslides, such as the Rio Icacos watershed, can be significantly biased [*Riebe et al.*, 2003]. Moreover, the episodic character of hillslope erosion may not be reflected by cosmogenic rates averaged over relatively large (e.g.,  $10^4$ - $10^7$  yr) time scales [*Kirchner et al.*, 2001]. This may potentially explain the fact that  $^{10}\text{Be}$  methods [*Brocard et al.*, 2015; *Brown et al.*, 1995] do not capture the recently observed [*McDowell and Asbury*, 1994; *Shanley et al.*, 2011; *Stallard*, 2012; *Stallard and Murphy*, 2012] increase in erosion rates at the Icacos watershed.

Table 6.3. Comparison of projected hillslope erosion rates (B1 and A2 climatic scenarios) with recently reported bedrock weathering rates (values are given in  $\text{mm kyr}^{-1}$ ).

Watershed	Erosion rate (scenario B1)	Erosion rate (scenario A2)	Bedrock weathering rate
Icacos (quartz diorite)	887	815	45*
Mameyes (volcaniclastic)	738	703	335**

\**Chabaux et al.* [2013]

\*\**Dosseto et al.* [2012]

## 6.5 Summary

The potentially important influence of climate change on landscape evolution and on the critical zone is not sufficiently understood. Quantifying the relative contribution of different hydro-climatic factors on the rates of hillslope erosion and soil accumulation across the complex morphology of a watershed remains a challenge. This study quantifies topsoil erosion and landslide occurrence in response to a range of climatic projections in the Luquillo Critical Zone Observatory, a site of particular geomorphological interest. The adjacent Mameyes and Icacos watersheds are studied, which are underlain by contrasting lithologies. A high resolution coupled hydro-geomorphic model based on tRIBS (Triangulated Irregular Network-based Real-time Integrated Basin Simulator) is used. Observations of landslide activity and hillslope erosion are used to evaluate the model performance. The process-based model quantifies feedbacks among different hydrologic processes, landslide occurrence, and topsoil erosion and deposition. Simulations suggest that the propensity of landslide occurrence in the Luquillo Mountains is controlled by tropical storms, soil moisture redistribution, and by non-climatic factors, and is expected to remain significant through 2099. The Icacos watershed, which is underlain by quartz diorite, is dominated by relatively large landslides. The relative frequency of smaller landslides is higher at the Mameyes watershed, which is underlain by volcaniclastic rock. According to the results, the projected precipitation decrease at the study site may lead to moderate decline in erosion rates. Yet the simulated erosional potential of the two diverse landscapes likely remains at significant levels. Comparison of projected erosion rates with recent bedrock weathering estimates indicates substantial denudation rates in the granitic landscape. The volcaniclastic landscape is likely characterized by a state of dynamic

equilibrium. Results suggest that the equilibrium conditions in the two contrasting landscapes may remain reasonably invariant with climate change.

## **CHAPTER 7. Thesis summary and future research**

### **7.1 Hydrologically-induced erosion of soil organic carbon in diverse tropical montane and temperate forest ecosystems**

The hydrologically driven soil erosion and SOC redistribution were studied at the diverse ecosystems of the Calhoun CZO and the Luquillo CZO. The Holcombe's Branch watershed in the Calhoun CZO was studied, located in the southern Piedmont of USA. This temperate forest ecosystem has experienced some of the most serious agricultural erosion in the USA [Trimble, 1974], starting about 1800 with cultivation of cotton and other crops, and continuing to the early 20<sup>th</sup> century [Richter and Markewitz, 2001]. The environmental history of the Calhoun CZO is characterized by rapid reforestation of eroded agricultural soils (chapter 3). Located in the northeastern Puerto Rico, the Luquillo CZO is a tropical montane forest ecosystem characterized by steep geomorphic gradients and by different lithological characteristics (section 4.3). This work focused on the adjacent watersheds of Rio Mameyes and Icacos, which are characterized by comparable climatic conditions and by contrasting underlying lithologies. The Mameyes watershed is primarily underlain by volcaniclastic rock, and the Icacos watershed is underlain by quartz diorite [Murphy *et al.*, 2012]. The different geological characteristics have also influenced landscape morphologies and sediment properties at the two watersheds (see section 6.2.1).

The mean annual precipitation (MAP) and mean annual temperature at the study sites are summarized in Table 7.1. The mean temperature is lower in the Holcombe's Branch,

which is located in a higher latitude (34.6177° N, 81.6914° W). The MAP in the two tropical watersheds [Murphy and Stallard, 2012] is significantly higher compared to the Calhoun CZO (Table 7.1). Different erosional mechanisms controlled by topography, vegetation cover, and soil hydrological and geomorphic properties (Figure 7-1), are dominant in the two study areas. Shallow landslides are the main hillslope erosion drivers in the Luquillo CZO [Larsen, 2012]: 93 % of the total hillslope erosion at the Mameyes watershed corresponds to rainfall-triggered landslides. The contribution of landslides to total hillslope erosion at the Icacos watershed is 98 %. In the Calhoun CZO, extensive logging and abandonment of agricultural sites led to accelerated erosion and to the development of large gully systems. Gully erosion (e.g., sidewall erosion) is the main erosional mechanism in this degraded landscape [James *et al.*, 2007]. Biogeochemical characteristics of different soil types at the two sites are given in sections 2.4.1 and 4.4.1.

Table 7.1. Mean annual precipitation (MAP) and mean annual temperature at the Holcombe's Branch (Calhoun CZO) and at the Mameyes and Icacos watersheds (Luquillo CZO).

	Holcombe's Branch	Rio Mameyes	Rio Icacos
MAP (mm yr <sup>-1</sup> ) [Murphy and Stallard, 2012]	1,260	3,760	4,150
Mean annual temperature (°C) (section 2.3)	17	23	21

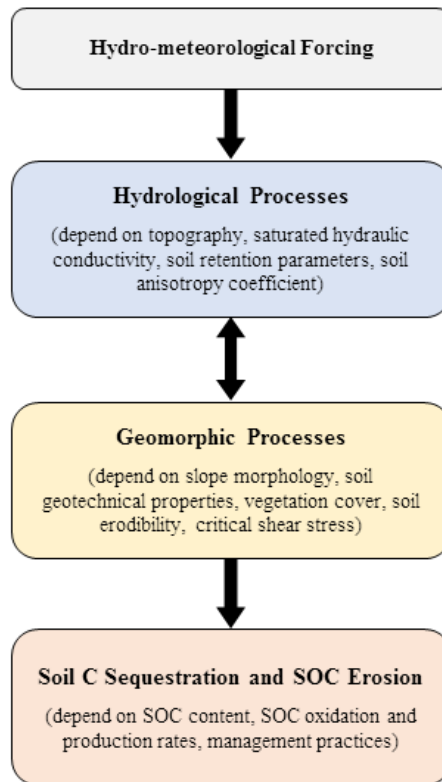


Figure 7-1. Conceptual diagram of feedbacks among coupled hydrological, geomorphic, and biogeochemical processes modelled using tRIBS-ECO at diverse ecosystems. Geophysical and biogeochemical properties (section 2.4) controlling different processes are given in parentheses. Geomorphic processes include topsoil erosion, which is the primary erosional mechanism in the Calhoun CZO, and shallow landslides, which are the main erosional drivers at the Luquillo CZO [Larsen, 2012]. Arrows denote dynamic feedbacks among linked processes. For example, increase in moisture conditions at soils characterized by low values of cohesion and friction angle (e.g., sandy loam) may lead to instability of relatively steep slopes. Dynamic replacement of eroded soil organic C (SOC) at landslide sites by C sequestration [Harden *et al.*, 1999] and subsequent SOC burial can drive a net atmospheric C sink (chapter 4). Depending on the rates of SOC oxidation and production, and on the influence of land management practices on C fluxes, soil C sequestration and SOC erosion may induce a net atmospheric C sink or a net C source (see sections 3.4.2 and 4.6.5).

The simulated erosion rates at the study sites are given in Table 7.2. The simulated erosion rates correspond to 100-year averages based on stationary hydro-climatic forcings



(see sections 2.4.4 and 4.4.4). Slope instability in the Luquillo CZO induced significant soil loss at landslide sites [Larsen, 2012]. Yet the total hillslope erosion rates averaged over upland eroding sites in the Mameyes and Icacos watersheds (0.93 and 1.12 mm yr<sup>-1</sup>, respectively) are comparable with the rate of accelerated erosion simulated in the Holcombe's Branch (1.33 mm yr<sup>-1</sup>).

Table 7.2. Simulated soil erosion rates at the Holcombe's Branch (Calhoun CZO) and at the Mameyes and Icacos watersheds (Luquillo CZO).

	Holcombe's Branch	Rio Mameyes	Rio Icacos
Soil erosion rate (mm yr <sup>-1</sup> )	1.33	0.93	1.12

The net erosion-induced C exchanges with the atmosphere simulated at the Calhoun CZO and at the Luquillo CZO are given in Table 7.3, for the maximum source, the intermediate, and the maximum sink scenarios of C fluxes (sections 3.3.3 and 4.4.2). The simulated soil-atmosphere C exchange in the Calhoun CZO ranged from a net source of 10.3 g C m<sup>-2</sup> yr<sup>-1</sup> to a net sink of -8.4 g C m<sup>-2</sup> yr<sup>-1</sup>. The C exchange with the atmosphere in the Luquillo CZO ranged from a net source of 17.8 g C m<sup>-2</sup> yr<sup>-1</sup> to a net sink of -20.8 g C m<sup>-2</sup> yr<sup>-1</sup>. The simulated ranges are controlled by forest types, management practices, and plant inputs to SOC in eroding soils at the two diverse ecosystems (Figure 7-1). According to the analysis of section 4.6.4, in soils covered with forests a high NPP, such as the Tabonuco forest (which dominates the Luquillo CZO), lateral removal of topsoil layers may alter the depth-dependent SOC production rates more significantly, leading to higher

net SOC loss to erosion (maximum source scenario). The maximum C sink strength is also greater for the Luquillo CZO, because the alteration of the SOC oxidation rate at the maximum sink scenario was more significant in the tropical eroding soils (see section 4.6.4), compared to the eroding soils at the Calhoun CZO. As a result, in the modelled extreme scenarios of soil-atmosphere C exchange, soil erosion led to a wider range of C fluxes in the tropical soils of the Luquillo CZO, compared to the eroding soils of the Calhoun CZO.

Table 7.3. Simulated erosion-induced soil-atmosphere C exchange in the Calhoun CZO and the Luquillo CZO for the maximum source, the intermediate, and the maximum sink scenarios (sections 3.3.3 and 4.4.2) of C fluxes (values in  $\text{g C m}^{-2} \text{yr}^{-1}$ ).

	Calhoun CZO	Luquillo CZO
Max. sink scenario	-8.4	-20.8
Intermediate scenario	-1.5	-5.6
Max. source scenario	10.3	17.8

In agricultural landscapes, removal of atmospheric  $\text{CO}_2$  by plants, accelerated erosion and burial of fixed C as soil organic matter at depositional environments may lead to a net atmospheric C sink [Lal, 2004]. According to results for the intermediate scenario of C fluxes, the influence of accelerated soil erosion on the degraded landscape of the Calhoun CZO leads to a net atmospheric C sink of  $-1.5 \text{ g C m}^{-2} \text{yr}^{-1}$ . In montane ecosystems, landslides remove surficial soil horizons at upper slopes leading to deep burial of organic material across the landscape. This study suggests that atmospheric  $\text{CO}_2$  sequestration,

hillslope erosion, and shallow landslide occurrence in the tropical watersheds of the Luquillo CZO likely induce a net atmospheric C sink of significant strength ( $-5.6 \text{ g C m}^{-2} \text{ yr}^{-1}$  for the intermediate scenario of Table 7.3). C erosion and burial in diverse ecosystems have the potential to offset the anthropogenic enrichment of atmospheric  $\text{CO}_2$  [IPCC, 2007], and therefore have an important impact on the global C cycle [Lal, 2003]. Removal of atmospheric  $\text{CO}_2$  and increase of SOC storage can be achieved by increasing the input rates of SOC to deep soils, and by changing decomposability of organic matter inputs [Post and Kwon, 2000]. Recommended management practices driving soil C sequestration include conservation tillage, no till, and mulch farming, integrated nutrient management, integrated pest management, and precision farming [Lal, 2004]. Site-specific adaptation of such land management practices can lead to enhancement of the SOC pool with reduction of tillage-induced soil disturbances, increase in plant C inputs, and increase of the organic matter mean residence time in soils [Lal, 2004].

The influence of wet versus dry climatic regimes on the erosion rates of SOC was studied at the two sites. This analysis classified years with annual precipitation lower than the MAP at each site as “dry”, and as “wet” those years exceeding the MAP (Table 7.1). The percentile C erosion from upland sites corresponding to wet and dry years is given in Table 7.4: around 59 % of C erosion occurred during wet years in the Holcombe’s Branch. The relative amount of C erosion during wet years at the Luquillo CZO was approximately equal to 69% and 65% for the Mameyes and Icacos watersheds, respectively. The proportions of hydrologically-induced erosion of organic material were also analyzed in 24-hour precipitation intervals, which represent the influence of significant hydro-meteorological events on the watershed’s response in terms of landslide occurrence

[*Larsen and Simon, 1993*] and upland SOC erosion, integrated over 24-hour periods (Table 7.4). Days where precipitation exceeded the daily mean at each site were characterized as “relatively wet”. Days where precipitation occurred with intensities lower than the mean daily one were considered as “relatively dry”. According to this analysis, 56.4 % of C erosion occurred in response to relatively wet events in the Calhoun CZO (Table 7.4). The contribution of intense hydro-climatic events on the erosion of organic material at the Mameyes and Icacos watersheds was important (62.2 % and 58.3 %, respectively).

Results indicate that the annual precipitation depth influences the cumulative C erosion in the Calhoun CZO and the Luquillo CZO. The influence of relatively wet days on the rates of hydrologically-induced SOC transport is also important in the study sites. This reflects the episodic character of C erosion in response to hydro-meteorological events, per findings of chapter 2. The relative contribution of wet days on SOC mobilization is more significant in the Mameyes and Icacos watersheds, where shallow landslides triggered by intense precipitation events remove surficial and deeper soil layers and associated organic material (chapter 4), at higher rates than the topsoil C erosion that characterizes upland soil profiles in the Calhoun CZO (Table 7.4).

Table 7.4. Proportions of C erosion occurring in dry vs. wet years, and in relatively dry vs. relatively wet days, in the Calhoun CZO and in the Luquillo CZO.

	Holcombe's Branch	Rio Mameyes	Rio Icacos
Dry years	41.2 %	33.2 %	35.1 %
Wet years	58.8 %	66.8 %	64.9 %
Relatively dry days	43.6 %	37.8 %	41.7 %
Relatively wet days	56.4 %	62.2 %	58.3 %

## 7.2 Conclusions

### 7.2.1 Understanding a severely degraded agricultural landscape: Soil erosion and burial of soil organic carbon

This study introduced a parsimonious, spatially- and depth-explicit biogeochemical model, the tRIBS-ECO (*TIN-based Real-time Integrated Basin Simulator-Erosion and Carbon Oxidation*), to examine whether soil erosion at the landscape scale enhances net C sequestration or CO<sub>2</sub> return to the atmosphere. The model is based on existing physically-based hydrologic and geomorphic components [Francipane *et al.*, 2012; Ivanov *et al.*, 2004a; b]. This is the first study that couples physically-based formulations to represent dynamic feedbacks among linked hydrological, geomorphological, and biogeochemical processes in a novel spatially-explicit framework, to assess the impact of episodic soil erosion and deposition on atmospheric CO<sub>2</sub>. This work focused on the Calhoun Critical Zone Observatory (CZO), a region undergoing recovery from past intensive agricultural use much as many other regions of the world, and used multiple measurements of

biochemical variables extending to deep soils and observations of hydro-geomorphological processes.

According to results, accelerated erosion at the anthropogenically disturbed Holcombe's Branch watershed (Calhoun CZO) led to the redistribution of relatively large amounts of upland soil and SOC from interfluvies and slopes to depositional sites and alluvial sediments (legacy sediments). This study demonstrated that the physically-based representation of the spatial heterogeneity of erosion and of the dynamics of mobilized SOC have a significant influence on the net soil-atmosphere C exchange. Observations suggested that 32% of the original SOC content at the study area has been eroded. The episodic representation of erosion reproduced the SOC loss in eroded sites better than a model that assumed a constant erosion rate, suggesting that time varying erosion may be an important feature for accurate representation of erosion-induced SOC dynamics.

A stochastic representation of the variability and temporal dependence of the influence of management practices on C fluxes was proposed (chapter 3). Land use practices (e.g., fertilization and associated enhancement of system productivity) can have a substantial influence on SOC production and oxidation rates at eroding sites, which can significantly impact the net C exchange with the atmosphere. Depending on the influence of land management practices on C fluxes at eroding soils, watershed-integrated estimates of erosion-induced soil-atmosphere C exchange ranged from a net C source to a net C sink of significant strengths, encompassing C fluxes inferred from observations, and published estimates of the contribution of erosion to atmospheric CO<sub>2</sub>. SOC sequestration and burial can induce a net atmospheric C sink (chapter 2), which could lead to a potential short-term strategy for mitigating anthropogenic enrichment of atmospheric CO<sub>2</sub> [Lal, 2004]. This

study emphasizes the crucial importance of land management practices and conservation methods in preventing agricultural erosion and soil degradation [Montgomery, 2007], and in promoting human and ecosystem health and sustainability.

This work highlighted the important topographic heterogeneity that characterizes erosion and burial of organic material, driven by land use and land use change. The hydrogeomorphic behavior of the Holcombe's Branch watershed in the Calhoun CZO was simulated during the recent agro-ecosystem and the secondary forest ecosystem periods, that characterize the study area (chapter 3). Although rapid reforestation of the region likely led to a decline in erosion rates, the present state of the degraded landscape is characterized by important erosional potential of soil and organic material. Observations and model results indicated substantial SOC storage at depositional sites, suggesting that a significant fraction of eroded SOC is only partially oxidized upon transport. For the most part, the eroded organic material has been buried in alluvial deposits, rather than travelling down the stream network to the ocean.

On average, 34% of eroded C has been replaced by C sequestration at an intermediate scenario of C fluxes (chapter 2). The simulated topographic variation of the C replacement at small spatial scales is comparable to the variability among multiple point estimates reported in a global-scale study [Van Oost *et al.*, 2007]. The strong spatial heterogeneity is attributed to the small-scale complexity of natural processes that drive C erosion. This variability is sometimes partially neglected with landscape- or global-scale studies that are often based on domain averaged C fluxes, or on scarce point measurements, yet it appears to be an important feature to consider in modelling efforts. Though such an approach necessarily adds significant complexity to modelling efforts, accounting for small-scale

heterogeneity in topography and temporally varying erosion rates can have meaningful influence on model projections of erosion-induced, vertical and lateral SOC fluxes and resulting SOC profile storage. It is recommended that future attempts to quantify the contribution of erosion on atmospheric CO<sub>2</sub> explicitly account for the fate of eroded SOC, and for the significant uncertainty pertinent to the fine spatio-temporal variation of hydro-geomorphic and biochemical processes that drive C erosion.

#### 7.2.2 Hillslope erosion, landslide occurrence and carbon dynamics at tropical watersheds

This work studies hydrologically-driven hillslope erosion, landslide occurrence and SOC redistribution in the Mameyes and Icacos watersheds at the Luquillo CZO, a tropical site of particular hydrological and geomorphological interest, characterized by diverse topographies and contrasting underlying lithologies (chapter 4). To quantify effects of geomorphic perturbations on the dynamics of SOC in the Luquillo CZO, an existing slope stability component [Arnone *et al.*, 2011] was coupled with tRIBS-ECO. The model accounts for feedbacks between hydrologically-induced topsoil erosion and landslide occurrence, and simulates the fate of eroded SOC across the landscape. Measurements of diverse SOC profiles and oxidation rates were used to initialize the model, and observations of hydrologic and geomorphic processes were used for model evaluation.

Based on the spatially-explicit physical representation of SOC erosion this work highlighted the capacity of tropical watersheds to serve as a net C sink or a C source in response to hydro-geomorphic perturbations. Simulations suggested that the type of forest controls the erosion-induced C exchange with the atmosphere in these montane tropical



watersheds. Hillslope erosion altered SOC production and decomposition rates in tabonuco and palm forests, characterized by markedly greater NPP values relative to colorado forests (section 4.4). The associated effects on colorado forest soil profiles were less significant.

The two tropical watersheds are characterized by significant rates of hillslope erosion and landslide occurrence. According to simulations, frequent events of sediment transport lead to significant SOC erosion across the Luquillo CZO. SOC is transported with sediment from eroding hillslopes and landslide sites across the landscape. Also, landslides occurring at relatively steep slopes remove surficial and deeper soil layers and associated organic matter. Soil profiles at fresh landslide scars undergo rapid C replacement by atmospheric C sequestration during succession.

To quantify the uncertainty in landside hazard prediction associated with the natural spatial variation of soil properties, a probabilistic approach for the prediction of rainfall-triggered landslide occurrence at basin scale (chapter 5) was implemented in an existing distributed eco-hydrological and landslide model, the tRIBS-VEGGIE-landslide (*TIN-based Real-time Integrated Basin Simulator - VEGetation Generator for Interactive Evolution*) model [Lepore *et al.*, 2013]. The model assesses the likelihood of shallow landslides by accounting for uncertainty related to geotechnical and hydrological factors that directly affect slope stability. The methodology was used in the Mameyes basin (Luquillo CZO). Effects of different hyetograph shapes on shallow landslide occurrence were also studied.

The use of this physically-based approach allowed the simulation of the complex nonlinear interactions between rainfall forcing and soil basin characteristics (mainly

topography and soil types) in evaluating the hydrological and slope stability basin responses. The parsimonious probabilistic approach is computationally feasible, as opposed to numerical probabilistic analyses at basin scale that require prohibitive numbers of model runs. Results indicated that hyetographs with a rainfall peak near the end of the event, typical of tropical cyclones, can be most catastrophic in terms of rainfall-triggered landslide occurrence. Events with maximum intensities around the middle part of their duration (frontal events) resulted in lower probabilities of failure. Also, differences in probability of failure due to diverse hyetograph shapes were observed at intermediate slopes, where the stability is controlled by the combined impact of soil moisture and soil weight, in contrast to steeper or flatter slopes. The overlap between simulated landslide occurrence and historical landslide events confirmed the model capability to identify the areas at dense frequency of landslides, even if this comparison cannot be considered a rigorous validation procedure. The use of the proposed probabilistic approach for shallow landslide prediction was able to reveal and quantify landslide risk at slopes assessed as stable by simpler deterministic methods.

To quantify the influence of climate change on the rates of hillslope erosion and soil accumulation at the contrasting landscapes of the Luquillo CZO, the hydro-geomorphic models of the Mameyes and Icacos watersheds were forced with a range of hydro-climatic projections (chapter 6). The rates of hillslope erosion and landslide occurrence at the diverse watersheds of Rio Icacos and Rio Mameyes were quantitatively estimated by systematically accounting for dynamic feedbacks among linked hydrologic and geomorphic processes. Observations were used to confirm model behavior, including multiple landslide scars and recent sediment exports.

By the means of the process based and spatially-explicit representation of slope instability, this modelling study demonstrated that the propensity for landslide occurrence at the Luquillo Mountains is expected to remain significant in the 21<sup>st</sup> century. The simulated landslide occurrence at the two watersheds over the simulation period can be roughly approximated by scale-invariant distributions, which can be characteristic of landslide frequency distributions observed in natural systems [*Bak et al.*, 1987; *Hergarten*, 2003]. The projected landslide frequency distributions suggest that landslides of relatively larger magnitudes are expected to persist at the Icacos watershed, underlain by quartz diorite. The occurrence of smaller shallow landslides at the volcanoclastic Mameyes watershed will likely remain relatively high. While the exact timing of landslide occurrence depends on storm hyetograph characteristics, the cumulative frequency of slope instability simulated in the 21<sup>st</sup> century exhibited small variation over the range of hydro-climatic scenarios. The time-integrated landslide occurrence projected by 2099 is heavily controlled by non-climatic factors, including local topographic gradients, soil characteristics and forest types.

According to results, the projected climate change in the south Caribbean may drive a moderate decrease in hillslope erosion rates, yet the erosional potential of the two diverse landscapes remains significant. Comparison with recently reported rates of regolith production [*Chabaux et al.*, 2013; *Dosseto et al.*, 2012] indicates that substantial rates of denudation characterize the granitic landscape (Icacos watershed), while the adjacent volcanoclastic landscape of the Mameyes watershed likely reaches a state close to dynamic equilibrium. According to simulations, the soil thickness equilibrium states in the two diverse landscapes likely remain reasonably invariant with changing climate. It is

suggested that high resolution process-based models that systematically account for dynamic feedbacks among complex hydrologic and geomorphic processes can be used to predict the relative influence of climatic and nonclimatic factors on landscape evolution, and the critical zone response to a range of natural and anthropogenic perturbations.

### **7.3 Future Research Directions**

Future research efforts can focus on utilizing various data sets from other locations and sites to further evaluate the ability of this modelling framework to simulate sediment and SOC erosion and the soil-atmosphere C exchange. The modelling framework developed in this study can then be used to investigate different hypotheses addressing scientifically and socially significant problems.

Prediction of the influence of hydrologically-induced erosion and landslide occurrence on soil-atmosphere CO<sub>2</sub> exchange can be improved using additional observations of hydro-geomorphic and biogeochemical variables. Given the significant topographic variability of C fluxes demonstrated in chapter 2, measurements from interfluvies, slopes, and depositional sites will help in evaluating the ability of tRIBS-ECO to efficiently reproduce C inventories and decomposition rates in anthropogenically disturbed landscapes. Measurements from long-term soil-ecosystem experiments [*Richter and Markewitz*, 2001] can be used to constrain modelled C fluxes based on the potentially significant [*Mobley et al.*, 2015; *Richter et al.*, 1999] temporal variation in plant inputs to the SOC pool, driven by land use and land cover change. Ecophysiological indices, such as the carbon use efficiency [*DeLucia et al.*, 2007], can be used in tRIBS-ECO to represent

the coexistence of microbial activity and biomass production at different forest types. Also, the effect of land uses on SOC decomposition and production varies among differently managed sites [Doetterl *et al.*, 2016]; Systematically accounting for this spatial variation may further constrain estimates of the erosion-induced soil-atmosphere C exchange.  $^{14}\text{C}$  based observations from eroding sites will help evaluate the statistical properties of  $a_k$  (sections 2.4.2 and 3.3.3), and characterize better the uncertainty associated with land management in the prediction of SOC decomposition rates.

Evaluation of the hydro-geomorphic model's performance can be improved using additional measurements of discharge and sediment yield from future campaigns. With regard to modelling landslide hazard, systematic mapping and recording of the time of landslide events can improve model validation. This will further test the extent to which the simulated response to hurricanes and tropical storms [Hilton *et al.*, 2008; Larsen and Torres-Sánchez, 1992; Larsen and Simon, 1993] reproduces natural landslide occurrence, and will hence confirm the potential of the methodology to improve landslide hazard assessment in montane watersheds [Larsen and Torres-Sánchez, 1998].

As previously discussed, the coupled and physically-based character of tRIBS-ECO allows the quantification of dynamic feedbacks among hydro-geomorphic and biogeochemical processes at fine temporal and spatial scales to test multiple hypotheses. The critical influence of hillslope erosion driven by different hydro-climatic projections on the redistribution of SOC can be assessed in diverse tropical ecosystems [Fiener *et al.*, 2015]. The physically-based model can be used to estimate sediment and C fluxes triggered by tropical hurricanes, which could potentially lead to important insights on how extreme hydro-climatic phenomena perturb tropical ecosystems.

This work highlights the episodic character of upland SOC erosion in response to hydro-meteorological events (chapter 2). The influence of future precipitation intensity change on episodic C erosion and on the soil-atmosphere CO<sub>2</sub> exchange in the Calhoun ecosystem and in managed landscapes can be assessed using tRIBS-ECO. The hydrologically-induced movement of organic material can have important consequences on the net C exchange with the atmosphere in a changing climate [Battin *et al.*, 2009; Lal, 2004].

Furthermore, tRIBS-ECO can be used to evaluate seasonal or long-term controls of ecological, hydrological, and biogeochemical processes [Richter and Billings, 2015]. The uncertainty associated with the natural spatial variability of hydrological, geomorphological, and biogeochemical properties can be significant (chapter 5), and needs to be accounted for in estimates of atmospheric C fluxes derived from erosional processes. The spatial variation of rainfall fields driven by topography (chapter 5), forest cover, and atmospheric phenomena (e.g., spatial variation of cloud cover) may be important in larger spatial scales of analysis, and should be also accounted for in future studies. The model can also be used to assess how topography among contrasting depositional environments may influence the degree to which eroded SOC may be preserved in diverse ecosystems. Given our lack of knowledge about the fate of most eroded SOC on timescales of decades to centuries, this is of particular interest for future studies. Investigations addressing these issues are especially compelling in areas where soil erosion has been accelerated by anthropogenic activity, and in sites where extreme hydro-meteorological phenomena and geomorphic gradients have the potential to induce significant sediment transport.

## APPENDIX A. Estimation of SOC content at each time step

In the tRIBS-ECO model, the depth-dependent SOC content is estimated at each time step by calculating the parameter  $C_{a,t}$  in equation (2.2) based on the SOC difference given by equation (2.1). More precisely, the total SOC content (per unit area) is given by (see section 2.2.1 for notation):

$$SOC_t = \int_0^{H_t} C_t(z) \rho(z) dz \quad (A.1)$$

Substituting  $C_t(z)$  from equation (2.2) yields:

$$SOC_t = \int_0^{H_t} (C_{a,t} e^{C_b z} + C_c) \rho(z) dz = C_{a,t} \left( \frac{\rho(z) (e^{C_b H_t} - 1)}{C_b} \right) + C_c H_t \rho(z) \quad (A.2)$$

At time step  $t+1$ , the SOC content is estimated by applying equation (2.1). The value of  $C_{a,t+1}$  is then calculated from equation (A.2) as following:

$$C_{a,t+1} = \frac{C_b (SOC_{t+1} - C_c H_{t+1} \rho(z))}{\rho(z) (e^{C_b H_{t+1}} - 1)} \quad (A.3)$$

Expressing  $C_{a,t}$  as a time variant parameter implies mixing among surficial horizons in the soil column (see section 2.4). Equation (A.3) is applied at eroding and depositional sites across the watershed.

## APPENDIX B. Estimation of initial depth-dependent SOC production rates

The initial SOC production rate is estimated by assuming steady state conditions for time  $t=0$  (section 2.4). For steady-state conditions at time  $t = 0$ :  $\frac{\Delta SOC}{\Delta t} = 0$  and therefore equation (2.1) yields (see section 2.2.1 for notation):

$$\int_0^{H_t} I_t(z) dz \Big|_{t=0} = \int_0^{H_t} k_t(z) \rho(z) C_t(z) dz \Big|_{t=0} \quad (B.1)$$

From equation (2.5) and (B.1) we obtain:

$$\frac{I_{a,t}}{I_b} \left( e^{H_t I_b} - 1 \right) \Big|_{t=0} = \int_0^{H_t} k_t(z) \rho(z) C_t(z) dz \Big|_{t=0} \quad (B.2)$$

The SOC production rate at soil surface ( $z=0$ ) is equal to  $I_{a,t}$  (equation (2.5)). By assuming zero net soil-atmosphere C exchange at the soil surface [Yoo *et al.*, 2005] at the beginning of the simulation we obtain:

$$I_{a,t} \Big|_{t=0} = k_t(z=0) \rho(z=0) C_t(z=0) \Big|_{t=0} \quad (B.3)$$

The model was initialized with estimates of depth-dependent soil bulk density, SOC oxidation rate and SOC concentration, based on observations (see Figure 2-3 and Table 2.1). The initial depth-dependent SOC production rates at each topographic location were estimated by calculating  $I_{a,t}$  and  $I_b$  from equations (B.3) and (B.2), respectively. The corresponding parameter values are presented in Table 2.1.



## APPENDIX C. Estimation of the variability of carbon storage

The variance of SOC storage (associated with uncertainty in the influence of management practices) conditioned to the previous state is obtained at each time step from equation (3.7) as following:

$$Var[SOC_t | SOC_{t-1}] = Var \left[ SOC_{t-1} + \int_0^{H_t} I_{a,t} e^{I_b z} dz - \int_0^{H_t} (k_{a,t} e^{k_b z} + k_c) \rho(z) C_t(z) dz + L_t \right] \quad (C.1)$$

By dropping the constant terms from the right hand side of equation (C.1) we obtain

$$Var[SOC_t | SOC_{t-1}] = c_{1,t}^2 Var[I_{a,t} | I_{a,t-1}] + c_{2,t}^2 Var[k_{a,t} | \kappa_{a,t-1}] + 2c_{1,t}c_{2,t} Cov[k_{a,t}, I_{a,t} | \kappa_{a,t-1}, I_{a,t-1}] \quad (C.2)$$

where  $I_{a,t-1}$ ,  $\kappa_{a,t-1}$ ,  $SOC_{t-1}$  are the values of  $I_a$ ,  $k_a$ , and SOC storage estimated at time  $t-1$ , respectively, and  $c_{1,t}$  and  $c_{2,t}$  are given by equation (3.12). Based on the representation of the effect of management practices on  $k_t(z)$  and  $I_t(z)$  (section 2.2.1), it can be shown that the conditional variances of  $I_{a,t}$  and  $k_{a,t}$  are equal to the ones given in equation (3.6):

$$\begin{aligned} Var[I_{a,t} | I_{a,t-1}] &= Var[a_1] (1 - \rho_{\alpha_1}^2) \\ Var[k_{a,t} | \kappa_{a,t-1}] &= Var[a_k] (1 - \rho_{\alpha_k}^2) \end{aligned} \quad (C.3)$$

where  $Var[a_1]$ ,  $Var[a_k]$ ,  $\rho_{\alpha_1}$  and  $\rho_{\alpha_k}$  are time invariant statistical properties (variances and lag-1 autocorrelation coefficients, respectively) of the stationary processes  $a_1$ , and  $a_k$ . Also, at each time step  $Cov[k_{a,t}, I_{a,t} | \kappa_{a,t-1}, I_{a,t-1}]$  is equal to the covariance of the white noise term

of the bivariate stationary AR(1) model (equation (3.1)). Thus, from equations (C.2) and (3.11) we obtain:

$$Var[SOC_t | SOC_{t-1}] = \underline{\mathbf{P}}_t^T \mathbf{B} \mathbf{B}^T \underline{\mathbf{P}}_t \quad (\text{C.4})$$

## REFERENCES

1. A.S.C.E. (1993), Criteria for Evaluation of Watershed Models, *Journal of Irrigation and Drainage Engineering*, 119 (3), 429-442, doi: 10.1061/(ASCE)0733-9437(1993)119:3(429)
2. Abaci, O., and A. N. T. Papanicolaou (2009), Long-term effects of management practices on water-driven soil erosion in an intense agricultural sub-watershed: monitoring and modelling, *Hydrological Processes*, 23 (19), 2818-2837, doi: 10.1002/hyp.7380
3. Abbaszadeh, M., K. Shahriar, M. Sharifzadeh, and M. Heydari (2011), Uncertainty and Reliability Analysis Applied to Slope Stability: A Case Study From Sungun Copper Mine, *Geotechnical and Geological Engineering*, 29 (4), 581-596, doi: 10.1007/s10706-011-9405-1
4. Anderson, S. P., F. von Blanckenburg, and A. F. White (2007), Physical and Chemical Controls on the Critical Zone, *Elements*, 3 (5), 315-319, doi: 10.2113/gselements.3.5.315
5. Arnone, E. (2011), An Integrated System for the Analysis of Rainfall-Triggered Landslides, Phd Thesis thesis, Universita' degli Studi di Palermo, Palermo.
6. Arnone, E., L. V. Noto, C. Lepore, and R. L. Bras (2011), Physically-based and distributed approach to analyze rainfall-triggered landslides at watershed scale, *Geomorphology*, 133 (3–4), 121-131, doi: <http://dx.doi.org/10.1016/j.geomorph.2011.03.019>
7. Arnone, E., Y. G. Dialynas, L. V. Noto, and R. L. Bras (2013), Effect of DEM resolution on rainfall-triggered landslide modeling within a triangulated network-based model. A case study in the Luquillo Forest, Puerto Rico. American Geophysical Union Fall Meeting, Abstract NH23A-1522, San Francisco, CA, Dec. 09-13
8. Arnone, E., Y. G. Dialynas, L. V. Noto, and R. L. Bras (2014), Parameter Uncertainty in Shallow Rainfall-triggered Landslide Modeling at Basin Scale: A Probabilistic Approach, *Procedia Earth and Planetary Science*, 9, 101-111, doi: 10.1016/j.proeps.2014.06.003
9. Arnone, E., Y. G. Dialynas, L. V. Noto, and R. L. Bras (2016), Accounting for soil parameter uncertainty in a physically based and distributed approach for rainfall-triggered landslides, *Hydrological Processes*, 30 (6), 927-944, doi: 10.1002/hyp.10609
10. Bak, P., C. Tang, and K. Wiesenfeld (1987), Self-organized criticality: An explanation of the 1/f noise, *Physical Review Letters*, 59 (4), 381-384, doi: <http://dx.doi.org/10.1103/PhysRevLett.59.381>
11. Bathurst, J. C., A. Burton, and T. J. Ward (1997), Debris flow run-out and landslide sediment delivery model tests, *Journal of Hydraulic Engineering*, 123 (5), 410-419, doi: [http://dx.doi.org/10.1061/\(ASCE\)0733-9429\(1997\)123:5\(410\)](http://dx.doi.org/10.1061/(ASCE)0733-9429(1997)123:5(410))
12. Battin, T. J., S. Luyssaert, L. A. Kaplan, A. K. Aufdenkampe, A. Richter, and L. J. Tranvik (2009), The boundless carbon cycle, *Nature Geosci*, 2 (9), 598-600, doi: 10.1038/ngeo618

13. Beinroth, F. H., P. J. Hernández, A.-M. Esnard, G. Acevedo, and B. C. Dubee (1992), Organic carbon content of the soils of Puerto Rico, in *Organic carbon sequestration in the soils of Puerto Rico—A case study of a tropical environment: Mayagüez, Puerto Rico*, edited by F. H. Beinroth, pp. 57-62, University of Puerto Rico Department of Agronomy and Soils, and U.S. Department of Agriculture Soil Conservation Service.
14. Bellugi, D., D. G. Milledge, W. E. Dietrich, J. A. McKean, J. T. Perron, E. B. Sudderth, and B. Kazian (2015), A spectral clustering search algorithm for predicting shallow landslide size and location, *Journal of Geophysical Research: Earth Surface*, 120 (2), 300-324, doi: 10.1002/2014JF003137
15. Benjamin, J. R. A., and C. A. A. Cornell (1970), *Probability, Statistics, and Decision for Civil Engineers*, McGraw-Hill Ryerson, Limited.
16. Bennett, N. D., B. F. W. Croke, G. Guariso, J. H. A. Guillaume, S. H. Hamilton, A. J. Jakeman, S. Marsili-Libelli, L. T. H. Newham, J. P. Norton, C. Perrin, S. A. Pierce, B. Robson, R. Seppelt, A. A. Voinov, B. D. Fath, and V. Andreassian (2013), Characterising performance of environmental models, *Environmental Modelling & Software*, 40, 1-20, doi: <http://dx.doi.org/10.1016/j.envsoft.2012.09.011>
17. Berhe, A. A., and M. Kleber (2013), Erosion, deposition, and the persistence of soil organic matter: mechanistic considerations and problems with terminology, *Earth Surface Processes and Landforms*, 38 (8), 908-912, doi: 10.1002/esp.3408
18. Berhe, A. A., J. Harte, J. W. Harden, and M. S. Torn (2007), The Significance of the Erosion-induced Terrestrial Carbon Sink, *BioScience*, 57 (4), 337-346, doi: 10.1641/b570408
19. Berhe, A. A., J. W. Harden, M. S. Torn, M. Kleber, S. D. Burton, and J. Harte (2012), Persistence of soil organic matter in eroding versus depositional landform positions, *Journal of Geophysical Research: Biogeosciences*, 117 (G2), doi: 10.1029/2011JG001790
20. Bestland, E. A., C. Liccioli, L. Soloninka, D. J. Chittleborough, and D. Fink (2016), Catchment-scale denudation and chemical erosion rates determined from <sup>10</sup>Be and mass balance geochemistry (Mt. Lofty Ranges of South Australia), *Geomorphology*, 270, 40-54, doi: <http://dx.doi.org/10.1016/j.geomorph.2016.07.014>
21. Beven, K. J., and M. J. Kirkby (1979), A physically based, variable contributing area model of basin hydrology / Un modèle à base physique de zone d'appel variable de l'hydrologie du bassin versant, *Hydrological Sciences Bulletin*, 24 (1), 43-69, doi: 10.1080/02626667909491834
22. Billings, S. A., R. W. Buddemeier, D. D. Richter, K. Van Oost, and G. Bohling (2010), A simple method for estimating the influence of eroding soil profiles on atmospheric CO<sub>2</sub>, *Global Biogeochemical Cycles*, 24 (2), GB2001, doi: 10.1029/2009GB003560

23. Bjerrum, L., and N. E. Simons (1960), Comparison of shear strength characteristics of normally consolidated clays, ASCE Research Conference on Shear Strength of Cohesive Soils, 711-726
24. Bonnin, G., D. Martin, B. Lin, T. Parzybok, M. Yekta, and D. Riley (2006), Precipitation Frequency for Puerto Rico and the US Virgin Islands - NOAA Atlas 14 Volume 3*Rep.*, NOAA/NWS/Office of Hydrologic Development, Hydrometeorological Design Studies Center, Silver Spring, MD, USA.
25. Bovy, B., J. Braun, and A. Demoulin (2016), A new numerical framework for simulating the control of weather and climate on the evolution of soil-mantled hillslopes, *Geomorphology*, 263, 99-112, doi: <http://dx.doi.org/10.1016/j.geomorph.2016.03.016>
26. Box, G. E., G. M. Jenkins, and G. C. Reinsel (2011), *Time series analysis: forecasting and control*, John Wiley & Sons.
27. Brakensiek, K. L., R. L. Engleman, and W. J. Rawls (1981), Variation within texture classes of soil water parameters., *ASAE*, 24 (2), 335-339
28. Brantley, S. L., M. B. Goldhaber, and K. V. Ragnarsdottir (2007), Crossing Disciplines and Scales to Understand the Critical Zone, *Elements*, 3 (5), 307-314, doi: 10.2113/gselements.3.5.307
29. Bras, R. L. (1990), *Hydrology: An Introduction to Hydrologic Science*, Addison-Wesley-Longman, Reading, MA.
30. Bras, R. L. (2015), Complexity and organization in hydrology: A personal view, *Water Resources Research*, 51 (8), 6532-6548, doi: 10.1002/2015WR016958
31. Bras, R. L., and I. Rodriguez-Iturbe (1985), *Random Functions and Hydrology*, Addison Wesley, Reading, MA.
32. Bras, R. L., Y. G. Dialynas, S. A. Billings, D. Richter, and D. Markewitz (2015), The Dependence on Topography of the Influence of Soil Erosion and Deposition on the Carbon Cycle at the Calhoun Critical Zone Observatory, *American Geophysical Union Fall Meeting, Abstract H52C-04, San Francisco, CA, Dec. 14-18*
33. Brecheisen, Z., and C. W. Cook (2015), Calhoun CZO 1933 aerial imagery composite, <http://nicholas.duke.edu/cczo/data>
34. Brocard, G. Y., J. K. Willenbring, F. N. Scatena, and A. H. Johnson (2015), Effects of a tectonically-triggered wave of incision on riverine exports and soil mineralogy in the Luquillo Mountains of Puerto Rico, *Applied Geochemistry*, doi: <http://dx.doi.org/10.1016/j.apgeochem.2015.04.001>
35. Brooks, R. H., and A. T. Corey (1964), Hydraulic properties of porous media. Hydrology Paper 3, Civil Engineering Dep., Colo. State Univ., Fort Collins

36. Brown, E. T., R. F. Stallard, M. C. Larsen, G. M. Raisbeck, and F. Yiou (1995), Denudation rates determined from the accumulation of in situ-produced  $^{10}\text{Be}$  in the luquillo experimental forest, Puerto Rico, *Earth and Planetary Science Letters*, 129 (1–4), 193–202, doi: [http://dx.doi.org/10.1016/0012-821X\(94\)00249-X](http://dx.doi.org/10.1016/0012-821X(94)00249-X)
37. Brown, E. T., R. F. Stallard, M. C. Larsen, D. L. Bourlès, G. M. Raisbeck, and F. Yiou (1998), Determination of predevelopment denudation rates of an agricultural watershed (Cayaguás River, Puerto Rico) using in-situ-produced  $^{10}\text{Be}$  in river-borne quartz, *Earth and Planetary Science Letters*, 160 (3–4), 723–728, doi: [http://dx.doi.org/10.1016/S0012-821X\(98\)00123-X](http://dx.doi.org/10.1016/S0012-821X(98)00123-X)
38. Burton, A., and J. C. Bathurst (1998), Physically based modelling of shallow landslide sediment yield at a catchment scale, *Environmental Geology*, 35 (2–3), 89–99, doi: [10.1007/s002540050296](http://dx.doi.org/10.1007/s002540050296)
39. Buss, H. L., and A. F. White (2012), Weathering processes in the Icacos and Mameyes watersheds in eastern Puerto Rico, in *Murphy, S.F., and Stallard, R.F., eds., Water quality and landscape processes of four watersheds in eastern Puerto Rico: U.S. Geological Survey Professional Paper 1789*, 249–262
40. Campbell, J. D., M. A. Taylor, T. S. Stephenson, R. A. Watson, and F. S. Whyte (2011), Future climate of the Caribbean from a regional climate model, *International Journal of Climatology*, 31 (12), 1866–1878, doi: [10.1002/joc.2200](http://dx.doi.org/10.1002/joc.2200)
41. Capparelli, G., and I. P. Versace (2010), FLAIIR and SUSHI: two mathematical models for early warning of landslides induced by rainfall, *Landslides*, 8, 67–79
42. Carretier, S., V. Regard, R. Vassallo, J. Martinod, F. Christophoul, E. Gayer, L. Audin, and C. Lagane (2015), A note on  $^{10}\text{Be}$ -derived mean erosion rates in catchments with heterogeneous lithology: examples from the western Central Andes, *Earth Surface Processes and Landforms*, 40 (13), 1719–1729, doi: [10.1002/esp.3748](http://dx.doi.org/10.1002/esp.3748)
43. Casadei, M., W. E. Dietrich, and N. L. Miller (2003), Testing a model for predicting the timing and location of shallow landslide initiation in soil-mantled landscapes, *Earth Surface Processes and Landforms*, 28 (9), 925–950, doi: [10.1002/esp.470](http://dx.doi.org/10.1002/esp.470)
44. Chabaux, F., E. Blaes, P. Stille, R. di Chiara Roupert, E. Pelt, A. Dosseto, L. Ma, H. L. Buss, and S. L. Brantley (2013), Regolith formation rate from U-series nuclides: Implications from the study of a spheroidal weathering profile in the Rio Icacos watershed (Puerto Rico), *Geochimica et Cosmochimica Acta*, 100, 73–95, doi: <http://dx.doi.org/10.1016/j.gca.2012.09.037>
45. Chaopricha, N. T., and E. Marín-Spiotta (2014), Soil burial contributes to deep soil organic carbon storage, *Soil Biology and Biochemistry*, 69, 251–264, doi: <http://dx.doi.org/10.1016/j.soilbio.2013.11.011>

46. Chappell, A., J. Baldock, and J. Sanderman (2016), The global significance of omitting soil erosion from soil organic carbon cycling schemes, *Nature Clim. Change*, 6 (2), 187-191, doi: 10.1038/nclimate2829
47. Chen, Y.-C., K.-t. Chang, Y.-J. Chiu, S.-M. Lau, and H.-Y. Lee (2013), Quantifying rainfall controls on catchment-scale landslide erosion in Taiwan, *Earth Surface Processes and Landforms*, 38 (4), 372-382, doi: 10.1002/esp.3284
48. Christian, J., C. Ladd, and G. Baecher (1994), Reliability Applied to Slope Stability Analysis, *Journal of Geotechnical Engineering*, 120 (12), 2180-2207, doi: doi:10.1061/(ASCE)0733-9410(1994)120:12(2180)
49. Ciais, P., C. Sabine, G. Bala, L. Bopp, V. Brovkin, J. Canadell, A. Chhabra, R. DeFries, J. Galloway, M. Heimann, C. Jones, C. L. Quéré, R. B. Myneni, S. Piao, and P. Thornton (2013), Carbon and Other Biogeochemical Cycles, in *Climate Change 2013: The Physical Science Basis. Contribution of Working Group I to the Fifth Assessment Report of the Intergovernmental Panel on Climate Change*, edited by T. F. Stocker, D. Qin, G.-K. Plattner, M. Tignor, S. K. Allen, J. Boschung, A. Nauels, Y. Xia, V. Bex and P. M. Midgley, pp. 465–570, Cambridge University Press, Cambridge, United Kingdom and New York, NY, USA.
50. Claessens, L., G. B. M. Heuvelink, J. M. Schoorl, and A. Veldkamp (2005), DEM resolution effects on shallow landslide hazard and soil redistribution modelling, *Earth Surface Processes and Landforms*, 30 (4), 461-477, doi: 10.1002/esp.1155
51. Coleman, K., D. S. Jenkinson, G. J. Crocker, P. R. Grace, J. Klír, M. Körschens, P. R. Poulton, and D. D. Richter (1997), Simulating trends in soil organic carbon in long-term experiments using RothC-26.3, *Geoderma*, 81 (1), 29-44, doi: 10.1016/S0016-7061(97)00079-7
52. Cook, T. L., B. C. Yellen, J. D. Woodruff, and D. Miller (2015), Contrasting human versus climatic impacts on erosion, *Geophysical Research Letters*, 42 (16), 6680-6687, doi: 10.1002/2015GL064436
53. Cusack, D. F., M. S. Torn, W. H. McDowell, and W. L. Silver (2010), The response of heterotrophic activity and carbon cycling to nitrogen additions and warming in two tropical soils, *Global Change Biology*, 16 (9), 2555-2572, doi: 10.1111/j.1365-2486.2009.02131.x
54. D'Odorico, P., S. Fagherazzi, and R. Rigon (2005), Potential for landsliding: Dependence on hypsograph characteristics, *Journal of Geophysical Research: Earth Surface*, 110 (F1), F01007, doi: 10.1029/2004jf000127
55. Daly, C., and R. P. Neilson (1992), A digital topographic approach to modeling the distribution of precipitation in mountainous terrain, in *Interdisciplinary Approaches in Hydrology and Hydrogeology*, edited by M. E. Jones and A. Laenen, pp. 437-454, American Institute of Hydrology, Minneapolis, MN.

56. Daly, C., E. H. Helmer, and M. Quinones (2003), Mapping the climate of Puerto Rico, Vieques and Culebra, *International Journal of Climatology*, 23 (11), 1359-1381
57. Daly, C., W. P. Gibson, G. H. Taylor, G. L. Johnson, and P. Pasteris (2002), A knowledge-based approach to the statistical mapping of climate, *Climate Research*, 22 (2), 99-113
58. De Rose, R. C. (2013), Slope control on the frequency distribution of shallow landslides and associated soil properties, North Island, New Zealand, *Earth Surface Processes and Landforms*, 38 (4), 356-371, doi: 10.1002/esp.3283
59. DeLucia, E. H., J. E. Drake, R. B. Thomas, and M. Gonzalez-Meler (2007), Forest carbon use efficiency: is respiration a constant fraction of gross primary production?, *Global Change Biology*, 13 (6), 1157-1167, doi: 10.1111/j.1365-2486.2007.01365.x
60. Dettinger, M., and J. Wilson (1961), First order analysis of uncertainty in numerical models of groundwater flow part: 1. Mathematical development, *Water Resources Research*, 17 (1), 149-161
61. Dialynas, Y. G., and R. L. Bras (2016), Influence of Climate Change on the Evolution of Contrasting Tropical Landscapes in the Luquillo Critical Zone Observatory, *American Geophysical Union Fall Meeting, Abstract H51N-08, San Francisco, CA, Dec. 12-16*
62. Dialynas, Y. G., and R. L. Bras (2017), Evolution of Contrasting Tropical Landscapes and Critical Zone Response to Changing Climate. *Earth Surface Processes and Landforms* (in review)
63. Dialynas, Y. G., R. L. Bras, and D. D. Richter (2017), Hydro-geomorphic perturbations on the soil-atmosphere CO<sub>2</sub> exchange: how (un)certain are our balances? *Water Resources Research* (in review)
64. Dialynas, Y. G., E. Arnone, L. V. Noto, and R. L. Bras (2013), A probabilistic approach for shallow rainfall-triggered landslide modeling at basin scale. A case study in the Luquillo Forest, Puerto Rico, *American Geophysical Union Fall Meeting, Abstract NH32A-06, San Francisco, CA, Dec. 09-13*
65. Dialynas, Y. G., S. Bastola, S. A. Billings, and R. L. Bras (2014), Assessing the Impact of Landscape Evolution on Carbon Dynamics: A Coupled Physically-Based Modelling Approach, *American Geophysical Union Fall Meeting, Abstract H42C-03, San Francisco, CA, Dec. 15-19*
66. Dialynas, Y. G., S. Bastola, R. L. Bras, S. A. Billings, D. Markewitz, and D. D. Richter (2016a), Topographic variability and the influence of soil erosion on the carbon cycle, *Global Biogeochemical Cycles* 30 (5), 644-660, doi: 10.1002/2015GB005302
67. Dialynas, Y. G., S. Bastola, R. L. Bras, E. Marín-Spiotta, W. L. Silver, E. Arnone, and L. V. Noto (2015), Influence of Soil Erosion and Landslide Occurrence on Soil Organic Carbon



Storage and Loss in the Luquillo Critical Zone Observatory, Puerto Rico, *American Geophysical Union Fall Meeting, Abstract EP23C-0987, San Francisco, CA, Dec. 14-18*

68. Dialynas, Y. G., S. Bastola, R. L. Bras, E. Marín-Spiotta, W. L. Silver, L. V. Noto, and E. Arnone (2016b), Impact of hydrologically driven hillslope erosion and landslide occurrence on soil organic carbon dynamics in tropical watersheds, *Water Resources Research*, 52 (11), 8895-8919, doi: 10.1002/2016WR018925
69. Dietrich, W., R. Reiss, M. Hsu, and D. Montgomery (1995), A process-based model for colluvial soil depth and shallow landsliding using digital elevation data, *Hydrological Processes*, doi: 10.1002/hyp.3360090311
70. Dixon, B., and J. Earls (2009), Resample or not?! Effects of resolution of DEMs in watershed modeling, *Hydrological Processes*, 23 (12), 1714-1724, doi: 10.1002/hyp.7306
71. Dlugosz, V., P. Fiener, K. Van Oost, and K. Schneider (2012), Model based analysis of lateral and vertical soil carbon fluxes induced by soil redistribution processes in a small agricultural catchment, *Earth Surface Processes and Landforms*, 37 (2), 193-208, doi: 10.1002/esp.2246
72. Doetterl, S., K. Van Oost, and J. Six (2012), Towards constraining the magnitude of global agricultural sediment and soil organic carbon fluxes, *Earth Surface Processes and Landforms*, 37 (6), 642-655, doi: 10.1002/esp.3198
73. Doetterl, S., A. A. Berhe, E. Nadeu, Z. Wang, M. Sommer, and P. Fiener (2016), Erosion, deposition and soil carbon: A review of process-level controls, experimental tools and models to address C cycling in dynamic landscapes, *Earth-Science Reviews*, 154, 102-122, doi: <http://dx.doi.org/10.1016/j.earscirev.2015.12.005>
74. Dosseto, A., H. L. Buss, and P. O. Suresh (2012), Rapid regolith formation over volcanic bedrock and implications for landscape evolution, *Earth and Planetary Science Letters*, 337-338, 47-55, doi: <http://dx.doi.org/10.1016/j.epsl.2012.05.008>
75. Dosseto, A., H. L. Buss, and F. Chabaux (2014), Age and weathering rate of sediments in small catchments: The role of hillslope erosion, *Geochimica et Cosmochimica Acta*, 132, 238-258, doi: <http://dx.doi.org/10.1016/j.gca.2014.02.010>
76. Dykes, A. P., and J. Warburton (2007), Significance of geomorphological and subsurface drainage controls on failures of peat-covered hillslopes triggered by extreme rainfall, *Earth Surface Processes and Landforms*, 32 (12), 1841-1862, doi: 10.1002/esp.1499
77. Efstratiadis, A., Y. G. Dialynas, S. Kozanis, and D. Koutsoyiannis (2014), A multivariate stochastic model for the generation of synthetic time series at multiple time scales reproducing long-term persistence, *Environmental Modelling & Software*, 62, 139-152, doi: 10.1016/j.envsoft.2014.08.017

78. Ewel, J. J., and J. L. Whitmore (1973), The ecological life zones of Puerto Rico and the U.S. Virgin Islands., *U.S. Forest Service Research Paper Rep.*, Institute of Tropical forestry, Rio Piedras, Puerto Rico.
79. Fatichi, S., V. Y. Ivanov, and E. Caporali (2011), Simulation of future climate scenarios with a weather generator, *Advances in Water Resources*, 34 (4), 448-467, doi: 10.1016/j.advwatres.2010.12.013
80. Feller, W. (1971), *An introduction to probability theory and its applications*, Wiley.
81. Fiener, P., V. Dlugob, and K. Van Oost (2015), Erosion-induced carbon redistribution, burial and mineralisation — Is the episodic nature of erosion processes important?, *CATENA*, 133, 282-292, doi: <http://dx.doi.org/10.1016/j.catena.2015.05.027>
82. Finney, H. J. (1984), The effect of crop covers on rainfall characteristics and splash detachment, *Journal of Agricultural Engineering Research*, 29 (4), 337-343, doi: 10.1016/0021-8634(84)90089-1
83. Flores, A. N., D. Entekhabi, and R. L. Bras (2010), Reproducibility of soil moisture ensembles when representing soil parameter uncertainty using a Latin Hypercube-based approach with correlation control, *Water Resources Research*, 46 (4), W04506, doi: 10.1029/2009wr008155
84. Formetta, G., S. Simoni, J. W. Godt, N. Lu, and R. Rigon (2016), Geomorphological control on variably saturated hillslope hydrology and slope instability, *Water Resources Research*, 52 (6), 4590-4607, doi: 10.1002/2015WR017626
85. Foster, D. R., M. Fluet, and E. R. Boose (1999), Human or Natural Disturbance: Landscape-Scale Dynamics of the Tropical Forests of Puerto Rico, *Ecological Applications*, 9 (2), 555-572, doi: 10.1890/1051-0761(1999)009[0555:HONDLS]2.0.CO;2
86. Francipane, A. (2010), tRIBS-Erosion: a physically-based model for studying mechanisms of eco-hydro-geomorphic coupling, Ph.D thesis, University of Palermo, Italy.
87. Francipane, A., S. Fatichi, V. Y. Ivanov, and L. V. Noto (2015), Stochastic assessment of climate impacts on hydrology and geomorphology of semiarid headwater basins using a physically based model, *Journal of Geophysical Research: Earth Surface*, 120 (3), 507-533, doi: 10.1002/2014JF003232
88. Francipane, A., V. Y. Ivanov, L. V. Noto, E. Istanbuluoglu, E. Arnone, and R. L. Bras (2012), tRIBS-Erosion: A parsimonious physically-based model for studying catchment hydro-geomorphic response, *CATENA*, 92, 216-231, doi: 10.1016/j.catena.2011.10.005
89. Frattini, P., G. Crosta, and R. Sosio (2009), Approaches for defining thresholds and return periods for rainfall-triggered shallow landslides, *Hydrological Processes*, 23 (10), 1444-1460, doi: 10.1002/hyp.7269

90. Fredlund, D. F., and A. E. Dahlman (1972), Statistical Geotechnical Properties of Glacial Lake Edmonton Sediments, in *Statistics and Probability in Civil Engineering*, edited by H. K. U. Press, Oxford University Press, London.
91. Gabet, E. J., S. M. Mudd, D. T. Milodowski, K. Yoo, M. D. Hurst, and A. Dosseto (2015), Local topography and erosion rate control regolith thickness along a ridgeline in the Sierra Nevada, California, *Earth Surface Processes and Landforms*, 40 (13), 1779-1790, doi: 10.1002/esp.3754
92. Garcia-Martino, A. R., G. S. Warner, F. N. Scatena, and D. L. Civco (1996), Rainfall, Runoff and Elevation Relationships in the Luquillo Mountains of Puerto Rico, *Caribbean Journal of Science*, 32 (4), 413-424
93. Garrote, L., and R. L. Bras (1995), A distributed model for real-time flood forecasting using digital elevation models, *Journal of Hydrology*, 167, 279-306, doi: 10.1016/0022-1694(94)02592-Y
94. Gellis, A. C., R. M. T. Webb, S. C. McIntyre, and W. J. Wolfe (2006), Land-Use Effects on Erosion, Sediment Yields, and Reservoir Sedimentation: A Case Study in the Lago Loíza Basin, Puerto Rico, *Physical Geography*, 27 (1), 39-69, doi: 10.2747/0272-3646.27.1.39
95. Guns, M., and V. Vanacker (2014), Shifts in landslide frequency–area distribution after forest conversion in the tropical Andes, *Anthropocene*, 6, 75-85, doi: <http://dx.doi.org/10.1016/j.ancene.2014.08.001>
96. Guzzetti, F., B. D. Malamud, D. L. Turcotte, and P. Reichenbach (2002), Power-law correlations of landslide areas in central Italy, *Earth and Planetary Science Letters*, 195 (3–4), 169-183, doi: [http://dx.doi.org/10.1016/S0012-821X\(01\)00589-1](http://dx.doi.org/10.1016/S0012-821X(01)00589-1)
97. Hales, T. C., C. R. Ford, T. Hwang, J. M. Vose, and L. E. Band (2009), Topographic and ecologic controls on root reinforcement, *Journal of Geophysical Research: Earth Surface*, 114 (F3), n/a-n/a, doi: 10.1029/2008JF001168
98. Hansen, M. C., R. S. Defries, J. R. G. Townshend, and R. Sohlberg (2000), Global land cover classification at 1 km spatial resolution using a classification tree approach, *International Journal of Remote Sensing*, 21 (6-7), 1331-1364, doi: 10.1080/014311600210209
99. Harden, J. W., J. M. Sharpe, W. J. Parton, D. S. Ojima, T. L. Fries, T. G. Huntington, and S. M. Dabney (1999), Dynamic replacement and loss of soil carbon on eroding cropland, *Global Biogeochemical Cycles*, 13 (4), 885-901, doi: 10.1029/1999GB900061
100. Hayhoe, K. (2013), Quantifying Key Drivers of Climate Variability and Change for Puerto Rico and the Caribbean. Final Report 1 Oct 2011-30 Sep 2012. 2013. 241 p. Agreement No.: G10AC00582 (<http://caribbeanlcc.org/data-center/>)

101. Heartsill Scalley, T., F. N. Scatena, S. Moya, and A. E. Lugo (2012), Long-term dynamics of organic matter and elements exported as coarse particulates from two Caribbean montane watersheds, *Journal of Tropical Ecology*, 28 (02), 127-139, doi: 10.1017/S0266467411000733
102. Heimsath, A. M., W. E. Dietrich, K. Nishiizumi, and R. C. Finkel (1997), The soil production function and landscape equilibrium, *Nature*, 388 (6640), 358-361, doi: 10.1038/41056
103. Heimsath, A. M., W. E. Dietrich, K. Nishiizumi, and R. C. Finkel (1999), Cosmogenic nuclides, topography, and the spatial variation of soil depth, *Geomorphology*, 27 (1-2), 151-172, doi: [http://dx.doi.org/10.1016/S0169-555X\(98\)00095-6](http://dx.doi.org/10.1016/S0169-555X(98)00095-6)
104. Helmer, E. H., O. R. Ramos, T. M. Lopez, M. Quinones, and W. Diaz (2002), Mapping forest type and land cover of Puerto Rico, a component of the Caribbean biodiversity hotspot., *Caribbean Journal of Science*, 38, 165-183
105. Hergarten, S. (2002), *Self-Organized Criticality in Earth Systems*, Springer, Berlin.
106. Hergarten, S. (2003), Landslides, sandpiles, and self-organized criticality, *Nat. Hazards Earth Syst. Sci.*, 3 (6), 505-514, doi: 10.5194/nhess-3-505-2003
107. Hergarten, S., and H. J. Neugebauer (1998), Self-organized criticality in a landslide model, *Geophysical Research Letters*, 25 (6), 801-804, doi: 10.1029/98GL50419
108. Hillel, D. (1980), *Fundamentals of soil physics*, Academic Press, New York, NY, USA.
109. Hilton, R. G., A. Galy, N. Hovius, M.-C. Chen, M.-J. Horng, and H. Chen (2008), Tropical-cyclone-driven erosion of the terrestrial biosphere from mountains, *Nature Geosci.*, 1 (11), 759-762, doi: [http://www.nature.com/ngeo/journal/v1/n11/supinfo/ngeo333\\_S1.html](http://www.nature.com/ngeo/journal/v1/n11/supinfo/ngeo333_S1.html)
110. Holdridge, L. R. (1967), *Life zone ecology*, 206 pp., San Jose, Costa Rica, Tropical Science Center.
111. Hosking, J. R. M., and J. R. Wallis (1997), *Regional Frequency Analysis, an approach based on L-moments*, Cambridge University Press, Cambridge, UK.
112. Houghton, R. A. (2012), Carbon emissions and the drivers of deforestation and forest degradation in the tropics, *Current Opinion in Environmental Sustainability*, 4 (6), 597-603, doi: <http://dx.doi.org/10.1016/j.cosust.2012.06.006>
113. Hu, Y., and N. J. Kuhn (2014), Aggregates reduce transport distance of soil organic carbon: are our balances correct?, *Biogeosciences Discuss.*, 11 (6), 8829-8859, doi: 10.5194/bgd-11-8829-2014
114. Huggel, C., J. J. Clague, and O. Korup (2012), Is climate change responsible for changing landslide activity in high mountains?, *Earth Surface Processes and Landforms*, 37 (1), 77-91, doi: 10.1002/esp.2223

115. IPCC (2007), Climate Change 2007: The Physical Science Basis. Contribution of Working Group I to the Fourth Assessment Report of the Intergovernmental Panel on Climate Change [Solomon, S., D. Qin, M. Manning, Z. Chen, M. Marquis, K.B. Averyt, M. Tignor and H.L. Miller (eds.)]. Cambridge University Press, Cambridge, United Kingdom and New York, NY, USA, 996
116. Ivanov, V. Y., R. L. Bras, and D. C. Curtis (2007), A weather generator for hydrological, ecological, and agricultural applications, *Water Resources Research*, 43 (10), doi: 10.1029/2006WR005364
117. Ivanov, V. Y., R. L. Bras, and E. R. Vivoni (2008a), Vegetation-Hydrology Dynamics in Complex Terrain of Semiarid Areas: II. Energy-Water Controls of Vegetation Spatio-Temporal Dynamics and Topographic Niches of Favorability, *Water Resources Research*, 44 (20), W03430, doi: 10.1029/2006WR005595
118. Ivanov, V. Y., R. L. Bras, and E. R. Vivoni (2008b), Vegetation-hydrology dynamics in complex terrain of semiarid areas: 1. A mechanistic approach to modeling dynamic feedbacks, *Water Resources Research*, 44 (3), W03429, doi: 10.1029/2006WR005588
119. Ivanov, V. Y., E. R. Vivoni, R. L. Bras, and D. Entekhabi (2004a), Catchment hydrologic response with a fully distributed triangulated irregular network model, *Water Resources Research*, 40 (11), W11102, doi: 10.1029/2004WR003218
120. Ivanov, V. Y., E. R. Vivoni, R. L. Bras, and D. Entekhabi (2004b), Preserving, high-resolution surface and rainfall data in operational-scale basin hydrology: a fully-distributed physically-based approach, *Journal of Hydrology*, 298, 80-111, doi: 10.1016/j.jhydrol.2004.03.041
121. Iverson, R. M. (2000), Landslide triggering by rain infiltration, *Water Resources Research*, 36, 1897-1910
122. Jacinthe, P. A., and R. Lal (2001), A mass balance approach to assess carbon dioxide evolution during erosional events, *Land Degradation & Development*, 12 (4), 329-339, doi: 10.1002/ldr.454
123. James, L. A. (2013), Legacy sediment: Definitions and processes of episodically produced anthropogenic sediment, *Anthropocene*, 2, 16-26, doi: <http://dx.doi.org/10.1016/j.ancene.2013.04.001>
124. James, L. A., D. G. Watson, and W. F. Hansen (2007), Using LiDAR data to map gullies and headwater streams under forest canopy: South Carolina, USA, *CATENA*, 71 (1), 132-144, doi: 10.1016/j.catena.2006.10.010
125. Jenny, H. (1941), *Factors of Soil Formation: A System of Quantitative Pedology*, 269 pp., McGraw-Hill, New York.

126. Johnson, A. H., H. X. Xing, and F. N. Scatena (2015), Controls on Soil Carbon Stocks in El Yunque National Forest, Puerto Rico, *Soil Science Society of America Journal*, 79 (1), 294-304, doi: 10.2136/sssaj2014.05.0199
127. Keefer, D. K., and M. C. Larsen (2007), Assessing Landslide Hazards, *Science*, 316 (5828), 1136-1138, doi: 10.1126/science.1143308
128. Keijsers, J. G. S., J. M. Schoorl, K. T. Chang, S. H. Chiang, L. Claessens, and A. Veldkamp (2011), Calibration and resolution effects on model performance for predicting shallow landslide locations in Taiwan, *Geomorphology*, 133 (3-4), 168-177, doi: <http://dx.doi.org/10.1016/j.geomorph.2011.03.020>
129. Kilsby, C. G., P. D. Jones, A. Burton, A. C. Ford, H. J. Fowler, C. Harpham, P. James, A. Smith, and R. L. Wilby (2007), A daily weather generator for use in climate change studies, *Environmental Modelling & Software*, 22 (12), 1705-1719, doi: 10.1016/j.envsoft.2007.02.005
130. Kim, J., V. Y. Ivanov, and N. D. Katopodes (2013), Modeling erosion and sedimentation coupled with hydrological and overland flow processes at the watershed scale, *Water Resources Research*, 49 (9), 5134-5154, doi: 10.1002/wrcr.20373
131. Kim, J., V. Y. Ivanov, and S. Fatichi (2016), Environmental stochasticity controls soil erosion variability, *Scientific Reports*, 6, 22065, doi: 10.1038/srep22065
132. Kirchner, J. W., R. C. Finkel, C. S. Riebe, D. E. Granger, J. L. Clayton, J. G. King, and W. F. Megahan (2001), Mountain erosion over 10 yr, 10 k.y., and 10 m.y. time scales, *Geology*, 29 (7), 591-594, doi: 10.1130/0091-7613(2001)029<0591:meoyky>2.0.co;2
133. Koutsoyiannis, D. (1999), Optimal decomposition of covariance matrices for multivariate stochastic models in hydrology, *Water Resources Research*, 35 (4), 1219-1229, doi: 10.1029/1998WR900093
134. Koven, C. D., W. J. Riley, Z. M. Subin, J. Y. Tang, M. S. Torn, W. D. Collins, G. B. Bonan, D. M. Lawrence, and S. C. Swenson (2013), The effect of vertically resolved soil biogeochemistry and alternate soil C and N models on C dynamics of CLM4, *Biogeosciences*, 10 (11), 7109-7131, doi: 10.5194/bg-10-7109-2013
135. Kuhn, N. J., T. Hoffmann, W. Schwanghart, and M. Dotterweich (2009), Agricultural soil erosion and global carbon cycle: controversy over?, *Earth Surface Processes and Landforms*, 34 (7), 1033-1038, doi: 10.1002/esp.1796
136. Lal, R. (1995), Global soil erosion by water and carbon dynamics, in *Soils and Global Change*, edited by J. M. Kimble, E. Levine and B. A. Stewart, pp. 131-141, CRC/Lewis Boca Raton, FL.
137. Lal, R. (2003), Soil erosion and the global carbon budget, *Environment International*, 29 (4), 437-450, doi: 10.1016/S0160-4120(02)00192-7

138. Lal, R. (2004), Soil carbon sequestration to mitigate climate change, *Geoderma*, 123 (1–2), 1–22, doi: 10.1016/j.geoderma.2004.01.032
139. Langejan, A. (1965), Some aspects of the safety factor in soil mechanics considered as a problem of probability, paper presented at Sixt Int. Conf. Soil Mechanics and Foundation Eng, Montreal, Quebec.
140. Lanni, C., R. Rigon, E. Cordan, and A. Tarantino (2009), Analysis of the effect of normal and lateral subsurface water flow on the triggering of shallow landslides with a distributed hydrological model, in *International Conference 'Landslide Processes', France*,, edited.
141. Larsen, I. J., and D. R. Montgomery (2012), Landslide erosion coupled to tectonics and river incision, *Nature Geosci*, 5 (7), 468-473, doi: <http://www.nature.com/ngeo/journal/v5/n7/abs/ngeo1479.html#supplementary-information>
142. Larsen, M. C. (1997), Tropical geomorphology and geomorphic work—A study of geomorphic processes and sediment and water budgets in montane humid-tropical forested and developed watersheds, Puerto Rico, 341 pp, Boulder, University of Colorado Geography Department, unpublished Ph.D. dissertation.
143. Larsen, M. C. (2012), Landslides and Sediment Budgets in Four Watersheds in Eastern Puerto Rico, in *Water quality and landscape processes of four watersheds in eastern Puerto Rico*, edited by S. F. Murphy and R. F. Stallard, pp. 153-178, U.S. Geol. Surv. Prof. Pap. 1789.
144. Larsen, M. C., and A. J. Torres-Sánchez (1992), Landslides triggered by the rainfall associated with Hurricane Hugo, eastern Puerto Rico, September 1989, *Caribbean Journal of Science*, 28 (3-4), 113-120
145. Larsen, M. C., and A. Simon (1993), A rainfall intensity-duration threshold for landslides in a humid- tropical environment, Puerto Rico, *Geografiska Annaler, Series A*, 75 A (1-2), 13-23, doi: 10.2307/521049
146. Larsen, M. C., and A. J. Torres-Sánchez (1998), The frequency and distribution of recent landslides in three montane tropical regions of Puerto Rico, *Geomorphology*, 24 (4), 309-331
147. Larsen, M. C., A. J. Torres-Sánchez, and I. M. Concepción (1999), Slopewash, surface runoff and fine-litter transport in forest and landslide scars in humid-tropical steeplands, luquillo experimental forest, Puerto Rico, *Earth Surface Processes and Landforms*, 24 (6), 481-502, doi: 10.1002/(SICI)1096-9837(199906)24:6<481::AID-ESP967>3.0.CO;2-G
148. Lebedeva, M. I., and S. L. Brantley (2013), Exploring geochemical controls on weathering and erosion of convex hillslopes: beyond the empirical regolith production function, *Earth Surface Processes and Landforms*, 38 (15), 1793-1807, doi: 10.1002/esp.3424

149. Lebedeva, M. I., R. C. Fletcher, and S. L. Brantley (2010), A mathematical model for steady-state regolith production at constant erosion rate, *Earth Surface Processes and Landforms*, 35 (5), 508-524, doi: 10.1002/esp.1954
150. Lee, J. A. Y. (1991), Comparison of existing methods for building triangular irregular network models of terrain from grid digital elevation models, *International Journal of Geographical Information Systems*, 5 (3), 267-285, doi: 10.1080/02693799108927855
151. Lepore, C., E. Arnone, L. V. Noto, G. Sivandran, and R. L. Bras (2013), Physically based modeling of rainfall-triggered landslides: a case study in the Luquillo forest, Puerto Rico, *Hydrol. Earth Syst. Sci.*, 17 (9), 3371-3387, doi: 10.5194/hess-17-3371-2013
152. Liu, S., N. Bliss, E. Sundquist, and T. G. Huntington (2003), Modeling carbon dynamics in vegetation and soil under the impact of soil erosion and deposition, *Global Biogeochemical Cycles*, 17 (2), 1074, doi: 10.1029/2002GB002010
153. Lohnes, R. A., and T. Demirel (1973), Strength and structure of laterites and lateritic soils, *Engineering Geology*, 7, 13-33
154. Lumb, P. (1966), The Variability of Natural Soils, *Canadian Geotechnical Journal*, 3 (2), 74-97, doi: 10.1139/t66-009
155. Lumb, P. (1970), Safety factors and the probability distribution of soil strength, *Canadian Geotechnical Journal*, 7 (3), 225-242, doi: 10.1139/t70-032
156. Lumb, P. (1974), Applications of statistics in soil mechanics, in *Soil mechanics. New Horizons*, edited by L. JK, London.
157. Malkawi, A. I., W. F. Hassan, and F. A. Abdulla (2000), Uncertainty and reliability analysis applied to slope stability, *Structural Safety*, 22, 161-187
158. Markewitz, D., and D. D. Richter (1998), The Bio in Aluminum and Silicon Geochemistry, *Biogeochemistry*, 42 (1-2), 235-252, doi: 10.1023/A:1005901417165
159. Matsuo, M., and K. Kuroda (1974), Probabilistic Approach to Design of Embankments, *Soils and Foundations*, 14 (2), 1-17
160. McCuen, R. H., W. J. Rawls, and D. L. Brakensiek (1981), Statistical analysis of the Brooks-Corey and the Green-Ampt parameters across soil textures, *Water Resources Research*, 17 (4), 1005-1013, doi: 10.1029/WR017i004p01005
161. McDowell, W. H., and C. E. Asbury (1994), Export of carbon, nitrogen, and major ions from three tropical montane watersheds, *Limnology and Oceanography*, 39 (1), 111-125, doi: 10.4319/lo.1994.39.1.0111



162. Melchiorre, C., and P. Frattini (2012), Modelling probability of rainfall-induced shallow landslides in a changing climate, Otta, Central Norway, *Climatic Change*, 113 (2), 413-436, doi: 10.1007/s10584-011-0325-0
163. Metz, L. J. (1958), The Calhoun Experimental Forest. US Department of Agriculture Forest Service, Asheville, NC, USA
164. Meyer, L. D., and W. C. Harmon (1984), Susceptibility of Agricultural Soils to Interrill Erosion, *Soil Sci. Soc. Am. J.*, 48 (5), 1152-1157, doi: 10.2136/sssaj1984.03615995004800050040x
165. Meyer, P. D., M. L. Rockhold, and G. W. Gee (1997), *Uncertainty analyses of infiltration and subsurface flow and transport for SDMP sites*, Pacific Northwest National, Laboratory, Division of Regulatory Applications, Office of Nuclear Regulatory Research, U.S. Nuclear Regulatory Commission Washington, DC.
166. Mobley, M. L., K. Lajtha, M. G. Kramer, A. R. Bacon, P. R. Heine, and D. D. Richter (2015), Surficial gains and subsoil losses of soil carbon and nitrogen during secondary forest development, *Global Change Biology*, 21 (2), 986-996, doi: 10.1111/gcb.12715
167. Montgomery, D. R. (2007), Soil erosion and agricultural sustainability, *Proceedings of the National Academy of Sciences*, 104 (33), 13268-13272, doi: 10.1073/pnas.0611508104
168. Montgomery, D. R., and W. E. Dietrich (1994), A physically based model for the topographic control on shallow landsliding, *Water Resources Research*, 30, 1153-1171
169. Moos, C., P. Bebi, F. Graf, J. Mattli, C. Rickli, and M. Schwarz (2016), How does forest structure affect root reinforcement and susceptibility to shallow landslides?, *Earth Surface Processes and Landforms*, 41 (7), 951-960, doi: 10.1002/esp.3887
170. Moriasi, D. N., J. G. Arnold, M. W. V. Liew, R. L. Bingner, R. D. Harmel, and T. L. Veith (2007), Model evaluation guidelines for systematic quantification of accuracy in watershed simulations, *Transactions of the ASABE*, 50 (3), 885-900
171. Murphy, S. F., and R. F. Stallard (2012), Hydrology and Climate of Four Watersheds in Eastern Puerto Rico, in *Water quality and landscape processes of four watersheds in eastern Puerto Rico*, edited by S. F. Murphy and R. F. Stallard, pp. 43-83, U.S. Geol. Surv. Prof. Pap. 1789.
172. Murphy, S. F., R. F. Stallard, M. C. Larsen, and W. A. Gould (2012), Physiography, Geology, and Land Cover of Four Watersheds in Eastern Puerto Rico, in *Water quality and landscape processes of four watersheds in eastern Puerto Rico*, edited by S. F. Murphy and R. F. Stallard, pp. 1-23, U.S. Geol. Surv. Prof. Pap. 1789.
173. Nakićenović, N., and R. Swart (eds.) (2000), Special Report on Emissions Scenarios. A Special Report of Working Group III of the Intergovernmental Panel on Climate Change. Cambridge University Press, Cambridge, United Kingdom and New York, NY, USA, 599 pp.

174. NCALM (2014), Hyperspectral and LiDAR Survey of the Calhoun Critical Zone Observatory, <http://calm.geo.berkeley.edu/data/CZOSC2014/>
175. Noto, L., V. Ivanov, R. Bras, and E. Vivoni (2008), Effects of initialization on response of a fully-distributed hydrologic model, *Journal of Hydrology*, 352, 107-125, doi: doi:10.1016/j.jhydrol.2007.12.031
176. NRC (2001), *Basic Research Opportunities in Earth Science*, National Academy Press.
177. Odorico, P. D., S. Fagherazzi, and R. Rigon (2005), Potential for landsliding: Dependence on hyetograph characteristics, *Journal of Geophysical Research*, 110, 1-10
178. Ogden, F. L., and P. Y. Julien (1993), Runoff sensitivity to temporal and spatial rainfall variability at runoff plane and small basin scales, *Water Resources Research*, 29 (8), 2589-2597, doi: 10.1029/93wr00924
179. Pack, R. T., D. G. Tarboton, and C. N. Goodwin (1998), *SINMAP, a stability index approach to terrain stability hazard mapping. SINMAP user's manual*, Terratech Consulting Ltd.
180. Papanicolaou, A. N., K. M. Wacha, B. K. Abban, C. G. Wilson, J. L. Hatfield, C. O. Stanier, and T. R. Filley (2015), From soils to landscapes: A landscape-oriented approach to simulate soil organic carbon dynamics in intensively managed landscapes, *Journal of Geophysical Research: Biogeosciences*, 120 (11), 2375-2401, doi: 10.1002/2015JG003078
181. Pearson, K. (1895), Contributions to the Mathematical Theory of Evolution. II. Skew Variation in Homogeneous Material, *Philosophical Transactions of the Royal Society of London. A*, 186 (ArticleType: research-article / Full publication date: 1895 / Copyright © 1895 The Royal Society), 343-414, doi: 10.2307/90649
182. Pelletier, J. D., B. D. Malamud, T. Blodgett, and D. L. Turcotte (1997), Scale-invariance of soil moisture variability and its implications for the frequency-size distribution of landslides, *Engineering Geology*, 48 (3-4), 255-268, doi: [http://dx.doi.org/10.1016/S0013-7952\(97\)00041-0](http://dx.doi.org/10.1016/S0013-7952(97)00041-0)
183. Pike, A. S., F. N. Scatena, and E. E. Wohl (2010), Lithological and fluvial controls on the geomorphology of tropical montane stream channels in Puerto Rico, *Earth Surface Processes and Landforms*, 35 (12), 1402-1417, doi: 10.1002/esp.1978
184. Polyakov, V. O., and R. Lal (2004), Soil Erosion and Carbon Dynamics Under Simulated Rainfall, *Soil Science*, 169 (8), 590-599
185. Post, W. M., and K. C. Kwon (2000), Soil carbon sequestration and land-use change: processes and potential, *Global Change Biology*, 6 (3), 317-327, doi: 10.1046/j.1365-2486.2000.00308.x
186. Prentice, I. C., G. D. Farquhar, M. J. R. Fasham, M. L. Goulden, M. Heimann, V. L. Jaramillo, H. S. Keshgi, C. L. Quéré, R. J. Scholes, and D. W. R. Wallace (2001), The carbon cycle and

atmospheric carbon dioxide, in *Climate change 2001—The scientific basis. Contribution of Working Group I to the third assessment report of the Intergovernmental Panel on Climate Change*, edited by J. T. Houghton, Y. Ding, D. J. Griggs, M. Noguer, P. J. v. d. Linden, X. Dai, K. Maskell and C. A. Johnson, pp. 183-237, Cambridge University Press, Cambridge, United Kingdom.

187. PRGAP (2006), Puerto Rico GAP Analysis Project (PRGAP) Landcover: USDA Forest Service, International Institute of Tropical Forestry, Río Piedras, Puerto Rico
188. Quinn, P. F., K. J. Beven, and R. Lamb (1995), The  $\ln(a/\tan\beta)$  index: How to calculate it and how to use it within the topmodel framework, *Hydrological Processes*, 9 (2), 161-182, doi: 10.1002/hyp.3360090204
189. Quinton, J. N., G. Govers, K. Van Oost, and R. D. Bardgett (2010), The impact of agricultural soil erosion on biogeochemical cycling, *Nature Geosci*, 3 (5), 311-314, doi: 10.1038/ngeo838
190. Rackwitz, R. (2000), Reviewing probabilistic soils modelling, *Computers and Geotechnics*, 26 (3-4), 199-223, doi: [http://dx.doi.org/10.1016/S0266-352X\(99\)00039-7](http://dx.doi.org/10.1016/S0266-352X(99)00039-7)
191. Ramos Scharrón, C. E., E. J. Castellanos, and C. Restrepo (2012), The transfer of modern organic carbon by landslide activity in tropical montane ecosystems, *Journal of Geophysical Research: Biogeosciences*, 117 (G3), doi: 10.1029/2011JG001838
192. Rawls, W. J., D. L. Brakensiek, and K. E. Saxton (1982), Estimation of Soil Water Properties, *Transactions American Society of Agricultural Engineers, St. Joseph, MI*, 25, 1316-2320
193. Ray, A., and D. Baidya (2011), Probabilistic Analysis of a Slope Stability Problem, paper presented at Indian Geotechnical Conference, Kochi, December 15-17, 2011.
194. Regnier, P., P. Friedlingstein, P. Ciais, F. T. Mackenzie, N. Gruber, I. A. Janssens, G. G. Laruelle, R. Lauerwald, S. Luyssaert, A. J. Andersson, S. Arndt, C. Arnosti, A. V. Borges, A. W. Dale, A. Gallego-Sala, Y. Godderis, N. Goossens, J. Hartmann, C. Heinze, T. Ilyina, F. Joos, D. E. LaRowe, J. Leifeld, F. J. R. Meysman, G. Munhoven, P. A. Raymond, R. Spahni, P. Suntharalingam, and M. Thullner (2013), Anthropogenic perturbation of the carbon fluxes from land to ocean, *Nature Geosci*, 6 (8), 597-607, doi: 10.1038/ngeo1830
195. Revels, J. (2005), Historical and Architectural Survey of Union County, South Carolina. Columbia, SC.
196. Richter, D. D. (2016), Personal communication
197. Richter, D. D., and D. Markewitz (2001), *Understanding Soil Change*, 255 pp., Cambridge Univ. Press, Cambridge, U.K.
198. Richter, D. D., and S. A. Billings (2015), 'One physical system': Tansley's ecosystem as Earth's critical zone, *New Phytologist*, 206 (3), 900-912, doi: 10.1111/nph.13338

199. Richter, D. D., D. Markewitz, S. E. Trumbore, and C. G. Wells (1999), Rapid accumulation and turnover of soil carbon in a re-establishing forest, *Nature*, 400 (6739), 56-58, doi: 10.1038/21867
200. Richter, D. D., H. L. Allen, J. Li, D. Markewitz, and J. Raikes (2006), Bioavailability of slowly cycling soil phosphorus: major restructuring of soil P fractions over four decades in an aggrading forest, *Oecologia*, 150 (2), 259-271, doi: 10.1007/s00442-006-0510-4
201. Richter, D. d., M. Hofmockel, M. A. Callahan, D. S. Powlson, and P. Smith (2007), Long-Term Soil Experiments: Keys to Managing Earth's Rapidly Changing Ecosystems, *Soil Science Society of America Journal*, 71 (2), 266-279, doi: 10.2136/sssaj2006.0181
202. Richter, D. D., D. Markewitz, P. R. Heine, V. Jin, J. Raikes, K. Tian, and C. G. Wells (2000), Legacies of agriculture and forest regrowth in the nitrogen of old-field soils, *Forest Ecology and Management*, 138 (1-3), 233-248, doi: [http://dx.doi.org/10.1016/S0378-1127\(00\)00399-6](http://dx.doi.org/10.1016/S0378-1127(00)00399-6)
203. Richter, D. D., A. R. Bacon, S. A. Billings, D. Binkley, M. Buford, M. A. Callahan, A. E. Curry, R. L. Fimmen, A. S. Grandy, P. R. Heine, M. Hofmockel, J. A. Jackson, E. LeMaster, J. Li, D. Markewitz, M. L. Mobley, M. W. Morrison, M. S. Strickland, T. Waldrop, and C. G. Wells (2014), Evolution of Soil, Ecosystem, and Critical Zone Research at the USDA FS Calhoun Experimental Forest, in *USDA Forest Service Experimental Forests and Ranges*, edited by D. C. Hayes, S. L. Stout, R. H. Crawford and A. P. Hoover, pp. 405-433, Springer New York.
204. Riebe, C. S., J. W. Kirchner, and R. C. Finkel (2003), Long-term rates of chemical weathering and physical erosion from cosmogenic nuclides and geochemical mass balance, *Geochimica et Cosmochimica Acta*, 67 (22), 4411-4427, doi: [http://dx.doi.org/10.1016/S0016-7037\(03\)00382-X](http://dx.doi.org/10.1016/S0016-7037(03)00382-X)
205. Roering, J. J., J. W. Kirchner, and W. E. Dietrich (1999), Evidence for nonlinear, diffusive sediment transport on hillslopes and implications for landscape morphology, *Water Resources Research*, 35 (3), 853-870, doi: 10.1029/1998WR900090
206. Rosenbloom, N. A., J. W. Harden, J. C. Neff, and D. S. Schimel (2006), Geomorphic control of landscape carbon accumulation, *Journal of Geophysical Research: Biogeosciences*, 111 (G1), G01004, doi: 10.1029/2005JG000077
207. Rosso, R. (2002), *Manuale di protezione idraulica del territorio*, Cusl.
208. Rosso, R., M. C. Rulli, and G. Vannucchi (2006), A physically based model for the hydrologic control on shallow landsliding, *Water Resources Research*, 42, 16, doi: 10.1029/2005WR004369

209. Rumpel, C., V. Chaplot, O. Planchon, J. Bernadou, C. Valentin, and A. Mariotti (2006), Preferential erosion of black carbon on steep slopes with slash and burn agriculture, *CATENA*, 65 (1), 30-40, doi: <http://dx.doi.org/10.1016/j.catena.2005.09.005>
210. Rutter, A. J., A. J. Morton, and P. C. Robins (1975), A predictive model of interception in forests. 2. Generalization of the model and comparison with observations in some coniferous and hardwood stands, *J. Appl. Ecol.*, 12, 367-380, doi: 10.2307/2401739
211. Rutter, A. J., Kershaw, Robins, and Morton (1971), A predictive model of rainfall interception in forests, 1. Derivation of the model from observation in a plantation of Corsican pine, *Agric. Meteorol.*, 367-384, doi: 10.1016/0002-1571(71)90034-3
212. Ryu, J.-H., and K. Hayhoe (2013), Understanding the sources of Caribbean precipitation biases in CMIP3 and CMIP5 simulations, *Climate Dynamics*, 42 (11), 3233-3252, doi: 10.1007/s00382-013-1801-1
213. S.C.D.N.R. (2009), South Carolina Dep. of Natural Resources, 2008 South Carolina Lidar: Union County. National Oceanic and Atmospheric Administration, <http://coast.noaa.gov/dataviewer>
214. Sapozhnikov, V. B., and E. Foufoula-Georgiou (1996), Do the Current Landscape Evolution Models Show Self-Organized Criticality?, *Water Resources Research*, 32 (4), 1109-1112, doi: 10.1029/96WR00161
215. Scatena, F. N. (1989), An introduction to the physiography and history of the Bisley experimental watersheds in the Luquillo Mountains of Puerto Rico, U.S. Department of Agriculture General Technical Report SO-72, 22 p
216. Scatena, F. N., and M. C. Larsen (1991), Physical aspects of Hurricane Hugo in Puerto Rico, *Biotropica*, 23 (4 A), 317-323
217. Scatena, F. N., and A. E. Lugo (1995), Geomorphology, disturbance, and soil and vegetation of two subtropical wet steepland watersheds of Puerto Rico, *Geomorphology*, 13, 199-213
218. Schellekens, J. (2000), Hydrological processes in a humid tropical rain forest: a combined experimental and modelling approach, Vrije Universiteit - Amsterdam.
219. Schellekens, J., F. N. Scatena, L. A. Bruijnzeel, A. I. J. M. van Dijk, M. M. A. Groen, and R. J. P. van Hogezaand (2004), Stormflow generation in a small rainforest catchment in the Luquillo Experimental Forest, Puerto Rico, *Hydrological Processes*, 18 (3), 505-530, doi: 10.1002/hyp.1335
220. Schlesinger, W. H. (1995), Soil respiration and changes in soil carbon stocks, in *Biotic Feedbacks in the Global Climate System: Will the Warming Feed the Warming?*, edited by G. M. Woodwell and F. T. Mackenzie, pp. 159-168, Oxford Univ. Press, New York.

221. Schultze, E. (1975), Some Aspects Concerning the Application of Statistics and Probability to Foundation Structures, paper presented at 2nd International Conference on Applications of Statistics and Probability in Soil and Structural Engineering,, Aachen.
222. Shanley, J. B., W. H. McDowell, and R. F. Stallard (2011), Long-term patterns and short-term dynamics of stream solutes and suspended sediment in a rapidly weathering tropical watershed, *Water Resources Research*, 47 (7), doi: 10.1029/2010WR009788
223. Simon, A., M. C. Larsen, and C. R. Hupp (1990), The role of soil processes in determining mechanisms of slope failure and hillslope development in a humid-tropical forest eastern Puerto Rico, *Geomorphology*, 3 (3-4), 263 - 286
224. Simoni, S., F. Zanotti, G. Bertoldi, and R. Rigon (2008), Modelling the probability of occurrence of shallow landslides and channelized debris flows using GEOTop-FS, *Hydrological Processes*, 22 (4), 532-545, doi: 10.1002/hyp.6886
225. Singh, V. P. (1997), Effect of spatial and temporal variability in rainfall and watershed characteristics on stream flow hydrograph, *Hydrological Processes*, 11 (12), 1649-1669, doi: 10.1002/(sici)1099-1085(19971015)11:12<1649::aid-hyp495>3.0.co;2-1
226. Smith, A. L., J. H. Schellekens, and A.-L. M. Díaz (1998), Batholiths as markers of tectonic change in the northeastern Caribbean, *Geological Society of America Special Papers*, 322, 99-122, doi: 10.1130/0-8137-2322-1.99
227. Smith, S. V., W. H. Renwick, R. W. Buddemeier, and C. J. Crossland (2001), Budgets of soil erosion and deposition for sediments and sedimentary organic carbon across the conterminous United States, *Global Biogeochemical Cycles*, 15 (3), 697-707, doi: 10.1029/2000GB001341
228. Smith, S. V., R. O. Sleezer, W. H. Renwick, and R. W. Buddemeier (2005), Fates of eroded soil organic carbon: Mississippi basin scale study, *Ecological Applications*, 15 (6), 1929-1940, doi: 10.1890/05-0073
229. Stallard, R. F. (1998), Terrestrial sedimentation and the carbon cycle: Coupling weathering and erosion to carbon burial, *Global Biogeochemical Cycles*, 12 (2), 231-257, doi: 10.1029/98GB00741
230. Stallard, R. F. (2012), Weathering, Landscape Equilibrium, and Carbon in Four Watersheds in Eastern Puerto Rico, in *Water quality and landscape processes of four watersheds in eastern Puerto Rico*, edited by S. F. Murphy and R. F. Stallard, pp. 199-247, U.S. Geol. Surv. Prof. Pap. 1789.
231. Stallard, R. F., and S. F. Murphy (2012), Water quality and mass transport in four watersheds in eastern Puerto Rico, in *Water quality and landscape processes of four watersheds in eastern Puerto Rico*, edited by S. F. Murphy and R. F. Stallard, pp. 113-152, U.S. Geol. Surv. Prof. Pap. 1789.

232. Stark, C. P., and N. Hovius (2001), The characterization of landslide size distributions, *Geophysical Research Letters*, 28 (6), 1091-1094, doi: 10.1029/2000GL008527
233. Stark, C. P., and P. Passalacqua (2014), A dynamical system model of eco-geomorphic response to landslide disturbance, *Water Resources Research*, 50 (10), 8216-8226, doi: 10.1002/2013WR014810
234. Stephenson, S. T., A. A. Chen, and A. M. Taylor (2007), Toward the development of prediction models for the primary Caribbean dry season, *Theoretical and Applied Climatology*, 92 (1), 87-101, doi: 10.1007/s00704-007-0308-2
235. Stoner, A. M. K., K. Hayhoe, X. Yang, and D. J. Wuebbles (2013), An asynchronous regional regression model for statistical downscaling of daily climate variables, *International Journal of Climatology*, 33 (11), 2473-2494, doi: 10.1002/joc.3603
236. Tarolli, P., and D. G. Tarboton (2006), A new method for determination of most likely landslide initiation points and the evaluation of digital terrain model scale in terrain stability mapping, *Hydrol. Earth Syst. Sci.*, 10 (5), 663-677, doi: 10.5194/hess-10-663-2006
237. Thomlinson, J. R., M. I. Serrano, T. d. M. Lopez, T. M. Aide, and J. K. Zimmerman (1996), Land-Use Dynamics in a Post-Agricultural Puerto Rican Landscape (1936-1988), *Biotropica*, 28 (4), 525-536, doi: 10.2307/2389094
238. Tobutt, D. C. (1982), Monte Carlo Simulation methods for slope stability, *Computers & Geosciences*, 8 (2), 199-208, doi: [http://dx.doi.org/10.1016/0098-3004\(82\)90021-8](http://dx.doi.org/10.1016/0098-3004(82)90021-8)
239. Trimble, S. W. (1974), *Man-Induced Soil Erosion on the Southern Piedmont 1700-1970* pp., Soil Conserv. Soc. Am., Ankeny, Iowa.
240. Tucker, G. E., S. T. Lancaster, N. M. Gasparini, and R. L. Bras (2001a), The Channel Hillslope Integrated Landscape Development (CHILD) model, in *Landscape Erosion and Sedimentation Modeling*, edited, pp. 349-388.
241. Tucker, G. E., S. T. Lancaster, N. M. Gasparini, R. L. Bras, and S. M. Rybarczyk (2001b), An object-oriented framework for distributed hydrologic and geomorphic modeling using triangulated irregular networks, *Computers & Geosciences*, 27 (8), 959-973, doi: 10.1016/S0098-3004(00)00134-5
242. U.S.D.A. (1951), Soil survey manual, *U.S. Dep. Agric. Handbook*
243. U.S.G.S. (2009), 1/3-Arc Second National Elevation Dataset, U.S. Geological Survey, Sioux Falls, SD
244. van Genuchten, M. T. (1980), A Closed-form Equation for Predicting the Hydraulic Conductivity of Unsaturated Soils1, *Soil Sci. Soc. Am. J.*, 44 (5), 892-898, doi: 10.2136/sssaj1980.03615995004400050002x

245. Van Oost, K., G. Govers, T. A. Quine, G. Heckrath, J. E. Olesen, S. De Gryze, and R. Merckx (2005), Landscape-scale modeling of carbon cycling under the impact of soil redistribution: The role of tillage erosion, *Global Biogeochemical Cycles*, 19 (4), GB4014, doi: 10.1029/2005GB002471
246. Van Oost, K., G. Verstraeten, S. Doetterl, B. Notebaert, F. Wiaux, N. Broothaerts, and J. Six (2012), Legacy of human-induced C erosion and burial on soil-atmosphere C exchange, *Proceedings of the National Academy of Sciences*, 109 (47), 19492-19497, doi: 10.1073/pnas.1211162109
247. Van Oost, K., T. A. Quine, G. Govers, S. De Gryze, J. Six, J. W. Harden, J. C. Ritchie, G. W. McCarty, G. Heckrath, C. Kosmas, J. V. Giraldez, J. R. M. da Silva, and R. Merckx (2007), The Impact of Agricultural Soil Erosion on the Global Carbon Cycle, *Science*, 318 (5850), 626-629, doi: 10.1126/science.1145724
248. Vandre, B. C. (1985), Rudd Creek debris flow, in Bowles DS (ed) *Delineation of landslide, flash flood, and debris flow hazards in Utah*, edited, pp. 117-131, General Series Rep UWRL/G-85/03, Utah Water Research Laboratory, Utah State University, Logan, Utah.
249. Vivoni, E. R., V. Y. Ivanov, R. L. Bras, and D. Entekhabi (2004), Generation of triangulated irregular networks based on hydrological similarity, *Journal of Hydrologic Engineering*, 9, 288-302, doi: 10.1061/(ASCE)1084-0699(2004)9:4(288)
250. von Ruetten, J., P. Lehmann, and D. Or (2014), Effects of rainfall spatial variability and intermittency on shallow landslide triggering patterns at a catchment scale, *Water Resources Research*, 50 (10), 7780-7799, doi: 10.1002/2013WR015122
251. Wadsworth, F. H. (1950), Notes on the climax forests of Puerto Rico and their destruction and conservation prior to 1990, *Caribbean Forester*, 11, 38-56
252. Waide, R. B., J. K. Zimmerman, and F. N. Scatena (1998), Controls of Primary Productivity: Lessons from the Luquillo Mountains in Puerto Rico, *Ecology*, 79 (1), 31-37, doi: 10.1890/0012-9658(1998)079[0031:COPPLF]2.0.CO;2
253. Wang, H., C. A. S. Hall, F. N. Scatena, N. Fetcher, and W. Wu (2003), Modeling the spatial and temporal variability in climate and primary productivity across the Luquillo Mountains, Puerto Rico, *Forest Ecology and Management*, 179, 69-94
254. Wang, Z., S. Doetterl, M. Vanclooster, B. van Wesemael, and K. Van Oost (2015), Constraining a coupled erosion and soil organic carbon model using hillslope-scale patterns of carbon stocks and pool composition, *Journal of Geophysical Research: Biogeosciences*, 120 (3), 452-465, doi: 10.1002/2014JG002768
255. Weaver, P. L., and P. G. Murphy (1990), Forest Structure and Productivity in Puerto Rico's Luquillo Mountains, *Biotropica*, 22 (1), 69-82



256. West, A. J., C. W. Lin, T. C. Lin, R. G. Hilton, S. H. Liu, C. T. Chang, K. C. Lin, A. Galy, R. B. Sparkes, and N. Hovius (2011), Mobilization and transport of coarse woody debris to the oceans triggered by an extreme tropical storm, *Limnology and Oceanography*, 56 (1), 77-85, doi: 10.4319/lo.2011.56.1.0077
257. White, A. F., and S. L. Brantley (2003), The effect of time on the weathering of silicate minerals: why do weathering rates differ in the laboratory and field?, *Chemical Geology*, 202 (3–4), 479-506, doi: <http://dx.doi.org/10.1016/j.chemgeo.2003.03.001>
258. Wilk, M. B., and R. Gnanadesikan (1968), Probability Plotting Methods for the Analysis of Data, *Biometrika*, 55 (1), 1-17, doi: 10.2307/2334448
259. Wilson, C. B., J. B. Valdes, and I. Rodriguez-Iturbe (1979), On the influence of the spatial distribution of rainfall on storm runoff, *Water Resources Research*, 15 (2), 321-328, doi: 10.1029/WR015i002p00321
260. Wilson, C. G., A. N. T. Papanicolaou, and O. Abaci (2009), SOM dynamics and erosion in an agricultural test field of the Clear Creek, IA watershed, *Hydrol. Earth Syst. Sci. Discuss.*, 6 (2), 1581-1619, doi: 10.5194/hessd-6-1581-2009
261. Wohl, E., and F. L. Ogden (2013), Organic carbon export in the form of wood during an extreme tropical storm, Upper Rio Chagres, Panama, *Earth Surface Processes and Landforms*, 38 (12), 1407-1416, doi: 10.1002/esp.3389
262. Wu, T., and L. Kraft (1967), The Probability of Foundation Safety, *Journal of the Soil Mechanics and Foundations Division*, 93 (5), 213-231
263. Yalin, M. S. (1977), *Mechanics of Sediment Transport*, Pergamon, Tarrytown, NY.
264. Yoo, K., R. Amundson, A. M. Heimsath, and W. E. Dietrich (2005), Erosion of upland hillslope soil organic carbon: Coupling field measurements with a sediment transport model, *Global Biogeochemical Cycles*, 19 (3), GB3003, doi: 10.1029/2004GB002271
265. Yoo, K., R. Amundson, A. M. Heimsath, and W. E. Dietrich (2006), Spatial patterns of soil organic carbon on hillslopes: Integrating geomorphic processes and the biological C cycle, *Geoderma*, 130 (1–2), 47-65, doi: 10.1016/j.geoderma.2005.01.008
266. Yoo, K., J. Ji, A. Aufdenkampe, and J. Klaminder (2011), Rates of soil mixing and associated carbon fluxes in a forest versus tilled agricultural field: Implications for modeling the soil carbon cycle, *Journal of Geophysical Research: Biogeosciences*, 116 (G1), n/a-n/a, doi: 10.1029/2010JG001304
267. Yucemen MS, Tang WH, and A. AHS. (1975), Long term stability of soil slopes - a reliability approach, paper presented at Second Int. Conf. Applications of Statistics and Probability to Soil and Structural Eng., Aachen, Germany., 15-18 September 1975.

268. Zarin, D. J. (1993), Nutrient accumulation during succession in subtropical lower montane wet forests, Puerto Rico, 182 pp, Philadelphia, University of Pennsylvania, Ph.D. dissertation.
269. Zarin, D. J., and A. H. Johnson (1995), Base saturation, nutrient cation, and organic matter increases during early pedogenesis on landslide scars in the Luquillo Experimental Forest, Puerto Rico, *Geoderma*, 65 (3–4), 317-330, doi: [http://dx.doi.org/10.1016/0016-7061\(94\)00048-F](http://dx.doi.org/10.1016/0016-7061(94)00048-F)